REACTING JETS IN COMPRESSIBLE VITIATED CROSSFLOW WITH NEGLIGIBLE SWIRL

by

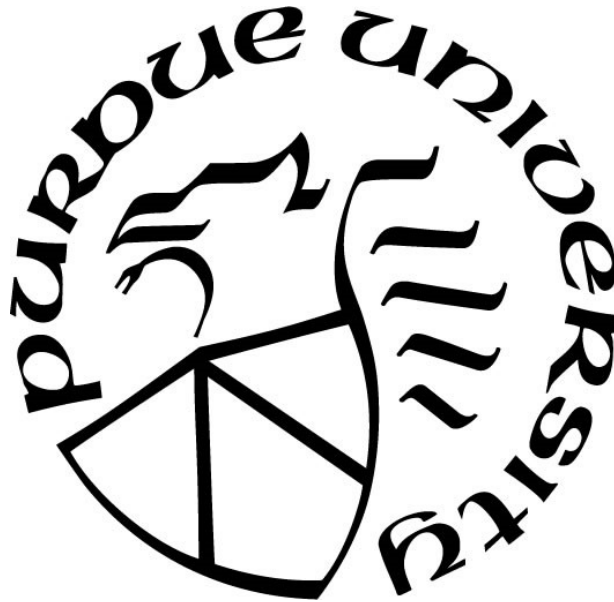**Neil S. Rodrigues**

A Dissertation

Submitted to the Faculty of Purdue University

In Partial Fulfillment of the Requirements for the degree of

Doctor of Philosophy

School of Mechanical Engineering

West Lafayette, Indiana

May 2020

THE PURDUE UNIVERSITY GRADUATE SCHOOL
STATEMENT OF COMMITTEE APPROVAL

Dr. Robert P. Lucht, Chair

School of Mechanical Engineering

Dr. Li Qiao

School of Aeronautics and Astronautics

Dr. Terrence R. Meyer

School of Mechanical Engineering

Dr. Paul E. Sojka

School of Mechanical Engineering

Approved by:

Dr. Nicole L. Key

To my parents and brother.

Go forth and set the world on fire.

- St. Ignatius of Loyola

Did you hear about the rose that grew

from a crack in the concrete?

Proving nature's law wrong it

learned to walk without having feet.

Funny it seems, but by keeping its dreams,

it learned to breathe fresh air.

Long live the rose that grew from the concrete

When no one else ever cared.

- Tupac Shakur

ACKNOWLEDGMENTS

Haiti and spending a year teaching Sunday school to 3rd graders. I'm also grateful for the many friendships I have made here through St. Tom's. I also am grateful for the long-distance friendships that I have maintained during my time as a Ph.D. student. Special thanks to those who have visited me over the last few years: Arinze, Kevin, KG, and Evan. I also thank Kate for her steady companionship for nearly the last three years of my Ph.D. work. I don't know of many people who can say that they were fortunate enough to earn a Ph.D. from working at the Zucrow Labs *and* were able to get something much better than a Ph.D.

PREFACE

This dissertation document is a compilation of research efforts relating to the study of a reacting jet in crossflow at engine-relevant conditions and within a high-speed vitiated crossflow. The research efforts span the course of design work, commissioning and validation of the experiment, and the application of laser-based diagnostics. Five distinct but closely related research efforts, that have been separated into Chapter 2 – 6, are discussed in this document. Chapter 2 and 3 already appear in the scientific literature:

Rodrigues NS, Busari O, Senior WCB, McDonald CT, North AJ, Chen Y, Laster WR, Meyer SE, Lucht RP. The Development and Performance of a Perforated Plate Burner to Produce Vitiated Flow with Negligible Swirl under Engine-Relevant Gas Turbine Conditions. *Review of Scientific Instruments 90*. July 2019, pp. 075107-1 – 075107-14, (2019) doi.org/10.1063/1.5100180.

Rodrigues NS, Busari O, Senior WCB, McDonald CT, Chen Y, North AJ, Laster WR, Meyer SE, Lucht RP. NO_X Reduction in an Axially Staged Gas Turbine Model Combustor through increase in the Combustor Exit Mach Number. *Combustion and Flame 212*. January 2020, pp. 282 – 294, doi.org/10.1016/j.combustflame.2019.10.039.

Work is currently in-progress to finalize the preparation of three additional manuscripts based on the materials in Chapters 4, 5, and 6.

TABLE OF CONTENTS

LIST OF TABLES

LIST OF FIGURES

ABSTRACT

Combustion will likely continue to be utilized over the next century to meet the world's energy needs. As increasingly stringent requirements on emissions, particularly of oxides of nitrogen (NO and NO_2) are imposed on power plants due to their harmful effects on the environment, advanced combustor strategies to limit NO_X productions are needed. One such advanced concept involves axially staging the fuel to create a distributed combustion system. The fundamental problem for staged combustion involves the injection of a reacting jet into crossflow. This canonical problem is modified for this dissertation through injection of a reacting premixed natural gas and air jet into a compressible vitiated crossflow with negligible swirl. In addition, the experimental efforts for this work were conducted at elevated inlet air temperature and combustor pressure.

The development and performance of a perforated plate burner (PPB) to provide vitiated crossflow and operating using premixed natural gas (NG) and air at engine-relevant conditions is discussed. A significant benefit of using burners with simplified flow fields, such as the PPB, for experimental studies in the laboratory is the potential for decoupling the complex fluid dynamics in typical combustors from the chemical kinetics. The stable operation of the PPB within a high-pressure test rig was validated: successful ignition, effective use of redlines for flashback mitigation, and long duration steady-state operation in both piloted and non-piloted modes were all observed. Exhaust gas emissions measured using a Fourier-transform infrared (FTIR) spectrometer showed very good performance of the PPB in terms of the combustion efficiency and low levels of NO_X in non-piloted operation that were generally within 3 ppm.

Emissions measurements of the premixed reacting jet in vitiated crossflow were obtained for a variety of conditions and a significant NO_X reduction was achieved when the staged combustor exit Mach number was increased and the axial residence time was decreased. Based on this preliminary investigation, a test matrix was developed to independently vary the exit Mach number for a constant axial residence time by using modular rig hardware to change the length of the axial combustor. Up to 70% reduction in NO_X produced by the axial stage was observed when the combustor exit Mach number was increased from about 0.26 to 0.66 at a constant residence time of 1.4 ms. NO_X reduction based on variation in the Mach number and at a constant residence time has not been previously reported in the literature to the best of our knowledge. This decrease

in NO_X is hypothesized to be due to the lower static temperature of a compressible flow and potentially better mixing of the jet with the crossflow due to the interaction occurring at high speeds.

Based on the strong effect of Mach number for NO_X reduction even at a constant residence time, further investigation using laser-based diagnostics is needed to provide insight on physical processes controlling this phenomenon. An optically-accessible secondary combustion zone was developed and fabricated to study the flame position and structure of reacting jets injected into a high-speed vitiated crossflow. The windowed combustor was capable of long-duration, steady-state operation despite a trifecta of: elevated pressures, high combustion gas temperatures, and high-speed reacting flows. High-speed imaging using OH* and CH* chemiluminescence was used to validate operation of the optically-accessible secondary combustion zone.

High-repetition-rate (1 – 10 kHz) planar laser-induced fluorescence (PLIF) imaging of OH and CH were performed on both premixed NG-air reacting jets and premixed NG-hydrogen-air reacting jets to investigate the flame structure of the reacting jet within a high-speed crossflow. OH-PLIF was performed in the A-X electronic system using excitation at near 283 nm in the (v′ = 1, v″ = 0) band and near 311 nm in the (v′ = 0, v″ = 0) band. The crossflow velocity and equivalence ratio were observed to have a strong impact on the stabilization of the reacting jet flame. Additional insight on the stabilization mechanism was obtained using 50 kHz OH* chemiluminescence imaging. CH-PLIF was performed in the C-X electronic system using R-branch excitation near 311 nm in the (v′ = 0, v″ = 0) band. The CH-PLIF images indicated local stoichiometric regions near the leeward side of jet injection and in regions where significant interaction of the fuel rich jet with the vitiated crossflow is expected. In addition, the CH-PLIF images showed evidence of broken, thickened, non-premixed reaction layers.

1.   INTRODUCTION

Natural gas fired power plants will likely continue to power the world's increasing energy needs over the next century due to their low carbon intensity, little processing needs, and relatively clean combustion (Tertzakian, 2009). As increasingly stringent requirements on emissions, particularly of nitric oxides (NO and NO_2) are imposed on power plants due to their harmful effects on the environment, advanced combustor strategies to limit nitric oxide productions are needed. One such advanced concept involves axially staging the fuel to create a distributed combustion system. This concept has been investigated for nearly 50 years with rig-level research efforts starting with Pratt & Whitney engines in the 1990s (Segalman *et al.*, 1993). The fundamental problem for staged combustion involves the injection of a reacting jet into crossflow. This canonical problem is modified for this dissertation through injection into: (1) vitiated flow at typical combustion gas temperatures/composition and elevated inlet air and combustor pressure conditions, thereby allowing for engine-relevant chemical kinetics, (2) vitiated flow at high-speeds, thereby introducing compressibility effects into the physics of the problem, (3) vitiated flow without the swirling component in the flow, thereby allowing for easier evaluation with high-fidelity computational fluid dynamics simulations.

Due to their non-intrusive nature, laser-based diagnostics are the preferred method of investigating combustion phenomena. An overview of a variety of diagnostics techniques can be found in references such as Eckbreth (1996). The two most relevant techniques for this work are: emissions sampling of the exhaust gas using Fourier transform infrared spectroscopy (FTIR) and imaging of the combustion zone using planar laser induced fluorescence (PLIF). The FTIR technique is based on: passing an infrared beam through the gas sample, deconstructing the resultant signal using the Fourier transform, and comparing the absorbance spectrum of an unknown gas sample to a calculated spectrum based on calibrations. A review of the FTIR technique can be found at websites of manufacturers such as MKS Instruments and Thermo Fisher Scientific. PLIF is a spatially-resolved absorption spectroscopy technique involving the excitation of a molecule from the ground electronic level by laser absorption to a higher level. Some of the exited molecules emit photons (i.e. fluorescence) after a period of time as they relax from the exited state to a lower electronic level. The most common application of PLIF for combustion involves exciting the OH (hydroxyl) molecule.

The work presented in this Dissertation focuses on the experimental investigation of reacting jets in a compressible vitiated crossflow with negligible swirl at elevated inlet air temperatures and elevated combustor pressures. Chapter 2 of this document focuses on the development and performance of a perforated plate burner at engine-relevant conditions. The design development of the burner is described for operation within a high-pressure test rig at gas turbine engine-relevant conditions. The performance of the burner is illustrated with temperature and pressure measurements used for rig-condition monitoring and emissions measurements of the exhaust gas using an FTIR system. The perforated plate burner was used as the source for the vitiated crossflow with negligible swirl. Chapter 3 focuses on NO_X emissions produced by the transverse injection of a reacting jet in compressible, vitiated crossflow with negligible swirl at engine-relevant conditions. Exhaust gas measurements using the FTIR system were obtained for the axially staged combustion system as a function of the exit Mach number and axial residence time. A test matrix was developed and executed in order to decouple the effects of exit Mach number and axial residence time.

Based on the reduction in NO_X observed in Chapter 3, it is clear that optical access would provide much more insight on the physics behind the emissions reduction. The design development of an optically-accessible secondary combustion zone is described in Chapter 4. This design does not feature an inner nitrogen film-cooling but rather incorporates an air-cooling design in-between double windows to manage the heat load. Successful operation of the windowed section was demonstrated using chemiluminescence imaging. Chapter 5 describes the flame stabilization, position, and structure of premixed reacting jets into a high-speed crossflow using OH*-chemiluminescence and OH-PLIF. In particular, the effect of flame stabilization mechanism on NO_X emissions and mixing of the reacting jet with the vitiated crossflow is described. Chapter 6 demonstrates CH-PLIF in the C-X electronic system using R-branch excitation. This PLIF technique has been very recently demonstrated in Dr. Cam's Carter's group at AFRL at this chapter is the first work to our knowledge with demonstration at engine-relevant conditions.

2.   DEVELOPMENT AND PERFORMANCE OF A PERFORATED PLATE BURNER TO PRODUCE VITIATED CROSSFLOW WITH NEGLIGIBLE SWIRL UNDER ENGINE-RELEVANT CONDITIONS.

2.1   Introduction

Combustion of natural gas (NG) has the benefit of being more environmentally friendly than combustion of coal and other fossil fuels. Recent developments in natural gas extraction technologies have also allowed for economical production costs (Tester *et al*., 2005). Therefore, over the last decade natural gas combustion has become an increasingly important source of energy for electrical power generation. Understanding NG-air combustion under practical application conditions continues to be of great interest as the acceptable limits of emissions levels, particularly for oxides of nitrogen (NO_X) and carbon monoxide (CO), set by regulatory agencies continues to decrease. Furthermore, investigations of advanced combustion strategies, such as axially staging the fuel, are needed to limit NO_X production and meet regulatory requirements.

Strategies to control emissions generally focus on using premixed fuel and air at lean conditions (thereby decreasing the combustion flame temperature) and reducing the residence time of the combustion gases before the turbine expansion (Cooper and Alley, 2011). In recent years, low-swirl burners have been used as part of dry-low-NO_X combustors (Johnson *et al.*, 2015). Burning at very lean conditions, however, can lead to mechanical damage caused by pressure pulsations from combustion instabilities. In addition, emissions of carbon monoxide (CO) and unburned hydrocarbons (UHC) increase significantly as the lean blow-out (LBO) limit is approached. There is also a lower limit for the residence time since the oxidation of CO to CO_2 occurs relatively late in the combustion process (Glassman *et al.*, 2015).

Identifying the limit at which traditional natural gas fired combustors can be operated for reduced NO_X and acceptable levels of CO and UHC must involve isolating the effects of: (1) the degree of mixing for the premixed fuel and air, (2) lower flame temperatures, and (3) reduced residence times. Due to the dependence of chemical kinetics on inlet conditions such as premixed gas temperature and combustor pressure, experimental investigations at practical engine conditions are necessary. In addition, prominent kinetic drivers can only be discovered by decoupling the complex fluid dynamics in typical combustors from the chemical kinetics. This is particularly true for axially staged combustion experiments. At its core, the axial stage of the

staged combustor is a reacting jet issuing into a vitiated crossflow. Reacting jet in crossflow (RJICF) experiments with a swirling crossflow are very difficult to replicate via numerical simulations due to the complexity of the swirl. Therefore, a source of vitiated flow with negligible swirl would help provide valuable data sets for improved understanding of axially staged combustors.

This chapter summarizes the development and initial performance data for a perforated plate burner (PPB) operating at conditions relevant to gas turbine engines for power generation purposes. The simple geometry of the PPB and the resulting simplified flow field provides less complex fluid mechanics for the evaluation of detailed chemical kinetics models. The design methodology of the burner for successful operation at elevated temperature and pressure is elucidated, with particular emphasis on burner geometry selection and flashback mitigation. A description of the test rig to house the PPB, including instrumentation and flow control, is provided. Experimental measurements of the burner at gas turbine engine-relevant conditions using temperature and pressure instrumentation are presented, including typical ignition and activation of red-line aborts due to flashback and high burner plate metal temperature. Exhaust gas emissions measurements using a Fourier-transform infrared (FTIR) spectroscopy system are obtained to characterize the PPB. Our primary motivation for the development of this PPB was to use it as the source of vitiated crossflow with negligible swirl for axially staged combustion experiments and this is demonstrated with a premixed natural gas and air reacting jet.

2.2   Perforated plate burner design

A perforated plate burner (PPB) was selected early in the design process as the most suitable concept to provide a source of vitiated flow for jet-in-crossflow experiments in order to eliminate the complex fluid mechanics inherent in typical swirl burners. Aiding in reaching this decision during the concept selection process was reviewing work conducted by Cabra (2004), who selected the PPB concept after examining a variety of concepts including: catalytic burners, tube bundle burners, and porous disk burners.

2.2.1 PPB geometry and material selection

The only known works in existing literature where a PPB was operated at engine-relevant conditions, to the best of our knowledge, were conducted by Leonard and Steigmeir (1990) and Elkady *et al.* (2012). Both studies used the PPB for detailed study of NO_X production for perfectly premixed flames. Recent works of PPB operation at atmospheric pressure include studies by Van Maaren *et al.* (2007), Rodrigues and Fernandes (2014), and Rashwan *et al.* (2016). Cabra (2004) and North (2013) used PPBs to produce the vitiated co-flow for jet flame experiments at atmospheric pressure. A schematic of the flow field at the PPB surface for turbulent flames is provided in Fig. 2.1. Optimal spacing between the holes can result in better bluff-body recirculation zones, which can extend the extinction limit due to the higher temperatures associated with the recirculation of the hot gas (Cabra, 2004).

Operating limits for burner design were determined based on the requirements for mass flow rates of air (0.3 – 1.0 kg/s), elevated inlet temperature (T_3 = 550 K), and combustor pressure (P_4 = 500 kPa). The PPB geometry was selected based on consideration of laminar flame speed calculations and quenching diameter correlations. A thorough literature review was also conducted when deciding the PPB hole size. However, values from literature could only be used as guidelines, since most of the existing studies did not operate the burner at engine-relevant conditions.

CHEMKIN (V. 18.1) was used to calculate the laminar flame speed S_L at a range of equivalence ratios (0.45 < ϕ < 0.85) for premixed natural gas and air combustion at four different inlet temperature and combustor pressure combinations. The laminar flame speed provides some insight into the possibility of flashback due to the flame potentially propagating upstream of the burner holes. Figure 2.2 presents the laminar flame speed versus equivalence ratio for: atmospheric conditions (T_3 = 298 K and P_4 = 101 kPa), elevated combustor pressure only (T_3 = 298 K and P_4 = 500 kPa), elevated inlet temperature only (T_3 = 550 K and P_4 = 101 kPa), and both elevated inlet temperature and combustor pressure (T_3 = 550 K and P_4 = 500 kPa). As expected, increasing ϕ resulted in a faster S_L for each of the four cases. An increase in inlet temperature from T_3 = 298 K to T_3 = 550 K results in an increase in laminar flame speed of nearly 700% at ϕ = 0.45 and just over 200% at ϕ = 0.85 for P_4 = 101 kPa and P_4 = 500 kPa cases. An

increase in combustor pressure from $P_4 = 101$ kPa to $P_4 = 500$ kPa results in a decrease in S_L by nearly 65% at $\phi = 0.45$ and over 40% at $\phi = 0.85$ for both the $T_3 = 298$ K and $T_3 = 550$ K cases. Since increased inlet temperature and increased combustor pressure have opposing effects on the laminar flame speed, comparing the $T_3 = 550$ K and $P_4 = 500$ kPa case with the atmospheric temperature and pressure case shows an increase in S_L by 180% for $\phi = 0.45$ and by 73% for $\phi = 0.85$. A design requirement for the hole velocity U_h within the PPB holes was established as at least an order of magnitude greater than the laminar flame speed.

The quenching diameter for methane-air flames was considered during PPB hole size selection in order to reduce the risk of flashback. Turns (2012) reports a quenching diameter of 3.6 mm for $\phi = 0.6$ at $T_3 = 298$ K and $P_4 = 101$ kPa along with scaling analysis for elevated temperatures and pressures. Figure 2.3 presents the quenching diameter at $\phi = 0.6$ versus inlet temperatures at combustor pressures of 101 kPa, 300 kPa, and 500 kPa. The quenching diameter was calculated to decrease quite significantly with both increased inlet temperatures and elevated combustor pressures. When scaled to the design condition of $T_3 = 550$ K and $P_4 = 500$ kPa, the quenching diameter at $\phi = 0.6$ was reduced from 3.6 mm at atmospheric conditions to 0.7 mm at the elevated conditions. The decrease in quenching diameter with an increase in pressure is mainly due to the thermal diffusivity, which is directly proportional to the quenching diameter and inversely proportional to pressure.

Based on this analysis and consultation with several machine shops, it was decided that a PPB hole diameter less than the quenching diameter would be prohibitive due to cost (due to the thousands of holes needed to satisfy the air mass flow rate range). Instead, several other considerations were later included into the design of the test rig to aid with flashback mitigation. A hole diameter $d_h = 1.98$ mm (5/64″) was ultimately selected due to this dimension being similar to perforated plate burners in existing literature and due to the ease of fabrication using a CNC mill at this specification. The overall diameter of the PPB was selected to be 39.4 cm to fit within the pressure vessel, which was designed in parallel to the burner.

The porosity of the perforated plate P_{PPB} is an important parameter for flame stabilization and flashback prevention and is defined as:

$$P_{\text{PPB}} = \frac{nA_{\text{h}}}{A_{\text{PPB,active}}}, \tag{2.1}$$

where n is the total number of holes, A_{h} is the area of each hole, and $A_{\text{PPB,active}}$ is the active area of the perforated plate burner (total area of holes plus area between holes). The active area was determined based on the locations of the outermost holes closest to the edge of the plate. Lower porosity can improve stabilization since the greater spacing between holes can lead to larger bluff-body recirculation zones (Cabra, 2004). Lower porosity can also aid in flashback prevention by increasing the PPB acceleration ratio a_{PPB}, which is defined as:

$$a_{\text{PPB}} = \frac{U_{\text{h}}}{U_{\text{p}}} = \frac{1}{P}, \tag{2.2}$$

where U_{h} and U_{p} are the premixed gas velocity inside a PPB hole and in the plenum upstream of the PPB, respectively. The required air flow rates and spacing between holes were also considered when determining porosity. Lower porosity reduces the effective flow area. Although larger spacing between holes promotes bluff-body recirculation, during the ignition process a hole must be close enough to its neighbors to ignite them, which subsequently ignites the entire plate.

A porosity of 0.15 was ultimately selected for this PPB, which corresponds to an acceleration ratio of 6.7. A spacing of 5.08 mm was selected between holes, which were arranged in a hexagonal pattern to pack the maximum number of holes into the given area. A section of the PPB hole pattern is shown in Fig. 2.4. Based on the active plate area, hole diameter, and porosity, the final design featured 5404 individual holes (not including the center hole, which was outfitted with a protruding tube for a hydrogen pilot flame). A plate thickness of 1.3 cm was ultimately selected since it was of a similar thickness to some PPBs in literature and allowed for costs to remain at a manageable level. Compared to the PPBs operated at elevated pressure in literature, this perforated plate burner features a greater number of holes by over two orders of magnitude (less than 40 holes were used by Leonard and Correa and Elkady *et al.*). Another major difference is the combustion air flow rate range up to 1.15 kg/s targeted for this PPB, compared to the 0.03 kg/s combustion air flow rate by Leonard and Correa and 0.55 kg/s of total air (combustion air plus liner cooling air) by Elkady *et al.* The key design parameters for the PPB used in this work are summarized in Table 2.1.

Brass and copper were the top choices for PPB material due to their high thermal conductivity, high melting temperature, and relatively low cost. High thermal conductivity was desired because it allows the PPB to reach steady-state temperature in a short time. 260 brass was ultimately selected as the material of choice upon consultations with several machine shops, since drilling a large number of holes into brass would be less expensive than drilling into copper. Two thermocouple probes were installed on the upstream surface of the PPB at radial locations $r = 1$ cm and $r = 17$ cm from the center of the plate to monitor the plate temperature during operation.

Table 2.1: Key design parameters for the Perforated Plate Burner.

PPB Design Parameters (260 Brass)	
Plate Thickness	13 [mm]
Hole Diameter	1.98 [mm]
Number of Holes	5404
Hole Pitch	5.08 [mm]
Porosity	0.15 [-]
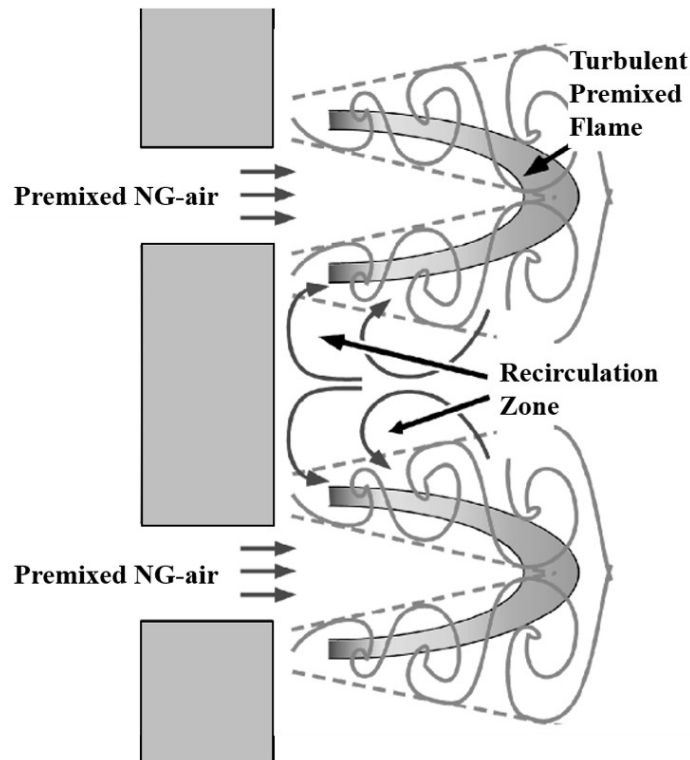
Figure 2.1: Schematic of flow field associated with turbulent premixed flames stabilized over a Perforated Plate Burner (modified from Cabra, 2005).
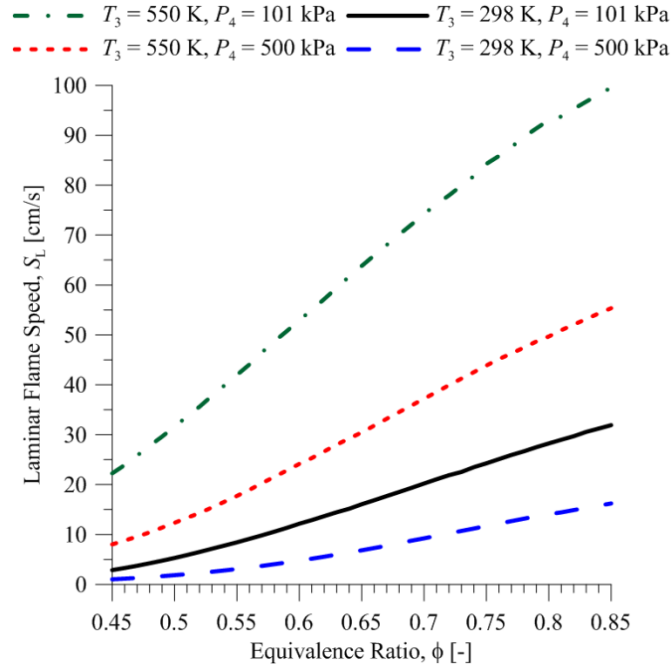
Figure 2.2: Laminar flame speed versus equivalence ratio for NG-air combustion at four inlet temperature and combustor pressure combinations.
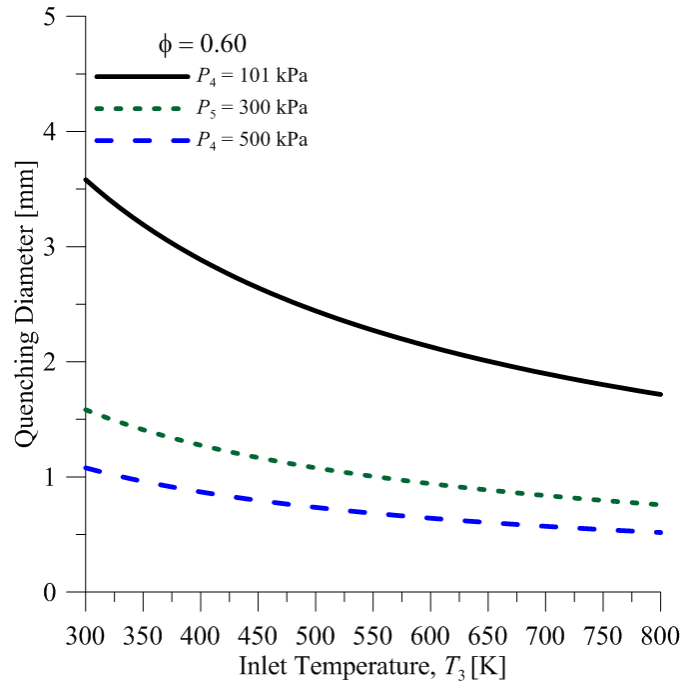
Figure 2.3: Quenching diameter versus inlet temperature for methane-air combustion at $\phi = 0.60$ and three combustor pressures.
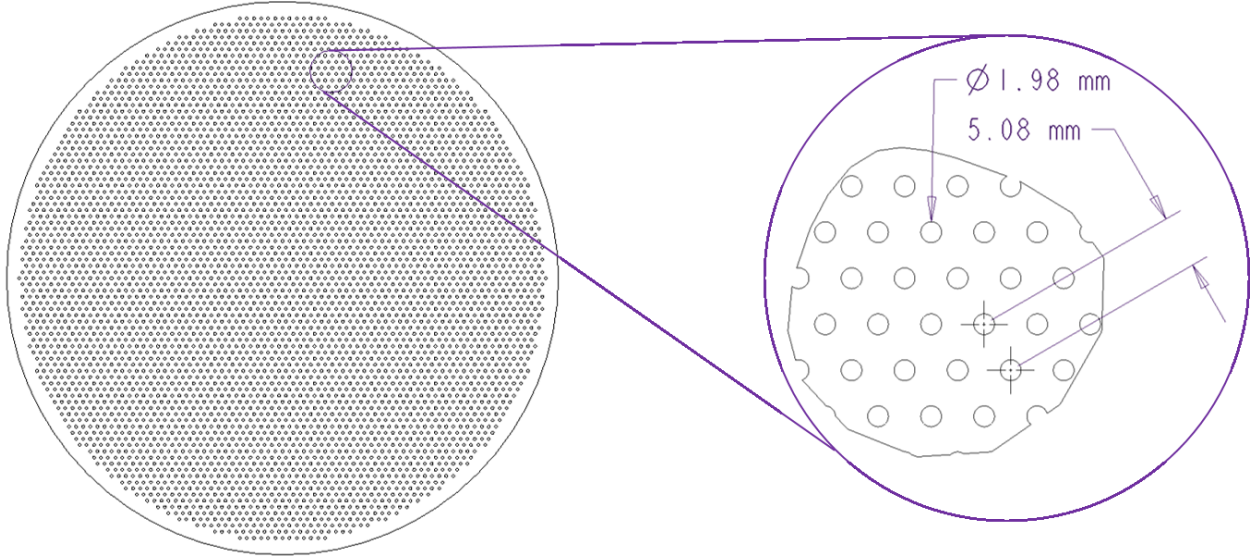
Figure 2.4: Schematic of the PPB hole geometry.

2.2.2 Flashback mitigation

The PPB design incorporated several features to mitigate the risk of flashback: a flame arrestor, red-line logic in the control system to shut off fuel, installation of a burst-disc in the upstream plenum, and the ignition of the PPB using a hydrogen pilot flame (which was to be ignited using laser ignition). A custom flame arrestor was designed featuring a 12 mm thick brass plate with 19 hexagonal pockets cut into the materials. 4123 holes in total were drilled into the 19 pockets, with the holes featuring a diameter of 0.9 mm and a depth of about 3.2 mm. The flame arrestor design featured a porosity of 0.02 and an acceleration ratio of 44.

Remote control of the experiment was required due to the significant potential energy contained within a high pressure experiment. A National Instruments LabVIEW Virtual Instrument (VI) was developed for live control of the experiment and was programmed with a live red-line monitoring system in the event of flashback. Fuel to the experiment was automatically shut off if the red-line abort was activated. Conditions to activate the *flashback red-line* consisted of: (1) premixed gas temperature measurement by a thermocouple (TC) exceeding 810 K, which is approximately 50% greater than the design inlet temperature, and (2) combustor pressure measurement exceeded 670 kPa, which is approximately 35% greater than the design combustor pressure. A *plate temperature red-line* was also incorporated to shut off fuel if a thermocouple probe located on the upstream surface of the PPB exceeded 810 K, which is about 70% of the melting temperature of brass. A burst-disc with a rupture rating of 1105 kPa was also installed in

the plenum upstream of the sintered metal plate in case a flashback event was to result in detonation rather than deflagration. Figure 2.5 presents the pressure due to a constant volume combustion event, along with the nominal operating combustor pressure, the red-line pressure abort, and the burst-disc pressure rating.

Due to the elevated risk of flashback with igniting the PPB inside a pressure vessel, a smooth ignition event is desirable rather than the potentially hard ignition event from a sparkplug located near a wall. Ignition as a result of a spark created from a tightly focused laser beam was therefore chosen as the preferred means of ignition. In addition, rather than using a laser to ignite the premixed natural gas and air mixture, an ignition pilot flame was incorporated into the burner design. The middle hole of the PPB was designed to be slightly larger to allow the press-fit of a stainless-steel tube (with an inner diameter of about 2.2 mm) to protrude by about 10 mm. A natural gas jet flame was initially proposed for the pilot ignition flame. However, initial experiments showed that the natural gas jet had a propensity to blow-off due to the presence of the co-flowing air. Therefore, a hydrogen jet flame, which has excellent flame stability, was ultimately selected for the ignition pilot flame. Figure 2.6 presents a schematic of the ignition process with the laser beam first igniting the hydrogen flame and the hydrogen flame then igniting the NG-air flame. Operating the PPB with both the NG-air premixed flame and the hydrogen pilot flame is referred to as the *piloted PPB*. Operating with only the NG-air premixed flame (with the hydrogen flame turned off) is referred to as the *non-piloted PPB*. During non-piloted PPB operation, instead of hydrogen, a very small amount of nitrogen (less than 1% of combustion air) was designed to flow through the protruding tube in order to prevent the tube from being burned by the NG-air flame.

2.3 Test rig and facility

The perforated plate burner (PPB) was installed within a high pressure combustion test rig, which was designed and developed for staged combustion experiments. A schematic is presented in Fig. 2.7, which shows the main assemblies of the test rig: *headend stage*, *axial stage*, and *NO_X quench and sampling*. The headend stage consisted primarily of the NG-air premixing pipe, the perforated plate burner, a film cooling flange, and a flow contraction. The NG-air adiabatic flame temperature at the perforated plate burner was primarily varied by adjusting the equivalence ratio.
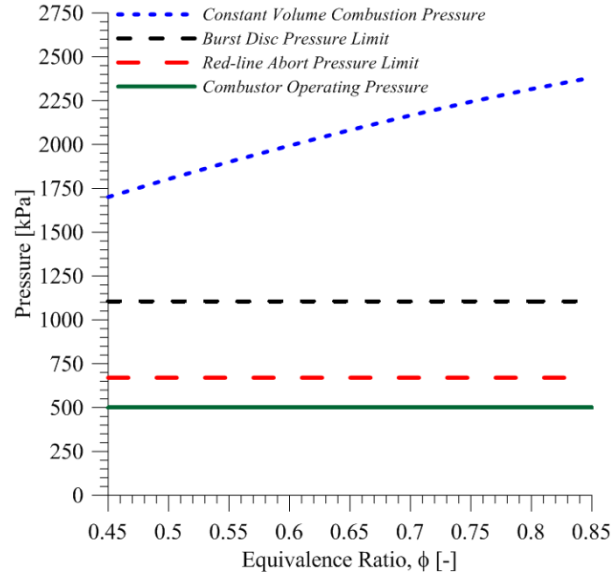
Figure 2.5: Constant volume combustion pressure (from flashback) versus equivalence ratio; also shown are combustor operating pressure, red-line pressure limit, and burst disc pressure limit.
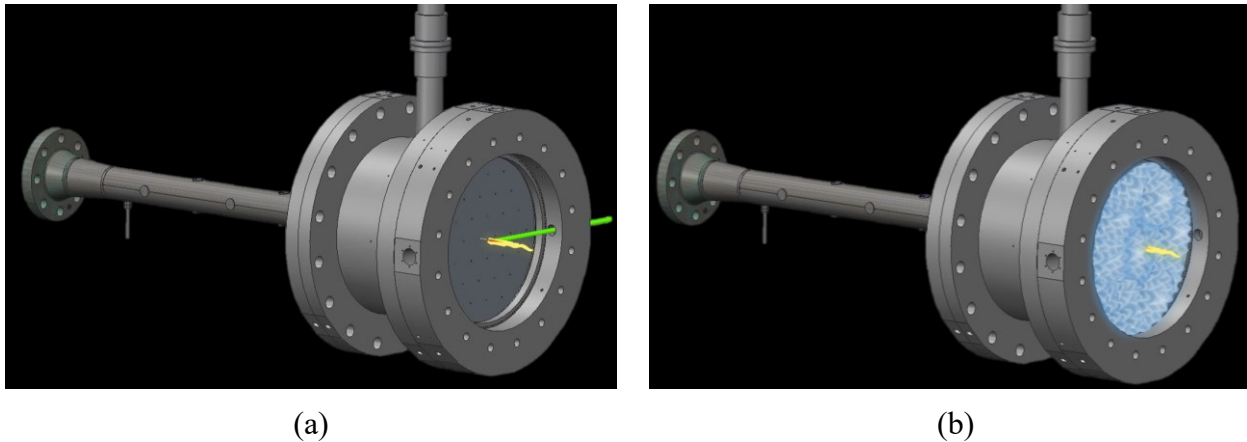
Figure 2.6: 3D schematic of the PPB ignition within the test rig: (a) ignition of the hydrogen pilot flame via laser spark, (b) ignition of the NG-air flame over the PPB via the hydrogen pilot.

Film cooling air at 5% of the PPB air flow rate and ambient temperature was introduced just downstream of the PPB to protect the flow contraction hardware. A detailed schematic of the headend premixing pipe, PPB, and film cooling assembly is presented in Fig. 2.8.

The axial stage consisted of a second NG-air premixer, an injector for transverse injection, and a post-injection combustor length. The axial injector was designed to continuously flow heated air at about 6.5% of the total air flow rate. When desired, an independent circuit of natural gas was introduced into the axial premixing assembly to create the reacting jet. The heat loss

through the water-cooled combustor walls, which also featured a thermal barrier coating, was well characterized through temperature measurements of the rig and the coolant circuit.

The NO_X quench section located at the end of the axial stage enabled accurate control of the residence time by freezing the chemical reactions in the flow and thereby inhibiting further thermal NO_X production. This was achieved by injecting water into the combustion gas flow to reduce the gas temperature to less than 1300 K. The variation of residence time between the flame zone and the emissions measurement location was primarily controlled through the air flow rate. A sampling probe was used to collect samples of the water-quenched exhaust gas, which was transported to the emissions sampling instrumentation using a heated line at 464 K to prevent condensation.

As discussed earlier, the experiment was remotely controlled using a National Instruments LabVIEW Virtual Instrument (VI) due to the significant potential energy contained within an experiment operating at elevated pressures. Low frequency pressure transducers (GE Sensing UNIK50E6) and K-type thermocouples (Omega) were installed at multiple locations throughout the test rig and fluid supply lines. These instruments were sampled at 260 Hz for test condition and rig health monitoring. The key flashback mitigation instrumentation (measured temperature aborts, measured pressure aborts, and the bust disc rupture pressure) are presented in Figure 2.9.

Sonic venturis were used for all gaseous fluid lines and cavitating venturis were used for all water lines in order to have a deterministic system with known mass flow rates, which were calculated using an ASME standard (Miller *et al.*, 2004). Experimental test conditions such as mass flow rates and equivalence ratios were monitored in real-time using equations programmed into the VI. REFPROP V9.1 (Lemmon *et al.*, 2013) was used during the data reduction process for all fluids to more precisely incorporate real gas effects. Real gas effects were found to be particularly significant for natural gas flow rate calculations. The natural gas composition used for this work is provided in Appendix A.

Exhaust gas emissions were characterized using a Fourier transform infrared (FTIR) spectrometer from MKS Instruments. The FTIR system was configured to collect data in the mid-infrared region and was used to measure nitric oxide (NO), nitrogen dioxide (NO_2), carbon monoxide (CO), carbon dioxide (CO_2), and a *flame ionization detector equivalent* unburnt hydrocarbon (UHC). Measurements of the wet exhaust gas were obtained at about 1 Hz with a nominal gas cell temperature and pressure of 464 K and 101 kPa, respectively. A background

spectrum using nitrogen (N_2) was obtained at the start of each test day. The algorithm for processing measured spectra to emissions values used peaks in the spectra with an absorbance level of less than 1 [a.u.] and wavenumbers of $500 - 3500$ cm^{-1}. Figure 2.10 presents a sample spectrum corresponding to dry values of: NO = 2.2 ppm, NO_2 = 0.2 ppm, CO = 2.3 ppm, and UHC = 8.3 ppm. The FTIR spectrometer was used to obtain exhaust-gas emissions for typically 100 seconds of steady state operation. All raw values were converted to a dry basis and NO_X values were also referenced to 15% O_2 levels. Carbon balances and the combustion efficiency of the burner were calculated using an SAE International reference (ARP1433, 2016). The carbon balance, which was used to validate the emissions sampling system and the metering of the air and natural gas flow into the test rig, generally showed agreement between $95 - 97\%$.

All mean values of temperature and pressure were reported using an arithmetic mean of 100 seconds (260 Hz sampling frequency) at steady-state rig conditions. The precision component of total uncertainty was very small given the 26,000 samples per condition. Calculated experimental uncertainty for temperature and pressure measurements were 0.2% and 0.04%, respectively, based on previous uncertainty analysis using the same facility (Slabaugh *et al.*, 2014). Experimental uncertainty for equivalence ratio was calculated to be 1.6%, without accounting for uncertainties in the thermodynamic properties acquired from REFPROP. All derived quantities, including equivalence ratio, were also reported as an arithmetic mean of 100 seconds at stead-state rig conditions. Emissions values were reported using an arithmetic mean of 100 seconds (but with a 1 Hz sampling frequency) at steady-state rig conditions; one standard deviation was used as the experimental uncertainty for emissions measurements.
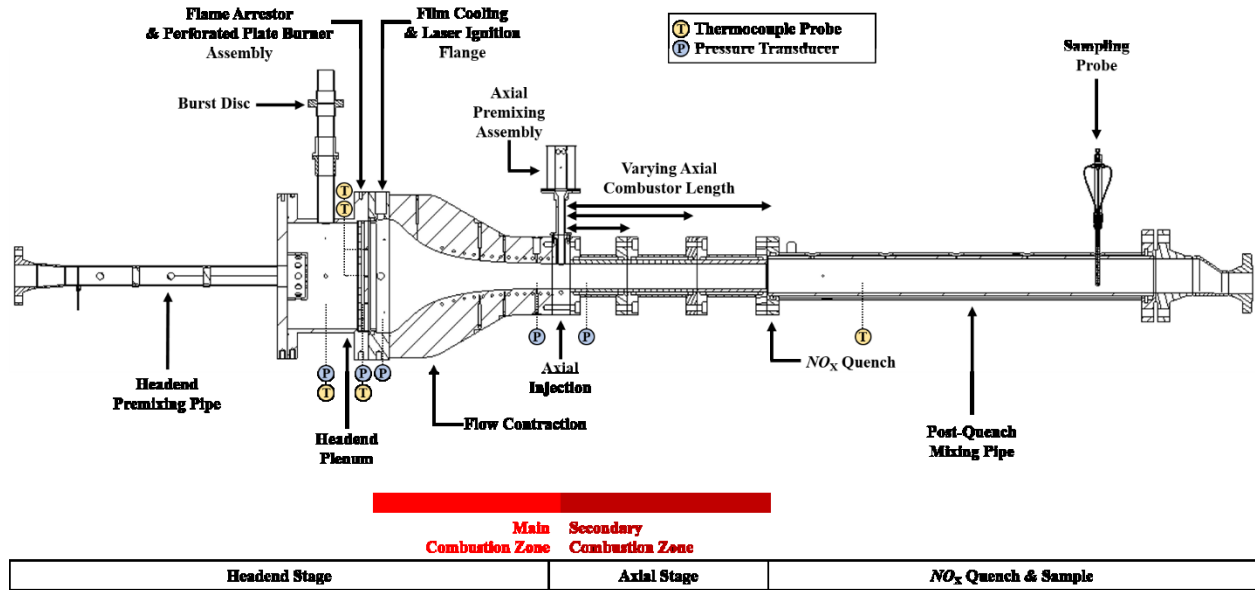
Figure 2.7: Schematic of the test rig.
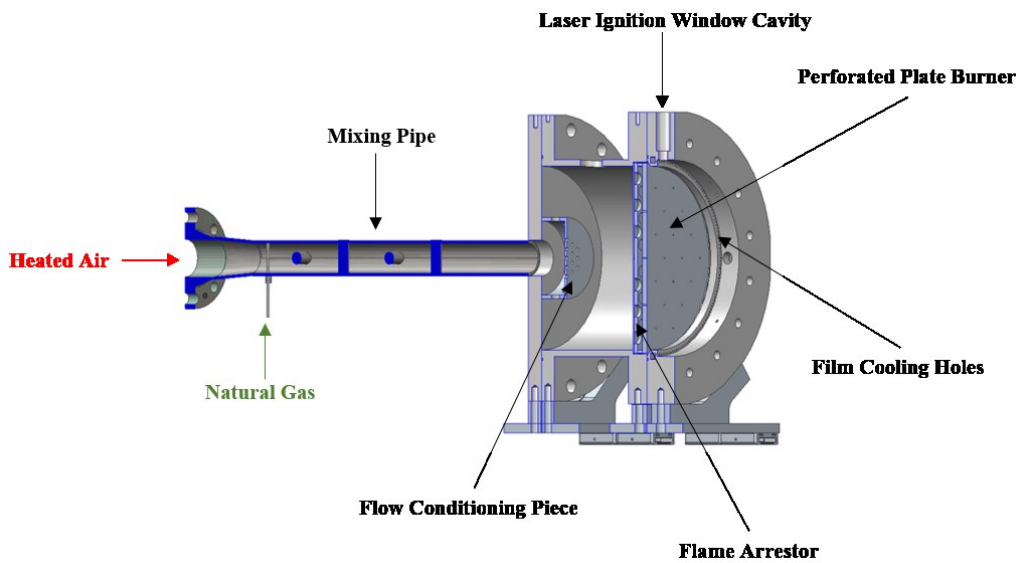
Figure 2.8: 3D schematic of key components within the headend stage.

35
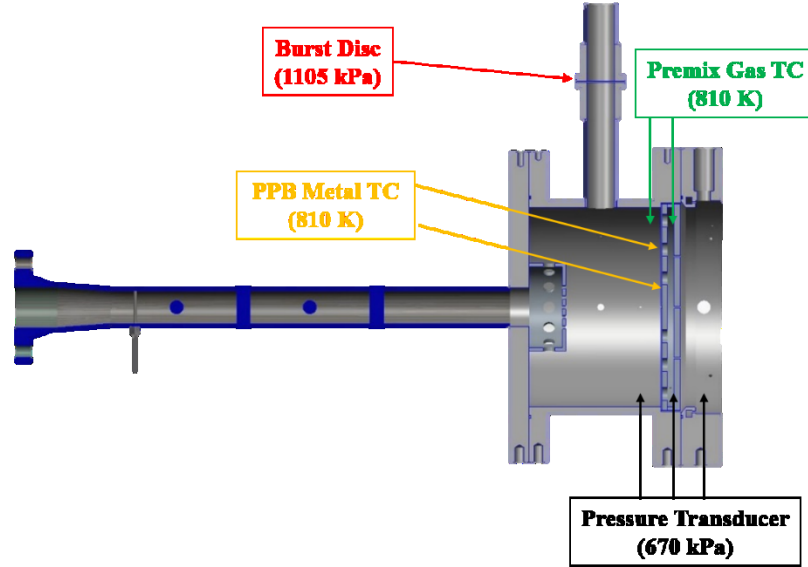
Figure 2.9: 3D schematic showing red-line aborts
at their respective measurement locations and the burst disc rupture pressure.
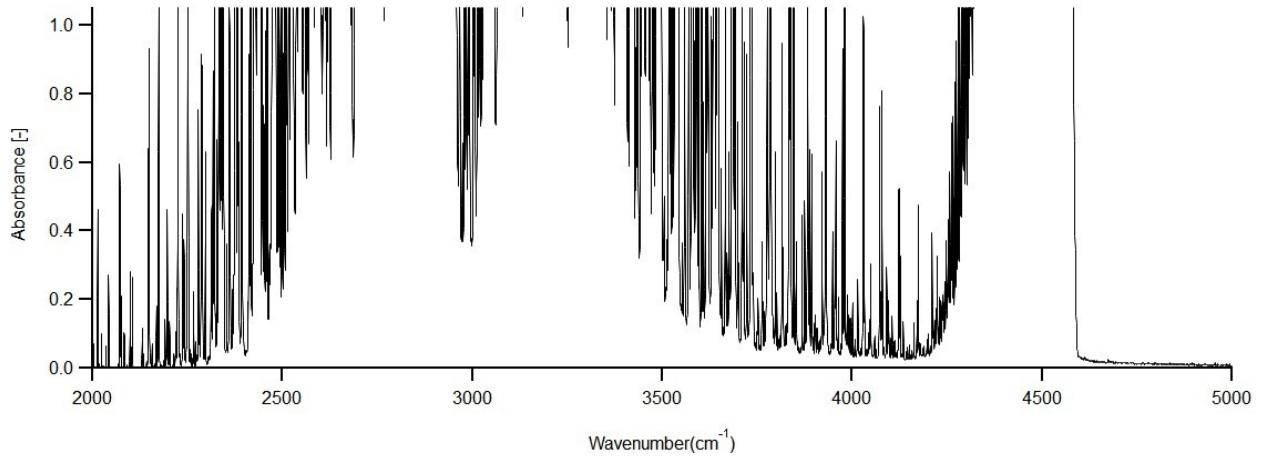
Figure 2.10: Sample FTIR spectrum (for absorbance levels below 1.0 a.u.) corresponding to dry
values of: NO = 2.2 ppm, NO_2 = 0.2 ppm, CO = 2.3 ppm, and UHC = 8.3 ppm.

2.4 Performance at engine-relevant conditions

Experimental results illustrating the performance of the perforated plate burner at engine-relevant conditions are presented in this section. A typical ignition event, a representative flashback event, and an ignition event triggering the PPB upstream temperature red-line aborts are described based on the temperature and pressure measurements used for rig condition monitoring. A stability diagram of the PPB is also presented as a function of the NG-air equivalence ratio and

the PPB hole velocity. NO_X emissions measurements from the FTIR spectrometer are presented for the PPB in both piloted and non-piloted modes. Demonstration of the PPB as a source of vitiated flow with negligible swirl for reacting jet in crossflow (RJICF) experiments are also presented towards the end of this section.

2.4.1 PPB operation

The measured pressure drop across the perforated plate burner (PPB) and the custom designed flame arrestor located upstream of the PPB are presented Fig. 2.11 for non-reacting (or warm flow) conditions corresponding to elevated inlet air temperatures (T_3 = 543 K) and combustor pressures (P_4 = 505 kPa). Greater pressure drop was measured across both the flame arrestor and the PPB for increased mass flow rates. For a given mass flow rate, higher pressure drop was observed across the flame arrestor compared to the PPB, which can be attributed to the lower porosity of the flame arrestor (P = 0.023) compared to that of the PPB (P = 0.150). The discharge coefficient of the PPB is shown in Fig. 2.12 as a function of the PPB hole Reynolds number. The PPB discharge coefficient was calculated using the measured pressured drop, calculated gas density, and plate geometry (Shaaban, 2015). It was observed to decrease from 0.44 to 0.27 with an increase in Reynolds number from about 1400 to 4800.

A typical ignition event sequence involves: (1) igniting the H_2 pilot flame using the spark created from a tightly focused Nd:YAG laser beam, (2) setting the air flow rate to the desired condition, (3) adjusting the back-pressure valve installed on the test rig to set the pre-ignition combustor pressure to P_4 = 300 – 400 kPa, and (4) introducing natural gas into the premixing pipe at the desired equivalence ratio. Figure 2.13 presents the measured combustor pressure and the calculated hole velocity in the PPB holes versus time during a typical natural gas ignition event. The hydrogen pilot flame was ignited well before the t = 0 s in Fig. 13. The premixed natural gas and air mixture was ignited by the hydrogen pilot flame at a time of about t = 0.5 s, as indicated by the initial increase in pressure from P_4 = 370 kPa to 520 kPa. A slight decrease in combustor pressure was observed, followed by another increase to P_4 = 530 kPa. It is believed that at the initial pressure rise, the mixture had ignited but the flame had not yet stabilized on the burner surface, which may explain the subsequent decrease in pressure. Under this hypothesis, the

spreading of the flame over the entire PPB may be responsible for the second pressure rise. It should be noted that the dashed line shown in Fig. 2.13 is the red-line pressure abort.

One concern when igniting and operating the PPB is an unacceptable rise in the metal temperature of the burner itself. Two wall-mounted thermocouple probes were installed on the upstream side of the PPB at about $r = 1$ cm and $r = 17$ cm in the radial direction from the center of the plate. The PPB surface temperatures from a typical ignition event are presented in Fig. 2.14. Both plate temperature measurements were observed to reach steady-state within 60 seconds of ignition. During steady-state operation, the temperature reading at $r = 17$ cm was observed to be greater than the reading at $r = 1$ cm. This may be due to the cooling effect provided by the tube transporting hydrogen for the pilot flame. In Fig. 2.14, the hydrogen pilot flame was once again ignited well before $t = 0$ s and the dashed line shown is the red-line plate temperature abort.

Exploratory testing to determine the range of operating conditions best suited for the perforated plate burner at elevated inlet temperatures and combustor pressures resulted in well over a dozen flashback events to date. However, due to the flame arrestor and red-line aborts incorporated into the design as flashback mitigation features, the occurrence of flashback was not catastrophic. A representative flashback event during operation at a steady-state combustor pressure of $P_4 = 510$ kPa is illustrated in Fig. 15 using pressure and temperature measurements. Figure 2.15(a) presents the measured combustor pressure (P_4) downstream of the perforated plate burner. At about $t = 1.8$ s, a sharp increase in pressure to nearly 800 kPa was observed, which was greater than the 690 kPa red-line abort pressure. With the red-line abort triggered, natural gas flow into the premixing pipe was stopped and the flame was extinguished, as indicated by the decrease in pressure to 450 kPa at about $t = 2.5$ seconds. The thermocouple probe located in the premixed gas flow between the flame arrestor and the PPB was also able to detect the flashback event, as indicated by an increase in measured gas temperature to nearly 900 K in Fig. 2.15(b). In contrast, the premixed gas temperature upstream of the flame arrestor was less affected and this temperature increase was within the red-line limit. The PPB metal temperature at $r = 1$ cm also significantly increased due to the flashback event, but the measured temperature at $r = 17$ cm was only slightly affected. About 12 seconds after triggering the red-line abort, natural gas was actually allowed to flow back into the premixing pipe once it seemed clear that the test rig did not sustain any damage (based on temperature and pressure readings throughout the rig and live monitoring using a facility camera). The perforated plate burner was re-ignited, as indicated by the increase in combustor

pressure to P_4 = 500 kPa at about t = 14 s. Stable operation was observed after re-ignition and testing continued. Since a flashback event does not end a test day, let alone cause a significant downtime due to damaged hardware, this perforated plate burner experiment could also be used for fundamental studies on flashback at engine-relevant conditions, including investigating the coupled thermoacoustic interaction between heat release instabilities in the flame and the characteristic acoustic fields of the experiment before and during a flashback event.

A limitation of operating the PPB at higher equivalence ratios while at elevated inlet temperatures is that the temperature of the plate substantially increases from the presence of a richer flame. This is mainly because the cooling effect from unburnt gas flowing through the PPB holes is significantly reduced at elevated inlet temperatures. In addition, it is believed that the position of the flame relative to the PPB may vary with the equivalence ratio, with a richer flame residing closer to the PPB surface. Figure 2.16 presents the upstream surface temperatures of the PPB during an ignition event at ϕ = 0.54 and T_3 = 607 K, which triggered the plate temperature red-line abort. Although the temperature measurement at r = 1 cm reached a steady-state value of about 730 K within 40 seconds of ignition (likely due to the cooling effect from the hydrogen flowing inside the tube at the center of the plate), the temperature at r = 17 cm continued to increase and reached the set red-line limit of 810 K at t = 55 s. At this point, the red-line abort was triggered and fuel into the rig was shut off. Similar behavior for the plate temperature was also observed at a higher T_3 = 650 K but at a lower equivalence ratio of ϕ = 0.50 − 0.52. It is believed that the operating parameters that control the PPB plate temperature are the premixed gas temperature, equivalence ratio, and velocity through the PPB holes (which influences the convective heat transfer).

The PPB was initially only operated in a piloted mode to allow for easy re-light in the event of a red-line abort activation. This was achieved by allowing the hydrogen diffusion flame to remain lit despite the extinguishment of the NG-air flame. During the post-flashback re-ignition process, the hydrogen pilot flame would be used to quickly and easily re-light the NG-air flame. The hydrogen pilot flame would then remain lit for the duration of the stead-state data acquisition period. As more experience was gained with operation of the burner, the hydrogen flame would be turned off during steady-state data acquisition and a small amount of nitrogen (< 1% of air) would instead flow through the protruding tube. This mode of operation is referred to as the non-piloted PPB. Figure 17 presents both piloted and non-piloted PPB exhaust gas measurements of

NO, NO_2, CO, and CO_2, which were converted to dry values, at a representative condition for a duration of 100 seconds. If the hydrogen flame was once again desired (for instance between steady-state operating conditions), hydrogen would replace the nitrogen flow and the NG-air flame would serve as the ignition source for the hydrogen pilot flame.

The behavior of the NG-air flame, outside of differences in NO_X, was generally nearly identical in piloted (with the hydrogen flame) and non-piloted (without the hydrogen flame) modes. This was determined based on temperature and pressure instrumentation used for rig condition monitoring and the exhaust gas measurements of CO and UHC, which were used to calculate the combustion efficiency. Figure 2.18 presents a burner stability diagram of the PPB as a function of the NG-air equivalence ratio and the PPB hole velocity. Operating the PPB at too low of an equivalence ratio for a specified hole velocity resulted in lower levels of combustion efficiency. Since the design purpose of the PPB was to produce vitiated flow with low levels of CO and UHC (under 10 ppm, dry), a stringent combustion efficiency of $\eta \geq 99.95\%$ was set as a requirement. In contrast, operating at too high of an equivalence ratio resulted in flashback or an unacceptable increase in the PPB metal temperature. The range of optimal equivalence ratios shifted to slightly richer conditions as the hole velocity was increased. For instance, the PPB operated well between $0.48 \leq \phi \leq 0.52$ for a hole velocity of 10 m/s, compared to $0.52 \leq \phi \leq 0.56$ for a hole velocity of 20 m/s. This may be attributed to the balance between the residence time at the burner (decreasing with higher hole velocities) and the chemical time scale of the flame (decreasing with higher equivalence ratios). Although the operational range of the PPB was found to be somewhat restricted in terms of the premixed NG-air equivalence ratio, the burner operated very successfully within this range.
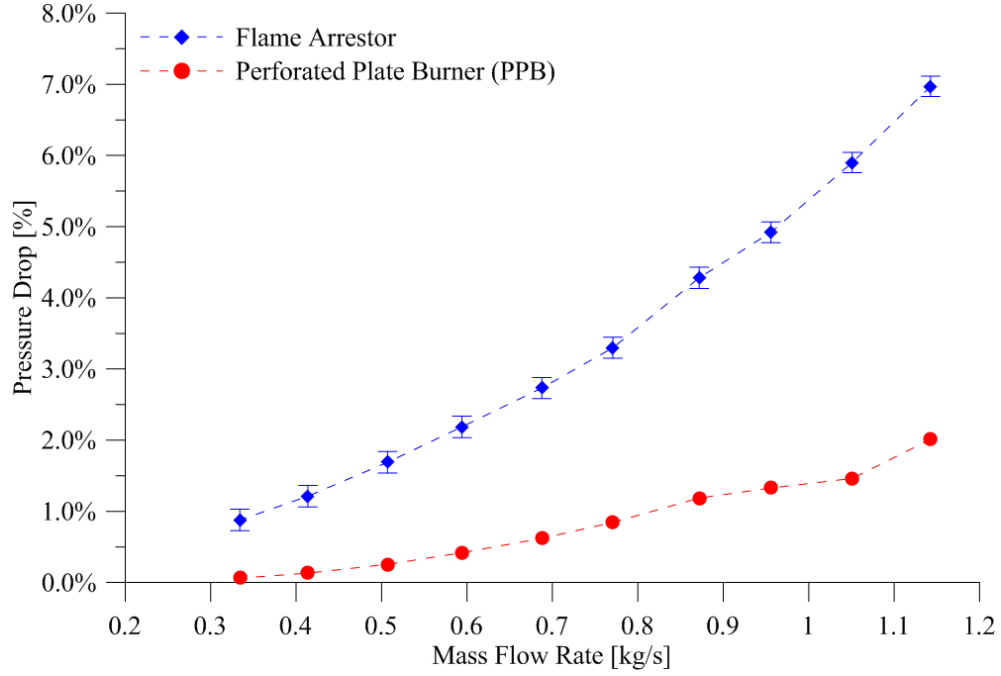
Figure 2.11: Pressure drop vs. mass flow rate across the flame arrestor and perforated plate burner (PPB) at $T_3 = 543 \pm 6$ K and $P_4 = 505 \pm 5$ kPa.
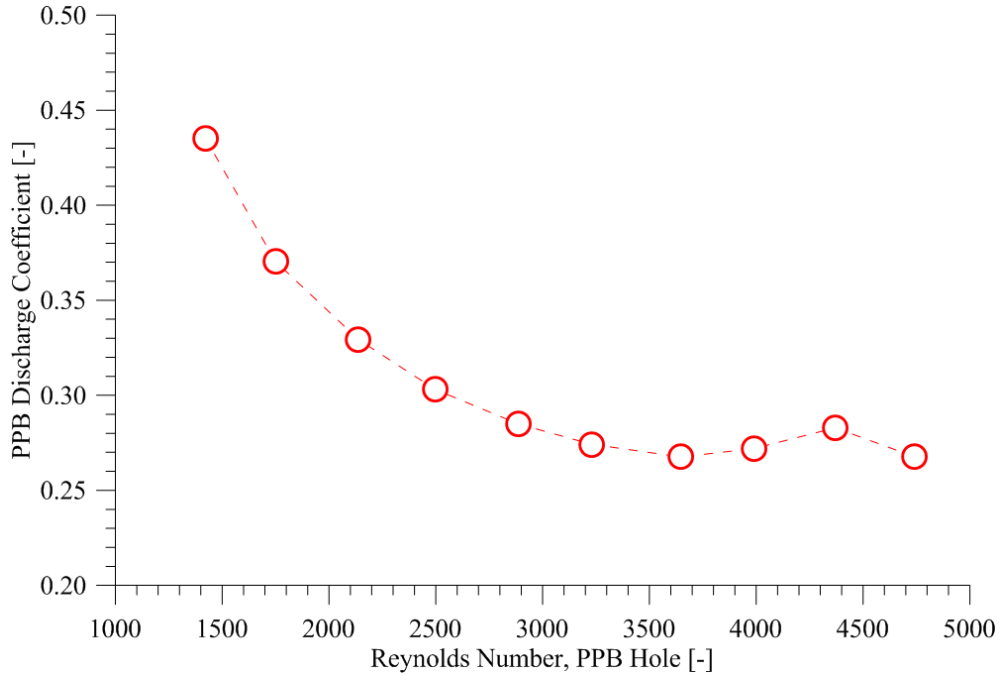
Figure 2.12: PPB Discharge Coefficient vs. PPB hole Reynolds number at $T_3 = 543 \pm 6$ K and $P_4 = 505 \pm 5$ kPa.
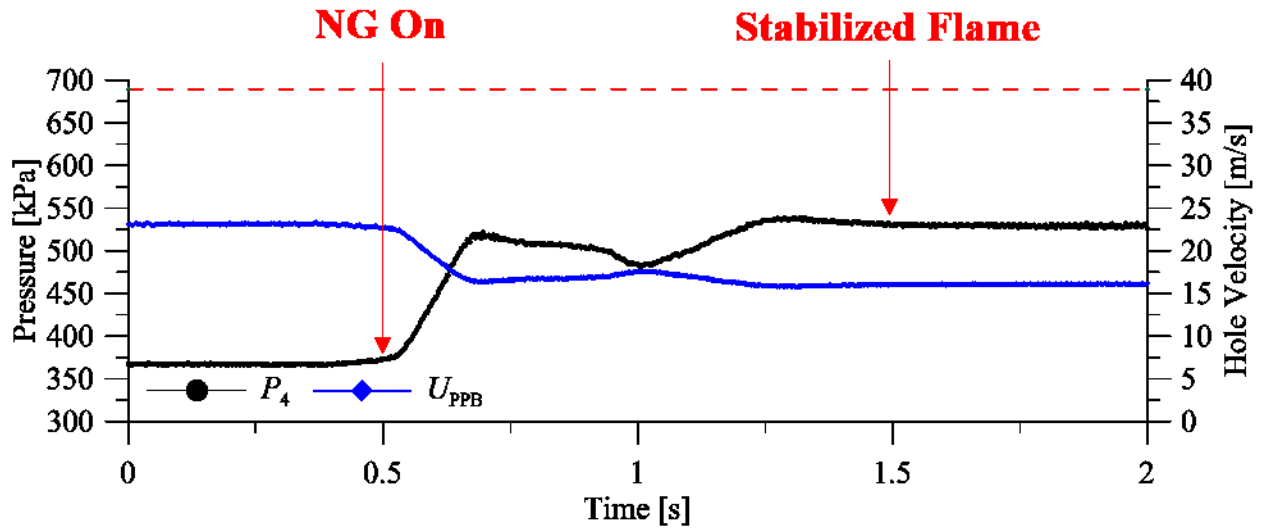
Figure 2.13: Upstream surface temperature of PPB at $r = 1$ cm and $r = 17$ cm from plate center vs. time for a typical ignition event (hydrogen flame was ignited well before $t = 0$ s).
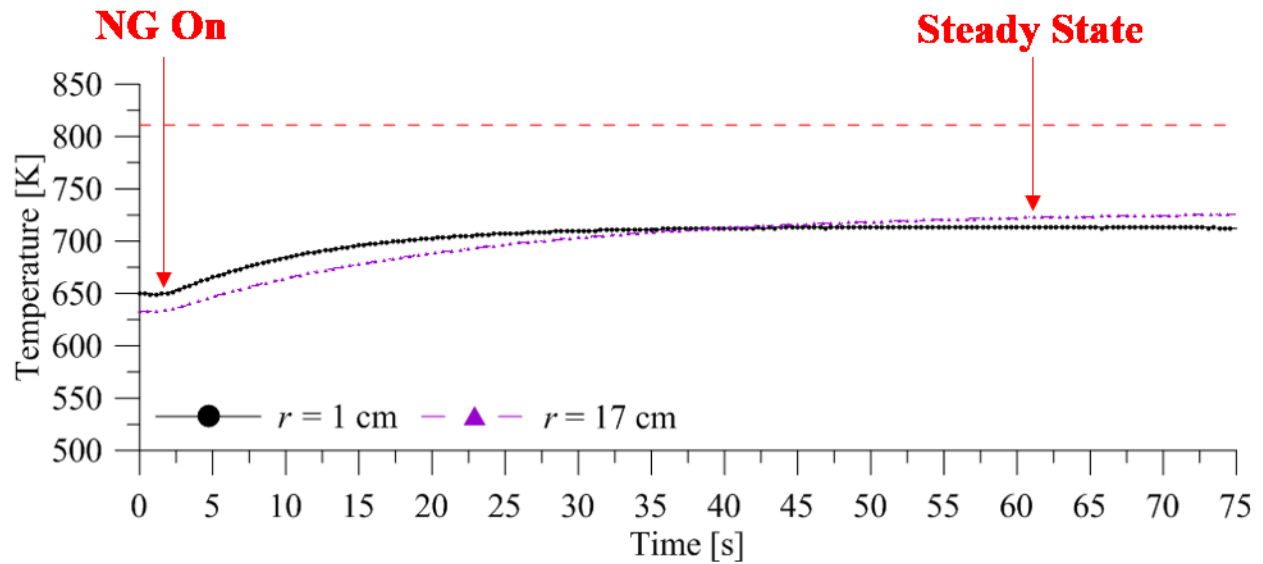
Figure 2.14: Upstream surface temperature of PPB at $r = 1$ cm and $r = 17$ cm from plate center vs. time for a typical ignition event (hydrogen flame was ignited well before $t = 0$ s).
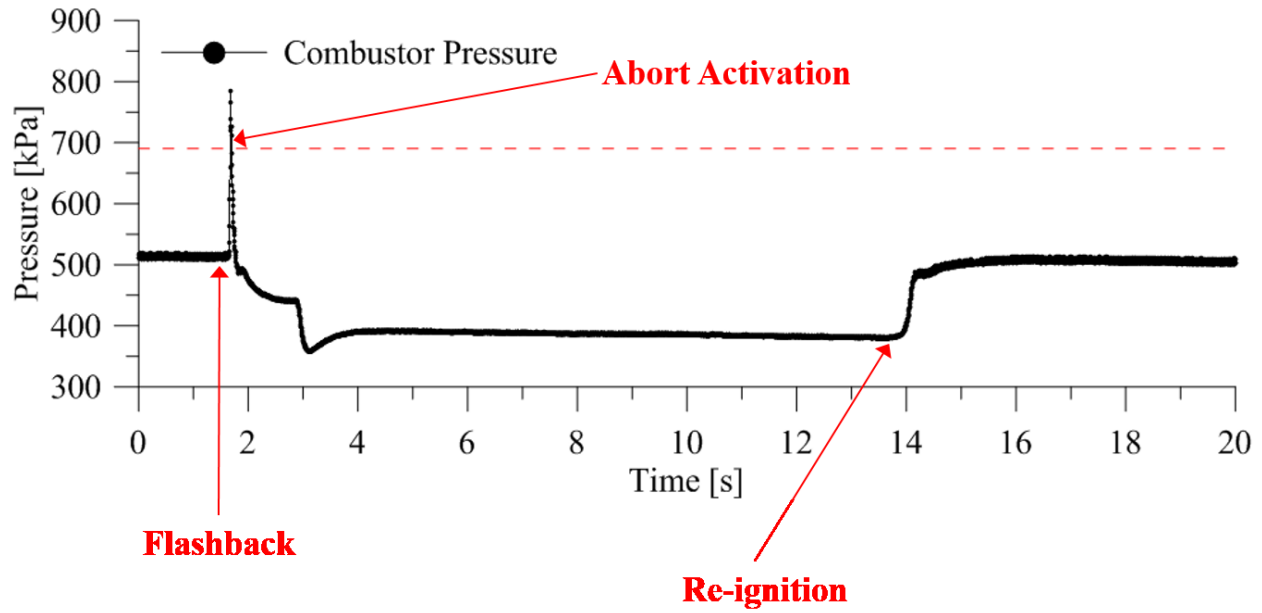
(a)
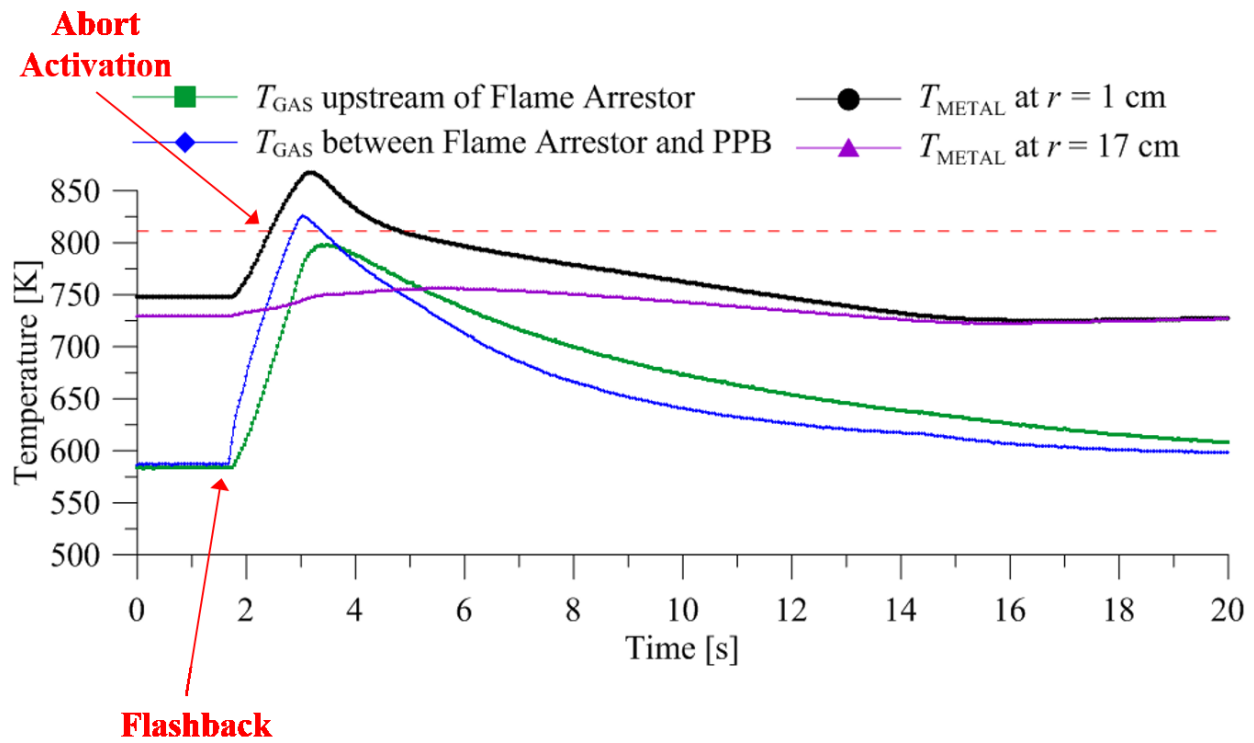
(b)

Figure 2.15: (a) Pressure and (b) temperature measurements vs. time for a representative flashback event (PPB ignited well before $t = 0$ s).
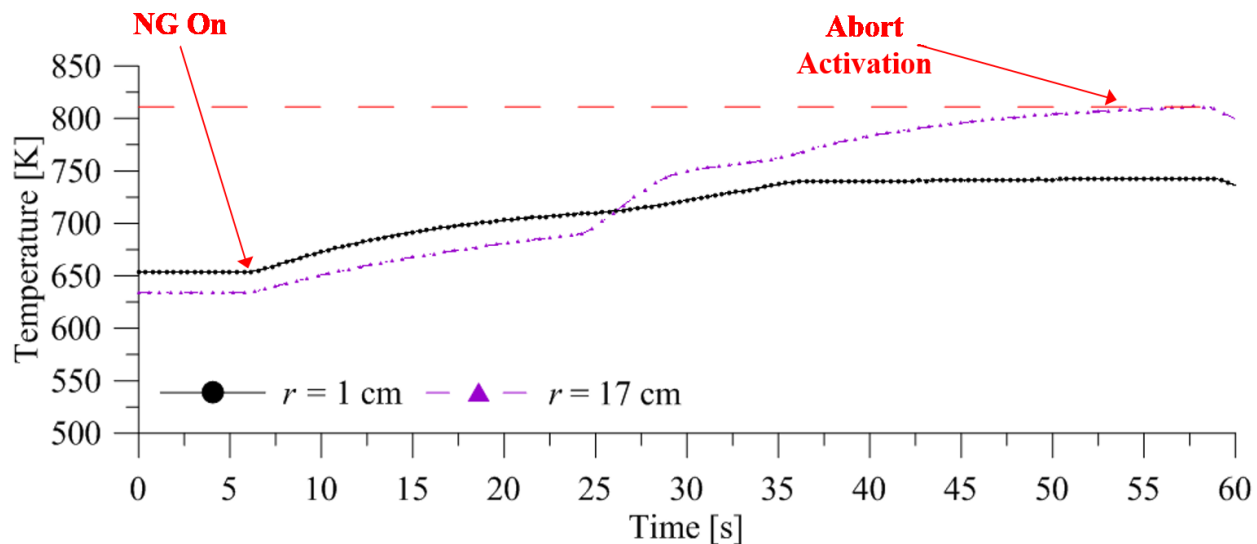
Figure 2.16: Upstream surface temperature of PPB at $r = 1$ cm and $r = 17$ cm from plate center vs. time for an ignition event resulting in a plate temperature abort (hydrogen flame was ignited well before $t = 0$ s).
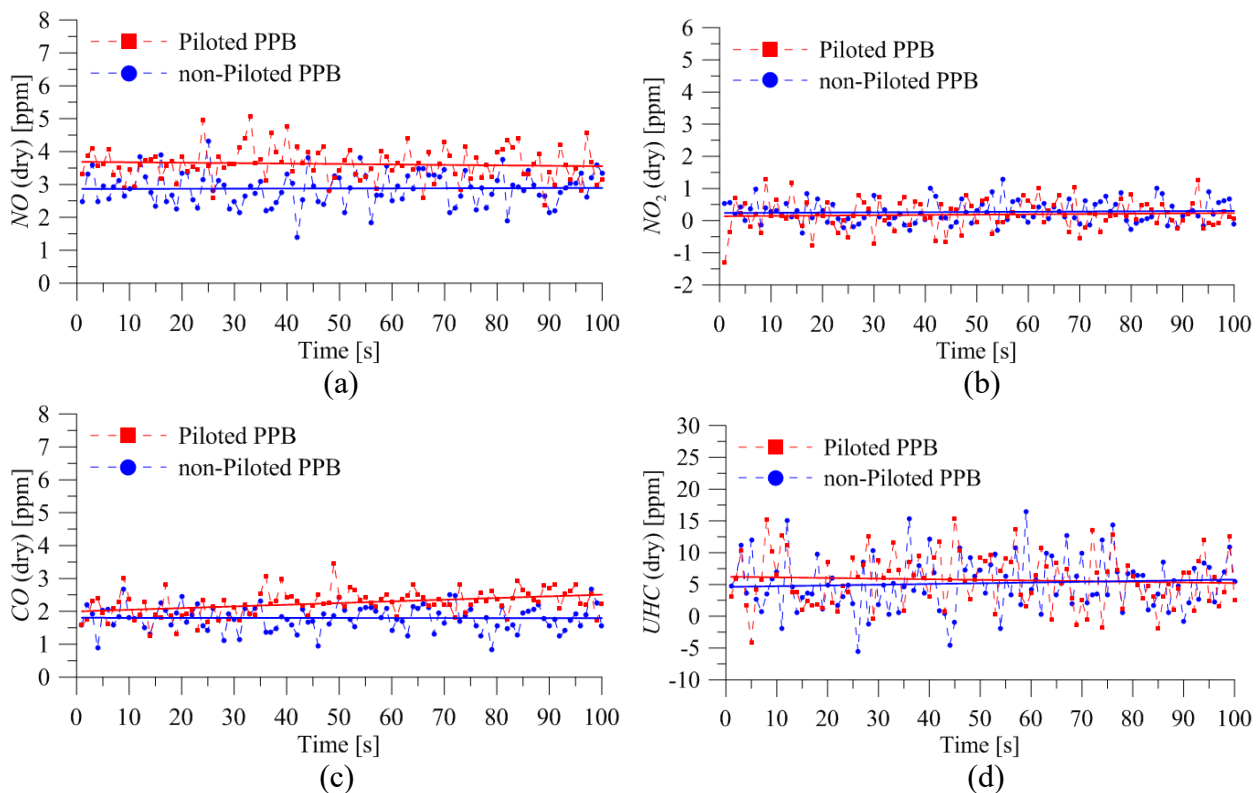
Figure 2.17: Key exhaust gas measurements (with linear fits) of the piloted and non-piloted PPB at a representative steady-state condition: (a) NO, (b) NO_2, (c) CO, (d) UHC.
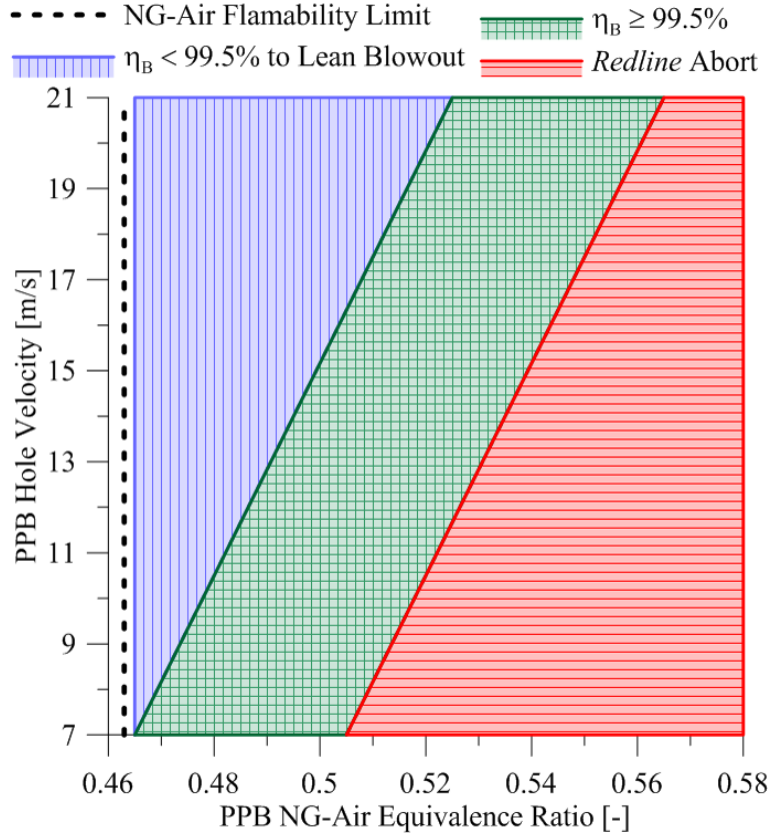
Figure 2.18: PPB stability diagram as a function of the NG-air equivalence ratio and hole velocity.

2.4.2 PPB NO$_X$ emissions

Emissions measurements of NO$_X$ (NO + NO$_2$, on a dry basis and referenced to 15% O$_2$) are presented in Fig. 2.19 for the non-piloted PPB as a function of the adiabatic flame temperature $T_{4,AD}$ and at a baseline residence time of $\tau = 15$ ms. This data was compared to two existing engine-relevant PPB studies in literature: Leonard and Correa (1990) and Elkady *et al.* (2012). Both of these studies operated the PPB at similar inlet temperatures but their combustor pressures corresponded to about 1 MPa rather than the 500 kPa used for this work. In addition, the residence times for the data included in Fig. 2.19 was different from the present work: $\tau = 10$ ms was used by Leonard and Correa and $\tau = 20$ ms was used by Elkady *et al.* Nevertheless, fair agreement was observed between the present work and these earlier studies despite differences in pressure and residence time. This can be attributed to the relative independence of pressure and weak dependence on residence time on NO$_X$ formation at low flame temperatures, due to the limited

role of thermal NO_X (Leonard and Correa, 1990). Furthermore, NO_X was not observed to vary significantly with $T_{4,AD}$ due to the range of low flame temperatures used in this work and the majority of the measured NO_X from the non-piloted PPB is believed to be prompt NO_X rather than thermal NO_X.

Figure 2.20 presents values of NO_X (dry and referenced to 15% O_2) vs. the T_3 premixed gas temperature for two different residence times: τ = 15 ms and τ = 29 ms. Increasing the residence time from 15 ms to 29 ms was observed to increase NO_X by about 50%, although the magnitude of this increase was relatively small with an increase from about 2 ppm to 3 ppm. This indicates that further NO_X production via the thermal NO_X mechanism continues over a long residence time despite low flame temperatures, although this is only a slight effect in terms of ppm levels. For the low flame temperatures considered, NO_X was observed to slightly decrease with increasing premixed gas temperatures. This was somewhat surprising and may be due to a decrease in the flame length at higher premixed gas temperatures, which in turn may result in a slightly smaller reaction zone volume and consequently perhaps reduced prompt NO_X formation.

Although operating the PPB in piloted vs. non-piloted mode did not have a noticeable impact on PPB stability, the presence of the hydrogen pilot flame did have an influence on the PPB NO_X emissions. The hydrogen pilot flame functions as a diffusion flame in vitiated co-flow and therefore results in local adiabatic flame temperatures up to 2500 K for stoichiometric regions within the jet shear layer. Figure 2.21 presents NO_X (dry) as a function of the unburnt hydrogen jet velocity U_J for a constant vitiated co-flow velocity U_{CoF} = 5.2 m/s and a constant residence time τ = 26 ms. Greater levels of NO_X (dry) from about 3 ppm to 6 ppm was observed by increasing U_J from about 11 m/s to 35 m/s. This may be attributed to a longer length of the jet flame at higher jet velocities, which would result in a larger region of high temperature gas within the stoichiometric jet shear layer and consequently greater thermal NO_X production. In comparison, the non-piloted PPB at the same operating conditions produced only about 2 ppm of NO_X (dry).

The impact of the vitiated co-flow velocity for a constant unburnt hydrogen jet velocity was also investigated and is presented in Fig. 2.22. For a constant U_J = 24 m/s, NO_X (dry) was observed to decrease from about 6 ppm to 4 ppm by increasing U_{CoF} from 4.7 m/s to 7.1 m/s. The increased co-flow velocity may indeed contribute to a decrease in NO_X (perhaps by decreasing the

jet flame length), however this effect was coupled with a decrease in the residence time from $\tau =$ 29 ms to 18 ms. Since lower residence time was observed to decrease NO_X for the non-piloted PPB, a definite conclusion on the effect of the co-flow velocity cannot be drawn. Fig. 2.22 also presets NO_X emissions values for the non-piloted PPB at conditions identical to the piloted PPB in order to reinforce: (a) the effect of the hydrogen flame resulting in increased NO_X levels, and (b) the effect of lower residence time resulting in decreased NO_X levels.

2.4.3 Demonstration of the PPB to produce vitiated flow for RJICF studies

The PPB was used to produce vitiated crossflow with negligible swirl for investigations of the reacting jet in vitiated crossflow. As described in Fig. 2.7, the PPB was part of the *headend* stage and the reacting jet was part of the *axial* stage. Before beginning the procedure for igniting the axial stage jet, the PPB was ignited at the desired condition and stable operation at $P_4 = 500$ kPa was verified. The standard procedure for igniting the axial stage within the staged model combustor involved: (1) adjusting the backpressure valve to reduce the headend combustor pressure to between 400 - 450 kPa, (2) verifying stable combustion at the PPB using the pressure instrumentation and PPB-only exhaust gas measurements, (3) turning off the N_2 purge going to the axial premixer and introducing a small amount of NG to the heated air flowing within the axial premixer, (4) slowly increasing the axial equivalence ratio until auto-ignition of the premixed jet, (5) tuning the backpressure valve and axial equivalence ratio in tandem to reach the desired axial equivalence ratio condition while maintaining the desired $P_4 = 500$ kPa. A typical axial stage ignition is illustrated in Fig. 2.23, which shows the pressure at the headed stage downstream of the PPB (P_4) and the pressure at the axial stage downstream of the jet (P_{4X}) stages, along with the axial equivalence ratio ϕ_{AX} (calculated using metered values of axial air and natural gas) for a 20 second axial ignition process. The implementation of this deliberate process ensured that the pressure rise from the heat release at the axial stage would not result in the PPB experiencing flashback.

A great benefit of using the PPB to provide the vitiated flow for reacting jet studies is the negligible swirl in the crossflow prior to jet injection. Removing the swirling component allows for easier comparison of the data to computational models and therefore tremendously valuable data sets can be obtained from this experiment. Emissions measurements were acquired from the
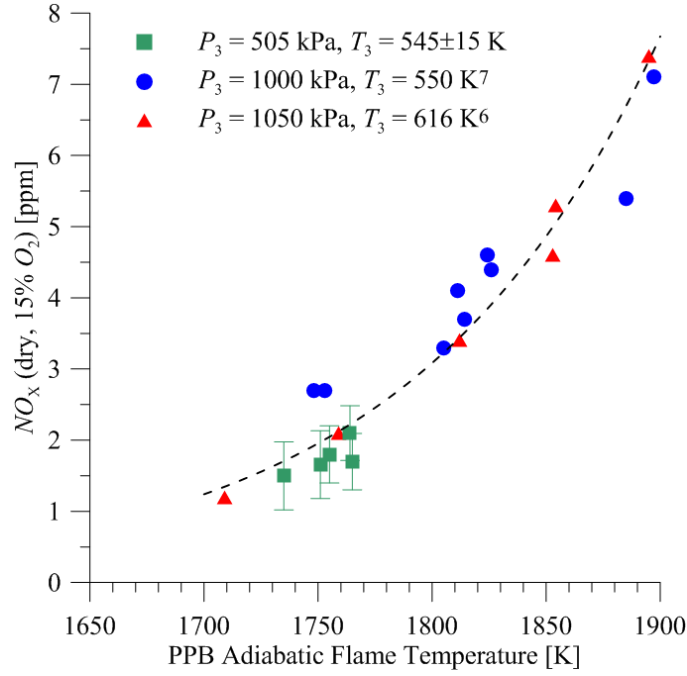
Figure 2.19: NO$_X$ (dry, 15% O_2) vs. PPB adiabatic flame temperature for the non-piloted PPB at a baseline residence time τ = 15 ms, compared with reported values in literature.
[[6] corresponds to Leonard and Correa (1990) and [7] corresponds to Elkady *et al.* (2012)]
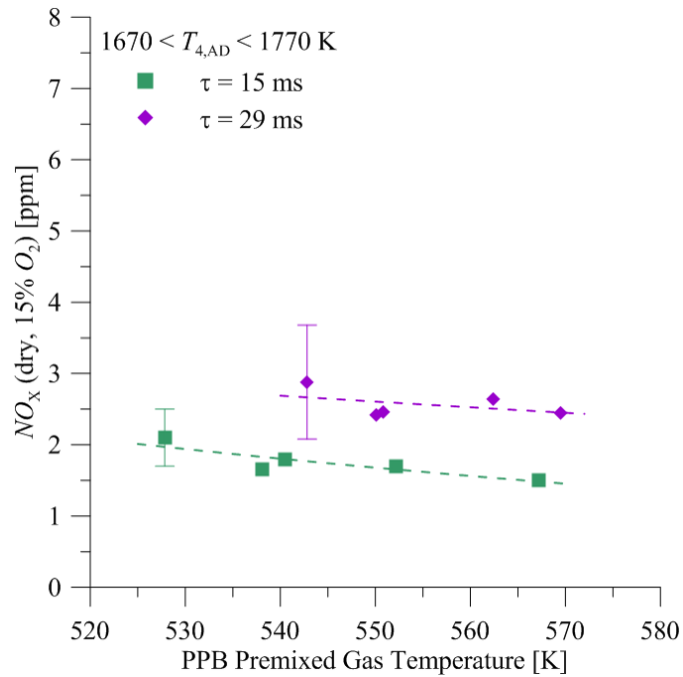
Figure 2.20: NO$_X$ (dry, 15% O_2) vs. PPB premixed gas temperature for the non-piloted PPB at two different residence times.
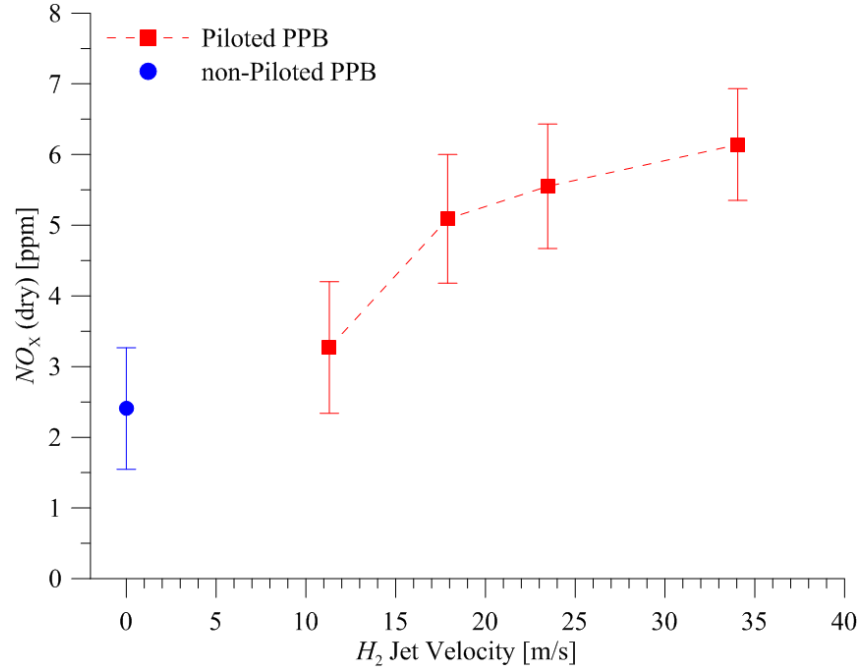
Figure 2.21: NO$_X$ (dry) vs. hydrogen jet velocity for the piloted PPB at a constant U_{CoF} = 5.2 m/s and τ = 26 ms.
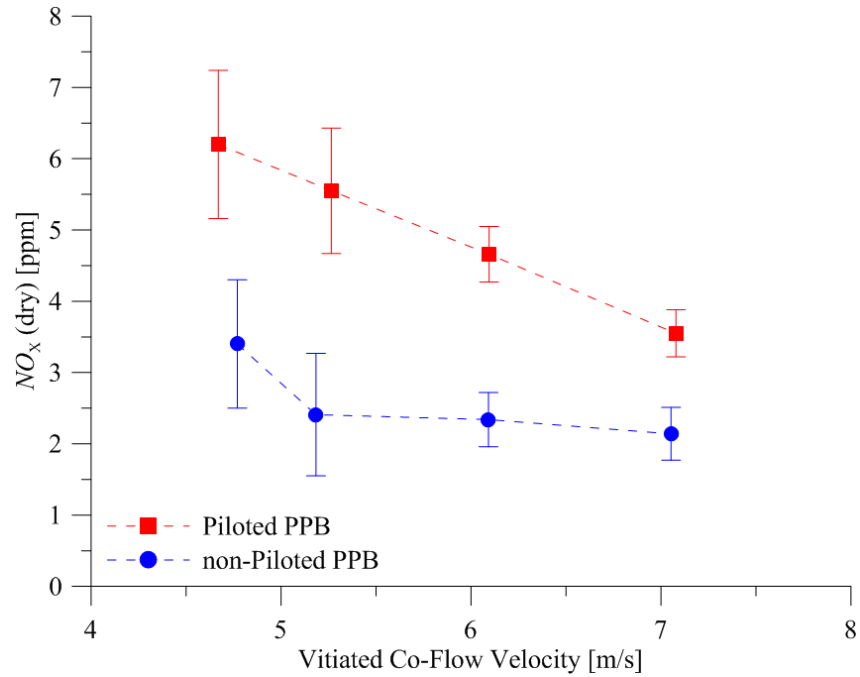
Figure 2.22: NO$_X$ (dry) vs. vitiated co-flow velocity for a constant U_J = 24 m/s (piloted PPB) with non-piloted PPB as reference; the residence time varies inversely to the co-flow velocity.

staged combustion system for rich ($1.0 \leq \phi_{AX} \leq 2.5$) premixed jets. Figure 2.24 presents the increase in NO_X (dry) produced by the axial stage as a function of the axial equivalence ratio. The NO_X emissions initially appeared to vary linearly with increased ϕ_{AX} before transitioning to a sharp increase beyond $\phi_{AX} = 1.6$. This is believed to be due to the increased prompt NO_X at higher axial equivalence ratios and the increased thermal NO_X due to the greater combustor exit temperatures. Key parameters for this data set include a low jet-to-crossflow momentum ratio $J = 2$, an axial air split $S_{AX} = 6.6\%$, and an axial residence time $\tau_{AX} = 4$ ms. Although rich axial equivalence ratios were used, low (< 10 ppm, dry) CO and UHC emissions were observed outside of the $\phi_{AX} = 1.1$ test case, where CO (dry) $= 80$ ppm and UHC (dry) $= 18$ ppm are reported. This may be attributed to mixing of the jet with the very lean vitiated crossflow ($\phi_{X\infty} = 0.46$), calculated using the PPB equivalence ratio and the 5% film cooling fraction. The total pressure loss across the axial stage was calculated based on the measured static pressure (before and after the jet) and fundamental gas dynamics equations. As presented in Fig. 2.25, an increase in total pressure loss from 1.3% to 1.7% was observed with higher axial equivalence ratios from $\phi_{AX} = 1.1$ to 2.2. This can be attributed to the greater heat release rates at the axial stage for higher ϕ_{AX}.

2.5   Summary and Conclusions

This chapter summarizes the development and performance of a perforated plate burner (PPB) at inlet temperatures and combustor pressures relevant to practical gas turbine engines. The methodology used for the design of the PPB is discussed. The key challenge of designing the PPB was that the velocity of the premixed natural gas and air mixture through the holes needed to be low enough for the stabilization of a flame on the downstream surface of the plate, but high enough so that flashback did not occur. Features incorporated into the design for flashback mitigation included a flame arrestor plate, several red-line aborts in the operating software, and a burst-disc installed in the plenum upstream of the PPB. A laser ignition system utilizing a hydrogen pilot flame was also designed for the PPB ignition.

Very good performance of the PPB was observed during testing at engine-relevant conditions. The ignition process using a combination of the laser ignition and a hydrogen diffusion

Figure 2.23: Combustor pressures at headend (P_4) and axial (P_{4X}) stages and the axial equivalence ratio (ϕ_{AX}) vs. time for a typical axial stage ignition event (PPB was ignited well before $t = 0$ s).
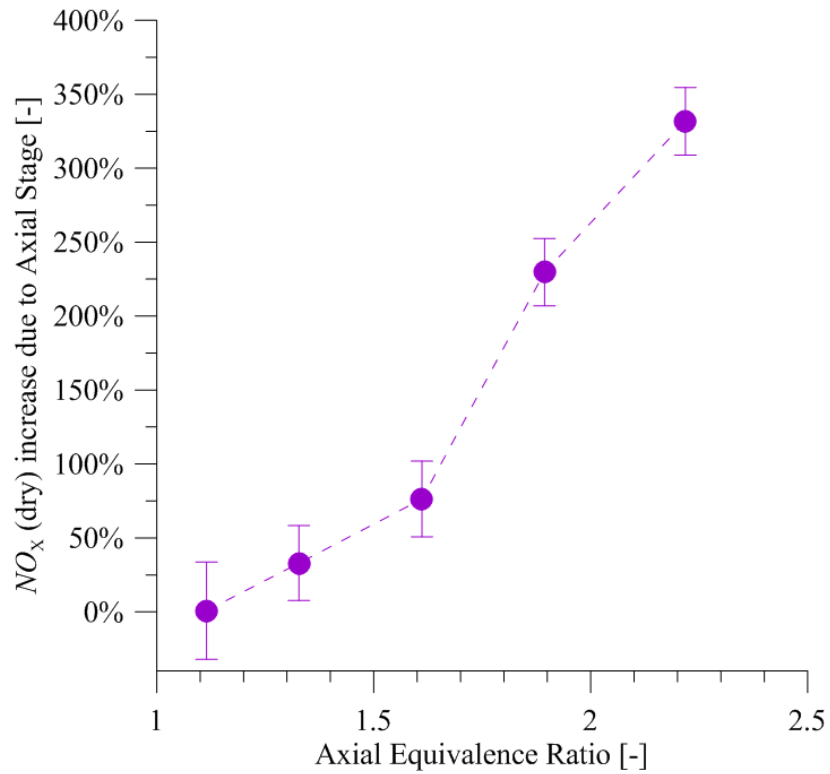
Figure 2.24: NO$_X$ (dry) increase due to the axial stage vs. the axial equivalence ratio at $\tau_{AX} = 4$ ms and $J = 2$.
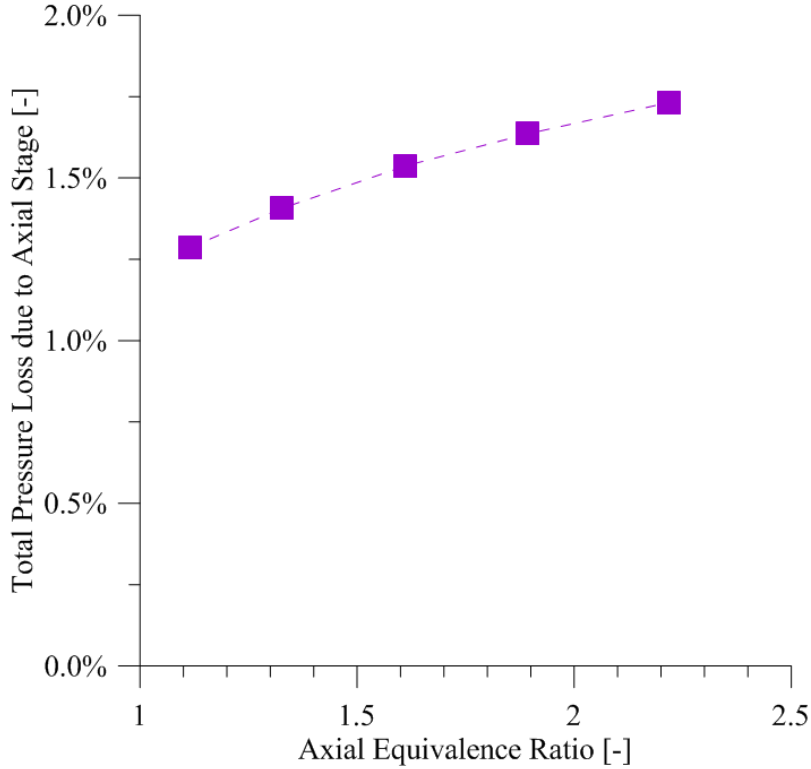
Figure 2.25: Total pressure loss due to the axial stage vs. the axial equivalence ratio at $J = 2$.

flame pilot was successful. Temperature and pressure measurements were used to illustrate a typical ignition event, a representative flashback event that triggered a red-line abort, and an ignition event that triggered a red-line abort due to high PPB metal temperature. A PPB stability diagram was developed as a function of the NG-air equivalence ratio and the PPB hole velocity. The operational range of the PPB was found to be somewhat restricted in terms of the premixed gas equivalence ratio, but the burner was operated very successfully within this range. Operating the PPB at too low of an operational equivalence ratio resulted in lower combustion efficiency, while operating at too high of an equivalence ratio resulted in flashback or an unacceptable increase in the PPB metal temperature. Exhaust gas measurements showed very low levels of NO_X (under 3 ppm, dry and referenced to 15% O_2) for the non-piloted PPB. The hydrogen pilot flame was observed to slightly increase NO_X emissions during operation in piloted PPB mode.

The motivation behind development of the PPB for engine-relevant operation was to use it as the source of vitiated crossflow with negligible swirl for reacting jet in vitiated crossflow experiments. This was demonstrated through the transverse injection of premixed natural gas and air in an axially staged combustor configuration. The vitiated crossflow from the PPB was

demonstrated to successfully auto-ignite the axial stage premixed jet. Measurements showed an increase in NO_X emissions and stagnation pressure losses with greater axial equivalence ratios. Since the PPB effectively produces vitiated crossflow without the swirling component and thereby allows for easier comparison with numerical simulations, tremendously valuable data sets can be acquired from this experiment. In Chapter 3 of this dissertation, the PPB is used as part of the axially staged combustor to study advanced strategies for NO_X emissions reductions. Other potential uses for the PPB that are beyond the scope of this dissertation include: fundamental studies of ignition, flashback, and blow-off for premixed flames; source of vitiated flow with negligible swirl for jet-in-coflow experiments; and the development of laser diagnostic techniques to study turbulent flames at realistic conditions. The simplified flow field from the burner at gas turbine engine-relevant conditions, high combustion efficiency, and low levels of NO_X, make this PPB an excellent candidate burner for combustion experiments in the laboratory.

3. NO$_x$ REDUCTION IN AN AXIALLY STAGED GAS TURBINE MODEL COMBUSTOR THROUGH INCREASE IN THE COMBUSTOR EXIT MACH NUMBER

3.1 Introduction

Gas turbine combustion remains the predominant method to produce energy for power generation and to provide thrust for air-breathing propulsion. Axial injection of reacting jets in crossflow (RJICF) as part of a staged combustion system remains an area of interest due to its potential to increase thermal power with only a minimal emissions increase. The primary objective of the work presented in this paper is to investigate the emissions produced by the transverse injection of a reacting jet issuing into a vitiated crossflow within an axially-staged, engine-relevant, gas turbine combustor operating at high sub-sonic conditions.

The jet-in-crossflow is a canonical problem and significant efforts have been made over the past decades to understand the physics behind the isothermal jet-in-crossflow and the reacting jet-in-crossflow at both lower temperature non-vitiated crossflow and high-temperature vitiated crossflow conditions. Substantial contributions to the literature have been made by Prof. Karagozian's research group at UCLA over the past 30 years and the interested reader is referred to review articles (Karagozian, 2010; Karagozian, 2014). Development of an analytical model by Heister and Karagozian (1990) for the isothermal jet-in-crossflow at compressible conditions is of particular relevance for the current paper. Many studies in the literature have also considered reacting jets in a non-vitiated crossflow. Recent efforts to better understand the flame structure and flow-flame interactions within this configuration include studies at DLR by Steinberg *et al.* (2013). Experimental and modeling efforts for the isothermal jet-in-crossflow and reacting jets in non-vitiated crossflows can provide further understanding of the physics involved, which can be used to provide insight on the reacting jet in vitiated crossflow configuration.

Staged combustion studies involving reacting jets in vitiated crossflow have become increasingly popular in the literature over the past few years. Experiments at elevated inlet temperatures and combustor pressures were performed at Purdue University to characterize exhaust gas emissions, flame structure, and velocity fields (Lamont *et al.*, 2012; Panda *et al.*, 2015; Panda *et al.*, 2016; Panda *et al.*, 2017; Panda *et al.*, 2019). Recent studies at Georgia Institute of Technology include investigating emissions, flame structure, and flame dynamics at elevated inlet

temperatures and atmospheric pressure (Nair *et al.*, 2019; Nair *et al.*, 2019b; Sirignano *et al.* 2019; Sirignano *et al.* 2019b), but an earlier study by Sullivan *et al.* (2014) reported results at both elevated inlet temperatures and elevated combustor pressures. RJICF experiments at ambient inlet temperature and atmospheric combustor pressure were conducted at University of Connecticut (Wagner *et al.*, 2017; Wagner *et al.*, 2017b; Dayton *et al.*, 2019). Experiments with slotted injectors at atmospheric pressures and elevated temperatures were used for measurements at University of Cincinnati (Pinchak *et al.*, 2018; Pinchak *et al.*, 2019; Pinchak *et al.*, 2019b). Several studies on the reacting jet in vitiated crossflow have also been conducted at DLR (Fleck *et al.*, 2013; Fleck *et al.*, 2013b) and Technical University of Munich (Ahrens *et al.*, 2016; Kolb *et al.*, 2016).

A theoretical study by Ahrens *et al.* (2014) considered the NO_X formation of a reacting jet in vitiated crossflow under two distinct assumptions: (1) best case scenario with the jet burning after mixing perfectly with the crossflow, (2) worst case scenario with the jet burning without any mixing with the crossflow. Based on the experimental and theoretical work, mixing of the jet with the crossflow prior to ignition was believed to have a strong effect on the potential for NO_X reduction. The theoretical minimum levels of NO_X in a staged combustion system were investigated more recently by Goh *et al.* (2019) using 0-D and 1-D chemical kinetics calculations. For the idealized case of perfect mixing between the reacting jet and vitiated crossflow (modeled using a perfect mixer and batch reactor), NO_X levels were reduced to about 1 ppm (corrected to 15% O_2) at a firing temperature of 1975 K. Although simple models do not incorporate the complex coupling between the highly turbulent fluid dynamics and the chemical kinetics, such approaches are useful for identifying the likely physical limits of staged combustion for NO_X reduction.

The two primary means of NO_X formation relevant to this work are the *thermal NO_X* mechanism (Zeldovich mechanism) and the *prompt NO_X* mechanism. Thermal NO_X is believed to dominate at temperatures greater than 1800 K and prompt NO_X is believed to be an important mechanism for hydrocarbon-air flames (Glarborg *et al.*, 2018). The initiating step for thermal NO is:

$$O + N_2 \rightleftharpoons NO + N, \tag{3.1}$$

where monatomic oxygen attacks the triple bond in N_2. The remaining monatomic nitrogen then rapidly oxidizes to NO by one of two means:

$$N + OH \rightleftarrows NO + H,$$

(3.2)

$$N + O_2 \rightleftarrows NO + O.$$

The initiating reaction for prompt NO is:

$$CH + N_2 \rightleftarrows NCN + H.$$

(3.3)

It is believed that two different reaction pathways for prompt NO exist depending on whether the equivalence ratio is under or over about $\phi = 1.2$. In addition, at very rich conditions there may be a shift to the formation of HCN rather than NO. Although both thermal and prompt NO mechanisms are important for gas turbine engines, the thermal NO mechanism is believed to be the main source of NO in combustion gas at high-temperature (Glarborg *et al.*, 2018).

Key studies relating to NO_X emissions at engine-relevant conditions in recent years include: Lamont *et al.* (2012), Sullivan *et al.* (14), and Prathap *et al.* (2012). These works investigated strategies to limit NO_X emissions by investigating axial jet equivalence ratios, jet-to-crossflow momentum flux ratios, and even the angle of injection. The general observation between these studies is an increase in NO_X levels at higher post-jet (or combustor exit) temperatures and jet equivalence ratios. The most significant difference between the current work and these earlier works is that the earlier studies were conducted at traditional low-subsonic conditions (exit Mach numbers below 0.20), whereas the work in this paper varies the combustor exit Mach number up to 0.70 and at low axial residence times below 3 ms. In fact, to the best of our knowledge, all existing works in RJICF literature have operated the staged combustor at traditional gas turbine environments: combustor exit Mach number $Ma_{EX} \leq 0.2$ and axial residence time $\tau_{AX} \geq 5$ ms.

The present work investigates the emissions, particularly NO_X, from a staged gas turbine model combustor operating at up to high-subsonic exit conditions. This was achieved by transversely injecting a premixed natural gas (NG) and air reacting jet into a compressible, vitiated crossflow with negligible swirl. The experimental study was conducted at gas turbine engine-relevant conditions with elevated inlet temperatures ($T_3 = 500 - 600$ K), elevated combustor pressure ($P_4 = 500$ kPa), and thermal powers of $1 - 3$ MW. The vitiated crossflow with negligible swirl was created using a perforated plate burner in the main combustion zone, which has been described further in Chapter 2.

Two different axial air splits S_{AX} at about 6.4% and 20.7% were used for this work and the axial air split was defined here as:

$$S_{AX} = \frac{\dot{r}}{\dot{r}} \tag{3.4}$$

In the above equation $\dot{r}$, $\dot{r}$, and $\dot{r}$ represent the air mass flow rates of the headend combustor, axial combustor, and film cooling air respectively. Axial equivalence ratios ranging from $\phi_{AX} = 0.8 - 2.1$ were targeted for the 6.4% air split and axial equivalence ratios ranging from $\phi_{AX} = 0.8 - 1.4$ were targeted for the 20.7% air split. The axial equivalence ratio was defined here as:

$$\phi_{AX} = \frac{(\dot{r}}{(\dot{r}} \tag{3.5}$$

where $\dot{r}$ is the natural gas mass flow rate to the axial stage and $(\dot{r}$ defines the stoichiometric air–to–fuel (natural gas) ratio.

The main benefits of a high-subsonic staged combustor are the potential for NO_X reduction due to: (1) lower residence time, (2) decreased static temperature of the compressible flow, and (3) potentially better mixing of the jet with the vitiated flow. The two primary parameters varied for this experimental investigation were the staged combustor exit Mach number Ma_{EX} and the axial residence time τ_{AX}. Derived from fundamental gas dynamics equations, the exit Mach number was calculated using,

$$Ma_{EX} = \sqrt{\frac{-1 + \sqrt{1 + \frac{2(\gamma_{EX} - 1)}{\gamma_{EX}} \frac{R_{EX} T_{0,EX} (\dot{r}}{P_{EX} A_{EX}}}}{\gamma_{EX} - 1}} \tag{3.6}$$

In the above equation, γ_{EX} and R_{EX} symbolize the exit combustion gas specific heat ratio and gas constant, respectively; $T_{0,EX}$ symbolizes the calculated exit adiabatic total temperature; P_{EX} symbolizes the measured exit static pressure; $\dot{r}$ symbolizes the exit mass flow rate based on metered fuel and air streams; and A_{EX} symbolizes the exit cross-sectional area. The axial residence time was calculated using,

$$\tau_{AX} = \frac{L_{AX}}{U_{EX}}. \tag{3.7}$$

Here, L_{AX} symbolizes the axial combustor length and U_{EX} symbolizes the average exit velocity, which was calculated based on the exit Mach number and exit speed of sound. Experimental results of exhaust gas emissions based on varying Ma_{EX} and τ_{AX} are presented in this paper. Initially, both Ma_{EX} and τ_{AX} were varied together. A test matrix was then developed to investigate the Mach number independently of the residence time using the test rig modularity.

3.2   Experimental Systems

A schematic of the test rig used for this work is presented in Fig. 3.1 to illustrate the primary sub-assemblies: *headend stage*, *axial stage*, and *NO$_X$ quench & sample stage*. For the staged combustion system, the main combustion zone is referred to as the *headend* combustor and the secondary combustion zone after jet injection is referred to as the *axial* combustor. All of the hot sections (combustion and post-combustion zones) within the test rig feature a thermal barrier coating and are either film or water-cooled to ensure hardware survivability over long duration steady-state operation. The experiment was remotely controlled using a National Instruments LabVIEW Virtual Instrument (VI) due to the significant potential energy contained within an experiment operating at elevated pressures. Pressure transducers (GE Sensing) and K-type thermocouple probes (Omega) were installed at multiple locations throughout the test rig and fluid supply lines and were sampled at 260 Hz. Locations for the key rig monitoring instrumentation are also presented in Fig. 3.1.

The *headend* sub-assembly primarily consisted of a natural gas (NG) and air premixing pipe, a perforated plate burner (PPB) with a hydrogen pilot flame, a film cooling flange, and a flow contraction section. Details of the perforated plate burner have been covered extensively in Chapter 2. The PPB was used to create the hot vitiated flow with negligible swirl for the staged combustion experiments. Film cooling (ambient temperature air at nominally 5% mass flow rate of headend air) was introduced just downstream of the PPB to protect the inlet of the contraction section. The flow was accelerated in a near-isentropic manner within the contraction section (featuring an exit-to-inlet area ratio of about 1:50) and the flow geometry was also transitioned from circular to rectangular using a nozzle design based on the Vitoshinski profile. The contraction

section featured a double-helical water-cooling design to ensure hardware survivability under significant thermal loading from the hot combustion gas flow at high speeds. The ability to produce compressible, vitiated flow with negligible swirl for staged combustion experiments is unique to this work.

The *axial* combustor featured an axial premixing assembly (where independently metered streams of heated air and natural gas were allowed to mix), a modular injector flange, and axial residence time extension pieces. In this work, the injector flange was equipped with a flush-mounted injector featuring jet diameters of either $d_j = 1.07$ cm or 2.30 cm (used with axial air splits of $S_{AX} = 6.4\%$ and $S_{AX} = 20.7\%$, respectively). Both injectors featured a straight nozzle profile with length-to-diameter ratios of about $L/d_j = 10$. The axial residence time extension pieces were installed directly downstream of the axial injection stage and were used to vary the axial combustor length for discrete values of about $L_{AX} = 28$ cm, 53 cm, and 73 cm. The extension pieces featured a constant-area, rectangular flow channel with a 5.4 cm hydraulic diameter. A test matrix was designed based on this capability to vary the combustor length in order to: (1) keep the axial residence time constant for three different exit (i.e. post-injection) Mach numbers, and (2) keep the exit Mach number constant for three different axial residence times.

A *NOX quench* stage located directly downstream of the last extension piece was used to enable accurate control of the residence time by freezing the chemical reactions in the flow and thereby inhibiting further thermal NOX production. This was achieved by radially injecting water into the combustion gas flow to reduce the gas temperature below 1300 K. A length of pipe, referred to here as a *post-quench mixing pipe*, was used to promote better mixing of the axial jet with the main combustor flow before emissions sampling. A sampling probe was used to collect samples of the water-quenched exhaust gas. The sample gas was transported to the emissions measurement system using a heated line at 464 K to prevent condensation. The remainder of the exhaust flow traveled through an exhaust assembly, which included a *final quench* stage for injection of the process water used for cooling the test rig and a backpressure valve to control rig pressure.

A schematic of the fluid systems used for the experiment is presented in Fig. 2. Sonic venturis were used for all gaseous fluid lines and cavitating venturis were used for all water lines to have a deterministic system with known mass flow rates, which were calculated using an ASME

standard (Miller, 1984). The total temperature for locations along the test rig is also shown in Fig. 3.2 for a representative test condition. Experimental test conditions such as mass flow rates and equivalence ratios were monitored in real-time using equations programmed into the VI. REFPROP V 9.1 (Lemmon *et al.*, 2013) was used during the data reduction process for all fluids to precisely incorporate real gas effects. Real gas effects were found to be particularly significant for natural gas flow rate calculations. The natural gas composition used for this work is the same as that in Chapter 2, with the two major (> 1% by volume) components being methane (92.7%) and ethane (6.1%).

Exhaust gas emissions were characterized using a Fourier transform infrared (FTIR) spectrometer (MKS Instruments). The FTIR system was configured to collect data in the mid-infrared region and was used to measure concentrations by volume of: nitric oxide (NO), nitrogen dioxide (NO_2), carbon monoxide (CO), carbon dioxide (CO_2), and unburnt constituents of natural gas, such as methane (CH_4), ethane (C_2H_6), and propane (C_3H_8). Measurements of the *wet exhaust gas* were obtained at about 1 Hz with a nominal gas cell temperature of 464 K and nominal pressure of 101 kPa. All raw emissions values were calculated to a dry basis. In addition, measurements at representative headend only conditions were used to determine the axial stage contribution for NO_X and CO. Carbon balances and the combustion efficiency of the burner were calculated using an SAE International reference (ARP 1433). The carbon balance, which was used to validate the emissions sampling system and the metering of the air and natural gas flow into the test rig, generally showed agreement between 95 – 97%. Further details on the emissions measurement system can be found in Chapter 2.

All mean values of temperature and pressure were typically reported using an arithmetic mean of 100 seconds (260 Hz sampling frequency) at steady-state rig conditions. The precision component of total measurement uncertainty was very small given the 26,000 samples per test condition. Calculated experimental uncertainty for temperature and pressure measurements were 0.2% and 0.04% respectively based on previous uncertainty analysis. Experimental uncertainty for equivalence ratio was calculated to be 1.6%, without accounting for uncertainties in the thermodynamic properties acquired from REFPROP. All derived quantities, including equivalence ratio, are reported as arithmetic mean values of 100 seconds at steady-state rig operation. All emissions values are also typically reported using an arithmetic mean of 100 seconds (1 Hz sampling frequency) at steady-state conditions in the test rig. One standard

deviation was used as the experimental uncertainty for emissions measurements. The arithmetic mean and one standard deviation are presented in this work when reporting a set of test conditions representing a single exit Mach number Ma_{EX} or axial residence time τ_{AX}.

3.3   Results and Discussion

3.3.1   Preliminary measurements varying the exit Mach number and axial residence time

The axial combustor length was held constant at L_{AX} = 53 cm during the initial phase of testing. The staged combustor exit Mach number and the axial residence times were varied together by changing the global air (headend combustion air, axial combustion air, and film cooling air) mass flow rates. Parametric sweeps were conducted of the axial equivalence ratio ϕ_{AX} during this phase of testing. Based on the emissions sampling configuration, it was discovered that ϕ_{AX} > 0.7 was needed to ensure high levels of combustion efficiency from transverse jet injection into the axial combustor. This was believed to be due to the high mean velocities of the jet (130 – 300 m/s) and the crossflow (180 – 440 m/s), low jet-to-crossflow momentum flux ratios J = 1.7 (± 0.2), and the use of axial injectors flush with the combustor wall. Fig. 3.3 presents the combustion inefficiency of the staged combustor as a function of the axial equivalence ratio for the S_{AX} = 6.4% (±0.1%) air split at three different combinations of exit Mach number Ma_{EX} and axial residence time τ_{AX}. The combustion inefficiency is defined as $1 - \eta_B$ and is expressed as a percent. Very good combustion efficiency was observed for many different test conditions. However, for the highest Ma_{EX} & lowest τ_{AX} combination (Ma_{EX} = 0.68 and τ_{AX} = 1.0 ms), significantly lower combustion efficiency was observed for the two reported conditions at $\phi_{AX} \leq$ 1.0.

ΔNO_X (NO + NO_2) from the axial stage was calculated based on the measured NO_X from the staged combustion system minus the NO_X from the headend combustor only. Data for the headend only NO_X was collected immediately before igniting the axial stage to collect a set of data
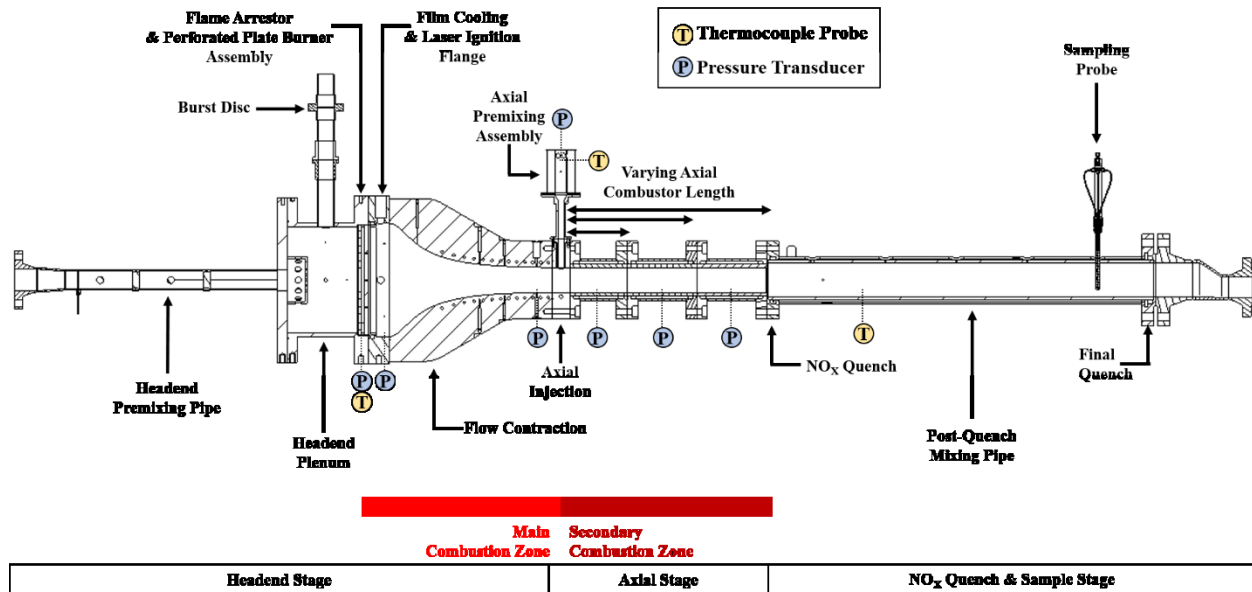
Figure 3.1: Schematic of high pressure test rig with key rig condition monitoring instrumentation.
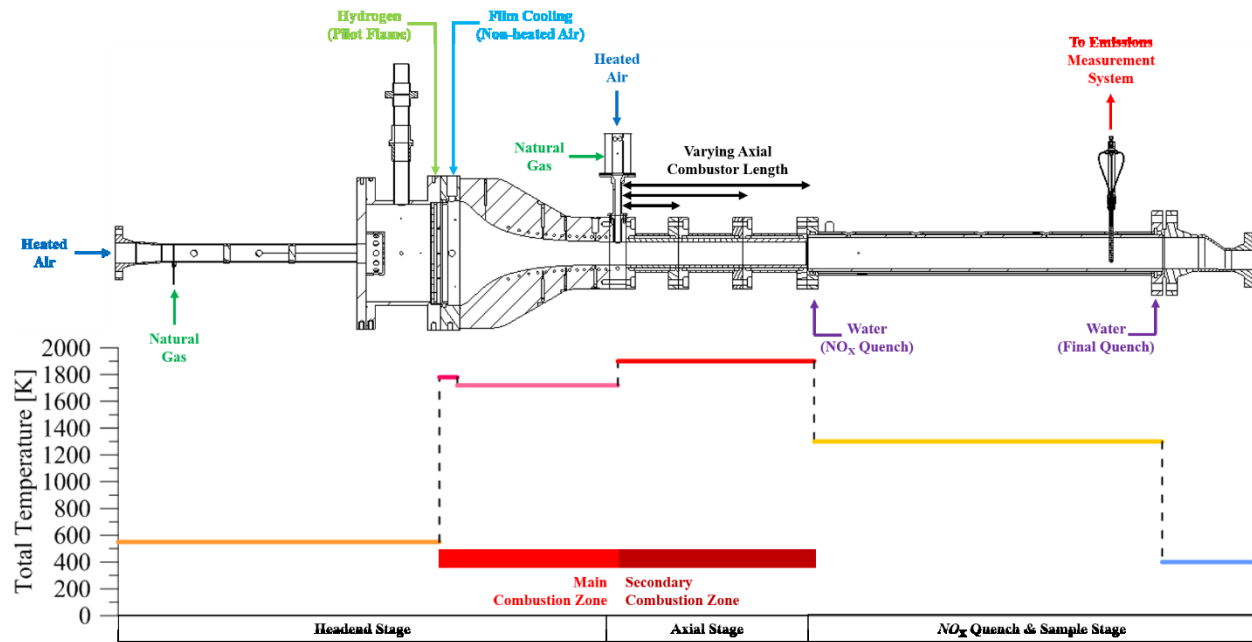
Figure 3.2: Schematic of rig fluid systems with total temperature profile within rig at a representative condition.

for the staged combustor at a specified exit Mach number and axial residence time. Values of ΔNO_X from the axial stage with respect to a representative headend only value of NO_X, referred

to here as the *NO$_X$ parameter*, are presented in Fig. 3.4 as a function of the staged combustor exit adiabatic total temperature for the three combinations of Ma_{EX} & τ_{AX}. Data points with high combustion efficiency ($\eta_B \geq 99.5\%$) are presented as colored symbols and the two values with $\eta_B < 99.5\%$ at $Ma_{EX} = 0.68$ & $\tau_{AX} = 1.0$ ms are presented as open symbols. The impact of higher exit Mach number and lower axial equivalence ratio for NO$_X$ reduction is clear. In fact, for $\phi_{AX} = 2.0$ the NO$_X$ parameter was observed to decrease from about 4.8 (ppm/ppm) at $Ma_{EX} = 0.26$ & $\tau_{AX} = 2.6$ ms to 0.7 (ppm/ppm) at $Ma_{EX} = 0.68$ & $\tau_{AX} = 1.0$ ms. This reduction in the NO$_X$ parameter is hypothesized to be due not only to the reduced axial residence time, which results in lower thermal NO$_X$ production, but also to the reduced static temperature and potentially better mixing of the jet with the vitiated crossflow (referred to in this work as the *Mach number effect*).

The reduction in combustion efficiency at lean axial equivalence ratios can be directly linked to the high levels of CO from the axial stage at these conditions. Figure 3.5 presents the ΔCO from the axial stage vs. the NO$_X$ parameter (ΔNO$_X$ from the axial stage with respect to a representative headend only value of NO$_X$)). For conditions at $Ma_{EX} = 0.49$ & $\tau_{AX} = 1.4$ ms and at $Ma_{EX} = 0.68$ & $\tau_{AX} = 1.0$ ms, increased levels of ΔCO were observed for test cases corresponding with the lowest ΔNO$_X$. This observation of increased ΔCO may be due to the greater crossflow velocity at the higher Ma_{EX} conditions affecting flame stabilization and the lower τ_{AX} inhibiting oxidation of CO to CO_2. However, it should be noted that CO emissions can vary considerably over the cross-section of the flow and can be significantly higher near the combustor walls due to quenching. Furthermore, as noted by Elkady *et al.* (2012), minor reaction progress can continue downstream of perceived quenching. Therefore, the CO results presented here should be viewed qualitatively for trends rather than as absolute values of ΔCO produced from the combustor (2012).

3.3.2   Test matrix to decouple the exit Mach number and axial residence time

The modular nature of the test rig, with the ability to extend the length of the axial combustor, was utilized to decouple the effect of Mach number from the axial stage residence time. Fig. 3.6 illustrates the three configurations for the test rig length used in this work. Notably, this modularity allowed for the variation of the Mach number while maintaining a constant residence

time after axial injection. Three different Ma_{EX} were used to investigate the Mach number effect at a constant $\tau_{AX} = 1.4$ ms for this portion of the test matrix. This was achieved experimentally by varying the global air flow rate into the rig together with the combustor length, as illustrated in Table 3.1 for a representative condition. The lowest targeted exit Mach number ($Ma_{EX} = 0.26$) was paired with the shortest axial combustor configuration, the intermediate targeted exit Mach number ($Ma_{EX} = 0.46$) was paired with the mid-length configuration, and the highest targeted exit Mach number ($Ma_{EX} = 0.66$) was paired with the longest configuration. Varying the axial combustor length also allowed for the variation of the axial residence time at a constant Mach number. This was achieved experimentally by using a fixed air flow rate and varying the axial combustor length to the specified configuration. The residence time effect for this parametric survey was primarily focused on the intermediate $Ma_{EX} = 0.44$, where the axial residence time was targeted to vary between $\tau_{AX} = 0.8 - 2.3$ ms. Table 3.2 summarizes the test matrix for the targeted exit Mach numbers and axial residence times. Measurements were obtained with an axial air split of $S_{AX} = 6.4\%$ at $\phi_{AX} = 1.0 - 2.0$ and $S_{AX} = 20.7\%$ at $\phi_{AX} = 0.8 - 1.4$. The selected range of axial equivalence ratios also allowed for direct comparison of the exit adiabatic total temperature and axial equivalence ratio between the two axial air splits.

Table 3.1: Illustration of varying exit Mach numbers at a constant residence time using modular axial combustor lengths and global air flow rates at a representative condition.

τ_{AX} [ms]	1.4		
L_{AX} [cm]	28	53	73
$\dot{i}$ [kg/s]	0.58	0.92	1.19
Ma_{EX} [-]	0.26	0.44	0.66
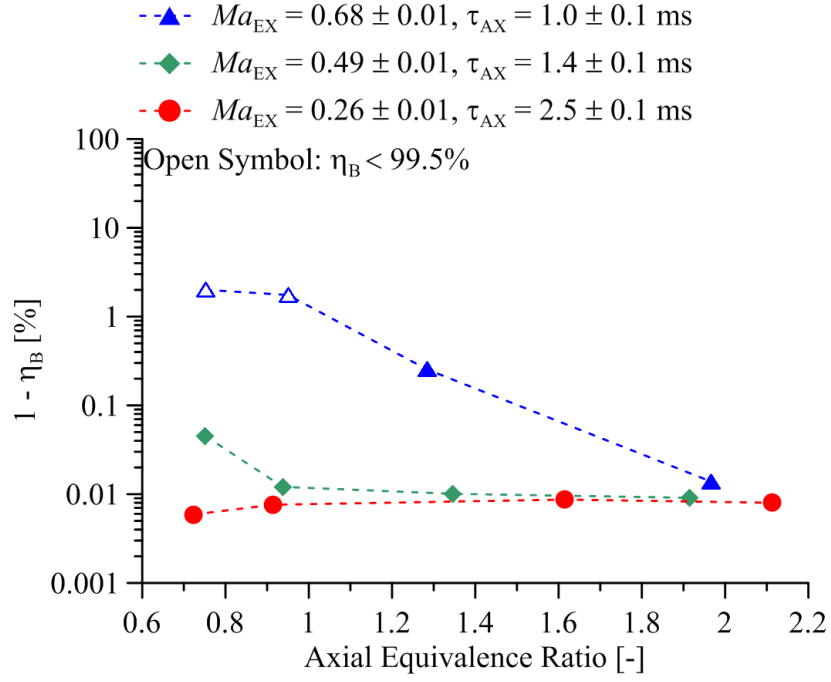
Figure 3.3: Combustion inefficiency of the staged combustor vs. axial equivalence ratio for S_{AX} = 6.4% at three different Ma_{EX} and τ_{AX} pairs.
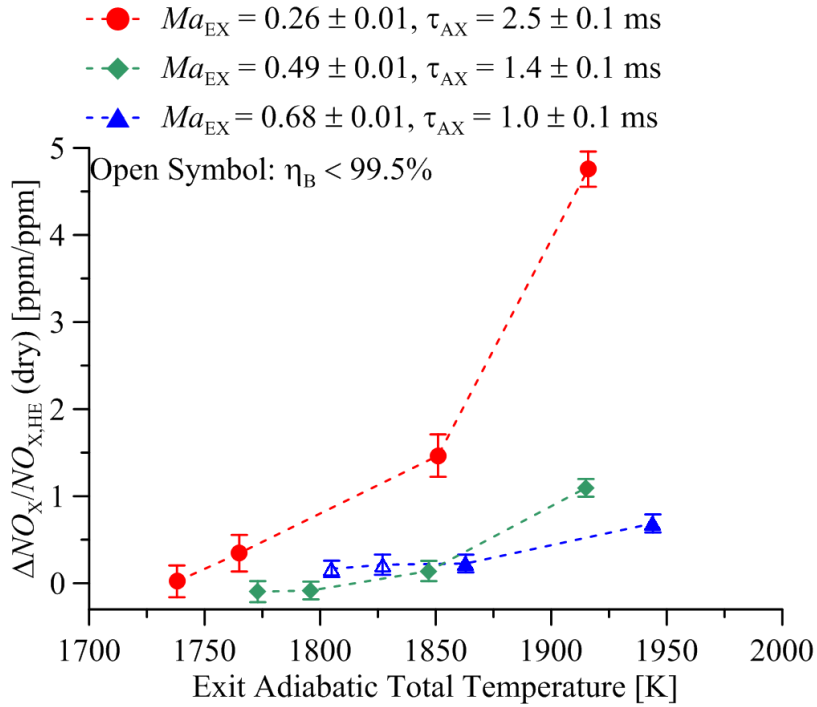
Figure 3.4: ΔNO_X from the axial stage with respect to HE NO_X vs. adiabatic staged combustor exit total temperature for S_{AX} = 6.4% at three different Ma_{EX} and τ_{AX} pairs.
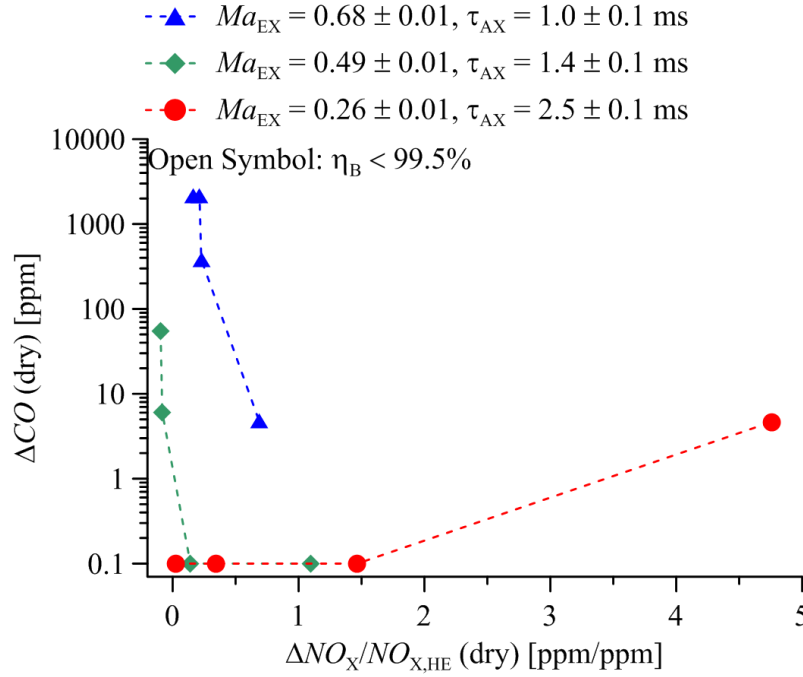
Figure 3.5: ΔCO from the axial stage vs. ΔNO$_X$ from the axial stage with respect to HE NO$_X$ for S_{AX} = 6.4% at three different Ma_{EX} and τ_{AX} pairs.
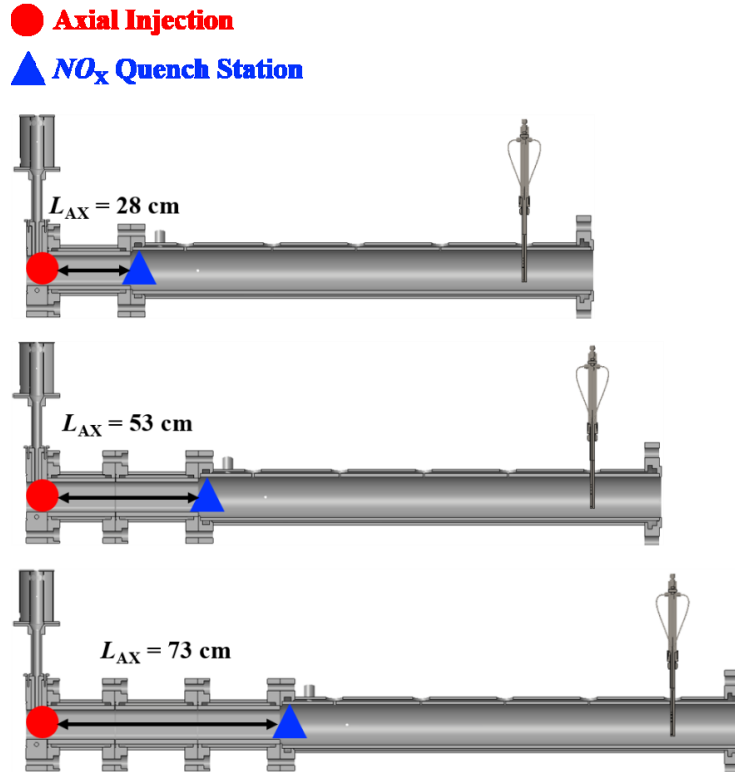
Figure 3.6: Schematic of the varying axial combustor length (distance between axial jet injection and NO$_X$ quench water injection station).

Table 3.2: Test matrix used to parametrically investigate the effects
of exit Mach number and axial residence time.

	Ma_{EX}		
τ_{AX} [ms]	0.26	0.44	0.66
0.8		X	
1.4	X	X	X
2.3		X	

3.3.3 Effect of Mach number on NOₓ emissions at a constant residence time

Emissions measurements were obtained at a total of eighteen different test conditions at a constant axial residence time τ_{AX} = 1.4 ms: nine conditions at S_{AX} = 6.4% (± 0.1%) and nine conditions at S_{AX} = 20.7% (± 1.3%). Fig. 3.7 presents ΔNOₓ (dry) values for the axial stage, with respect to a representative headend only value of NOₓ, vs. the exit Mach number at an axial residence time τ_{AX} = 1.4 ms (± 0.1 ms), for the two air splits. For the S_{AX} = 6.4% data set shown in Fig. 3.7a, ΔNOₓ was observed to decrease significantly with increasing Ma_{EX} at the highest adiabatic exit total temperature $T_{0,EX}$ = 1900 K (ϕ_{AX} = 1.97). In fact, the NOₓ parameter was observed to decrease by nearly 60% for this test case. ΔNOₓ was also observed to decrease most significantly at the highest $T_{0,EX}$ = 2020 K (ϕ_{AX} = 1.34) for the S_{AX} = 20.7% data set presented in Fig. 3.7b, where a nearly 70% reduction was observed for the NOₓ parameter. This reduction in NOₓ emissions through an increase in the Mach number has not been previously reported in literature to the best of our knowledge.

Very good combustion efficiency ($\eta_B \geq$ 99.5%) was observed for many of the test conditions presented in Fig. 3.7, particularly for rich axial equivalence ratios. The combustion inefficiency vs. the exit Mach number for the data set is presented in Fig. 3.8 and the corresponding ΔCO from the axial stage vs. ΔNOₓ (dry) from the axial stage, with respect to a representative headend only value of NOₓ, is presented in Fig. 3.9. For the S_{AX} = 6.4% and ϕ_{AX} = 0.96 test case, the observation of lower combustion efficiency in Fig. 3.8a at Ma_{EX} = 0.26 was somewhat unusual, since improved combustion efficiency was observed at higher exit Mach numbers. This may indicate that the residence time of τ_{AX} = 1.4 ms could be too short to achieve complete combustion at the lower Ma_{EX}, but may be sufficiently long enough to achieve improved combustion

efficiency at the higher Ma_{EX}. A plausible reason for this could be potentially superior mixing of the axial jet with the vitiated flow at higher Mach numbers. Reduced combustion efficiency was observed at the larger S_{AX} = 20.7% air split for the lean axial equivalence ratio ϕ_{AX} = 0.77 at all three Mach numbers. Interestingly, the lowest combustion inefficiency in Fig. 3.8b for the lean and stoichiometric jets at S_{AX} = 20.7% was observed at the intermediate Ma_{EX} = 0.44. Therefore, it might be possible that the residence time of τ_{AX} = 1.4 ms may be too short to obtain complete combustion at the lower Ma_{EX} values without the benefit of improved mixing of the jet with the vitiated flow at higher Ma_{EX} values. However, for the lean and stoichiometric conditions at Ma_{EX} = 0.65, the enhanced mixing with the oxygen-rich vitiated flow could have caused the jet to burn in a manner that was too lean, which would result in lower combustion efficiency. Based on Fig. 3.9, it is clear that conditions corresponding to very low values of the NO_X parameter also generally produce higher values of ΔCO. Comparable levels for oxidation of CO to CO_2 should be present at these conditions given the fixed residence time and therefore the variation in CO levels is believed to be due to the Mach number and equivalence ratio affecting flame stabilization. As mentioned previously, the CO values presented here should be considered in terms of trends with Mach number and flame temperature, rather than as absolute values of ΔCO emissions from the combustor (Elkady et $al.$, 2012).

One potential physical reason for the observed NO_X reduction at higher Ma_{EX} is due to the lower static temperature of a compressible flow. The static temperature as a function of the Mach number is presented in Fig. 3.10a for three different total temperatures. It is known that the reaction rate for $O+N_2 \rightarrow NO+N$ is an important pathway for thermal NO_X (Glarborg et $al.$, 2018). This reaction rate was calculated based on the static temperature and static pressure using CHEMKIN V. 18.1 (2017) and is presented in Fig 3.10b as a function of the Mach number. A strong decrease in the calculated reaction rate was observed with increasing Mach number, primarily through the reduced static temperature. The reduction in the reaction rate for NO_X is believed to heavily contribute towards lower NO_X at higher Ma_{EX}

Another physical reason for reduced NO_X at higher Mach numbers may be due to better mixing of the jet with the vitiated crossflow prior to combustion. It is well known that increasing the degree of mixing of the premixed fuel and air in gas turbine engines reduces NO_X emissions by limiting the formation of local hot spots in the combustion zone (Lieuwen and Yang, 2013).

Therefore, it is believed that improved mixing of the jet with the crossflow prior to jet combustion at higher Mach numbers, due to their interaction occurring at higher speeds, may also be contributing to the NO_X reduction. A compressible, isothermal jet-in-crossflow model developed by Heister and Karagozian (1990) was used to calculate the jet trajectory and vortex half-spacing at conditions representative of the experiment. Calculations were performed for three pairs of jet Mach number and crossflow Mach number combinations, which corresponded to conditions for low (Ma_{EX} = 0.26), intermediate (Ma_{EX} = 0.48), and (high Ma_{EX} = 0.69) exit Mach numbers. Figure 3.11a presents the calculated jet trajectory for the three Mach number pairs and reduced penetration into the crossflow was calculated for higher Mach numbers. The jet cross-section was modeled as an inviscid, compressible counter-rotating vortex pair. The vortex half-spacing, which represents an idealized shape for the isothermal jet-in-crossflow, scales with the varying area of the jet as it travels through the crossflow. Fig. 3.11b presents the calculated dimensionless vortex half-spacing h^* (made dimensionless using the jet diameter) vs. the dimensionless axial distance. Larger h^* values were calculated at higher Mach numbers. Entrainment of the crossflow with the jet is directly related to the vortex half-spacing (Heister and Karagozian, 1990). Therefore, it can be concluded that increasing the Mach number also likely enhances entrainment for the reacting jet-in-crossflow configuration and leads to better mixing of the jet with the crossflow.

3.3.4   Effect of low residence time on NO_X emissions at a constant Mach number

Emissions measurements were obtained at an additional twelve test conditions for Ma_{EX} = 0.45: six conditions each at S_{AX} = 6.4% (± 0.1%) and S_{AX} = 20.7% (± 1.3%). The purpose of this portion of the test matrix was to investigate the effect of axial residence time on NO_X emissions at a constant exit Mach number. Fig. 3.12 presents ΔNO_X (dry) values for the axial stage, with respect to a representative headend only value of NO_X, vs. the axial residence time at Ma_{EX} = 0.45. For the S_{AX} = 6.4% data set in Fig. 3.12a, ΔNO_X was observed to increase most significantly with increasing τ_{AX} for the ϕ_{AX} = 1.94 ($T_{0,EX}$ = 1900 K) test case. In fact, the NO_X parameter was observed to increase nearly 200% by increasing the axial residence time from 0.8 ms to 2.1 ms. For the S_{AX} = 20.7% data set in Fig. 3.12b, ΔNO_X was observed to increase most significantly with increased axial residence time for the ϕ_{AX} = 1.38 ($T_{0,EX}$ = 2050 K) test case. Here, the NO_X

parameter increased by about 60% with an increase in the axial residence time from 0.8 ms to 2.1 ms. An increase in NO_X emissions with greater residence time is an established trend in literature due to the increased presence of thermal NO_X (Lieuwen and Yang, 2013). Since the effect of thermal NO_X is more dominant at higher temperatures, greater sensitivity of NO_X to axial residence times should also be apparent for the higher axial equivalence ratios.
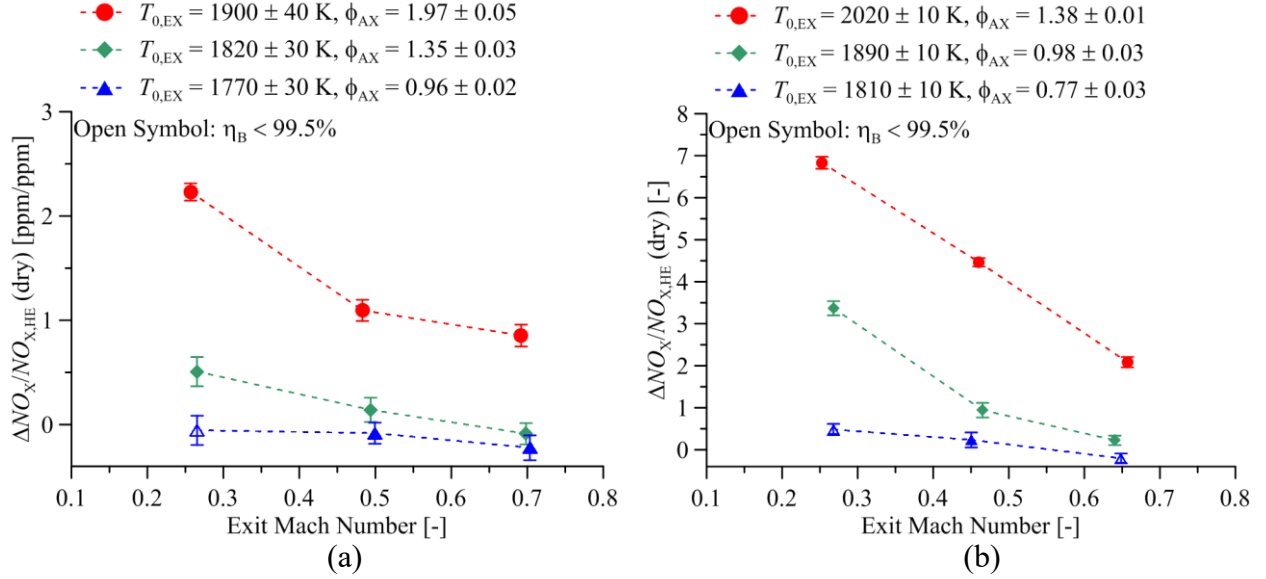
Figure 3.7: ΔNO_X from axial stage with respect to HE NO_X vs. exit Mach number for (a) $S_{AX} = 6.4\%$ and (b) $S_{AX} = 20.7\%$ at a constant $\tau_{AX} = 1.4$ ms and three different $T_{0,EX}$ and ϕ_{AX} pairs.
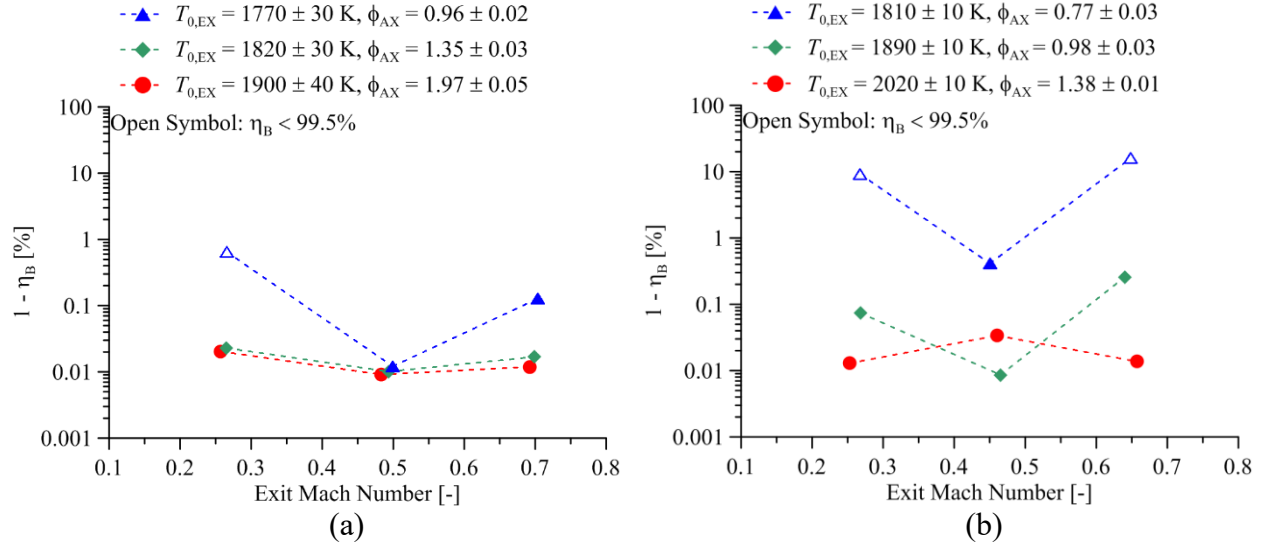
Figure 3.8: Combustion inefficiency of the staged combustor vs. exit Mach number for (a) S_{AX} = 6.4% and (b) S_{AX} = 20.7% at a constant τ_{AX} = 1.4 ms and three different $T_{0,EX}$ and ϕ_{AX} pairs.
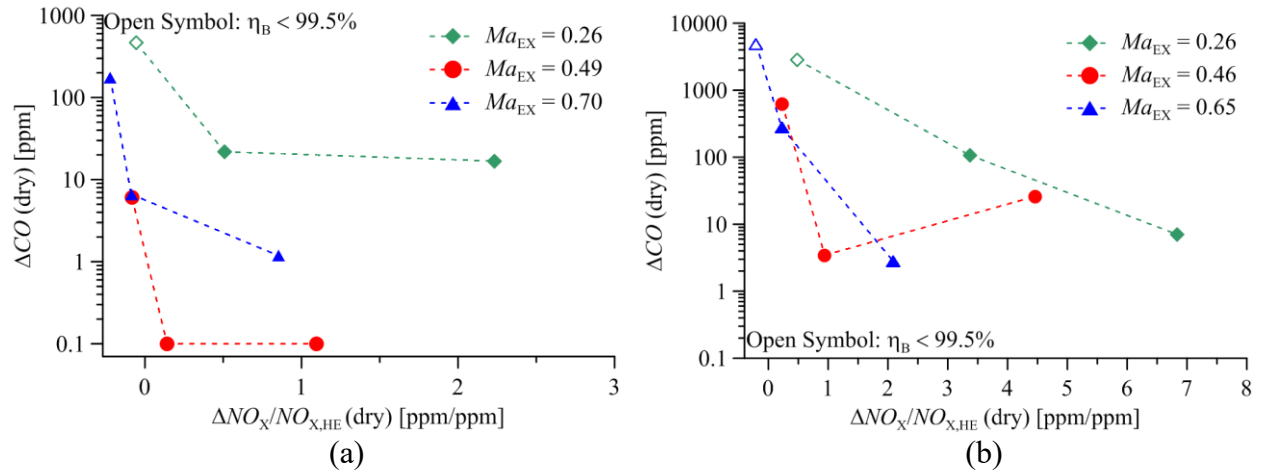
Figure 3.9: ΔCO from the axial stage vs. ΔNO$_X$ from axial stage with respect to HE NO$_X$ for: (a) S_{AX} = 6.4% and (b) S_{AX} = 20.7% at a constant τ_{AX} = 1.4 ms and three different exit Mach numbers.
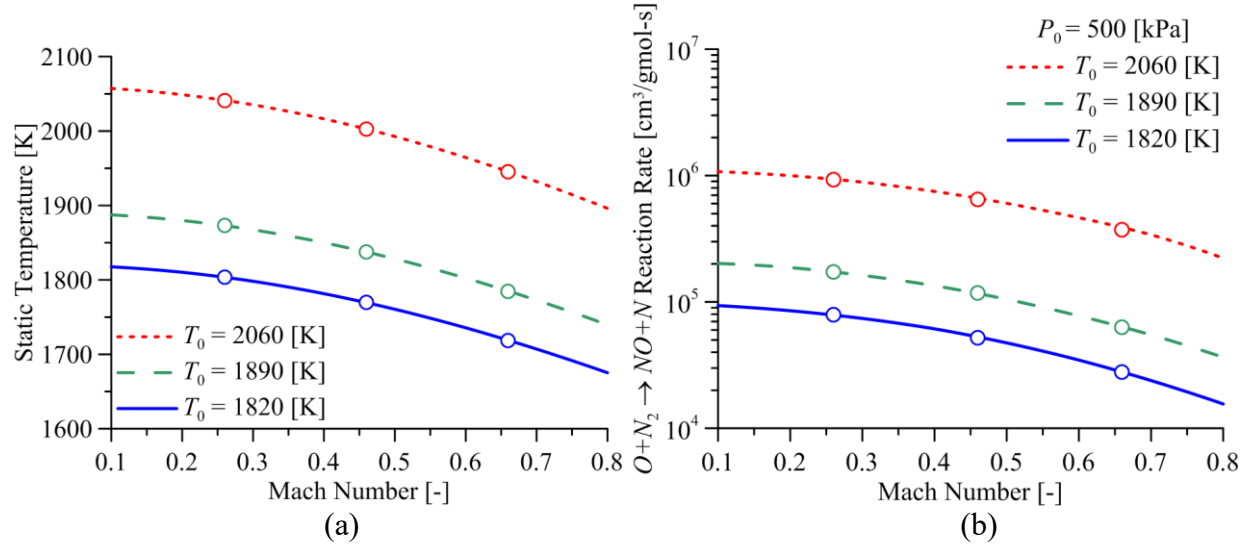
Figure 3.10: Effect of Mach number on (a) static temperature, (b) $O+N_2 \rightarrow NO+N$ reaction rate.

The combustion inefficiency vs. the axial residence time for the constant $Ma_{EX} = 0.45$ is presented in Fig. 3.13 and the ΔCO from the axial stage vs. the NO_X parameter is presented in Fig. 3.14. An improved combustion efficiency and lower levels of CO from the axial stage were generally observed with an increase in residence time. ΔCO was observed to decrease for conditions corresponding to higher NO_X levels and this can be attributed to the longer residence time allowing for greater oxidation of CO to CO_2. However, once again, the CO measurements should be considered qualitatively for trends with flame temperature and residence time, rather than absolute values for CO emissions from the combustor (Elkady *et al.*, 2013).

3.3.5   Comparison between axial air splits for similar Mach numbers and residence times

NO_X emissions using the two different axial air splits were directly compared at a constant τ_{AX} for similar axial equivalence ratios and similar adiabatic exit total temperatures. Figure 3.15 presents the ΔNO_X (dry) values for the axial stage, with respect to a representative headend only value of NO_X, vs. the exit Mach number for the 6.4% and 20.7% air splits at a constant axial equivalence ratio $\phi_{AX} = 1.35 \ (\pm 0.03)$ and a constant $\tau_{AX} = 1.4$ ms. Although the NO_X parameter was observed to decrease for both air splits, the magnitude of this decrease was significantly greater for $S_{AX} = 20.7\%$. Furthermore, ΔNO_X values with the 20.7% air split were observed to be greater than those from the 6.4% air split at all three exit Mach numbers. Both of these trends

may be explained by considering that the adiabatic exit total temperature of $T_{0,EX} = 2020$ K (± 10 K) for the 20.7% air split is significantly greater than the $T_{0,EX} = 1820$ K (± 30 K) for the 6.4% air split. As a result, thermal NO_X production with the 6.4% air split is significantly lower than that of the 20.7% air split due to the lower temperature. Furthermore, the ability to reduce NO_X by increasing the Mach number appears to be particularly strong at higher temperatures. It is known that thermal NO_X production strongly increases with higher temperatures, especially above 1800 K (Glarborg *et al.*, 2018). Therefore, reducing the static temperature of the flow by increasing the Mach number should have the greatest impact in terms of NO_X reduction at higher temperatures. Due to only a slight decreasing trend vs. the exit Mach number for the $S_{AX} = 6.4\%$ data, statistical analysis using the t-test was performed. Results from the t-test yielded p-values that were orders of magnitude smaller than the prescribed significance level of $\alpha = 0.05$.
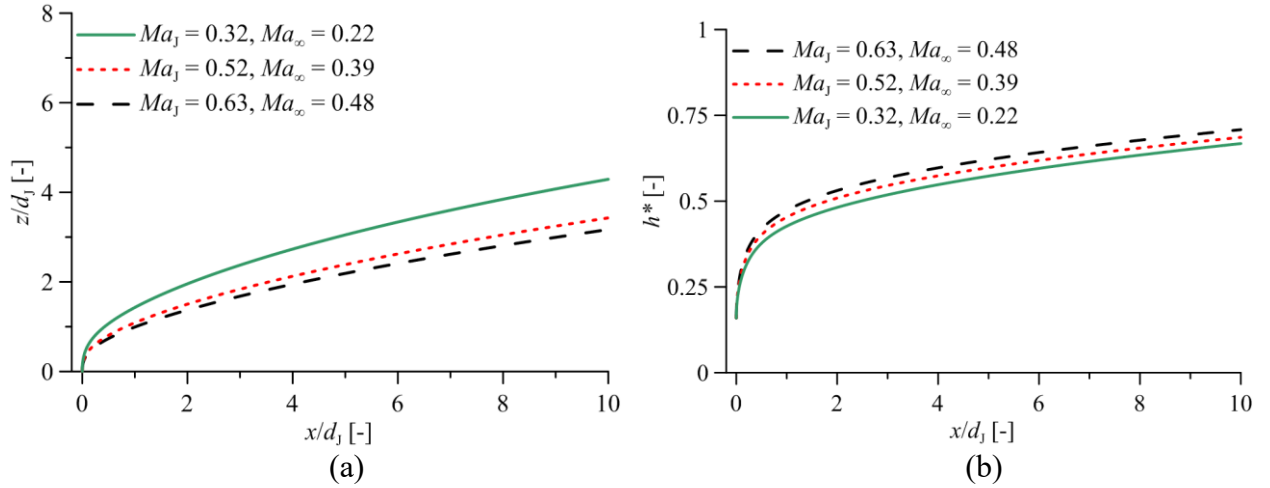
Figure 3.11: Calculated (a) jet trajectory and (b) vortex half-spacing vs. axial distance for three Mach number combinations using a compressible, isothermal jet-in-crossflow model.
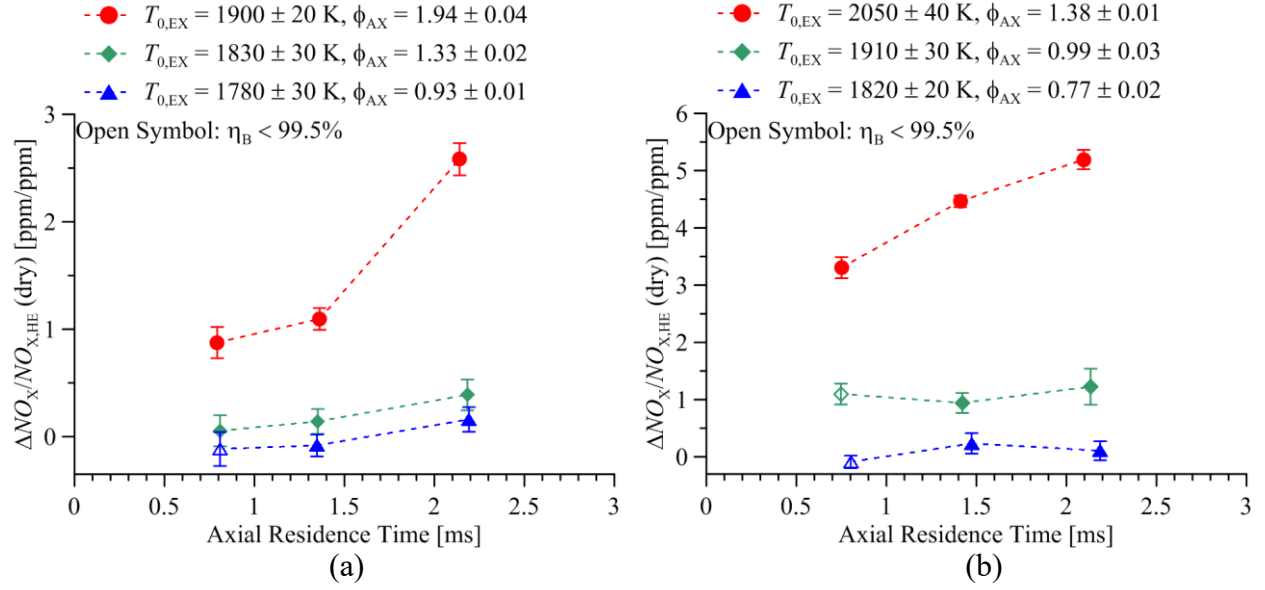
Figure 3.12: ΔNO_X from axial stage with respect to HE NO_X vs. axial residence time for (a) S_{AX} = 6.4% and (b) S_{AX} = 20.7% at a constant Ma_{EX} = 0.45 and three different $T_{0,EX}$ and ϕ_{AX} pairs.
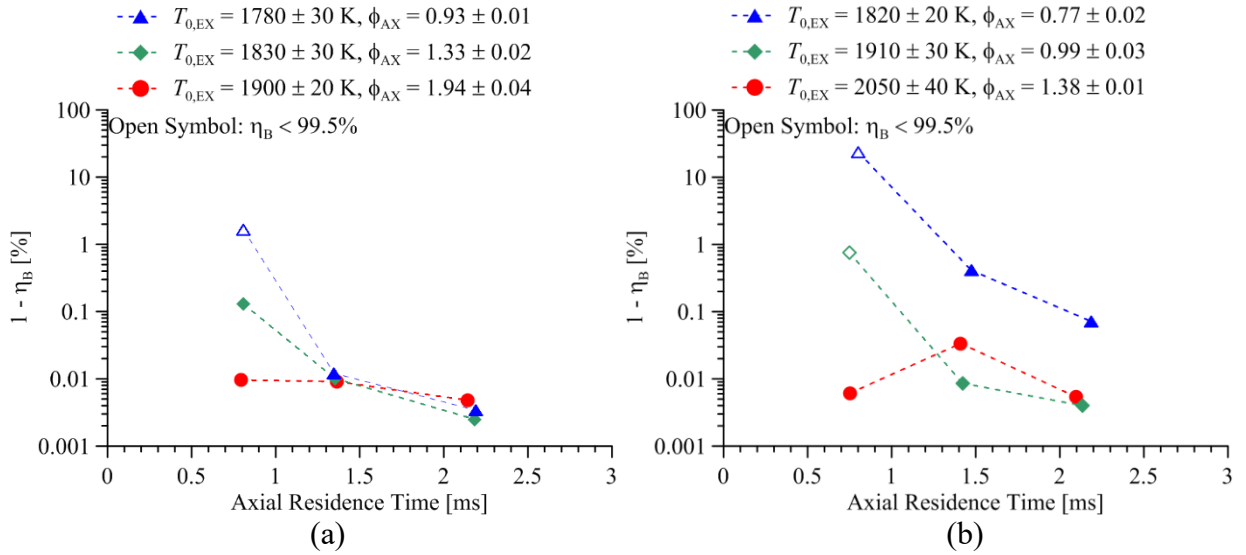
Figure 3.13: Combustion inefficiency of the staged combustor vs. axial residence time for (a) S_{AX} = 6.4% and (b) S_{AX} = 20.7% at a constant Ma_{EX} = 0.45 and three different $T_{0,EX}$ and ϕ_{AX} pairs.
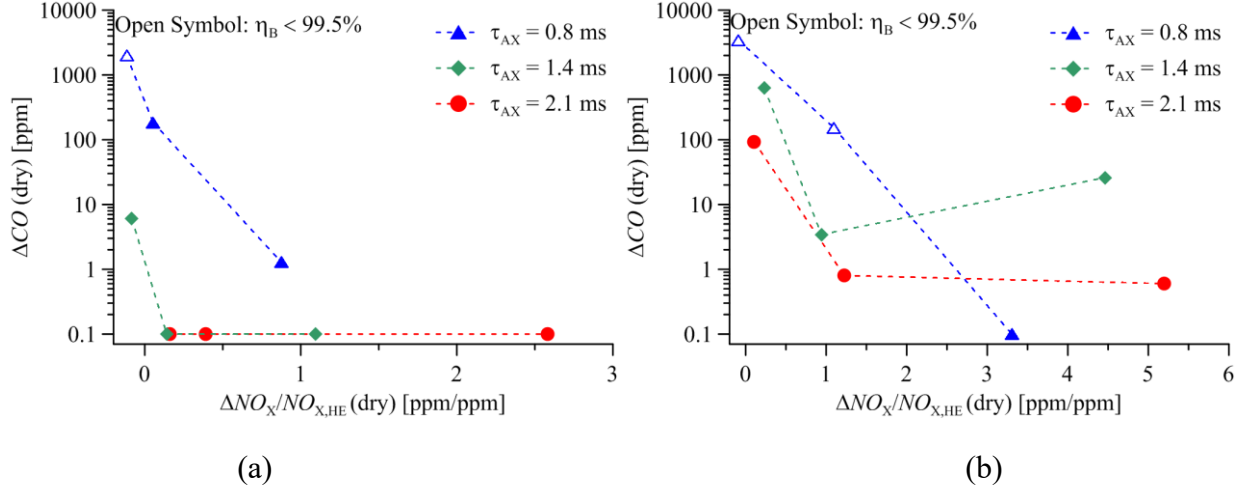
Figure 3.14: ΔCO from axial stage vs. axial residence time for (a) $S_{AX} = 6.4\%$ and (b) $S_{AX} = 20.7\%$ at a constant $Ma_{EX} = 0.45$ and three different $T_{0,EX}$ and ϕ_{AX} pairs.

An air split of $S_{AX} = 6.4\%$ at $\phi_{AX} = 1.97$ (± 0.05) and an air split of $S_{AX} = 20.7\%$ at ϕ_{AX} = 0.98 (± 0.03) provide similar adiabatic exit total temperatures, $T_{0,EX} = 1890$ K (± 20 K). A constant exit total temperature should result in similar thermal NO_X production after sufficient mixing of the reacting jet with the crossflow. Fig. 3.16 presents the ΔNO_X (dry) values for the axial stage, with respect to a representative headend only value of NO_X, as a function of the exit Mach number for the two air splits at a constant residence time $\tau_{AX} = 1.4$ ms. The NO_X parameter was observed to decrease with increasing Ma_{EX} for both air splits. However, an interesting trend from Fig. 3.16 is a higher NO_X parameter value for the 20.7% air split compared to the 6.4% air split at $Ma_{EX} = 0.26$, nearly identical values at $Ma_{EX} = 0.47$, and a lower value for the 20.7% air split compared to the 6.4% air split at $Ma_{EX} = 0.67$. This observation may be due to larger regions of higher flame temperature for the near stoichiometric $S_{AX} = 20.7\%$ jet, which lead to greater static temperature reduction impacts at higher Mach numbers before the jet completes mixing with the crossflow after combustion.

The ΔNO_X (dry) from the axial stage, with respect to a representative headend only value of NO_X, vs. the axial stage residence time for the $S_{AX} = 6.4\%$ and $S_{AX} = 20.7\%$ air splits is presented in Fig. 3.17 at a constant exit Mach number $Ma_{EX} = 0.46$ (± 0.03) and a constant axial equivalence ratio of $\phi_{AX} = 1.35$ (± 0.03). The NO_X parameter for the 20.7% air split was observed

75

to be significantly greater than that from the 6.4% air split for the range of residence times considered. It is believed that the thermal NO_X contribution is primarily responsible for this, given the higher $T_{0,EX} = 2050$ K ($\pm$ 40 K) for $S_{AX} = 20.7\%$, compared to the lower $T_{0,EX} = 1830$ K ($\pm$ 30 K) for $S_{AX} = 6.4\%$. Furthermore, since thermal NO_X production is strongly dependent on the residence time, a greater increase in the NO_X parameter was observed for the 20.7% air split compared to the 6.4% split with an increase in the axial residence time from 0.8 to 2.2 ms. Statistical analysis was also performed on the $S_{AX} = 6.4\%$ data due to only a slight increasing trend observed with respect to the axial residence time and results from the t-test also showed this trend to be significant (calculated p-values were orders of magnitude smaller than the $\alpha = 0.05$ value).

Fig. 3.18 presents the ΔNO_X (dry) from the axial stage, with respect to a representative headend only value of NO_X, as a function of the axial stage residence time for a constant $T_{0,EX} = 1910$ K ($\pm$ 30 K) at $Ma_{EX} = 0.46$ (± 0.03). Both the 6.4% and 20.7% axial air splits showed similar NO_X parameter values for axial residence times up to 1.4 ms. However, further increase in the residence time showed a substantial increase in the NO_X parameter for the 6.4% air split compared to the 20.7% air split. This result is likely due to the fact that the 6.4% air split case has more time transitioning past stoichiometric conditions, while still at excessive temperatures. Whereas the 20.7% air split case is only diluted further at the point of residence time increase, which could lead to further flame temperature reductions with increase in the residence time.

3.4   Summary and Conclusions

The effect of Mach Number and low residence time on NO_X emissions produced within a staged gas turbine model combustor operating with premixed natural gas and air at engine-relevant conditions ($T_3 = 500 - 600$ K and $P_4 = 500$ kPa) are presented in this chapter. The axial combustor length was held constant during the initial phase of testing, with the staged combustor exit Mach number and the axial residence time varied together. Parametric sweeps of the axial equivalence ratio were conducted and based on the exhaust gas measurements, it was discovered that axial equivalence ratios $\phi_{AX} > 0.7$ were needed to achieve high combustion efficiency ($\eta_B > 99.5\%$). The impact of higher exit Mach numbers and lower axial residence times for reduction

in NO_X produced by the axial stage was very clear. This reduction in NO_X is hypothesized to be due not only to the reduced axial residence time, which results in lower thermal NO_X production, but also to the reduced static temperature and potentially better mixing of the jet with the vitiated crossflow (referred to in this work as the *Mach number effect*).

Figure 3.15: ΔNO_X from axial stage with respect to HE NO_X vs. exit Mach number at a constant $\tau_{AX} = 1.4$ ms and $\phi_{AX} = 1.35$ for two different axial air splits and corresponding $T_{0,EX}$.
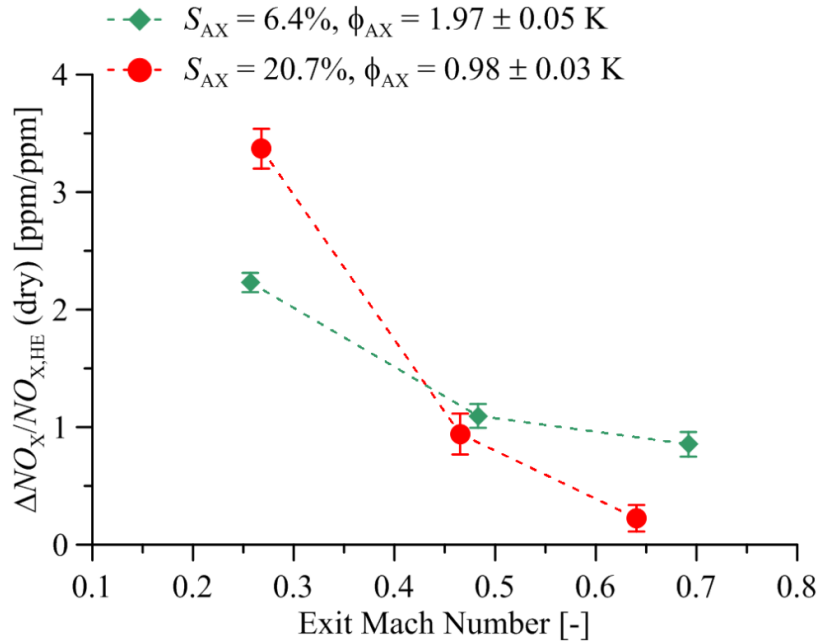
Figure 3.16: ΔNO_X from axial stage with respect to HE NO_X vs. exit Mach number at a constant $\tau_{AX} = 1.4$ ms and $T_{0,EX} = 1890$ K for two different axial air splits and corresponding ϕ_{AX}.
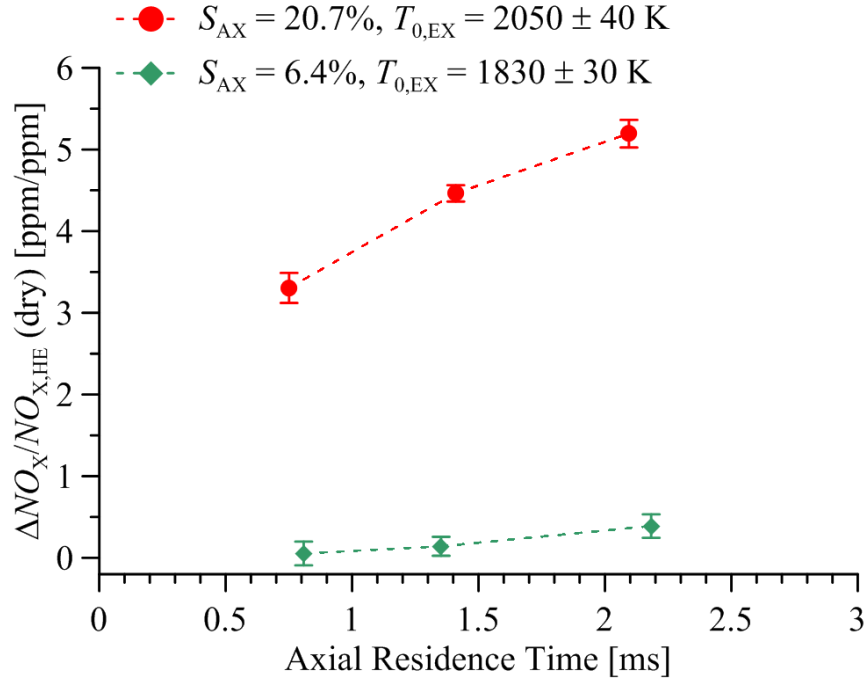
Figure 3.17: ΔNO_X from axial stage with respect to HE NO_X vs. axial residence time at a constant $Ma_{EX} = 0.46$ and $\phi_{AX} = 1.35$ for two different axial air splits and corresponding $T_{0,EX}$.
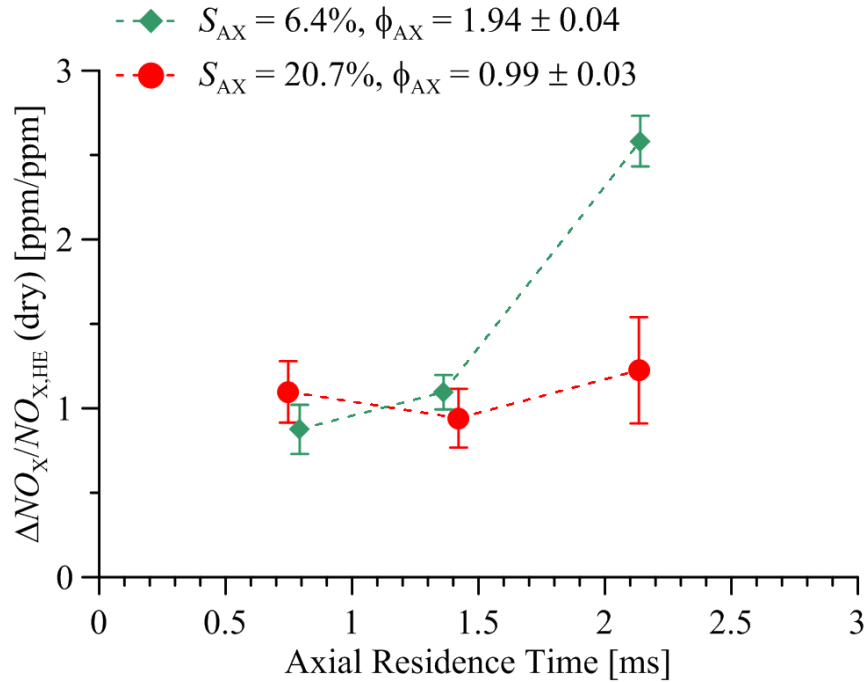
Figure 3.18: ΔNO_X from axial stage with respect to HE NO_X vs. axial residence time at a constant $Ma_{EX} = 0.46$ and $T_{0,EX} = 1910$ K for two different axial air splits and corresponding ϕ_{AX}.

Upon completion of these initial measurements, a test matrix was developed to independently study the effects of residence time and Mach number on NO_X emissions by using the modularity of the test rig. At a constant residence time $\tau_{AX} = 1.4$ ms, the NO_X produced from the axial stage showed a strong decrease with higher exit Mach numbers for conditions corresponding to a range of axial equivalence ratios. This effect was observed to be strongest (60 – 70% reduction) at the highest adiabatic exit total temperatures: $T_{0,EX} = 1900$ K for $S_{AX} = 6.4\%$ and $T_{0,EX} = 2020$ K for $S_{AX} = 20.7\%$. The reduction in NO_X emissions through an increase in the Mach number has not been previously reported in literature to the best of our knowledge. The effect of axial residence time (1 – 2.3 ms) on ΔNO_X produced by the two air splits at a constant $Ma_{EX} = 0.45$ was also investigated. The axial residence time was observed to have a stronger effect at conditions with staged combustor exit adiabatic total temperatures $T_{0,EX} > 1900$ K, likely due to the increased thermal NO_X production at higher temperatures. An increase in NO_X due to longer residence times as observed in this work agrees with established trends in the literature. Comparing the two axial air splits at similar conditions provides further insight on the strong influence of thermal NO_X and the ability to mitigate this through higher Mach numbers and lower residence times.

Figure 3.19 summarizes the main purpose of the test matrix by presenting the ΔNO_X parameter (referenced to 15% O_2) vs. the axial residence time at three different exit Mach numbers ($Ma_{EX} = 0.26, 0.44, 0.67$) and at a constant $\phi_{AX} = 2.0$. A potentially useful hypothesis can be drawn: the architecture of a practical, high-subsonic, axially-staged gas turbine engine can be designed to allow for as long of an axial residence time as is needed (i.e. longer combustor length) for high combustion efficiency (e.g. to ensure CO burnout), while still reaping NO_X reduction benefits from operation at higher Mach number. Axial injection at higher Mach numbers will be particularly useful for achieving higher turbine inlet temperatures beyond 2000 K (which can help increase the overall cycle efficiency to 65%), while maintaining low levels of NO_X and CO within 25 ppm and 10 ppm, respectively.

Based on the emissions results presented in this chapter, future work will involve investigating the fundamentals behind the Mach number effect. Provisions have been made to develop an optically-accessible axial stage combustion zone and investigate the flame structure over a range of Mach numbers using planar laser-induced fluorescence (PLIF). The development

of the optically-accessible secondary combustion zone is reviewed in Chapter 4. PLIF measurements were performed on this experiment and the results are presented in Chapter 5 and Chapter 6. Further numerical work beyond the scope of this dissertation would also be useful. Additional insights on the Mach number effect can also be gained through development of a simplified chemical kinetics model to compare experimental results with numerical predictions. This model would also be used to compare different reaction mechanisms including GRI-Mech 3.0, San Diego, and Glarborg. Comparing the experimental and numerical results with different physically-inspired parameters involving the activation energy of the $O+N_2 \rightarrow NO+N$ reaction or its reaction rate may also allow for additional insights to be gleaned from the measurements and simulations.
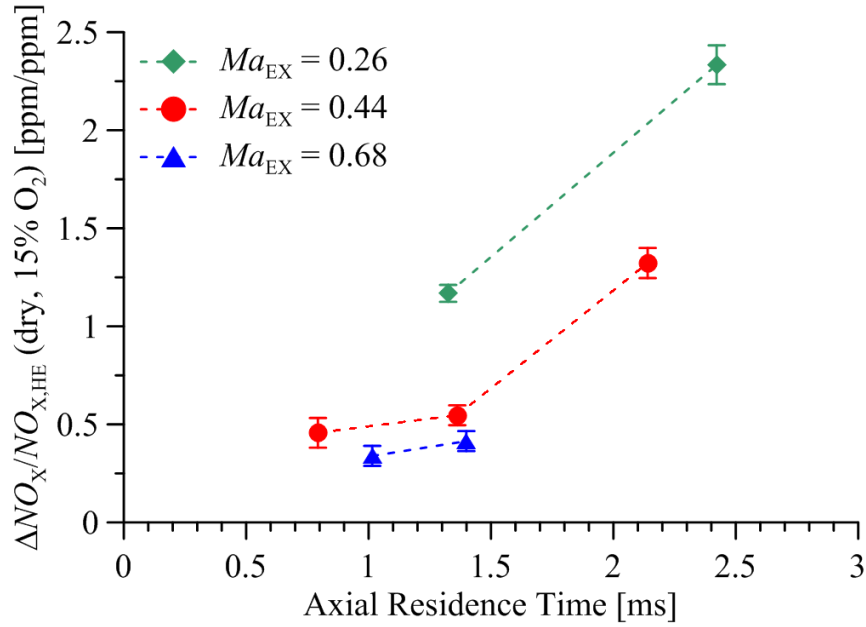
Figure 3.19: ΔNO_X from axial stage with respect to HE NO_X vs. axial residence time at a constant $\phi_{AX} = 2.0$ and $T_{0,EX} = 1910$ K for three different exit Mach numbers.

4.   THE DEVELOPMENT OF AN OPTICALLY-ACCESSIBLE SECONDARY COMBUSTION ZONE FOR REACTING JETS IN HIGH SPEED VITIATED CROSSFLOWS AT ENGINE-RELEVANT CONDITIONS

4.1   Introduction

The reacting jet in crossflow (RJICF) has become an increasingly popular topic of research over the last several years. The primary motivation for studying the RJICF is its application within axially staged combustors. Axially staged combustors have the potential to reduce NO_X emissions for power generation applications and to increase thrust for propulsion applications. Experimental groups that have pursued research activities towards understanding the complex physics associated with the RJICF include efforts at Purdue University, Georgia Institute of Technology, University of Connecticut, and University of Cincinnati.

A high-pressure test rig operating with optical access to investigate the RJICF was previously characterized extensively at the Zucrow Laboratories within Purdue University at combustor pressures of 500 – 800 kPa and elevated inlet temperatures up to 750 K. Experiments with both premixed natural gas (NG) and air as well as premixed hydrogen and nitrogen were performed using Fourier-transform infrared (FTIR) spectroscopy to characterize exhaust gas emissions (Lamont *et al*., 2012*; Roa *et al.,* 2014), planar laser induced fluorescence (PLIF) to characterize the flame structure (Panda *et al.*, 2016; Panda *et al.*, 2017, Panda *et al.*, 2019), particle imaging velocimetry (PIV) to characterize the velocity field (Panda *et al.*, 2015; Panda *et al.*, 2016; Panda *et al.*, 2017; Panda *et al.*, 2019), and coherent anti-Stokes Raman scattering (CARS) spectroscopy to provide point-wise temperature and specie-concentration measurements (Lamont *et al.*, 2013). Recent studies at the Georgia Institute of Technology include investigations of emissions, flame structure, and flame dynamics at elevated inlet temperatures but atmospheric pressure (Nair *et al.*, 2019; Nair *et al.*, 2019; Sirignano *et al.*, 2019; Yi *et al.*, 2019). However, earlier studies by Sullivan *et al.* (2013 and 2014) investigated reacting jets at both elevated temperatures and pressure. Measurements from the University of Connecticut were conducted at atmospheric pressure and ambient inlet temperatures using premixed air and fuel mixtures (Wagner *et al.*, 2017; Wagner *et al.*, 2019; Dayton *et al.*, 2019). Slotted injectors with premixed ethylene-air at atmospheric pressures and elevated inlet temperatures have also been used for

measurements at the University of Cincinnati (Pinchak *et al.*, 2018; Pinchak *et al.*, 2019, Pinchak *et al.*, 2019).

The existing works in RJICF literature all operate the staged combustor at traditional gas turbine conditions: combustor exit Mach number $Ma_{EX} \leq 0.2$ and axial residence time $\tau_{AX} \geq 5$ ms. A new experimental facility has recently been developed at Purdue University to study high-speed reacting jets into a high-speed crossflow at elevated pressure (500 kPa) and elevated inlet temperatures (500 – 600 K). This facility is shown schematically in Fig. 4.1 and has been described in Chapter 2. It uses a perforated plate burner to produced vitiated flow with negligible swirl and a contraction section to accelerate the hot combustion gas. As a result, the facility has the unique capability to investigate *reacting jets in a compressible, vitiated crossflow with negligible swirl*. A key design feature of the test rig is a modular axial combustion zone to parametrically vary the axial residence time separately from the exit Mach number. Exhaust gas emissions measurements have shown a strong decrease in the NO_X emissions through an increase in the exit Mach number, even at a constant axial residence time. These have been described further in Chapter 2. Motivated by the earlier decrease in NO_X with increasing Ma_{EX}, the primary objective of the current work is to describe the development of an optically-accessible secondary combustion zone to further investigate the physics behind the observed NO_X reduction.

Optically-accessible combustion test rigs allow for the use of advanced, optical and laser-based diagnostics to provide insight on the reacting flow physics. Obtaining these measurements at realistic engine-relevant conditions is useful because the turbulent flow physics and chemical kinetics can be dramatically different within these flowfields, primarily due to parameters such as the inlet temperature and combustor pressure. In addition to the Zucrow Laboratories at Purdue University, several facilities that are known to have the capability for laser-based combustion diagnostics at the gas turbine test rig level include: DLR (Stuttgart and Koln), Darmtadt Technical University, NASA Glenn Research Center, and the Pennsylvania State University.

4.2　Design Methodology and Analysis

A CAD schematic of the optically-accessible secondary combustion zone within the staged gas turbine model combustor is presented in Fig. 4.2. Vitiated flow, created by the headend combustor and mixed with film cooling, enters the optically-accessible test section (OATS) from the left. Independently metered heated air and fuel (nominally natural gas) enters the rig from the axial premixer from the bottom. Optical access is provided from three sides: 12 mm × 101 mm in the plane perpendicular to jet injection and 80 mm × 101 mm in the two planes parallel to jet injection. The perfectly premixed air and fuel that is supplied to the axial injector enters the test section at a jet centerline location 13 mm downstream of optical access (88 mm of optical access is available downstream of jet injection).

The use of the double-windowed design features: (1) a thin inner window to withstand the thermal load from the vitiated crossflow and the jet flame, and (2) a thick outer window to bear the mechanical stress due to operation at elevated pressure. Film cooling is not used to cool the inner surface of the inner window. This was decided early in the design process to prevent potential disturbances within the high-speed flow field due to film cooling injection. Rather, a unique air-cooling scheme using forced convection of air between the inner and outer windows is utilized in this design. In addition, the thermal load on the non-windowed portions of the hardware is actively managed using water-cooling circuits. The design also features instrumentation for pressure measurements (0.1-1 kHz to monitor rig conditions and 180 kHz to provide insight on the jet flame dynamics). The window design also allows for the outer windows to be replaced by instrumented blanks, which can be used to measure the outer surface temperature of the inner window using thermocouple probes. The heat loss to both the air-cooling and water-cooling circuits from the hot combustion gas can also be measured using thermocouple probes located in the fluid lines immediately upstream and downstream of the test section.

The primary risk associated with the design of the optically-accessible secondary combustion zone is the management of the thermal loads due to long-duration, steady-state operation at elevated pressure. One-dimensional heat transfer analyses were conducted during the design phase to analyze the effectiveness of the air-cooling and water-cooling schemes. The analysis used a modified Bartz correlation (Humble *et al.*, 1995), commonly used for the analysis of rocket nozzles, for the convective coefficient on the hot combustion gas side to account for the hot combustion gas traveling at high-speeds within this experiment.
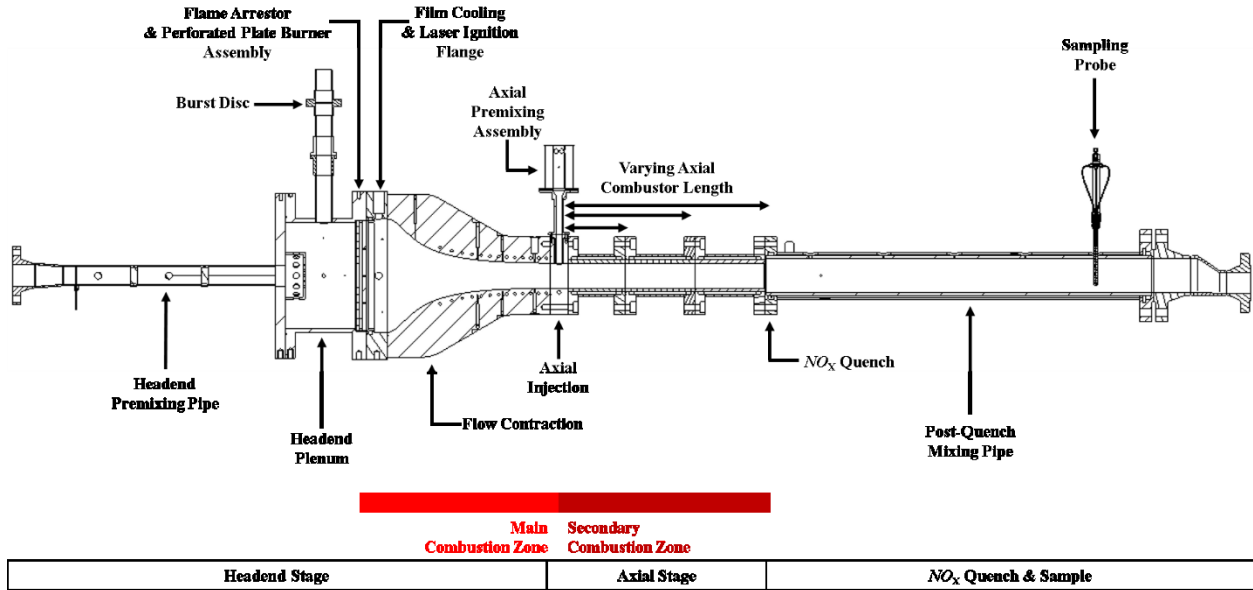
Figure 4.1: Schematic of the high-pressure test rig prior to the development of the optically-accessible secondary combustion zone.

(a)

(b)
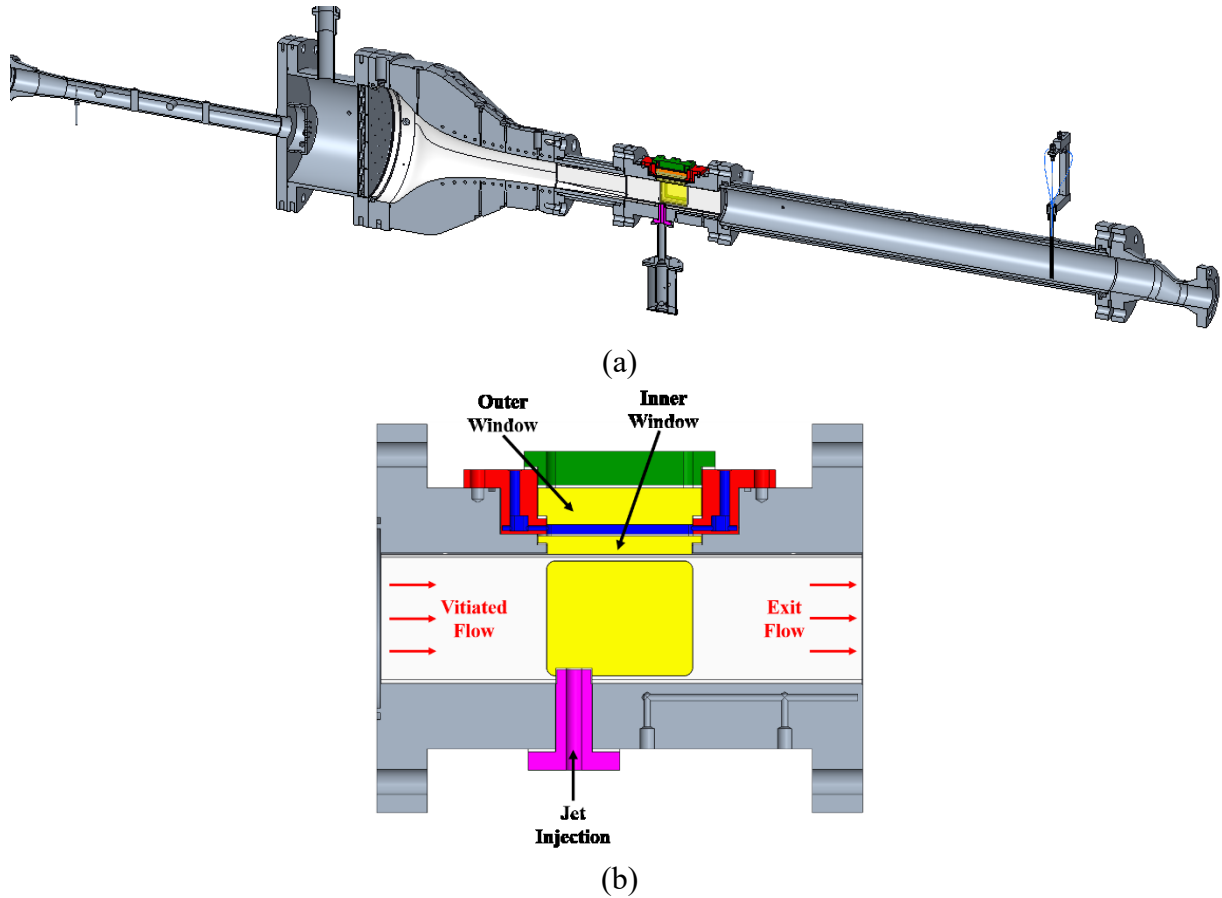
Figure 4.2: Cross-section of a 3D CAD schematic of the optically-accessible secondary combustion zone within the high-pressure test rig:(a) test rig, (b) optically-accessible secondary combustion zone.

4.2.1 Axial injection

Axial injection is incorporated into the design through a hole (65 mm diameter) in the centerline of the flow, with eight threaded bolt holes surrounding the larger hole. The modularity of the design allows for the use of any injector that can fit within the 65 mm hole and with a flanged end to be incorporated into the hardware. Initial measurements were performed with a jet diameter $d_j = 10.7$ mm to match conditions from emissions measurements acquired with the non-optically-accessible hardware. Measurements were later performed using an elevated injector. Both flush and elevated injector designs are shown schematically in Fig. 4.3. The elevated injector allows for jet injection at 10 mm into the vitiated crossflow, which is believed to be sufficiently beyond the turbulent boundary layer. For measurements with these two injectors, optical access is available for $y/d_j = 8$ jet diameters in the transverse direction and $x/d_j = 10$ jet diameters in the axial direction for the plane parallel to jet injection. Subsequent measurements were also performed using a smaller diameter flush injector ($d_j = 5.35$ mm) to allow for greater optical access in terms of $y/d_j = 16$ and $x/d_j = 20$. In addition, the design modularity allows for contoured nozzles, similar to those developed by Prof. Karagozian's group at UCLA (Megerian *et al.*, 2007) to be incorporated the hardware.

(a)   (b)
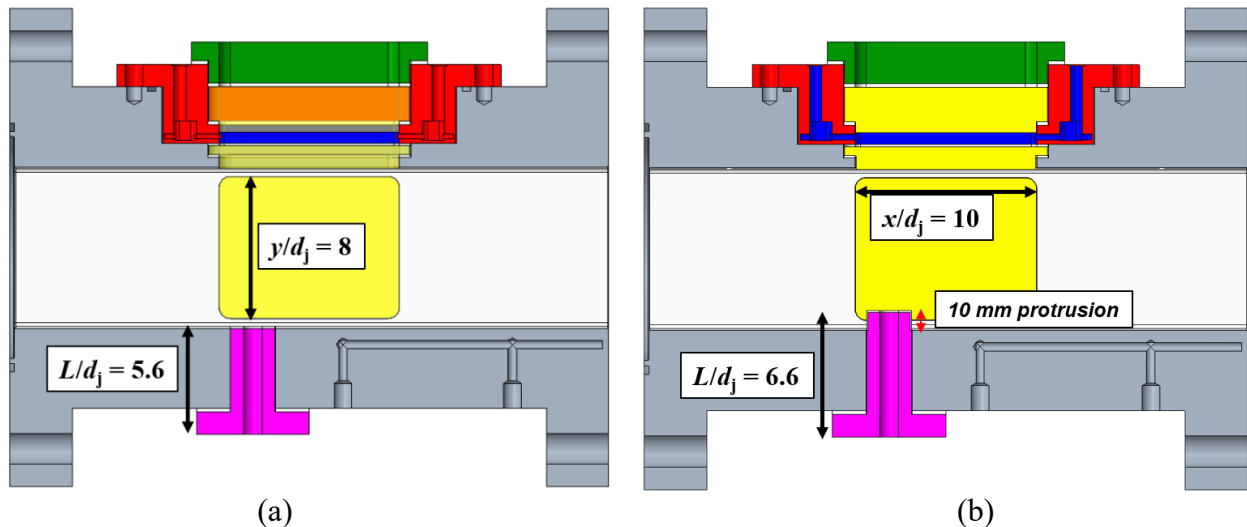
Figure 4.3: Schematic based on cross-section of CAD model depicting axial injection within the optically-accessible secondary combustion zone: (a) flush injector and (b) elevated injector.

4.2.2 Window configuration

A double-windowed design was incorporated within the optically-accessible secondary combustion zone to manage the thermal and mechanical loading from a windowed combustor operating under elevated pressure. The design features a thin inner quartz window to manage the thermal load and a thick outer quartz window to manage the mechanical load. The final design features a 12.7 mm thick inner window and a 25.4 mm thick outer window. Flange-like sealing surfaces were incorporated in each window design and Grafoil gaskets were used to provide sealing between the quartz windows and the metal surfaces. Figure 4.4 presents a schematic using the cross-section of a 3D CAD rendering to show the inner and outer windows and their respective flanges. Quartz was chosen as the window material due to its high melting temperature, adequate resilience to thermal shocks, and strong transmissivity (~92%) for laser wavelengths between 280 nm to 2 µm. For optical diagnostics requiring laser wavelengths below 280 nm, the quartz windows can be replaced with fused silica windows, which have high transmissivity (>90%) for laser wavelengths as low as 200 nm. The cavity in-between the two windows feature a pressurized heated air flow to enable thermal management of the inner window for long-duration steady-state operation.
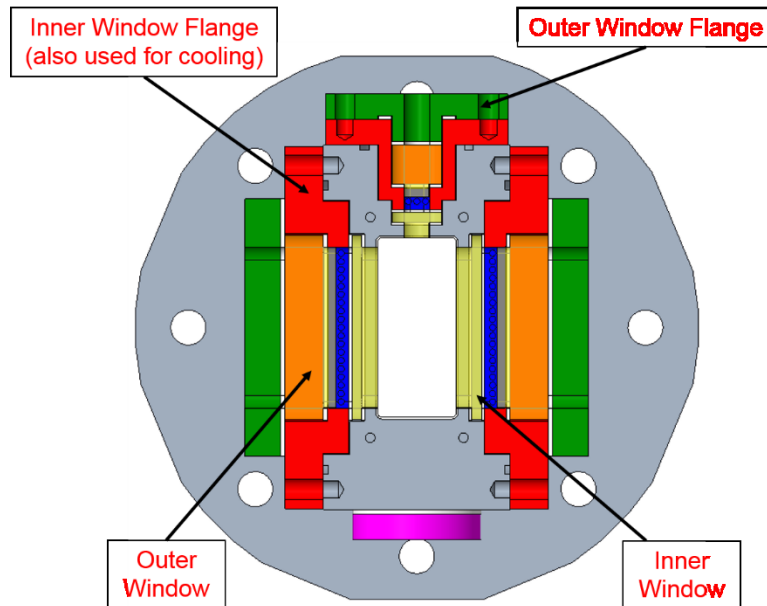
Figure 4.4: Schematic based on cross-section of CAD model depicting the inner and outer windows and their associated flanges.

4.2.3   Steady-state operation

Windowed combustors that are present in literature over the past decade feature a heated nitrogen film-cooling flow to protect the window (Slabaugh *et al.*, 2014). However, to best observe the injection of a high-speed reacting jet into a high-speed crossflow, a nitrogen film-cooling flow is not utilized for this design due to the potential of the film-cooling flow to complicate the fluid dynamics at jet injection. Instead, a unique air-cooling scheme was designed, with the cross-section shown in Figure 4.5. Each circuit of the heated air is independently metered and the design uses the test rig to backpressure the flow. The heated air enters the cavity between the two windows through narrow holes, passes axially through the cavity, and exits through the slots on the downstream side. Slots were incorporated into the design on the downstream side to reduce pressure drop and thereby maintain approximately equal pressure on either side of the inner window.

A one-dimensional heat transfer analysis was conducted to analyze the effectiveness of the back-side air-cooling concept. The analysis used a modified Bartz correlation (Humble *et al.*, 1995) for the convective coefficient on the hot combustion gas side, due to the combustion gas traveling at high speeds. A Dittus-Boelter channel flow correlation from Lefebvre and Ballal (2010) was used for the convective correlation on the air-cooling side. Figure 4.6 presents a schematic of the 1D air cooling heat transfer analysis. A constant vitiated flow temperature of 1689 K (based on a headend equivalence ratio $\phi_{HE} = 0.52$ and film cooling fraction $f_{FC} = 5\%$) was used for all conditions. Thermal properties for the quartz inner windows used for the analysis include: thermal conductivity of 2.0 W/m-K, softening temperature of 1770 – 1940 K, and melting temperature of about 1970 K. Sweeps varying the window thickness and the air-cooling split showed that the inner window surface temperature varied approximately linearly with these two parameters. As a result, a thickness of 12.7 mm for the inner window and an air-cooling split S_{AC} = 15% of total combustion air (headend air, axial air, film cooling air) was selected based on other considerations (previous experience at Purdue, factor of safety for mechanical loading on the inner window, pressure drop concerns with the inlet and outlet of the air cooling flow).

The effect of the combustor exit Mach number for three axial equivalence ratios ($\phi_{AX} = 0.7$, 1.0, and 1.3) on the inner and outer surfaces of the thin inner window is presented in Figure 4.7. Comparing the flame structure of lean, stoichiometric, and rich premixed jets over a range of Mach

numbers is one of the top priorities for the optically accessible secondary combustion zone. The vitiated flow temperature is also shown in Fig. 4.7 as reference. The two limiting cases for the bulk total temperature in the axial direction can be bounded by the vitiated flow temperature and the combustor exit temperature (assuming perfect mixing of the reacting jet with the vitiated crossflow). The inner surface temperature of the inner window increases with the exit Mach number, as shown in Figure 4.7(a). However, the inner surface temperature at these conditions is below the temperature range where quartz begins to soften by about 100 K. The increase in inner surface temperature at higher Mach number is due to the increased role of convection from the combustion gas flow to the window. The outer surface temperature of the inner window is shown a Figure 4.7(b) as reference. The outer surface temperature decreases with increasing Mach number because the air-cooling split S_{AC} was set to 15%, which means a higher Mach number in the combustor leads to a higher flow rate of coolant air in the cavity between windows.

A parametric sweep to investigate the effect of ϕ_{AX} for three different exit Mach numbers (Ma_{EX} = 0.25, 0.45, and 0.65) was also conducted to determine the limiting axial equivalence ratio that would result in an unacceptable increase in the inner window temperature. Figure 4.8 presents the inner and outer surface temperatures vs. the axial equivalence ratio. Based on this analysis, it is clear that ϕ_{AX} > 2.0 may create an unacceptable increase in the window temperature for the highest exit Mach number case. Based on the corresponding outer surface temperatures in Figure 4.8, redline aborts were incorporated into the VI to shut-off fuel to the axial stage combustor if the outer surface temperature as measured by the instrumented window blanks exceed specified values.

Steady-state operation at combustion gas temperatures and elevated pressures require intricate design schemes for water-cooling of the metal hardware. This design features water-cooling for the non-optically accessible portions of the hardware and air-cooling for the windowed regions. A schematic of the intricate water-cooling design is shown in Fig. 4.9. Figure 4.9(a) highlights one of the four primary legs used to cool the hardware (the other three legs are symmetric to the highlighted leg and are not highlighted for clarity). Water enters at the upstream flange, passes through a loop to cool the metal on the upstream side, travels axially through the combustor, passes through a loop on the downstream side, and exits the hardware on the downstream side. A fifth water cooling circuit, presented in Fig. 4.9(b), is designed to cool the

metal hardware on the same side as the axial injection (note that this is the side that does not feature optical access).

A one-dimensional heat transfer analysis was also conducted to analyze the effectiveness of the water-cooling design. The convective coefficient on the hot combustion gas side was once again determined from the modified Bartz correlation. The Sieder-Tate correlation was used for the convective correlation on the water-cooling side (Sieder and Tate, 1936). The effects of radiation, which were analyzed using relations from Lefebvre, were determined to be small in comparison to the effects of convection. A schematic of the 1D water-cooling heat transfer analysis is presented in Fig. 4.10. A constant vitiated flow temperature of 1689 K was once again used for all conditions. The thermal properties for the thermal barrier coating (TBC) include a thermal conductivity of 0.80 W/m-K and a temperature limit of 1570 K. A thickness of 900 μm was selected for the TBC. The thermal properties for the SS-316 include: a thermal conductivity of 19.9 W/m-K (selected based on a nominal temperature of 800 K) and a temperature limit of 1200 K. A nominal metal thickness of 12.7 mm (distance between the TBC and cooling water) was also selected for the 1D analysis. The mass flow rate of water was held constant at 0.5 kg/s for the water-cooling analysis.

Figure 4.11 shows the effect of the combustor exit Mach number on the inner surface of the TBC and the inner surface of the metal (which is in contact with the outer surface of the TBC) for the vitiated flow only and three axial equivalence ratios: $\phi_{AX} = 0.7$, 1.0, and 1.3. Although the inner surface temperature of both the TBC and the metal increases with the exit Mach number due to the greater thermal load, both temperatures are significantly lower than the temperature limits of the TBC and the metal respectively. Figure 4.12 presents a parametric sweep of ϕ_{AX} for three different exit Mach numbers ($Ma_{EX} = 0.25$, 0.45, and 0.65) to determine its effect of the inner surface temperatures of the TBC and the metal. The inner surface temperature of the TBC approaches the temperature limit of 1570 K at $\phi_{AX} = 3.4$. However, the metal temperature is significantly below the temperature limit of 1200 K for all conditions considered.
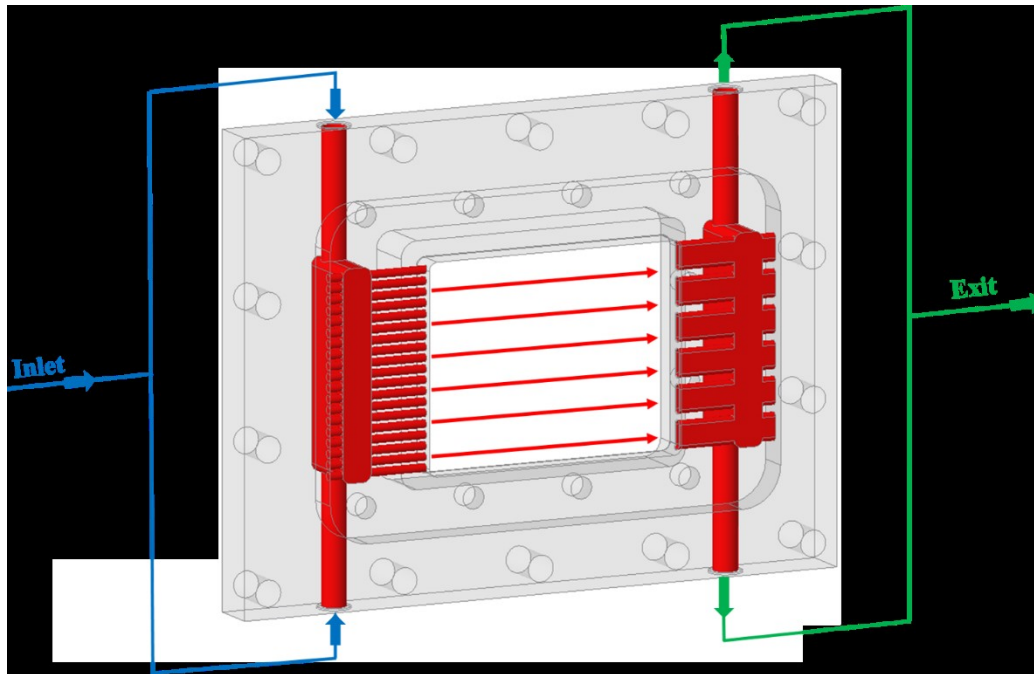
Figure 4.5: Schematic depicting the flow path of the air cooling flow
for a wide inner window flange.
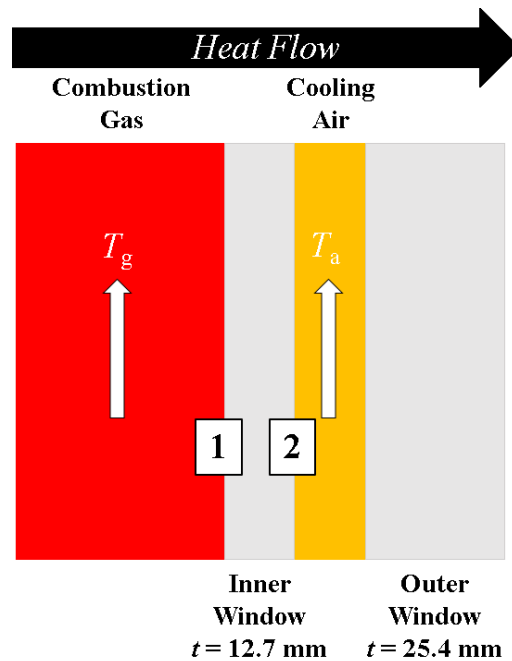
Figure 4.6: Schematic of the 1D heat transfer analysis used to determine: inner (1) and outer (2)
surface temperatures of the 12.7 mm thick inner quartz window.
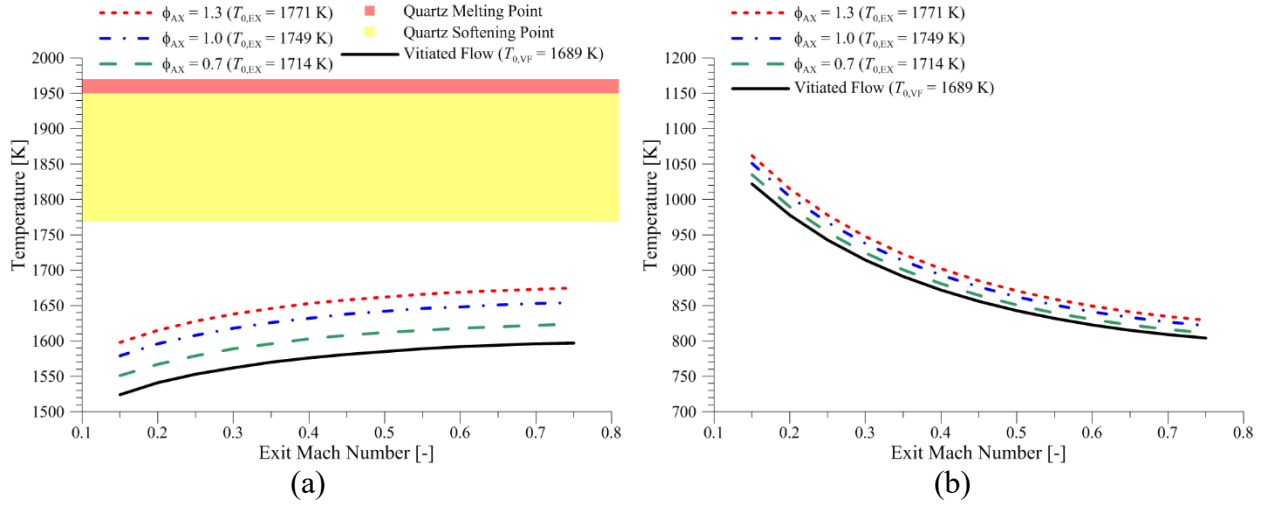
Figure 4.7: Temperatures of (a) inner surface and (b) outer surface for the 12.7 mm thick inner window vs. the exit Mach number for the vitiated flow and three axial equivalence ratios.
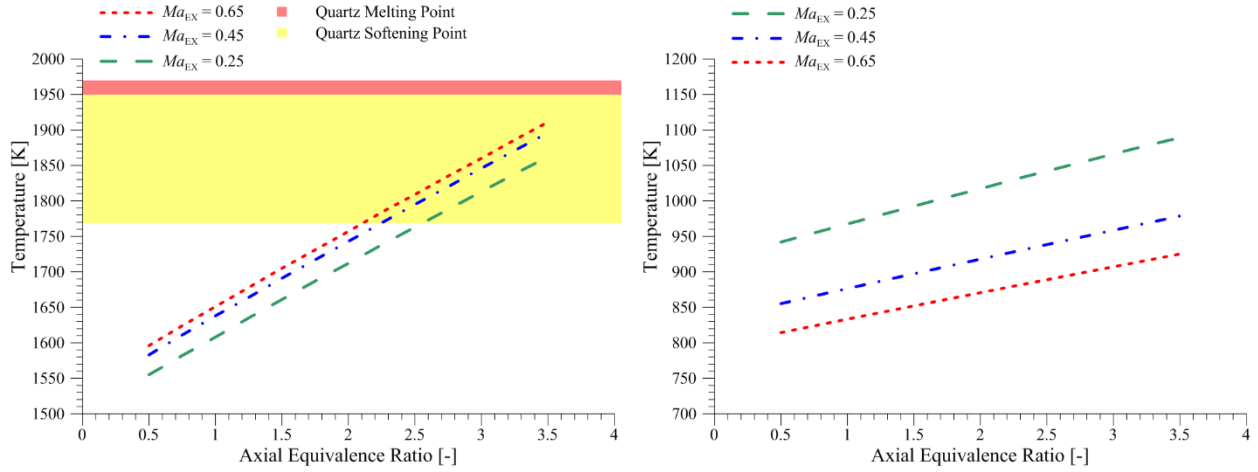
Figure 4.8: Temperatures of (a) inner surface and (b) outer surface for the 12.7 mm thick inner window vs. the axial equivalence ratio for the vitiated flow and three axial equivalence ratios.
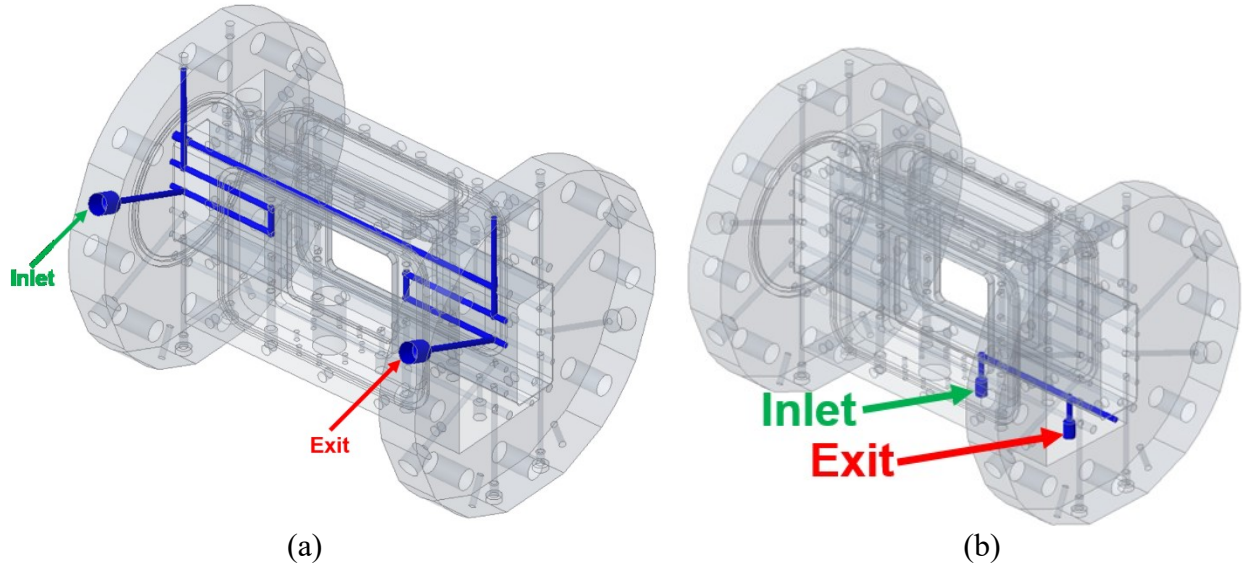
Figure 4.9: Schematic of the water-cooling design for the optically-accessible secondary combustion zone: (a) one of four main circuits, (b) the ancillary circuit for the bottom wall.
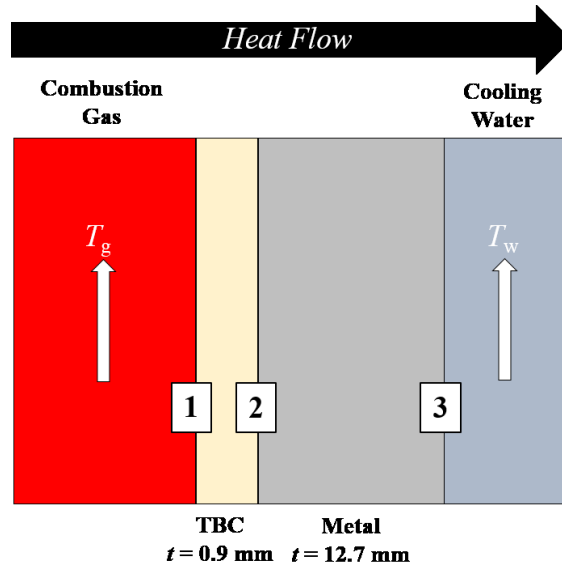
Figure 4.10: Schematic of the 1D heat transfer analysis used to determine the inner surface temperature of the TBC (1) and the inner surface temperatures of the SS-316 (2).
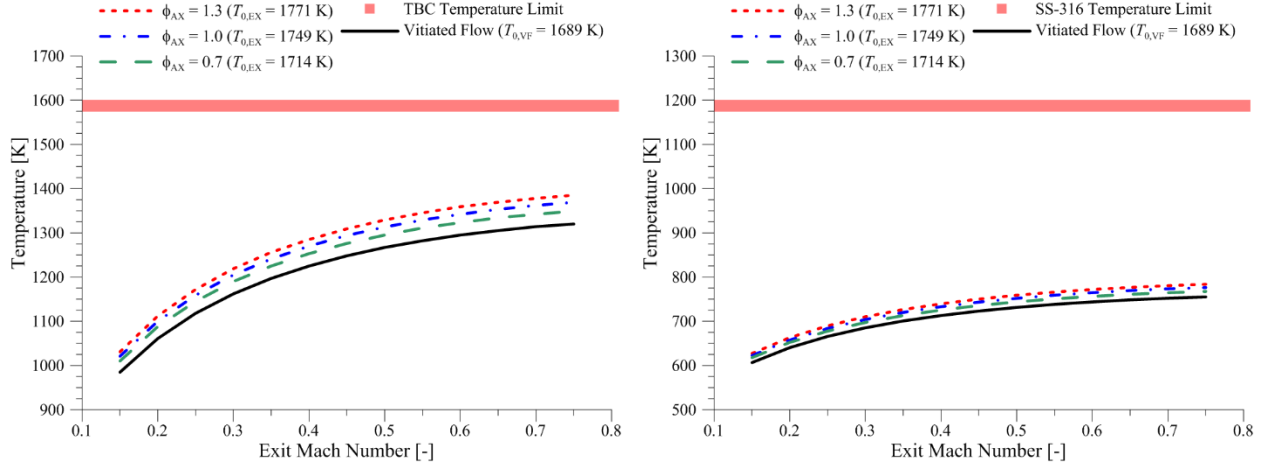
Figure 4.11: Temperatures of (a) inner surface of TBC (b) inner surface of the metal vs. the exit Mach number for the vitiated flow and three axial equivalence ratios.
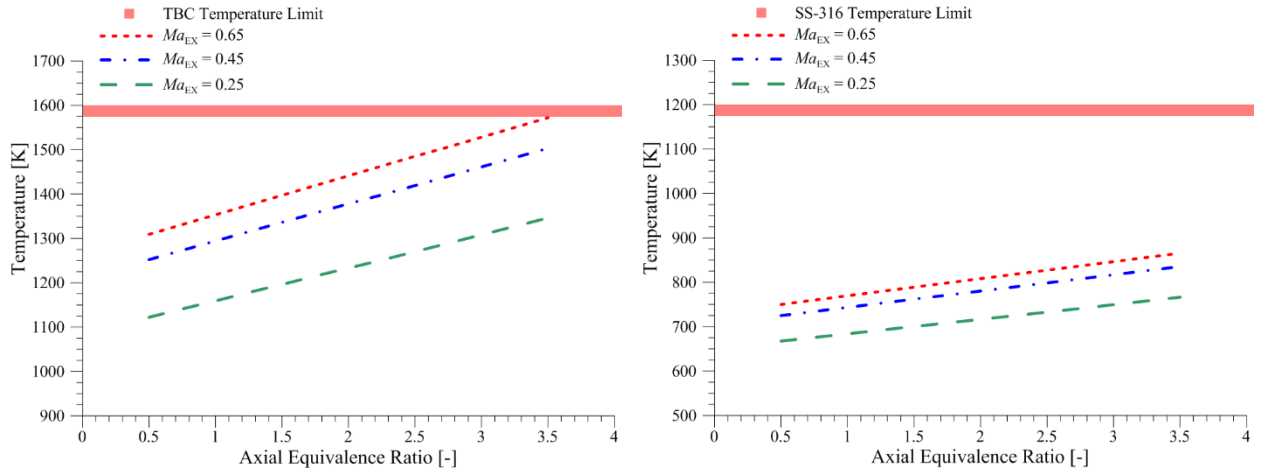
Figure 4.12: Temperatures at (a) inner surface and (b) inner surface of the metal vs. the exit Mach number for the vitiated flow and three axial equivalence ratios.

4.2.4 Instrumentation

The secondary combustion zone features two pressure transducers (0.1 – 1 kHz) for rig condition monitoring: one upstream and one downstream of jet injection. Two high-frequency pressure transducers (180 kHz) are also incorporated into the design within cavities to measure the pressure fluctuations coupled with the heat release. A schematic of the cross-section of the test section with the relevant instrumentation is shown in Fig. 4.13. Stainless steel blanks were also designed for the outer windows in order to monitor the air cooling pressure and the outer surface temperature of the inner window. Installation of the blanks was desired for initial shake-down

93

testing and could also be further utilized depending on the diagnostics desired. Configuration A, shown in Fig. 4.14 (a), features outer blanks for the narrow top window and one of the wide side windows. This configuration would be utilized for chemiluminescence imaging through the side with optical access. Each of the two installed blanks feature a pressure transducer to measure the pressure in the cavity between the two windows and the two thermocouple probes that could be installed would help determine limiting conditions for the thermal loading on the inner window. For planar laser induced fluorescence (PLIF) measurements, the blank on the narrow window would be removed to bring the laser sheet from the top window. In Configuration B, only one of the side windows would feature blanks, as shown in Fig. 4.14 (b).
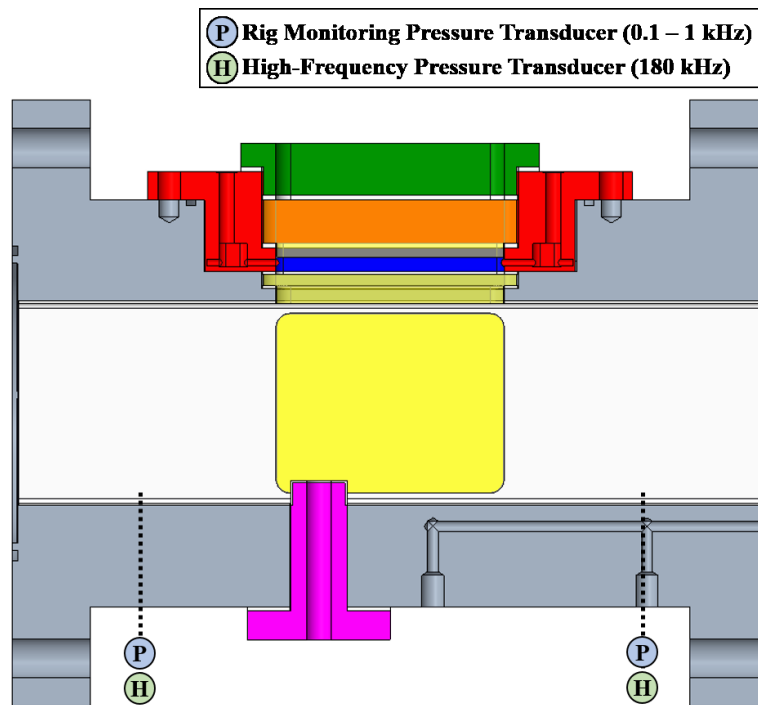
Figure 4.13: Schematic used a cross-section of the 3D model to illustrate locations of pressure instrumentation.
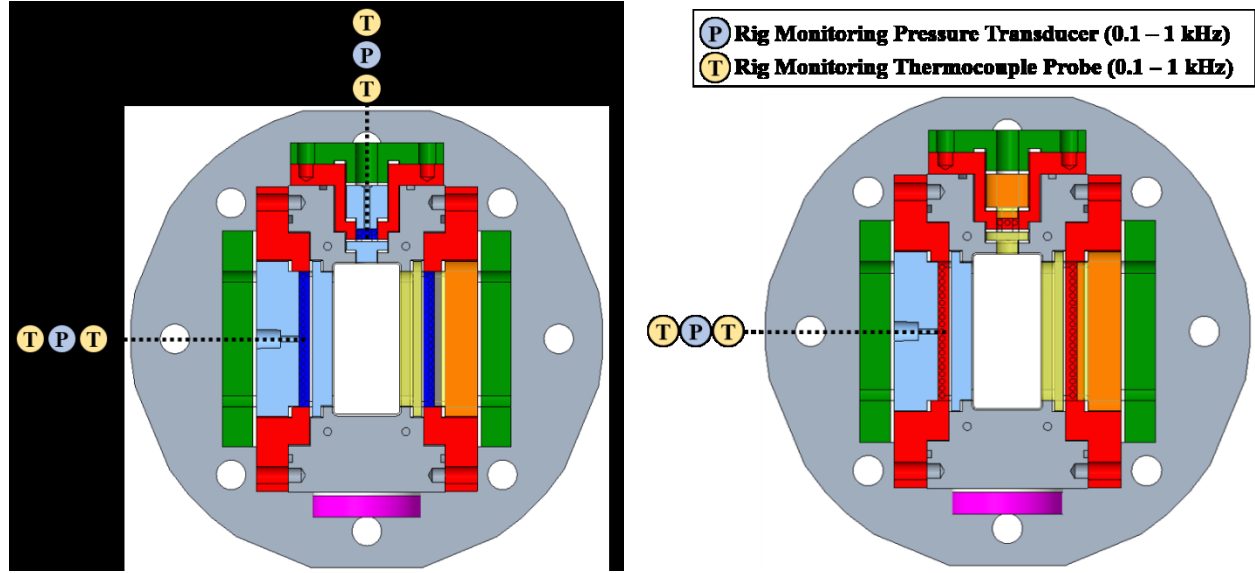
Figure 4.14: Schematic showing relevant instrumentation installed in the window blanks for operation in: (a) Configuration A, (b) Configuration B.

4.3   Experimental Systems

A schematic diagram of the optically-accessible, high-pressure test rig is shown in Fig. 4.15. The rig consists of three major sub-assemblies: the *headend* stage, the *axial* stage, and the *NOX quench and sample* stage. All of the hot sections (both combustion and post-combustion zones) within the test rig featured a thermal barrier coating and were either air-film-cooled or water-cooled to ensure hardware survivability for long-duration, steady-state operation. Capabilities for the test rig include operation at elevated inlet air temperatures and combustor pressures, production of high-speed vitiated crossflow up to $Ma_\infty = 0.7$, and adiabatic total temperature of the product gas at the combustor exit up to $T_{0,EX} = 2100$ K. The rig has been described in detail in Chapters 2 and 3.

The experiment was remotely controlled using a National Instruments LabVIEW Virtual Instrument (VI) with temperature and pressure instrumentation for rig condition monitoring. Sonic and cavitating venturis were used for all gaseous fluid and water lines, and real gas effects were included during the data reduction process. Measurements were obtained at 260 Hz for pressure and temperature and at 1 Hz for emissions. Experimental uncertainty for equivalence ratio was calculated to be 1.6% and one standard deviation was used as the experimental uncertainty for emissions measurements.

A schematic diagram of the optically-accessible test section is shown in Fig. 4.16. Chemiluminescence images of OH* emission and CH* emission was captured using a high-speed CMOS camera (Phantom v7.3 for 10 kHz and Photron SA-Z for 50.4 kHz) that was equipped with the same intensifier unit (LaVision HS-IRO). The camera system was equipped with a 98 mm focal length, f/2.8, UV objective lens and a band-pass filter (320/40 nm for OH* and 430/40 nm for CH*). The spatial resolution for the chemiluminescence images was approximately 0.16 mm/pixel for the images presented in this chapter.
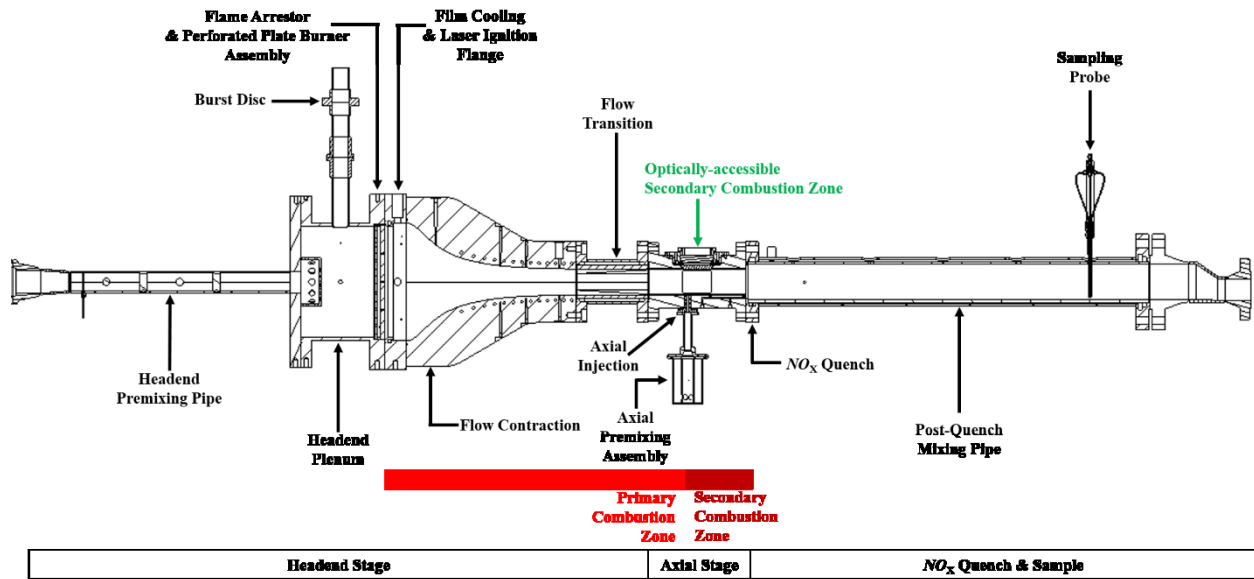
Figure 4.15: Schematic of the high-pressure test rig prior to the development of the optically-accessible secondary combustion zone.
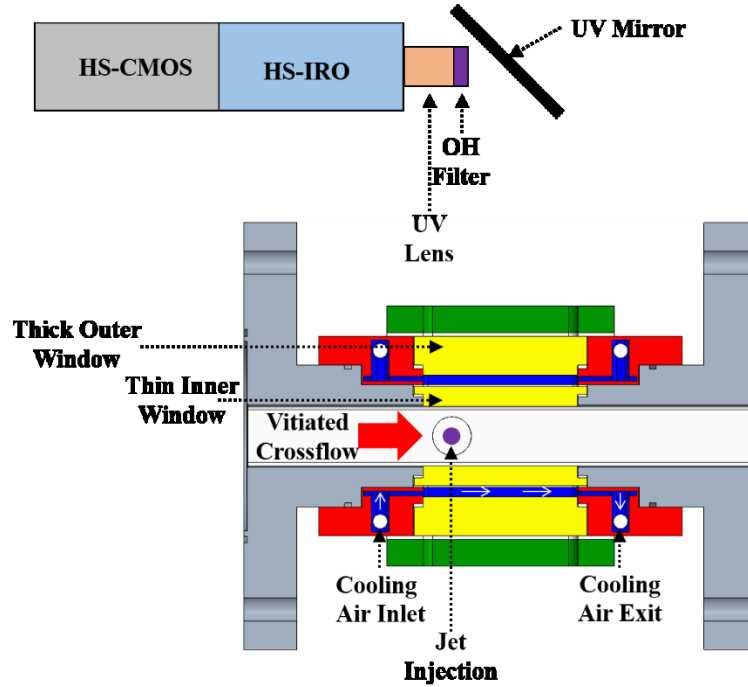
Figure 4.16: Schematic diagram of the optically-accessible
secondary combustion zone with imaging system.

4.4 Results and Discussion

Successful window performance was demonstrated using 10 kHz OH* chemiluminescence imaging. Figure 4.17 shows a sequence of instantaneous OH*-CL images for two different injectors: (a) the flush injector and (b) the elevated injector at a representative test condition. A blend of natural gas and hydrogen at $\phi_{AX} = 2.7$ was used as the fuel (mole fraction of hydrogen in the fuel blend $X_{H2} = 20\%$) with a vitiated crossflow Mach number Ma_∞ = of 0.34 and a jet Mach number of $Ma_J = 0.46$. These images were obtained at 10 kHz and with a 1 µs intensifier gate. The OH* chemiluminescence was collected using the 320 nm centered bandpass filter. Both sets of images reveal that the flame is stabilized close to the wall and somewhat downstream of the jet injection. In addition, due to the rapid dynamics of the jet in a high-speed crossflow, it is apparent that 10 kHz does not provide the required temporal resolution to track one image to the next image in the sequence.

A sequence of 50 kHz chemiluminescence images is show in Figure 4.18 to demonstrate the temporally-resolved behavior of the jet-in-crossflow flame at a representative condition: (a) OH* imaging and (b) CH* imaging. The 50.4 kHz OH* and CH* images were acquired in a

similar manner as the 10 kHz imaging, with the key difference being the use of a faster Photron SA-Z camera and a bandpass filter centered at 430 nm with a 40 nm FWHM for the CH* images. Note that these images were not acquired simultaneously but simultaneous chemiluminescence imaging capability is certainly possible due to windows on both sides of the combustor wall. These images show features of the vortex roll-up in the shear layer. Periodic behavior is also apparent at many conditions from the chemiluminescence images. Figure 4.19 presents a sequence of 50.4 kHz OH* images at a different representative condition and with the corresponding pressure trace for the image sequence. A sinusoidal behavior for pressure based on readings from the transducer located downstream of the jet is clearly evident. Furthermore, the capability to locate high-frequency pressure measurements in recessed cavities near the optical access also allows for the calculation of parameters such as the Rayleigh index from the pressure and chemiluminescence data.
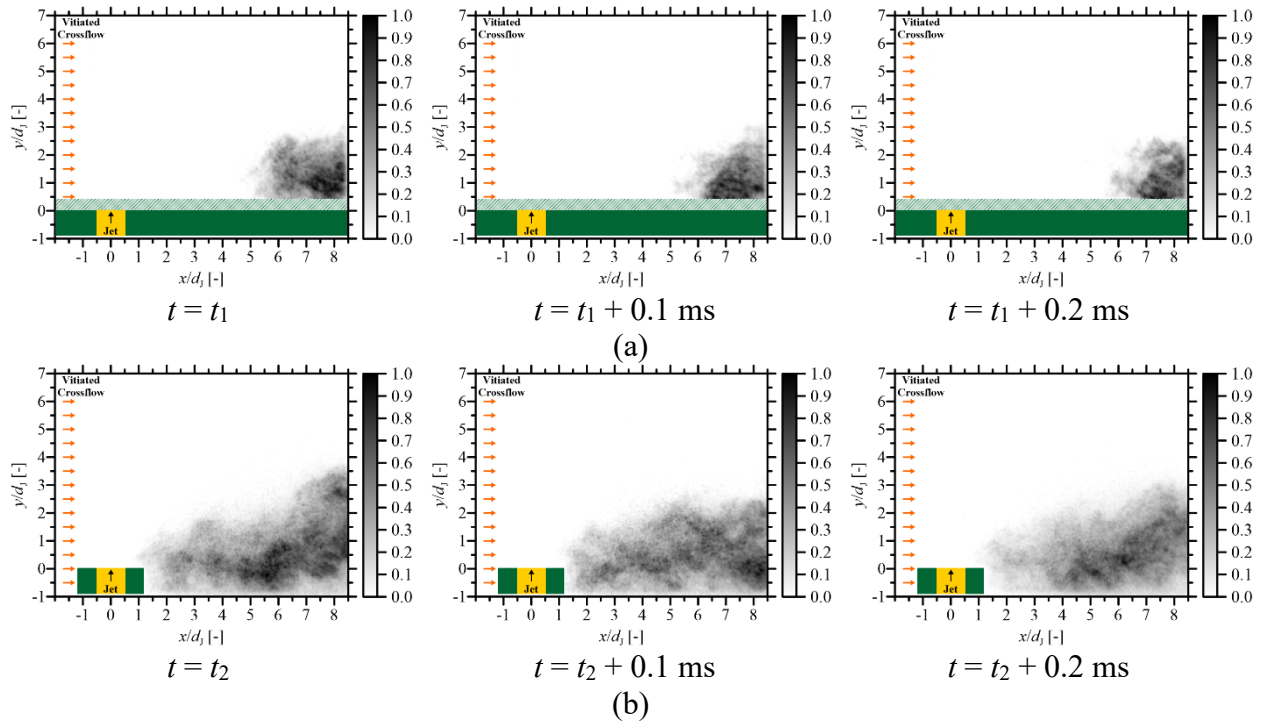
Figure 4.17: Sequence of instantaneous 10 kHz OH* chemiluminescence:
(a) flush injector, (b) elevated injector.
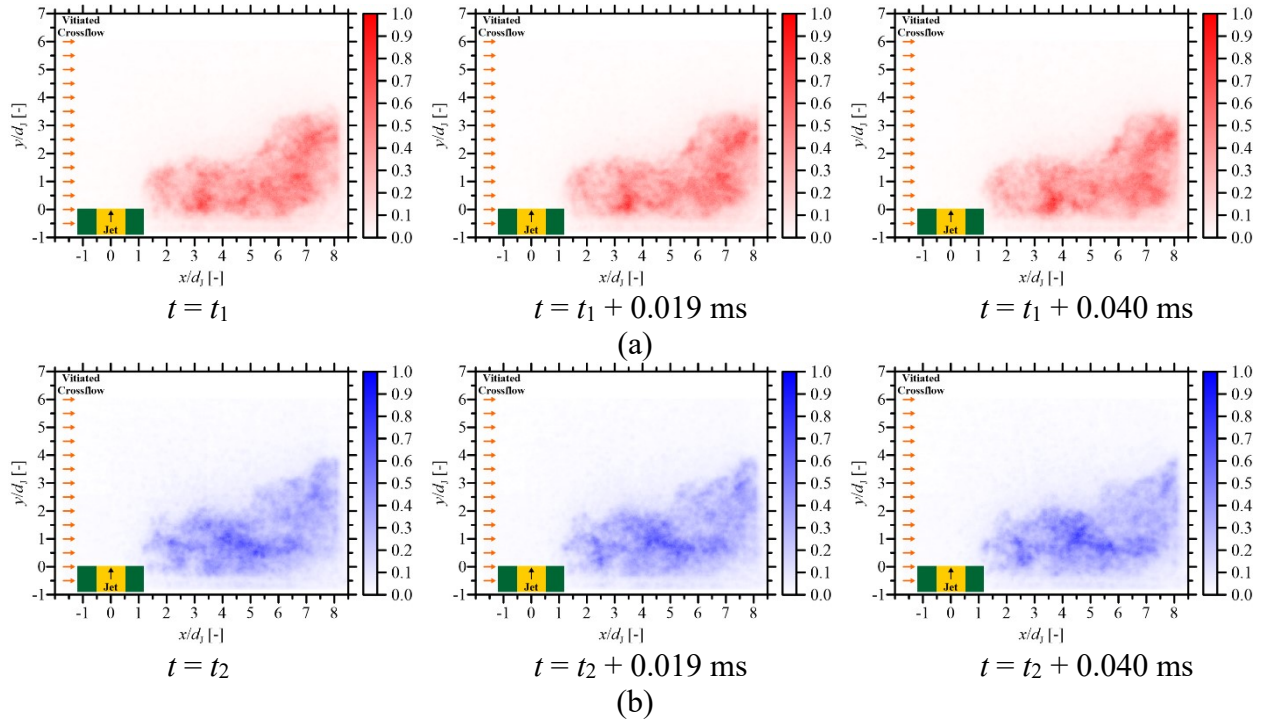
Figure 4.18: Sequence of instantaneous 50.4 kHz chemiluminescence of the elevated injector: OH* and (b) CH*.
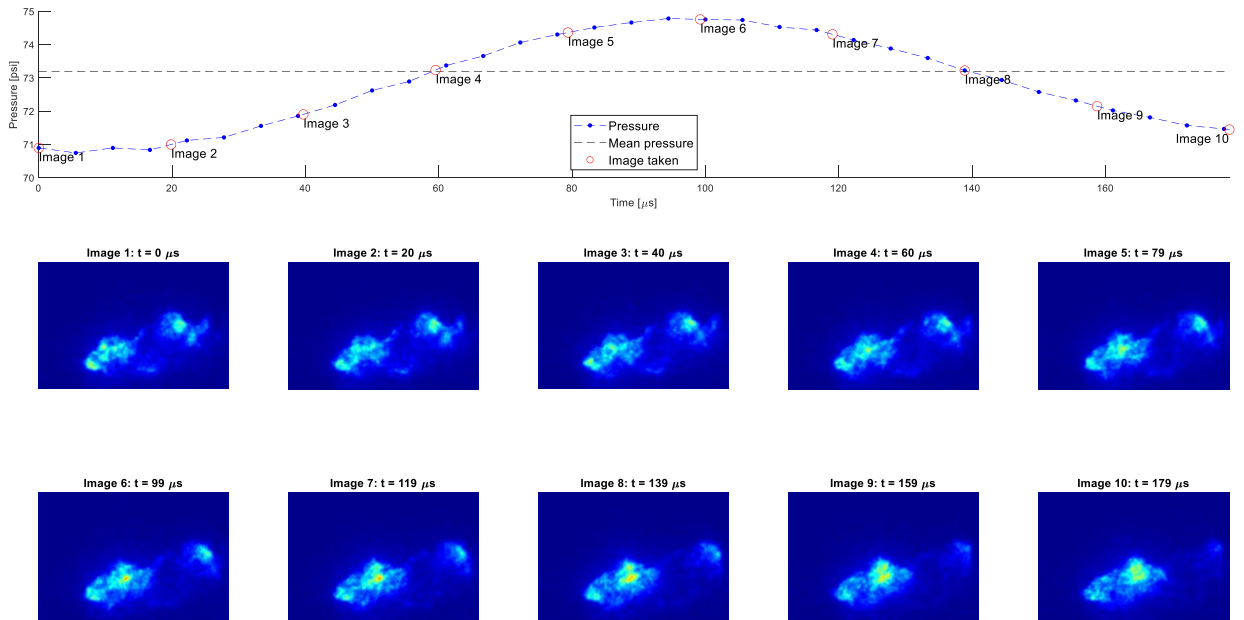
Figure 4.19: Sequence of instantaneous 50 kHz chemiluminescence of the elevated injector with corresponding high-frequency pressure measurements.

4.5   Summary and Conclusions

This chapter summarizes the development of an optically-accessible secondary combustion zone to study the interaction of reacting jets in vitiated crossflow at high speeds. This optically-accessible test section allows for the experimental study of reacting jets into a vitiated crossflow with negligible swirl at conditions corresponding to elevated inlet temperatures of 500 – 600 K, elevated combustor pressure of 500 kPa, and exit Mach numbers up to 0.7. The primary motivation behind the development of the optically-accessible combustion zone is the significant NO_X reduction that we have observed when increasing the combustor exit Mach number up to 0.7 (even at a constant residence time). These exhaust gas emissions measurements, which are detailed in Chapter 3, were obtained using an FTIR system for premixed NG-air jets but with a non-optically-accessible staged gas turbine model combustor.

Key design features for the new optically-accessible secondary combustion zone include a double-windowed design, a unique air-cooling scheme using forced convection of air in-between the inner and outer windows, and carefully designed water-cooling circuits to cool the metal hardware. Analysis of the air-cooling and water-cooling design using 1D heat transfer models are discussed in the work and indicate that the design will be able to handle long-duration, steady-state operation.

The optically-accessible secondary combustion zone is ideally suited to investigate features of the reacting jet in vitiated crossflow. Successful operation has been demonstrated here with chemiluminescence imaging and further work with PLIF imaging would provide insight on salient features such as the jet trajectory and lift-off height, flame structure, and flame dynamics. Chemiluminescence and OH-PLIF is used in Chapter 5 to provide insights on the jet in crossflow and CH-PLIF using excitation in the C-X electronic system is described in Chapter 6.

More detailed measurements of OH-PLIF and CH-PLIF and perhaps also CH_2O-PLIF could be undertaken in the future. Furthermore, future use of the windowed secondary combustion zone could include simultaneous OH-PLIF/PIV (particle imaging velocimetry) or CH-PLIF/PIV measurements. In addition, temperature and species measurements using coherent anti-Stokes Raman scattering (CARS) spectroscopy would yield further insight on the fundamental physics behind the observed reduction in NO_X.

5. TRANSVERSE INJECTION OF RICH, PREMIXED, NG-AIR AND NG-H₂-AIR REACTING JETS INTO A HIGH-SPEED VITIATED CROSSFLOW WITH NEGLIGIBLE SWIRL

5.1 Introduction

The jet in crossflow is a canonical problem with many practical applications, including gas turbine engines and high-speed combustion systems (Karagozian *et al.*, 2010). Due to its potential to increase turbine inlet temperatures with only a minimal increase in harmful emissions, transverse injection of reacting jets into a vitiated crossflow as part of an axially staged combustion system remains an area of interest. Much previous research has been performed to investigate the mixing, velocity field, and flame structure of a reacting jet in crossflow and the interested reader is referred to a recent review article (Karagozian *et al.*, 2014). Recent papers have described experimental studies of the mixing and flowfield of isodensity and isothermal jets-in-crossflow (Megerian *et al.*, 2007; Davitian *et al.*, 2010), the flame structure and flame-flow interactions of a reacting jet in a non-vitiated crossflow (Micka *et al.*, 2012; Steinberg *et al.*, 2013), and reacting jets in vitiated crossflows (Lamont *et al.*, 2012; Panda *et al.*, 2015; Panda *et al.*, 2019; Sullivan *et al.*, 2014; Nair *et al.*, 2019; Wagner *et al.*, 2017; Dayton *et al.*, 2019). Several recent papers also describe the application of direct numerical simulations (DNS) to characterize non-reacting and reacting jets in crossflows (Grout *et al.*, 2011; Kolla *et al.*, 2012; Grout *et al.*, 2012; Chan *et al.*, 2014; Lyra *et al.*, 2015; Minamoto *et al.*, 2015). Analytical models, such as the one by Heister and Karagozian (1990) for high-speed conditions within the compressible flow regime, have also been developed to predict the jet trajectory.

One area within the jet-in-crossflow literature that has been largely unexplored is the transverse injection of premixed, reacting jets with low jet-to-crossflow momentum flux ratios (J ~ 2) into a high-speed, vitiated crossflow. The low momentum flux ratios are of particular relevance to axially staged gas turbine engines with premixed jets, due to limited pressures for the compressed air entering the main combustion zone and the air used for axial injection. The primary motivation for injection into a high-speed crossflow is due to its potential to reduce NO$_X$ emissions while still maintaining high combustion efficiency. This has been detailed in Chapter 3 of this dissertation.

The main objective of the current work is to investigate the flame stabilization and flame structure of rich reacting jets injected into a high-speed, vitiated crossflow with negligible swirl. The reacting jets are premixed with natural gas (NG) and heated air or NG, hydrogen (H_2), and heated air. To the best of our knowledge, the only available work in literature that has explored flame structure and stabilization of transversely injected jets into a high-speed crossflow within the subsonic regime is by Micka *et al.* (2012). However, key differences between that work and the current work include: (1) vitiated crossflow instead of heated air crossflow is used in the present work, (2) premixed NG-air and NG-H_2-air instead of purely fuel jets of ethylene or ethylene-hydrogen blends are used in the present work, (3) the jet Mach number is subsonic rather than sonic in the present work. There is currently also a scarcity in jet-in-crossflow literature for experimental studies with blended hydrocarbon and hydrogen fuels premixed with heated air. As mentioned above, the work by Micka *et al.* (2012) used fuel jets with ethylene-hydrogen blends, whereas Panda *et al.* (2019) used either premixed NG-air or H_2-nitrogen jets, and Sullivan *et al.* (2014) used a diverse blend of methane, hydrogen, carbon monoxide, water vapor, and nitrogen. A review paper by Lieuwen *et al.* (2008) considers the impact of fuel composition on premixed gas turbine combustion in four key areas: blowout, flashback, combustion instability, and auto ignition. The addition of hydrogen to natural gas is known to substantially alter chemical kinetic rates and flame propagation speeds, which would greatly affect flame stabilization and flame structure for a reacting jet in crossflow.

An axially staged, gas turbine model combustor capable of operating up to transonic conditions was recently developed at Purdue. Emissions measurements showed up to a 70% reduction in NO_X produced from the axial stage by increasing the Mach number, even at a constant post-injection residence time. This has been described in Chapter 2 and Chapter 3 of this dissertation. The model combustor used in this earlier work has very recently been equipped with an optically-accessible secondary combustion zone. This has been described in Chapter 4 of this dissertation. The optical section allows for the use of high-speed imaging and laser-based techniques to draw insights on the flame structure behind the NO_X reduction at high-speed conditions. In this chapter OH*-chemiluminescence is used to investigate the flame stabilization based on vitiated crossflow Mach number and mole fraction of hydrogen in the fuel, OH planar laser-induced fluorescence (PLIF) to used investigate the flame structure and post-flame mixing, and a Fourier-transform infrared (FTIR) spectrometer is used to measure exhaust gas emissions.

5.2 Experimental Systems

A schematic diagram of the optically-accessible, high-pressure test rig is shown in Fig. 5.1. The rig consists of three major sub-assemblies: the *headend* stage, the *axial* stage, and the *NOX quench and sample* stage. All of the hot sections (both combustion and post-combustion zones) within the test rig featured a thermal barrier coating and were either air-film-cooled or water-cooled to ensure hardware survivability for long-duration, steady-state operation. Capabilities for the test rig include operation at elevated inlet air temperatures and combustor pressures, production of high-speed vitiated crossflow up to $Ma_\infty = 0.7$, and adiabatic total temperature of the product gas at the combustor exit up to $T_{0,EX} = 2100$ K.

The *headend* stage consists of a perforated plate burner to produce vitiated flow with negligible levels of swirl, and a contraction section to accelerate the flow up to high sub-sonic speeds. The perforated plate burner was operated using premixed natural gas and heated air; details on its operation are discussed in Chapter 2. The *axial* stage consists of an axial premixer assembly and the optically-accessible, secondary combustion zone. The secondary combustion zone features a double-windowed design to provide optical access from up to three sides. Cooling from heated air flowing in the cavity between the two windows enables long-duration, steady-state operation. Notably, film cooling was not used to protect the inner surface of the inner windows in order to prevent potential disturbances within the high-speed flowfield. A schematic diagram of the optically-accessible test section is shown in Fig. 5.2. The optical section has been further described in Chapter 3. An elevated, straight injector with $L/d = 6.5$ and a 10 mm protrusion into the crossflow was used for this work. The injector features an orifice diameter of 10.7 mm and an injector body with a diameter of about 25 mm that is elevated into the crossflow. The *NOX quench and sample* stage was located after jet injection to enable accurate control of the residence time by injecting water to freeze the chemical reactions in the flow and thereby inhibit further thermal NO_X production. The flow was allowed to mix within a length of pipe before a sample probe collected samples of the exhaust gas. The pressure in the headend combustor was held constant for the range of air flow rates and thermal powers through the use of two back-pressure valves operating in parallel.

The experiment was remotely controlled using a National Instruments LabVIEW Virtual Instrument (VI) with temperature and pressure instrumentation for rig condition monitoring. Sonic

and cavitating venturis were used for all gaseous fluid and water lines, and real gas effects were included during the data reduction process. Measurements were obtained at 260 Hz for pressure and temperature and at 1 Hz for emissions. Data for rig condition monitoring and emissions are presented in this work using an arithmetic mean of typically 20 seconds at steady-state rig conditions. Experimental uncertainty for equivalence ratio was calculated to be 1.6% and one standard deviation was used as the experimental uncertainty for emissions measurements.

In this chapter, results are presented and discussed for a variety of reacting jet-in-crossflow conditions at elevated combustor pressures and inlet temperatures ($T_{3X} = 466 \pm 20$ K) for three different crossflow Mach numbers: $Ma_\infty = 0.15$, 0.24, and 0.33. The headend combustor pressure at $P_4 = 507 \pm 4$ kPa was held constant and the Mach number was varied by increasing the air flow rate. The axial air split between the jet and the crossflow was held constant at $S_{AX} = 5.9 \pm 0.1\%$. The heated axial air was premixed with either natural gas only or natural gas and hydrogen blends (up to a fuel hydrogen mole fraction of 32%) for jet equivalence ratios from 1.1 to 3.0.
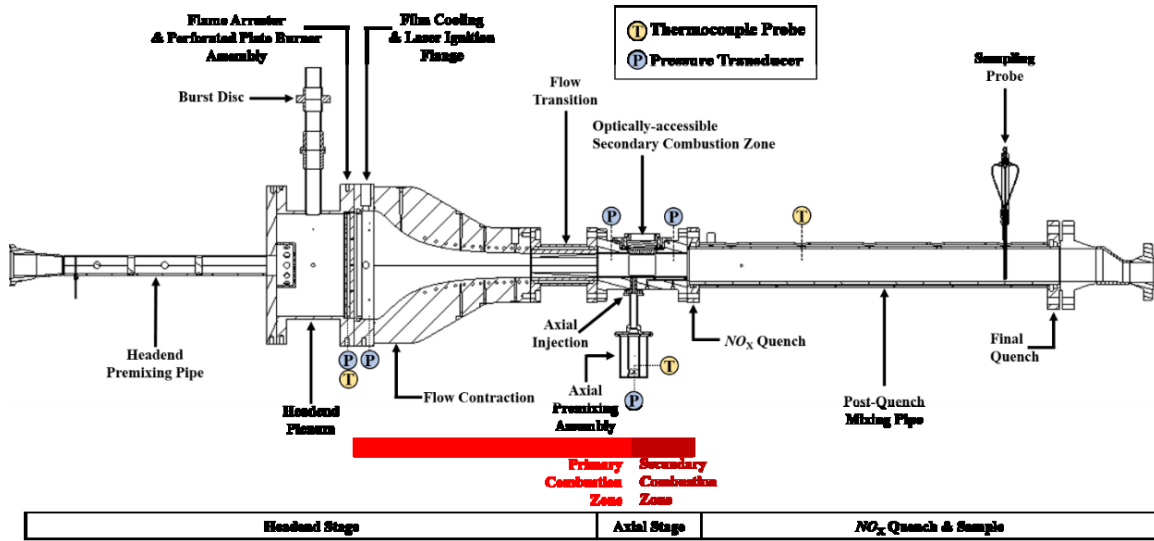
Figure 5.1: Schematic diagram of the optically-accessible, high-pressure model combustor.
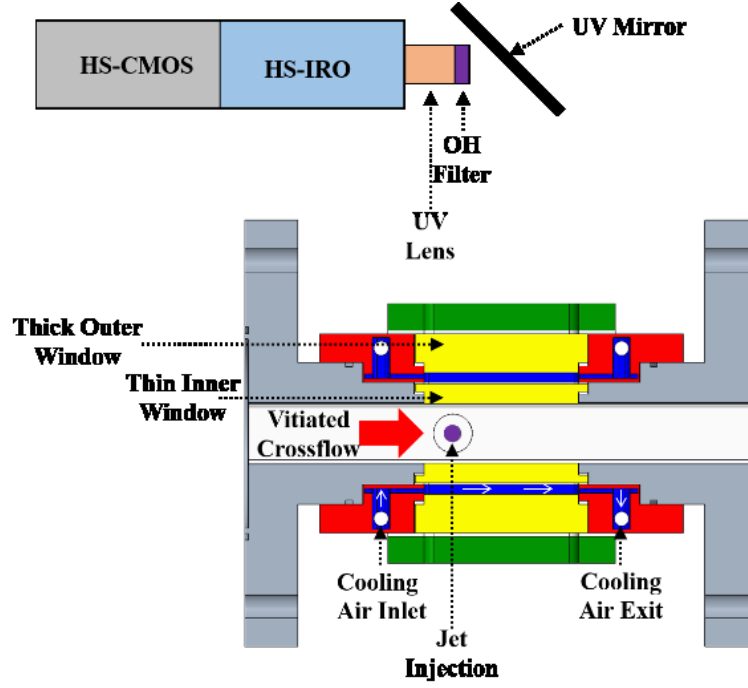
Figure 5.2: Detailed schematic of the optical access with the camera systems.

5.2.1 Laser and camera systems

OH-PLIF measurements were obtained using a high-repetition-rate, Q-switched, diode-pumped solid-state (DPSS) Nd:YVO$_4$ laser (Edgewave IS400-3-L) and a dye laser (Sirah Credo) designed for efficient high-repetition-rate operation. The second harmonic output of the DPSS laser at 532 nm was used to pump the dye laser. The DPSS laser produced 532 nm pulses with pulse durations of 6 ns and pulse energies of 6 mJ at a repetition rate of 10 kHz. The dye laser used Rhodamine 6G dye and was tuned for a fundamental output at 566.0 nm with 0.7 mJ per pulse. The fundamental output was frequency-doubled using a BBO crystal to 283.0 nm in order to excite the Q$_1$(5) transition of the A-X ($v' = 1$, $v'' = 0$) band. The frequency-doubled output was measured to be about 120 µJ at 283.0 nm and at a 10 kHz repetition rate. The laser sheet, which was placed at the jet centerline, was formed using a single cylindrical lens ($f_{\mathrm{PLIF,1}}$ = -50 mm) and focused using a second cylindrical lens ($f_{\mathrm{PLIF,2}}$ = +500 mm) to create a sheet about 200 µm in thickness.

The OH fluorescence was captured using an intensified, high-speed CMOS camera (Phantom v7.3 with a LaVision HS-IRO) that was gated to 200 ns to suppress the background chemiluminescence. The camera system was equipped with a 98 mm focal length, f/2.8, UV objective lens and a band-pass filter (320/40 nm). OH*-chemiluminescence (OH*-CL) images were obtained in an identical manner to OH-PLIF images, with the exception of increasing the intensified camera gate, generally to 1 µs. The laser and camera systems were installed to allow fast, remotely-controlled switching between the OH-PLIF and OH*-CL measurements. OH*-CL measurements were also obtained at 50.4 kHz with a Photron SA-Z and the same LaVision IRO. The spatial resolution for both the PLIF and chemiluminescence images were about 0.18 mm/pixel.

The data processing steps for the OH*-CL are shown in Fig 5.3. For the 5 and 10 kHz OH*-CL with the Phantom v7.3 camera, instantaneous images were directly used for data processing. However, a dark-noise correction was applied for the 50.4 kHz OH*-CL before further data processing. A median filter using MATLAB was applied to the instantaneous images and these are presented in this chapter with a contour that corresponds to 30% of the maximum intensity for that particular image. Instantaneous images are generally used to show the dynamic behavior of the jet-in-crossflow flame. Insights on flame shape and flame position were obtained using ensemble averaged OH*-CL images. The average image intensity was directly computed using the average (mean) of the images after a median filter operation. In order to add a contour for these images, the following procedure was developed: (1) the instantaneous images were binarized and an ensemble average of the binarized images was obtained, which is show in Fig. 5.3(e) as a contour plot, (2) the 0.3 contour from Fig 5.3(e) was then applied to the average image, such as the one shown in Fig 5.3(c). The average image with the 0.3 contour, shown in Fig. 5.3(f), is used in this chapter to compare flame shape and flame position at different conditions.

The data processing sequence for the OH-PLIF images is shown in Fig. 5.4. These images were cropped to the $4 < x/d_J < 6$ region in order to conduct analysis on the downstream region, where relatively high SNR was obtained. Comparing the average OH-PLIF images in this region to background OH*-CL yields an SNR of approximately $3 - 9$. Certain features of the jet shear layer, where super-equilibrium concentrations of OH are present due to continued reactions, yield an SNR as high as $18 - 20$. Computing an SNR in terms of the square of the mean to the square of the standard deviation in regions of near constant OH (the center of the jet) shows an SNR of 6 $- 25$. These SNR values were computed using an average PLIF image that was background

subtracted with the OH*-CL average image. However, background subtraction for the instantaneous images were not performed due to the possibility of removing features present in the OH-PLIF by subtraction from an average background image. Instead, based on the relatively high SNR in the $4 < x/d_J < 6$ range, it is believed that background chemiluminescence is minimal for this region.

As shown in Fig. 5.4, a laser sheet profile was obtained based on average images from acetone fluorescence without any flow in the rig. This laser sheet profile correction provided marginal improvement towards the edges of the profile in the $4 < x/d_J < 6$ range, although more robust methods are certainly desired. A median filter was applied to the laser sheet corrected image. For presentation of instantaneous images, the maximum counts of each image was used to normalize the instantaneous image. This was performed since shot-to-shot fluctuations in laser power are not accounted for in this experimental set-up. The data processing sequence was continued with the non-normalized images using the following steps: removal of crossflow OH, image binarization, and edge detection. An algorithm was developed to remove the OH fluorescence from the equilibrium OH in the vitiated crossflow. This threshold was applied on a column-by-column basis (to account for the laser sheet non-uniformity) and was set as 40% of the maximum intensity in a particular column. The image was then binarized using Otsu's method and this algorithm was applied on a column-by-column basis. The edge of the binarized images was detected using the Canny (1986) method. For presentation of instantaneous images, the detected edge was applied to the normalized instantaneous image, as shown in Fig. 5.5.
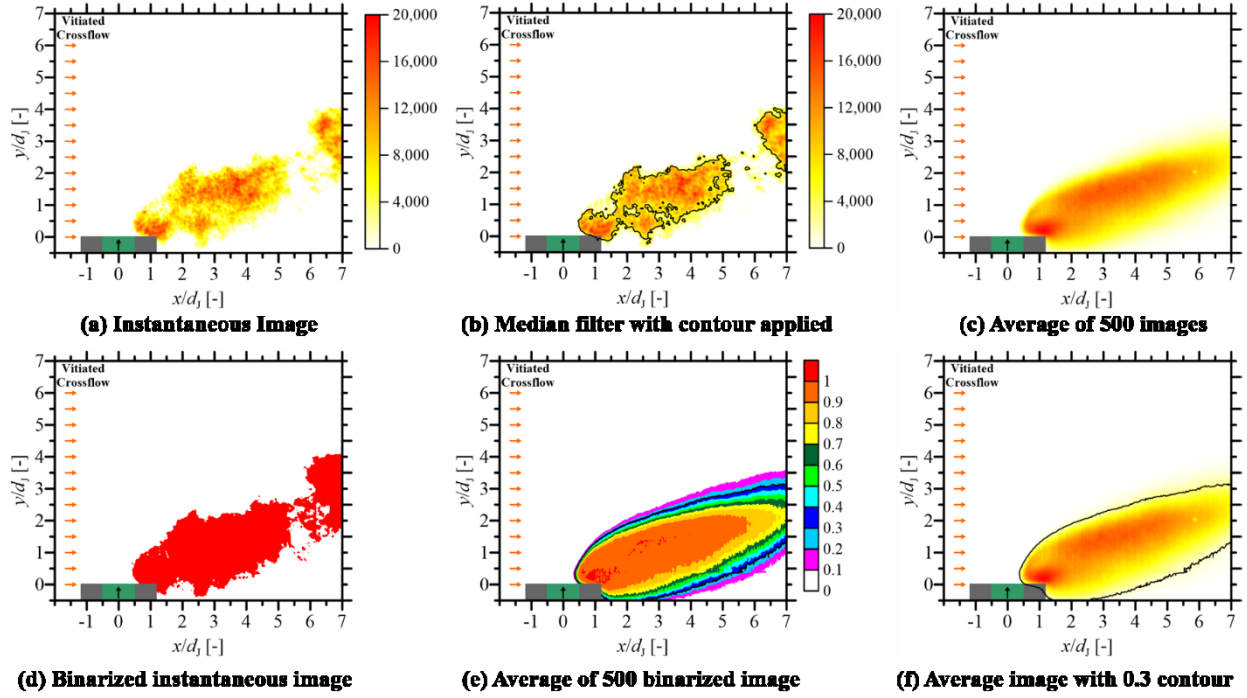
Figure 5.3: Data processing sequence for the OH*-CL.
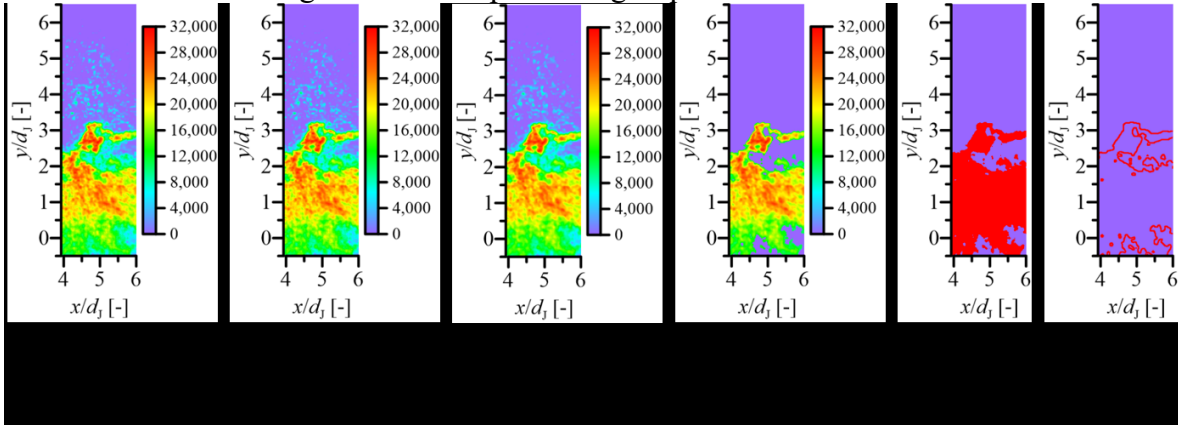
Figure 5.4: Data processing sequence for the OH-PLIF in the downstream $4 < x / d_J < 6$ region.
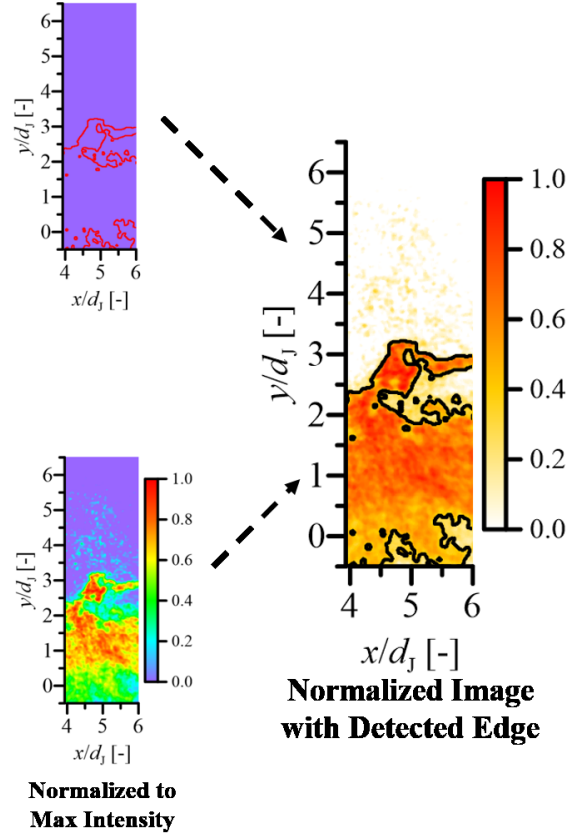
Figure 5.5: Illustration for the normalized image with edge detection used for analysis.

5.3 Results and Discussion

5.3.1 Premixed natural gas and air jets

Experimental investigations of premixed reacting jets in vitiated crossflows have traditionally been conducted within low-speed environments representative of land-based gas turbine combustors used for power generation. In this work, the effects of crossflow velocity beyond those typically used for land-based power generation is investigated. While maintaining a fixed combustor pressure and a constant flow rate corresponding to a velocity of 120 m/s or crossflow Mach number of 0.15, the jet equivalence ratio was increased until stabilization of the reacting jet was detected by OH*-chemiluminescence. Stabilization of the flame in the leeward side first occurred near $\phi_J = 1.4$ at jet conditions corresponding to $Ma_J = 0.21$ and $J = 1.9$.

Figure 5.6 depicts the stabilization process as the jet equivalence ratio approaches 1.4 using 50.4 kHz OH*-CL. Before stabilization, flame kernels can be seen both close to the injector ($x/d_J \sim 2$) and further downstream ($x/d_J > 7$). It is believed that these kernels are formed either through

auto ignition or they may be pulled upstream from a flame that resides downstream of the optical access. The kernel that formed at $t = \tau_0$ begins to grow over time in the wake region of the elevated injector, starting from about $t = \tau_0 + 0.179$ ms. This process continues through $t = \tau_0 + 0.536$ ms, with the kernel splitting, growing, and convecting downstream. At approximately $t = \tau_0 + 0.536$ ms, a kernel also begins to develop very close to the jet exit. At near $t = \tau_0 + 0.655$ ms, this kernel near the jet exit has grown substantially and resides near $x / d_J = 1$, where it is believed to reside in the wake of the jet. The earlier kernel has also grown substantially and is located near $x / d_J = 4$. It is believed that this kernel is stabilized in the wake of the elevated nozzle. For $t > \tau_0 + 0.655$ ms, these two kernels begin to merge such that the jet-in-crossflow flame is established at approximately $t = \tau_0 + 0.754$ ms.

A significant increase in the ΔNO_X (total NO_X from the staged combustor minus headend only NO_X) was also observed when the flame stabilized near the injector, compared to when it was stabilized further downstream. This is illustrated in Fig. 5.7, which shows values for ΔNO_X, ΔCO, ΔCO_2, and ΔO_2. Emissions data at $t < -44$ s corresponds to headend only data with air flowing in the axial stage. Natural gas was introduced to the jet at approximately $t = -44$ s and the initial injection of fuel lead to an increase in ΔCO. The jet equivalence ratio continued to increase over time and this can be clearly seen with an increase in ΔCO_2 and ΔO_2. At $t = 0$ s, however, the ΔNO_X experiences a sudden rise and this is believed to be due to the flame stabilization shifting from further downstream to near the injector. Steady-state emissions data for twenty seconds is obtained from near $t = 120$ s.

It is believed that both flame stabilization and auto ignition are significantly influenced by the local jet mixture equivalence ratio and the local unburnt jet mixture temperature. A contour plot of the local equivalence ratio is presented in Fig. 5.8(a) as a function of the equivalence ratio at the nozzle exit and the mass fraction of vitiated crossflow in the jet/crossflow mixture. An equivalence ratio that is slightly above stoichiometric at the exit may become very lean before auto ignition is initiated. Alternatively, if auto ignition occurs after significant mixing due to the high crossflow temperature, it may be that the flame speed of the mixture is too low because it has become significantly lean due to mixing with the crossflow. In a similar manner, a jet that is very rich at the exit ($\phi_J = 3.0$) may become close to stoichiometric due to mixing by the time a flame is stabilized. The corresponding mixture temperature as a function of the mass fraction of vitiated crossflow in the jet/crossflow mixture is presented in Fig. 5.8(b).

There may be evidence of flame stabilization occurring at near stoichiometric conditions due to mixing effects from the averaged 5 kHz OH*-CL. These are presented in Fig. 5.9 for jet equivalence ratios of: 1.5, 1.9, 2.3, and 2.8. The increased liftoff distance for richer equivalence ratios may be attributed to the flame position of the richer flame shifting to its location of maximum flame speed. The increased distance likely allows the jet flow to mix further with the crossflow and stabilize at near stoichiometric conditions. In addition to increased liftoff distance near the injector, the flame position also shifts towards the bottom wall for increasing ϕ_J. This is unexpected and may be due to two very different types of fluid dynamics associated with the flame-flow interactions for $\phi_J = 1.5$ compared to $\phi_J = 2.8$. The $\phi_J = 1.5$ seems to represent a traditional jet-in-crossflow flame that is stabilized by the wake vortices and the horseshoe vortices. Stabilization appears to occur on the leeward side of the jet and there seems to be some sort of attachment region near the body of the elevated injector. With increasing ϕ_J, however, the jet-in-crossflow features appear to be less significant and an increased role of the elevated injector body seems to be apparent. It is believed that the $\phi_J = 2.8$ flame has stabilized so far away from the jet exit that the jet-in-crossflow stabilization is no longer dominant, but rather a bluff-body stabilization due to the wake created by the protruding elevated injector is playing an important role in stabilization.

Emissions of ΔNO_X and ΔCO with increasing jet equivalence ratio is presented in Fig. 5.10, along with the corresponding test exit adiabatic flame temperature. A steady increase in the ΔNO_X emissions is observed with increasing jet equivalence ratios and this can be attributed to the increase in the exit product temperatures. Comparing the emissions to the averaged OH*-CL, it is believed that the levels of pre-flame mixing for the different ϕ_J are such that the local equivalence ratio for flame stabilization is near stoichiometric. Therefore, it is believed that comparable levels of prompt NO_X are created during the reaction. However, syngas (CO and H_2) production and combustion due to the richer flames may have an influence on ΔNO_X. Another additional consideration for the increased levels of ΔNO_X at richer equivalence ratios may be due to post-flame mixing. From the averaged OH*-CL, it appears that the $\phi_J = 1.5$ flame is much further from the bottom wall compared to the $\phi_J = 2.8$ flame. Since the $\phi_J = 2.8$ flame is much closer to the

bottom wall, it likely only experiences significant mixing with the crossflow at the top – compared to significant mixing at both the top and the bottom of the jet for the less rich equivalence ratio.

Figure 5.11 shows a sequence of instantaneous 10 kHz OH-PLIF images with the detected edge for two different jet equivalence ratios: $\phi_J = 1.4$ and $\phi_J = 2.5$. Similar to the averaged OH*-CL images, it is apparent that the less rich jet spends more time closer to the bottom wall and therefore has more significant interactions with the crossflow on that side. In contrast, the richer jet is much closer to the bottom wall. This is undesirable in an engine due to the damage to hardware. Furthermore, less significant mixing on that side may lead to higher post-flame temperatures, which would contribute towards higher levels of NO_X.

An ensemble average of 500 binarized OH-PLIF images were obtained and this is called a flame probability distribution for this work. This flame probability distribution is analogous to the mean progress variable used for premixed flames. However, since the reacting jet can use oxygen from the vitiated crossflow during combustion, this particular problem can be better characterized as a partially premixed flame and therefore the term flame probability distribution term is used here. The flame probability distribution for $\phi_J = 1.4$ and $\phi_J = 2.5$ is presented in Figure 5.12. It can be seen that the $\phi_J = 1.4$ flame has significant interactions with the crossflow at near both $y/d_J = 0.5$ and near $y/d_J = 2.5$. The center of the flame appears to be near $y/d_J = 1.5$ with an incline in the flame center with increasing y/d_J. In contrast, the $\phi_J = 2.5$ flame appears to only significantly interact with the crossflow at the top and near $y/d_J = 2$.

An ensemble average of the edges from 500 binarized OH-PLIF images were obtained and this is known as a 2D flame surface density. The 2D flame surface density is presented in Fig. 5.13 for the $\phi_J = 1.4$ and $\phi_J = 2.5$ flames. The high levels of flame surface density near 0.5 < $y/d_J < 1.0$ indicate significant levels of mixing with the crossflow. On the other hand, regions of comparatively high flame surface density are not present for the $\phi_J = 2.5$ flame. In addition, there is a significant region in the middle of the flame for the $\phi_J = 2.5$ case with flame surface density less than 0.02. This seems to indicate that hot gas products are always present there and this relatively large region is therefore at a much higher gas temperatures compared to the corresponding region for the $\phi_J = 1.4$ case.

A direct comparison of the two flames in terms of flame probability distribution (FPD) and the mean flame surface density (FSD) is presented in Fig. 5.14 and Fig. 5.15 respectively. The data in these plots are presented after a 3 pixel binning in the y/d_J direction and have been averaged along the $4.9 < x/d_J < 5.1$ horizontal region. The peak of the flame probability distribution for the $\phi_J = 1.4$ flame lies firmly near the $y/d_J = 2$ region and the distribution is fairly Gaussian. It is clear that there is vitiated crossflow on either side of this peak region. On the other hand, for the $\phi_J = 1.4$ flame, the peak is firmly towards the $0 < y/d_J < 1.5$ region and the peak is also much more broad. In addition, the FPD does not reach zero within the view of the optical access; note that the bottom wall resides at near $y/d_J = -0.7$, which is slightly below the optical access. Figure 5.15 shows that the flame surface density (FSD) is significantly higher on the side of the jet that is closer to the wall (y/d_J near 1.1), compared to the FSD towards the crossflow (y/d_J near 2.5). In fact, there is a rather broad region of flame surface density for the interaction near the crossflow. There is also a clear valley in the FSD for the $\phi_J = 2.5$ near $0.5 < y/d_J < 1.0$. This region corresponds to the bulk of the flame without any flame edges. A clear peak in FSD can be seen for the region near the interaction with the crossflow.

Figure 5.16 presents the mean flame surface density vs. the mean flame probability distribution. Interestingly, the FSD as a function of the FPD is very similar for the two flames for the region between the core of the jet to the region where the top of the jet interacts with the crossflow. Of course, there is an offset for this vertical region due to the $\phi_J = 1.4$ flame being further away from the wall. The main difference between the two flames that can be seen here, however, is the additional line for FSD vs. FPD at $\phi_J = 1.4$ that traverses from FPD = 0 to FPD = 1. The FSD for this line has a magnitude that is about twice that of the line between $1.75 < \phi_J < 3.75$. This region represents the interaction with the crossflow and this can be attributed to the shear-layer vortices at the bottom that are present in the flame with the jet-in-crossflow stabilization mechanism. This simply do not appear to be present for the richer flame that is stabilized with a bluff-body type of flame stabilization.

Figure 5.6: Ignition sequence using 50.4 kHz OH*-CL at $Ma_\infty = 0.15$ as ϕ_J approaches 1.4.
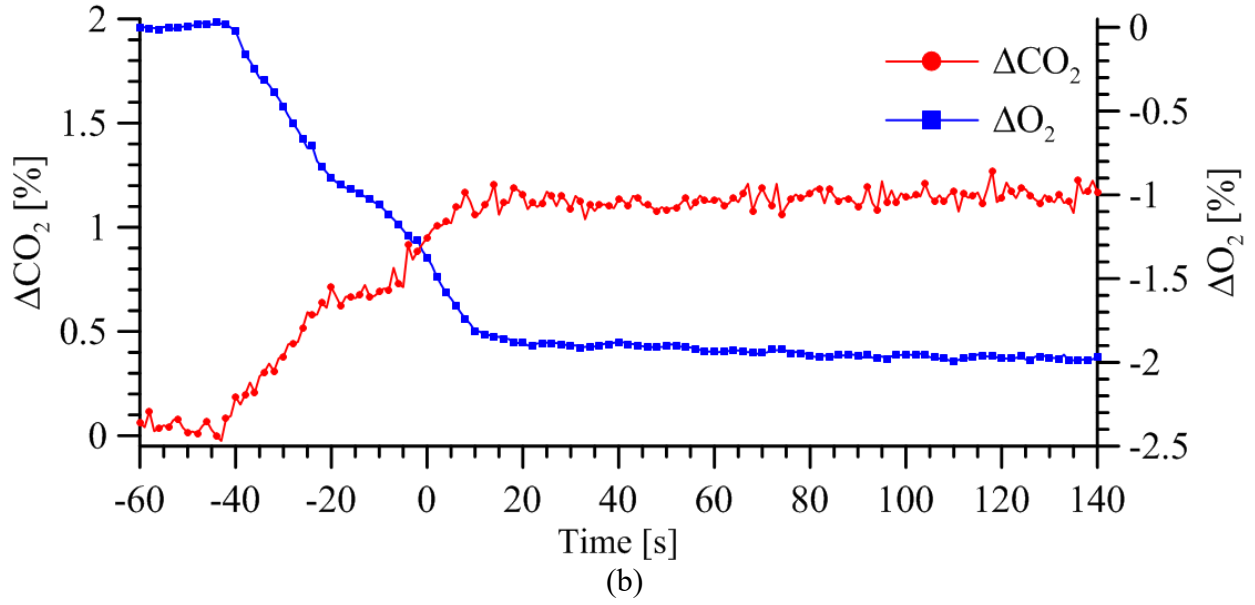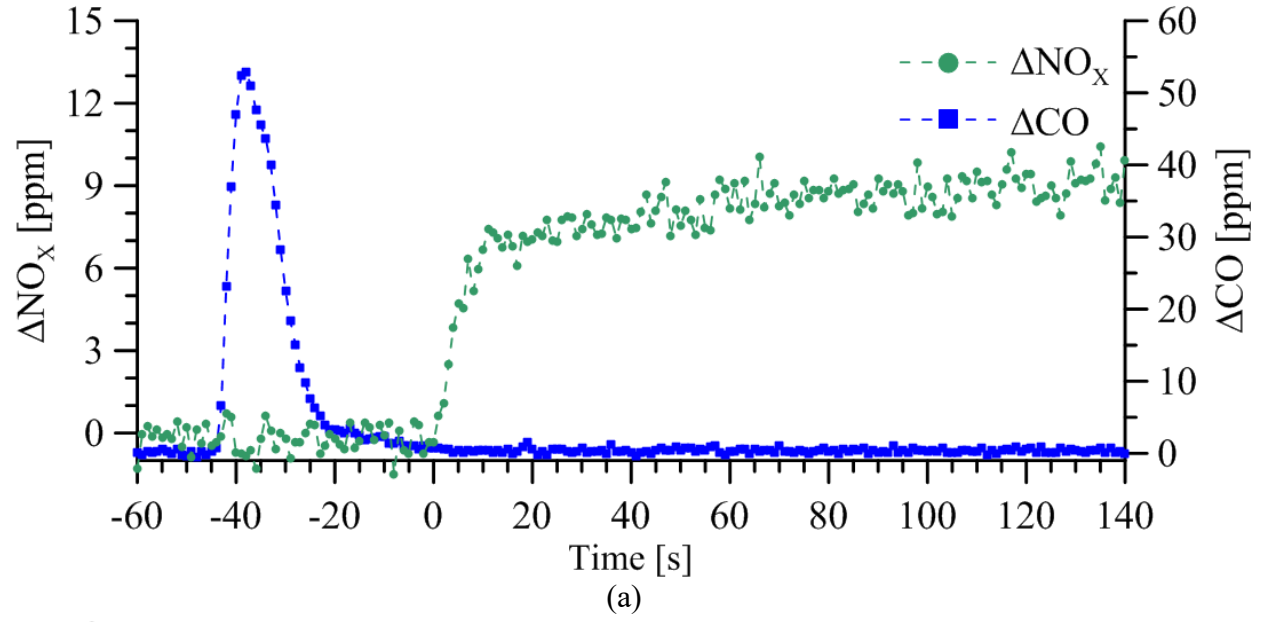
Figure 5.7: Emissions reading as a flame is stabilized near $\phi_J = 1.4$ at $Ma_\infty = 0.15$: (a) ΔNO_X and ΔCO vs. time, (b) ΔCO_2 and ΔO_2 vs. time.

115
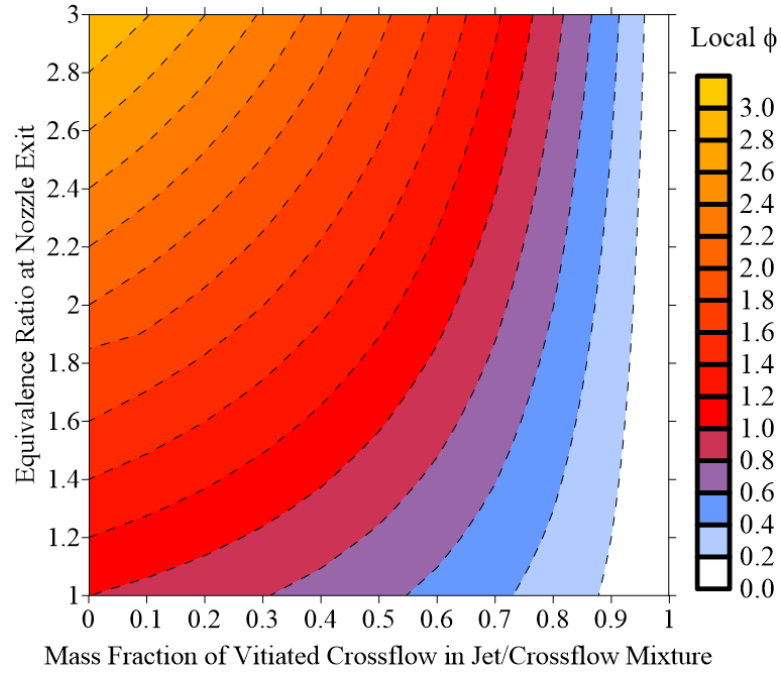
(a)
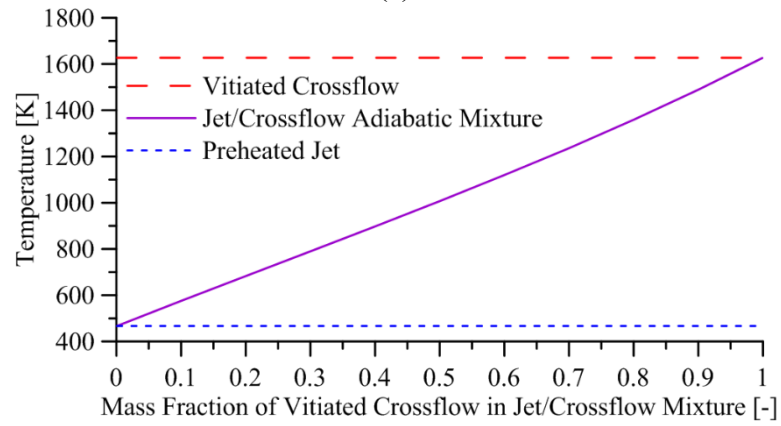
(b)

Figure 5.8: Calculated values for the jet/crossflow mixture:
(a) local ϕ as a function of ϕ_J and mass fraction of vitiated crossflow, (b)unburnt
jet temperature as a function of mass fraction of vitiated crossflow.
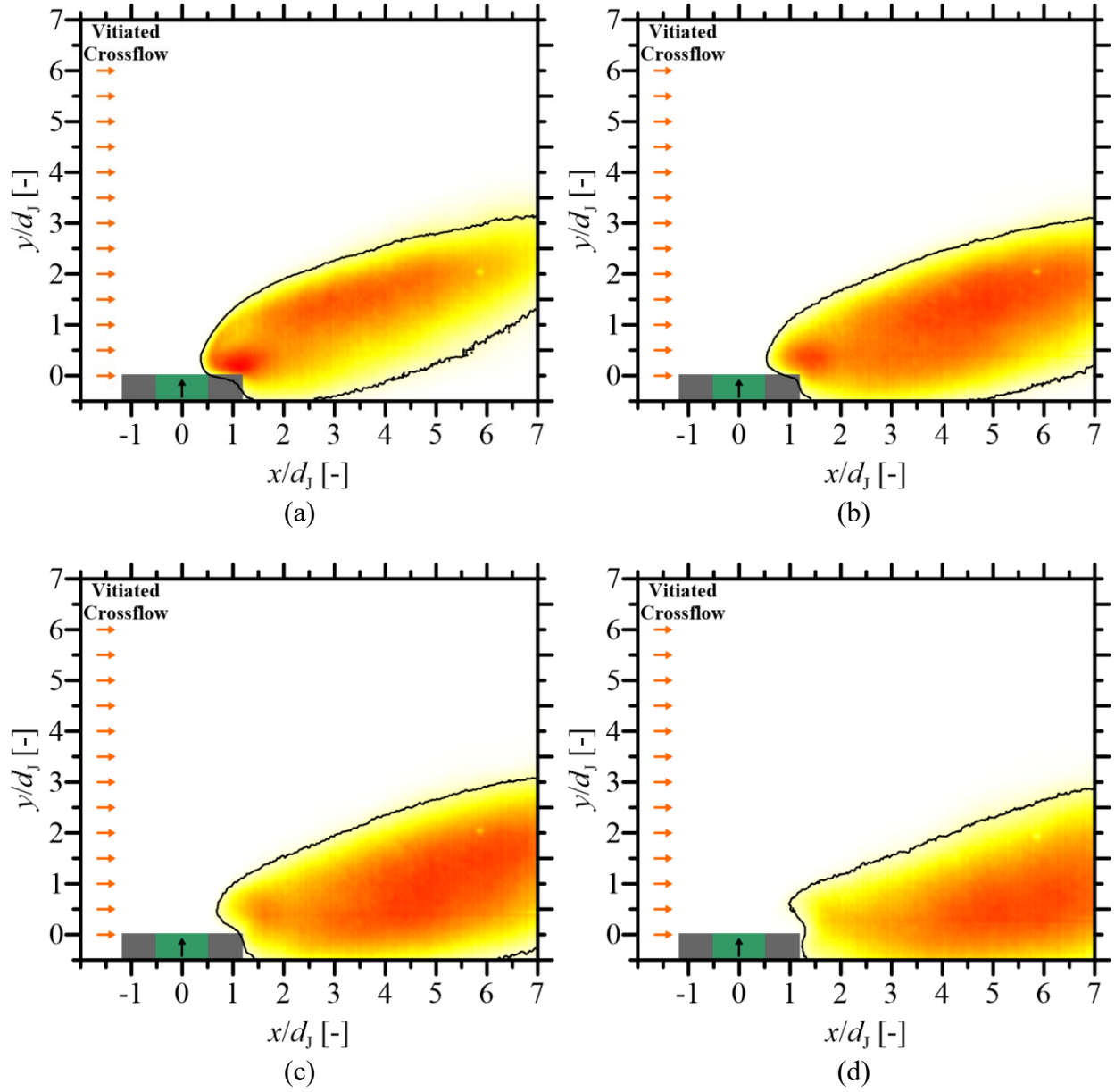
Figure 5.9: Ensemble average of 500 OH*-CL images obtained at 5 kHz for $Ma_\infty = 0.15$ and $Ma_J = 0.22$: (a) $\phi_J = 1.5$, (b) $\phi_J = 1.9$, (c) $\phi_J = 2.3$, and (d) $\phi_J = 2.8$.
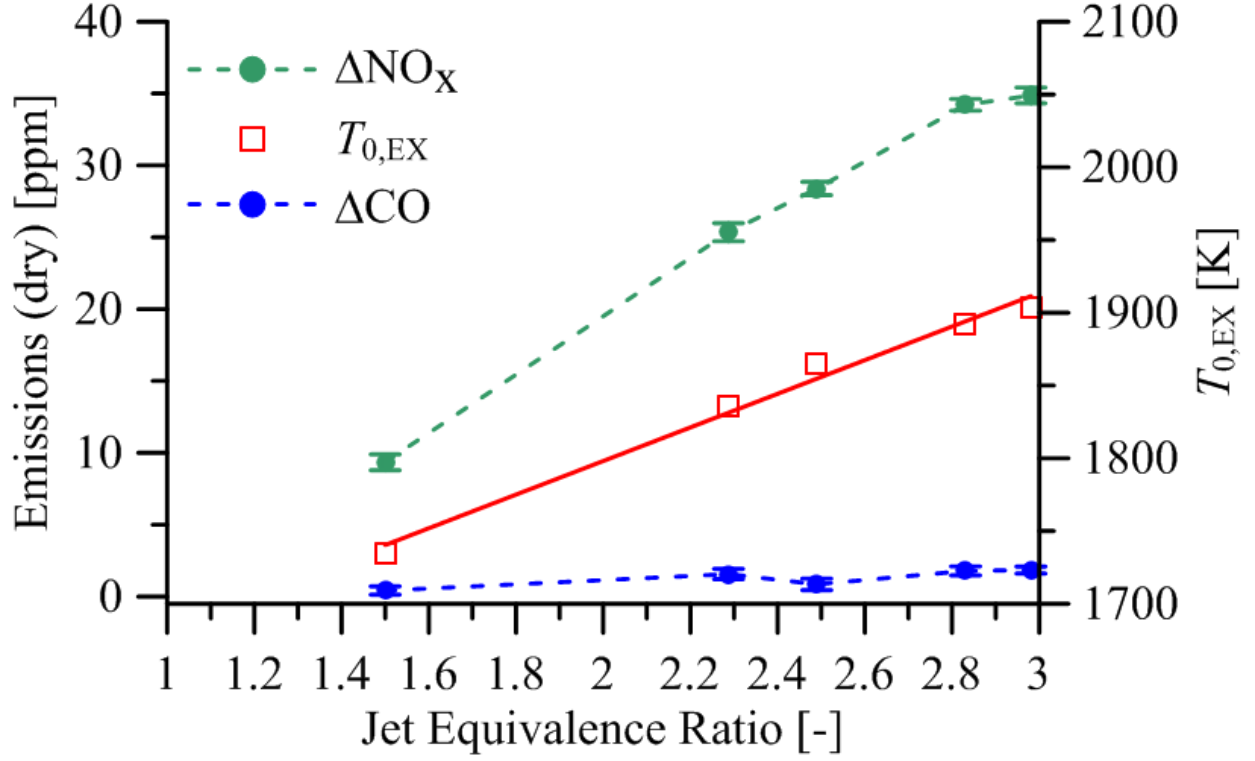
Figure 5.10: Emissions of ΔNO_X and ΔCO vs. ϕ_J with the corresponding adiabatic temperature at the combustor exit.
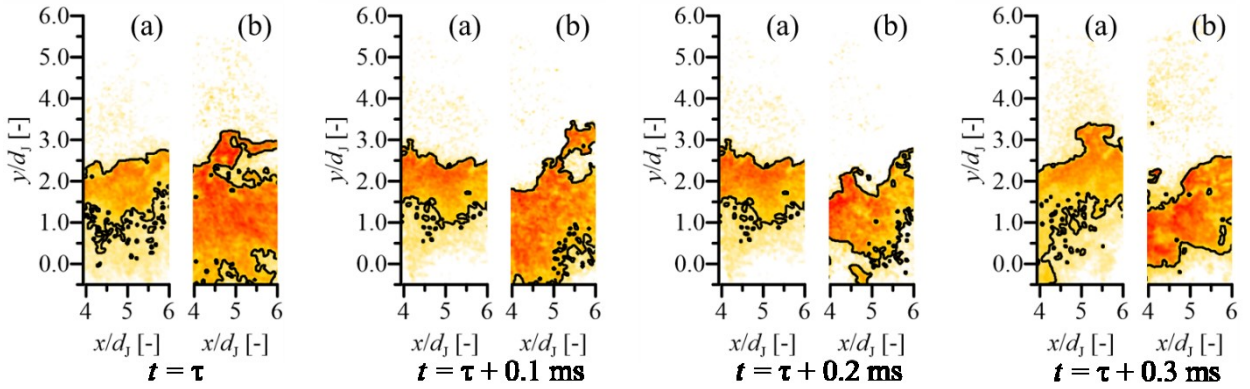
Figure 5.11: Sequence of instantaneous 10 kHz OH-PLIF with the detected edge in the $4 < x/d_J$ < 6 region at $Ma_\infty = 0.15$ for: (a) $\phi_J = 1.4$ and (b) $\phi_J = 2.5$.
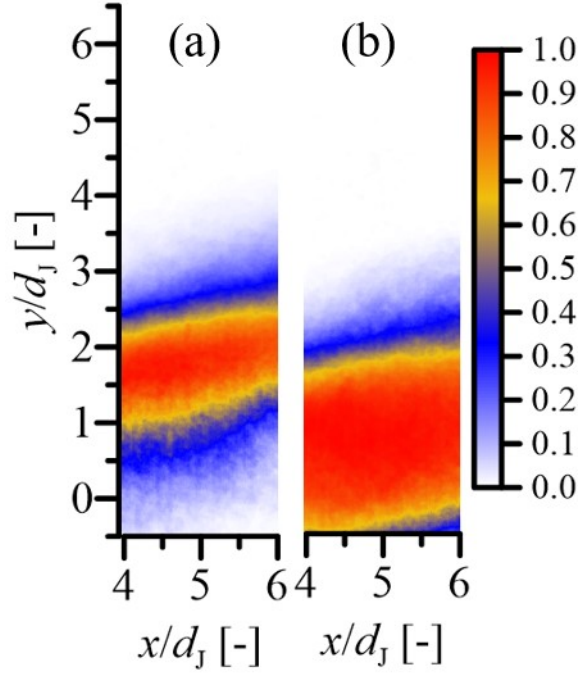
Figure 5.12: Flame Probability Distribution (a) $\phi_J = 1.4$ and (b) $\phi_J = 2.5$.
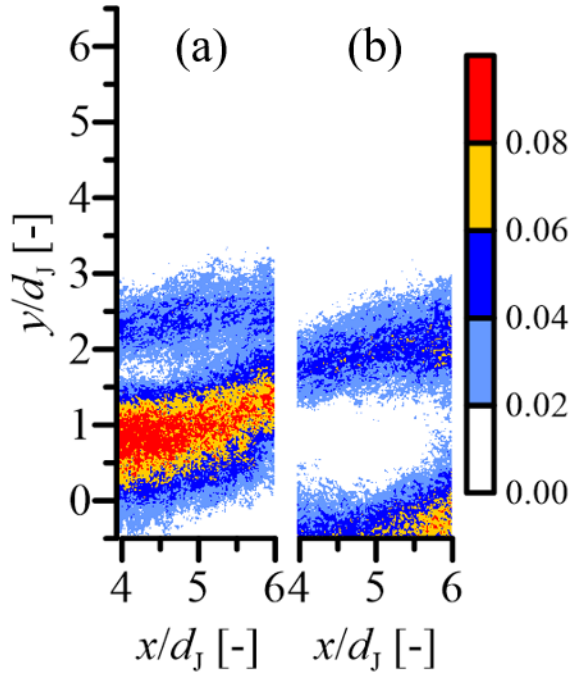
Figure 5.13: Flame Surface Density (a) $\phi_J = 1.4$ and (b) $\phi_J = 2.5$.
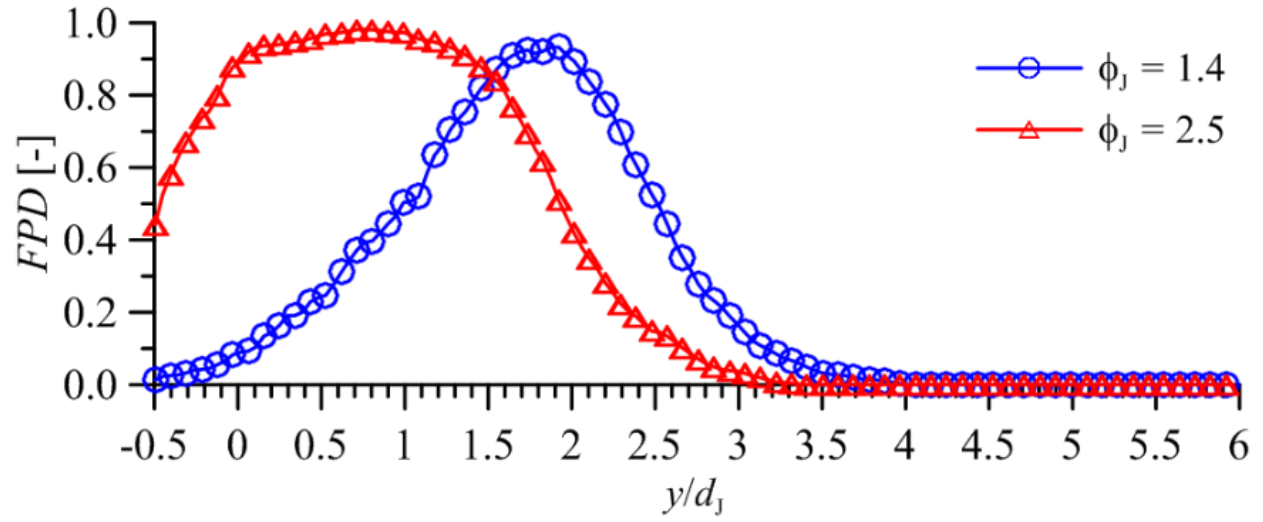
Figure 5.14: Flame Probability Distribution vs. y/d_J at $4.9 < x/d_J < 5.1$.
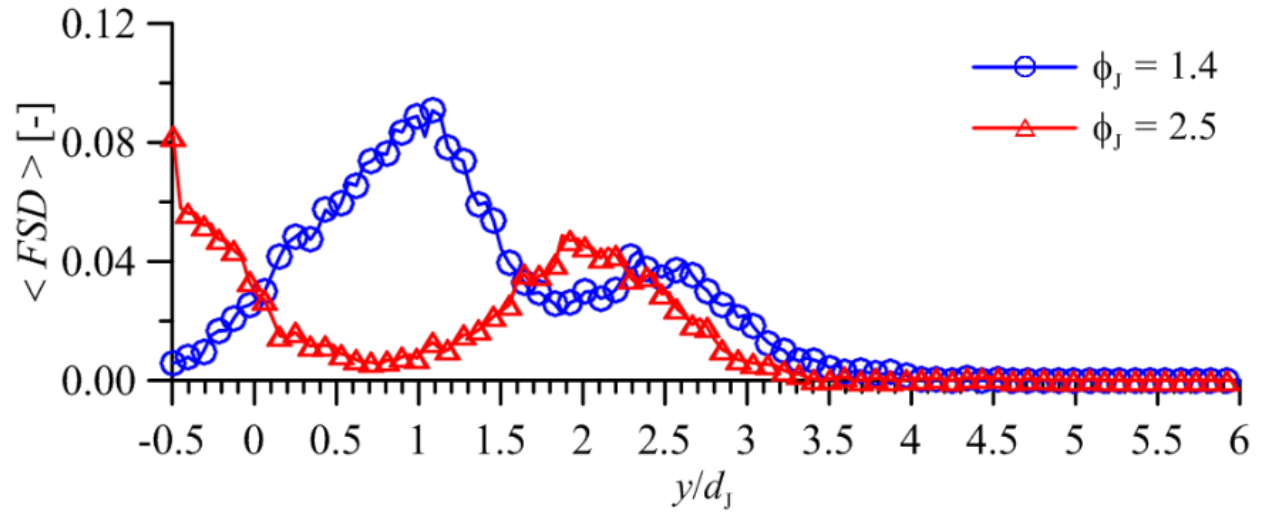
Figure 5.15: Mean Flame Surface Density vs. y/d_J at $4.9 < x/d_J < 5.1$.
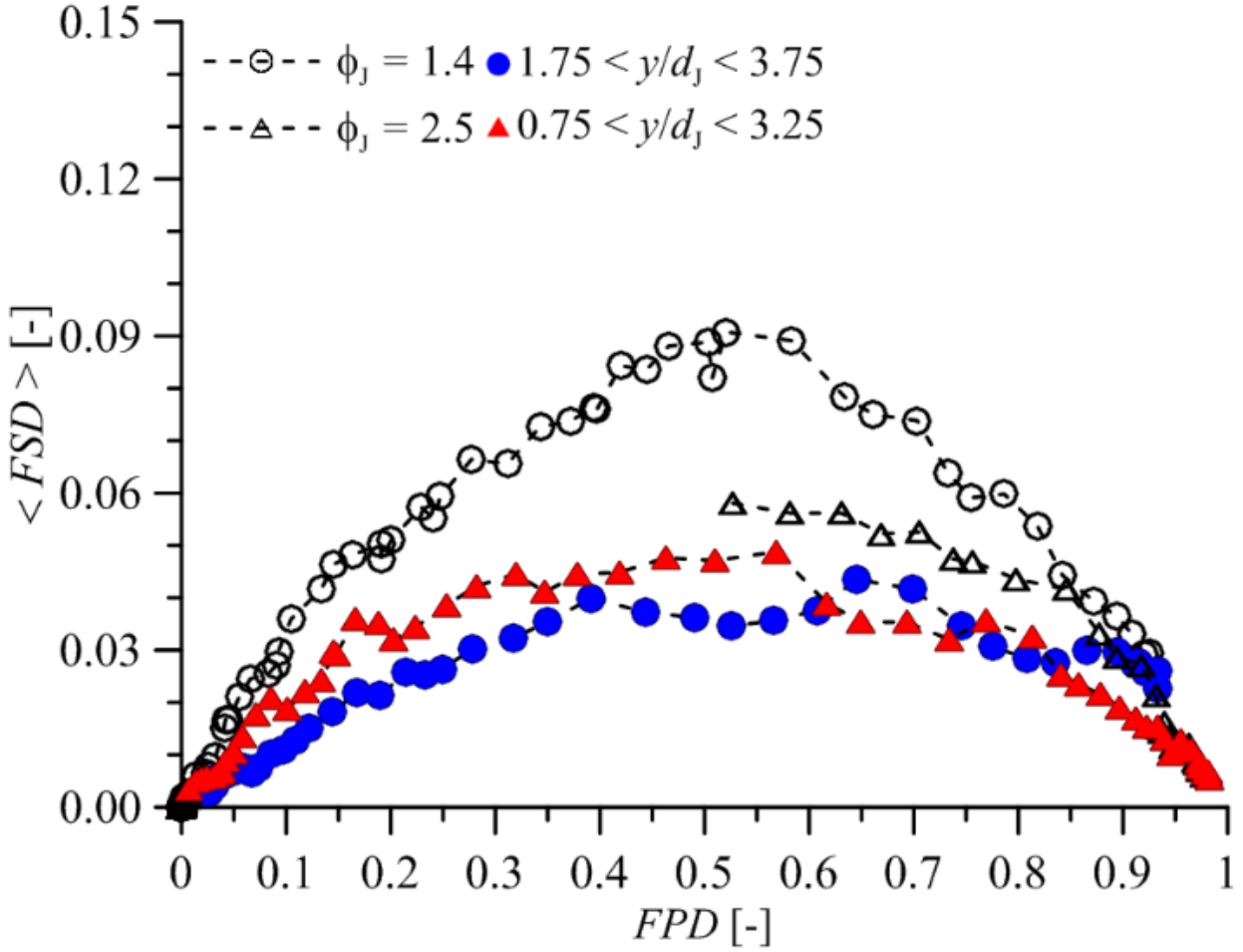
Figure 5.16: Mean Flame Surface Density vs. Flame Probability Distribution at $4.9 < x/d_J < 5.1$.

5.3.2 Premixed natural gas, hydrogen, and air jets

Premixed natural gas and air was also injected at higher crossflow velocities corresponding to $Ma_\infty = 0.24$ and $Ma_\infty = 0.33$. However, stabilization of the premixed NG-air flame on the leeward side or in the wake was not observed for either of these higher crossflow Mach numbers at jet equivalence ratios from 1.1 to 3.0. Although OH*-chemiluminescence was not observed within our viewing window (approximately 90 mm or 8.5 jet diameters downstream of injection), exhaust gas emissions showed very low levels of CO and UHC (< 10 ppm dry). This indicates that combustion of the jet did occur beyond the viewing window; there is an axial distance of approximately 120 mm between the downstream edge of optical access and the inlet to the quench section.

The drastic change in flame stabilization can be mainly attributed to the increased velocity of the crossflow, which increases the strain rate and the level of turbulence. In addition to promoting significant mixing between the jet and the crossflow, the increased crossflow velocity may create local flow speeds that are beyond a critical point to sustain a flame near the injector. As noted by Micka *et al.* (2012), which is the only other work, to our knowledge, featuring transverse injection at high crossflow velocities: effects from the high strain rates created by the high-speed crossflow are significant and mixing is dominated by a wake-like process that is controlled by the crossflow velocity. However, one main difference between the current work and the heated air crossflow study by Micka *et al.* is the lower oxygen content in our vitiated crossflow. Based on the high crossflow temperatures that are above the auto ignition temperature and the lack of CO and unburnt hydrocarbons measured by the FTIR, we believe that the jet is burning somewhere downstream of the ~8 jet diameters of optical access.

The Damkohler number, defined as the ratio between the flow time scale and the chemical time scale ($Da = \tau_{\mathrm{FLOW}} / \tau_{\mathrm{CHEM}}$), may be playing an important role in the observed flame stabilization. Relevant studies in literature that have used Damkohler number scaling include an ignition-based Damkohler number for the reacting jet in crossflow by Kohl *et al.* (2016) and a study of bluff-body type flame holders by El-Asrag *et al.* (2011). We believe that the appropriate scaling for our work incorporates the thermal diffusivity and the laminar flame speed ($\tau_{\mathrm{CHEM}} \sim \alpha / S_{\mathrm{L}}^{2}$) rather than the ignition delay. However, numerically defining this chemical time scale in a manner that is physically relevant is difficult due to the rapid mixing of the jet with the crossflow prior to combustion. Instead, we further investigate the transverse injection of a reacting jet into a high-speed vitiated crossflow by introducing hydrogen into the jet mixture to decrease the chemical time scale. A similar approach was actually taken by Micka *et al.*, who used a jet mixture composing of 50% ethane and 50% hydrogen in order to sustain a flame.

Several NG-air jet equivalence ratios were chosen for the $Ma_{\infty} = 0.24$ and $Ma_{\infty} = 0.33$ conditions and the hydrogen mole fraction in the fuel blend was slowly increased until stabilization of the flame near the injector was detected based on the OH*-chemiluminescence imaging. Figure 17 shows the minimum level of fuel H_2 mole fraction X_{H2} required to stabilize the flame near the injector as a function of the NG-H_2-air equivalence ratio. It should be noted that stabilization near the injector was a sharp and abrupt change that went from no OH* detection, to traces of OH*

close to the edge of optical access, and then to a sharp jump to the injector. This transition was very similar to the transition presented for the NG-air only flame in Fig. 5.6. For a given NG-H_2-air equivalence ratio, a greater concentration of hydrogen mole fraction was required to stabilize the flame at the higher crossflow Mach number $Ma_\infty = 0.33$, compared to $Ma_\infty = 0.24$. In addition, the minimum fuel H_2 mole fraction needed for stabilization was reduced as the jet equivalence ratio was increased from $\phi_J > 1.0$ up to an inflection point between $2.0 < \phi_J < 2.5$. In other words, for a constant fuel H_2 mole fraction, rapid mixing between the rich premixed jet and the vitiated crossflow resulted in optimal stoichiometric conditions at a particular ϕ_J for a given Ma_∞. This supports our belief that numerically defining a chemical time scale is difficult: the laminar flame speed (and the ignition delay time) decrease with equivalence ratios beyond stoichiometric conditions and defining the flame speed or ignition delay based only on the jet exit conditions would lead to non-physical trends.

Figure 5.18 presents the averaged OH*-CL images at $Ma_\infty = 0.24$ for four jet equivalence ratios of: $\phi_J = 1.6$ with $X_{H2} = 0.15$, $\phi_J = 2.0$ with $X_{H2} = 0.09$, $\phi_J = 2.3$ with $X_{H2} = 0.08$, and $\phi_J = 2.5$ with $X_{H2} = 0.10$. In a manner similar to Figure 5.18 for the NG-air jets at the $Ma_\infty = 0.15$ crossflow, there is a noticeable change in the flame shape and position. Once again, the increased liftoff distance for richer equivalence ratios may be attributed to the flame position of the richer flame shifting to its location of maximum flame speed. At the lower equivalence ratio, Figure 5.18(a), stabilization similar to a jet-in-crossflow is apparent. However, as the jet equivalence ratio is increased and there is a shift in the liftoff distance to further away from the injector, the flame transitions to what is hypothesized to be a bluff-body stabilization in the wake created by the protruding elevated injector. Figure 5.19 presents the averaged OH*-CL images at $Ma_\infty = 0.33$ for four jet equivalence ratios and hydrogen mole fraction combinations. Perhaps the most interesting aspect of the flame here is that it appears to be wider compared to the $Ma_\infty = 0.15$ and $Ma_\infty = 0.24$ cases. The increased width of the flame may be attributed to the hydrogen that is originally premixed in the jet diffusing out into the crossflow. As a result, the very edges of the jet flame may be hydrogen burning directly with the vitiated crossflow.

Exhaust gas measurements were acquired to study the effect of flame stabilization on NO_X emissions. Figure 5.20 shows the NO_X generated in the axial stage (headend NO_X subtracted) as

a function of the adiabatic exit total temperature for a constant vitiated crossflow at $Ma_\infty = 0.24$. Test conditions were separated between those where a flame was stabilized just downstream of the injector (premixed NG-H$_2$-air at the minimum fuel hydrogen concentration needed for stabilization near the injector) and far downstream of the injector (premixed NG-air without hydrogen). The calculated axial stage residence time for these conditions was approximately 1.0 ms. Enhanced mixing of the jet with the vitiated crossflow before combustion is believed to be responsible for lower NOx in the case of flame stabilized far downstream of the injector.
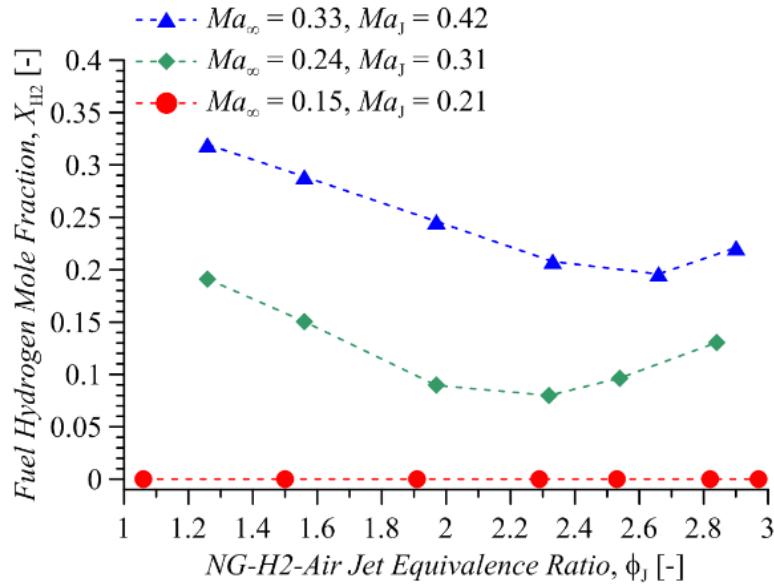
Figure 5.17: Minimum fuel hydrogen mole fraction for flame stabilization near the injector vs. jet equivalence ratio at three crossflow Mach number and jet Mach number combinations.
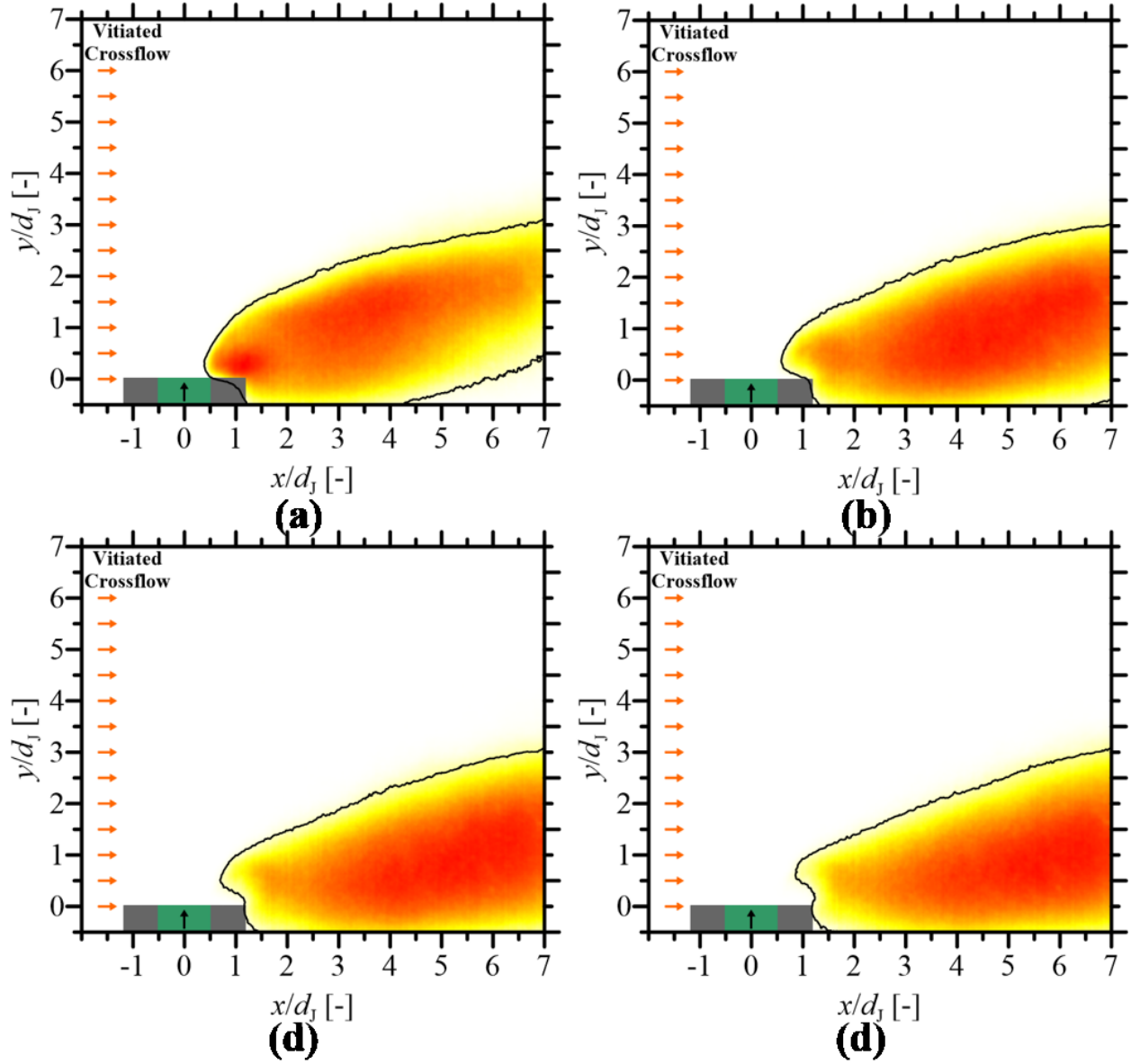
Figure 5.18: Ensemble average of 500 OH*-CL images obtained at 5 kHz for $Ma_\infty = 0.24$ and $Ma_J = 0.31$: (a) $\phi_J = 1.6$, $X_{H2} = 0.15$, (b) $\phi_J = 2.0$, $X_{H2} = 0.09$, (c) $\phi_J = 2.3$, $X_{H2} = 0.08$, and (d) $\phi_J = 2.5$, $X_{H2} = 0.10$.
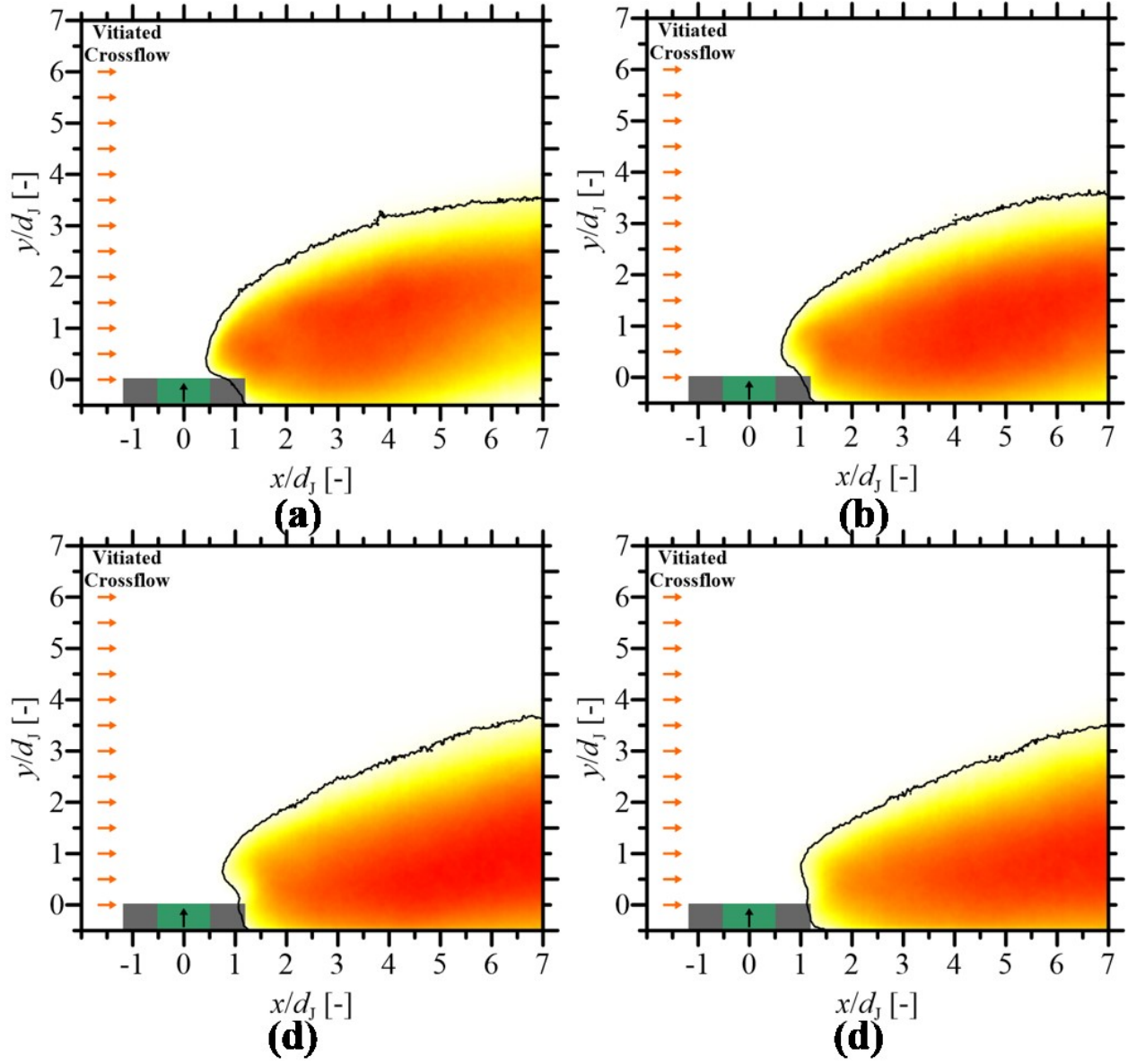
Figure 5.19: Ensemble average of 500 OH*-CL images at 5 kHz for $Ma_\infty = 0.33$ and $Ma_J = 0.43$: (a) $\phi_J = 1.6$, $X_{H2} = 0.29$, (b) $\phi_J = 2.0$, $X_{H2} = 0.25$, (c) $\phi_J = 2.7$, $X_{H2} = 0.20$, and (d) $\phi_J = 2.9$, $X_{H2} = 0.26$.
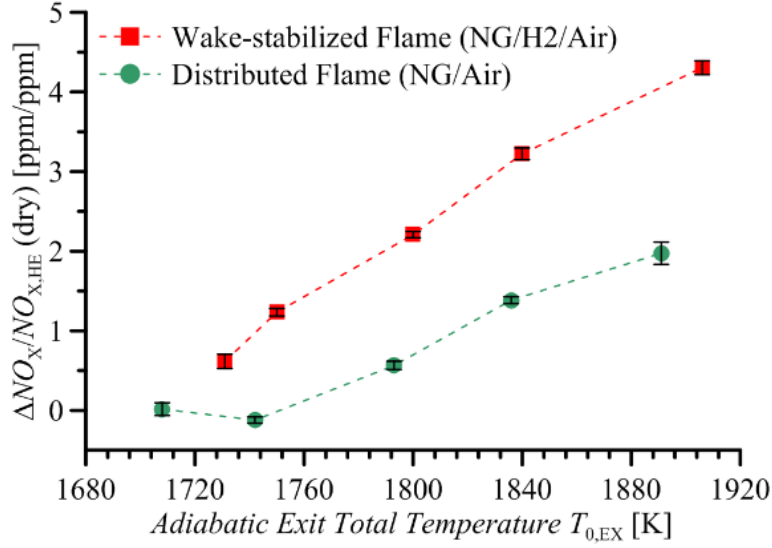
Figure 5.20: ΔNO_X from axial stage normalized by HE NO_X vs. adiabatic exit total temperature for two different flame stabilizations at $Ma_\infty = 0.24$ and $Ma_J = 0.31$.

5.4 Summary and Conclusions

Using a newly developed optically-accessible secondary combustion zone, we studied the stabilization mechanisms for a reacting jet in a high-speed vitiated crossflow at engine-relevant conditions. The crossflow velocity was observed to have a strong impact on the stabilization of the premixed NG-air flame. At the crossflow speed corresponding to $X_{H2} = 0.15$ (120 m/s), a minimum ϕ_J near 1.4 was needed to stabilize the flame near the injector. This is likely due to rapid mixing of the jet with the crossflow such that once auto ignition occurs; the local flame speed cannot maintain a flame in the highly turbulent wake region. However, reactants are still believed to be consumed downstream of the optical access.

50 kHz OH*-CL shows that as ϕ_J approaches 1.4, the flame kernel in the wake of the elevated injector begins to grow. A separate flame kernel develops on the leeward side of the jet. These two kernels merge to create a stabilized reacting jet-in-crossflow near the leeward side of the jet. Flame stabilization near the injector is marked with a significant increase in ΔNO_X emissions, compared to the downstream reaction. Beyond a certain threshold for ϕ_J (approximately 0.4), ΔCO emissions are negligible even when a flame is not observed near the injector.

127

Based on averaged OH*-CL, the flame position shifts with increasing jet equivalence ratios from 1.5 to 2.8, both near the injector and several diameters downstream. Increased liftoff distance may be due to the flame stabilizing at locations corresponding to maximum flame speed (increased pre-flame mixing for richer jets). The downstream shift near the wall may be due to reaction occurring in the wake of the elevated injector rather than the leeward side of the jet. OH-PLIF images taken at $4 < x/d_J < 6$ shows that the flame at $\phi_J = 1.5$ has significantly more interactions with the crossflow at the bottom of the jet compared to the $\phi_J = 2.5$ flame. The greater post-flame mixing for the $\phi_J = 1.5$ flame is believed to be a contributing factor towards lower ΔNO_X emissions at this condition, compared to the $\phi_J = 2.5$ flame.

Stabilization of the flame, as indicated by the OH*-chemiluminescence imaging, was not observed within our viewing region for higher crossflow Mach numbers. Hydrogen was therefore blended into the natural gas to reduce the chemical time scale. Minimum levels of hydrogen concentration for stabilization near the injector are reported for two different crossflow Mach numbers based on the jet equivalence ratio. Exhaust gas measurements at select conditions showed a dramatic increase in NO_X for the cases where the flame was stabilized near the injector compared to where it was stabilized further downstream. This can be primarily attributed to the decreased level of mixing for the near-injector stabilized cases, which consequently leads to reduced local lean flame equivalence ratios and an increased occurrence of local near-stoichiometric pockets of reacting gas.

6. DEMONSTRATION OF HIGH-REPETITION-RATE CH-PLIF IN THE C-X ELECTRONIC SYSTEM WITHIN A 1 MW STAGED GAS TURBINE MODEL COMBUSTOR USING R-BRANCH EXCITATION

6.1 Introduction

CH is an excellent flame-front marker and is a good indicator for locations of peak heat release. It exists only in the reaction zones for premixed flames and indicates near-stoichiometric regions for partially premixed and non-premixed flames. CH-PLIF has traditionally been performed in the A-X and B-X electronic systems. However, researchers at AFRL in Dr. Cam Carter's group have used CH-PLIF with excitation in the C-X electronic system in recent years. The laser was tuned to near 314 nm in their earlier works for CH-PLIF with Q-branch excitation to study laminar and turbulent flames at atmospheric conditions (Carter *et al*., 2014; Carter *et al*., 2016; Skiba *et al.,* 2017; Skiba *et al.,* 2018). These works have also compared the reaction zone imaged from CH-PLIF with overlapped regions of OH-PLIF and CH_2O-PLIF fluorescence.

More relevant to the present work, however, are the very recent studies by Hammack, *et al*. (2018) and Mitsingas *et al.* (2019), where CH-PLIF was performed simultaneously with particle imagining velocimetry (PIV) for atmospheric flames. The challenge of scatter produced by the PIV particles was overcome by employing two custom long-wave-pass edge filter with a steep slope to strongly suppress laser scattering below 311 nm. CH-PLIF was performed by tuning the laser to near 311 nm in order to excite R-branch CH transitions. The scatter produced by the PIV particles in analogous to the scatter that would be produced from a practical combustor and therefore their work is a strong springboard to apply CH-PLIF to enviroments within a practical combustor, such as the current work. In addition, as noted by Mitsingas *et al.* (2019), the coincidence of CH and OH bands at this laser wavelength could allow for switching between imaging of CH and OH. Furthermore, as discussed in Mitsingas *et al.* (2019), the R(13) transition is only mildly sensitive to temperature between 1800 – 2000 K in terms of the Boltzmann fraction (~6%) and the R(11) transition is very insensitive to temperature (<1%).

In this chapter, CH-PLIF using R-branch transitions within the C-X electronic system is demonstrated within a practical combustor at high laser repetition rates corresponding to 1 kHz. The combustor used for this work is the staged gas turbine model combustor used in previous chapters of this dissertation. Figure 6.1 shows simulated spectra of CH and OH rotational lines

within the 300 – 325 nm regions at 2000 K and at atmosphere pressure. Also shown here is the transmittance from the two long-wavelength-pass edge filters based upon the reported values by Mitsingas *et al.* (2019).
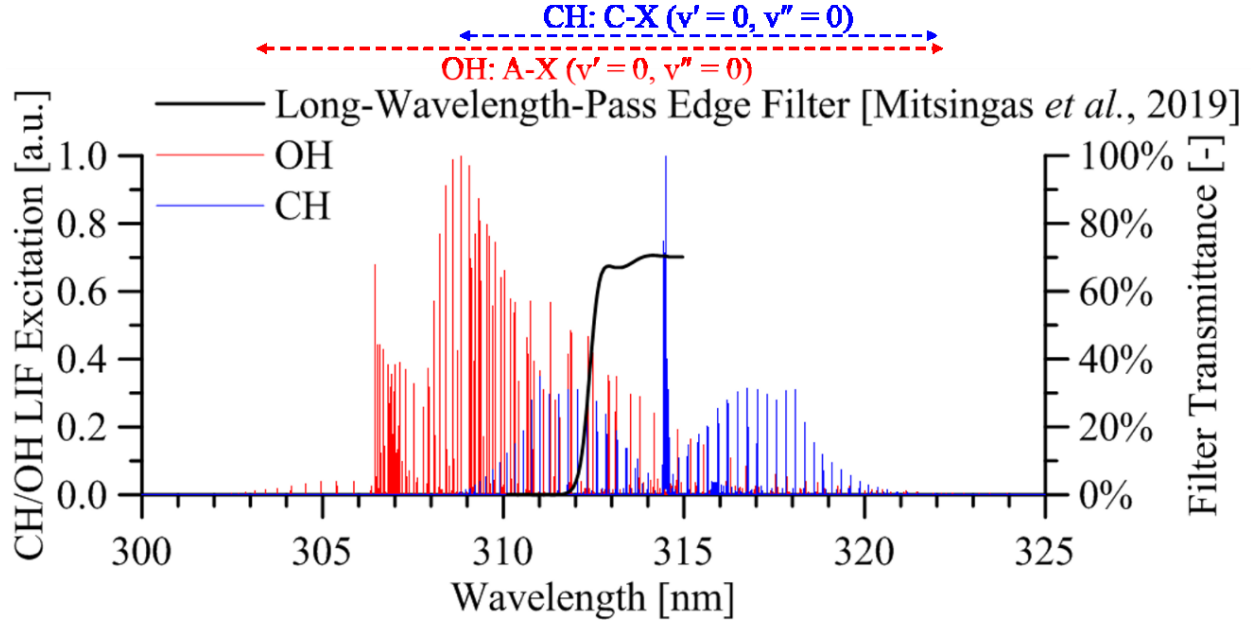
Figure 6.1: Simulated spectra of CH and OH rotational lines along with the transmittance of the long-wavelength-pass edge filter combination.

6.2   Experimental Systems

The optically-accessible, high-pressure, staged combustion test rig used for this work is the same as the one described in earlier chapters and shown schematically in Fig. 6.2. The rig consists of three major sub-assemblies: the *headend* stage, the *axial* stage, and the *NO_X quench and sample* stage. All of the hot sections (both combustion and post-combustion zones) within the test rig featured a thermal barrier coating and were either air-film-cooled or water-cooled to ensure hardware survivability for long-duration, steady-state operation. A detailed schematic of the optically-accessible section with the camera systems is presented in Fig. 6.3.

PLIF measurements were obtained using a high-repetition-rate, Q-switched, diode-pumped solid-state (DPSS) Nd:YAG laser (Edgewave) and a dye laser (Sirah Credo) designed for efficient high-repetition-rate operation. The second harmonic output of the DPSS laser at 532 nm was used to pump the dye laser. The DPSS laser produced 532 nm pulses with pulse durations of 6 ns and pulse energies of 4.5 mJ at a repetition rate of 1 kHz. Higher repetition rates resulted in about 4.2

mJ at 5 kHz and 3.5 mJ at 10 kHz. The dye laser used DCM dye and was tuned for a fundamental output near 622 nm with 0.3 mJ per pulse at 1 kHz. The fundamental output was frequency-doubled using a BBO crystal to near 311 nm in order to excite R-branch CH rotational lines of the C-X (v′ = 0, v″ = 0) band and P-branch or Q-branch OH rotational lines of the A-X C-X (v′ = 0, v″ = 0) band. The frequency-doubled output was measured to be about 50 μJ near 311 nm and at a 1 kHz repetition rate. The laser sheet, which was placed at the jet centerline, was formed using a single cylindrical lens ($f_{\mathrm{PLIF,1}}$ = -150 mm) and focused using a second cylindrical lens ($f_{\mathrm{PLIF,2}}$ = +500 mm) to create a sheet about 200 μm in thickness. Significant variations were present in the laser-sheet intensity profile; most significantly a region of lower laser sheet intensity was present in between two regions of reasonable laser fluence.

The OH and CH fluorescence was captured using an intensified, high-speed CMOS camera (Photron SA-Z with a LaVision HS-IRO) that was gated to 60 ns to suppress the background chemiluminescence. The camera system was equipped with a 98 mm focal length, f/2.8, UV objective lens and a band-pass filter (320/40 nm). The intensified camera system was also equipped with two custom AFRL long-wavelength pass filters. These filters were designed to suppress the laser scatter near 311 nm and transmit the fluorescence near 314 nm. Lens tube extenders were used to provide excellent spatial resolution of about 0.035 mm/pixel.
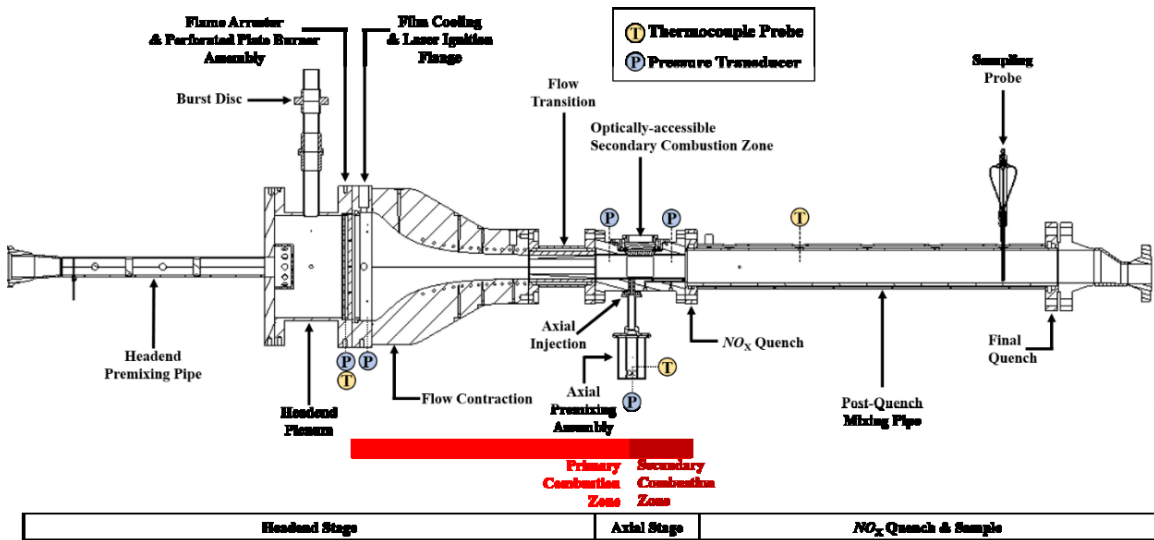
Figure 6.2: Schematic of the high-pressure model combustor used in this work.
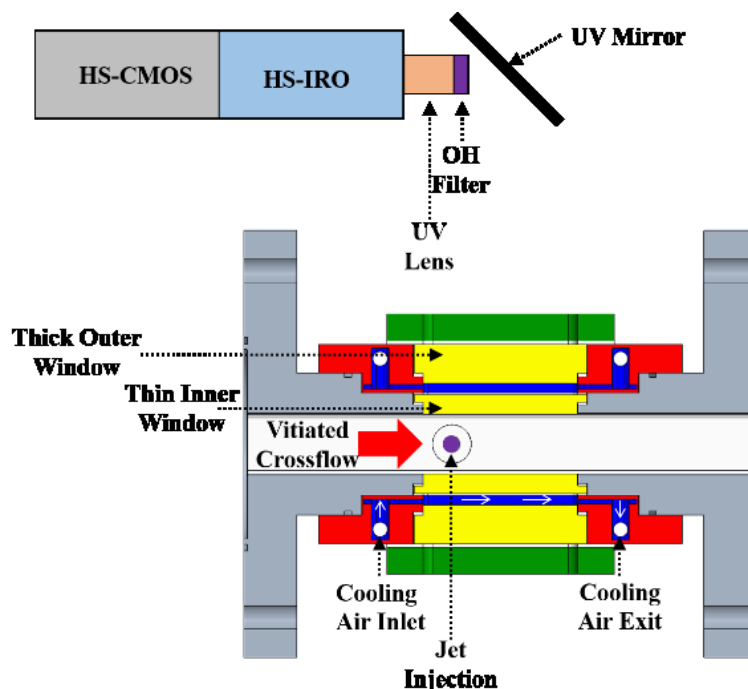
Figure 6.3: Schematic of the windowed secondary combustion zone with the camera systems.

OH*-chemiluminescence images were obtained in an identical manner to the PLIF images, with the exception of increasing the intensified camera gate to 1 µs. The laser and camera systems were installed to allow fast, remotely-controlled switching between the PLIF and OH*-chemiluminescence measurements.

Although two custom AFRL filters were used for the PLIF measurements, significant laser scatter was indeed observed due to the high-scatter environment within our combustor. It should be noticed that the laser sheet was configured to hit the bottom wall of the combustor, where the jet from this jet-in-crossflow experiment is injected. The thermal barrier coating that was applied at the bottom wall certainly attenuates the laser scatter. Figure 6.4 illustrates the significant laser scatter present in this experiment based on an average of 100 shots from CH excitation of the $R_1(13)$ line near 310.78 nm. Figure 6.4(a) shows that there is certainly noticeable CH signal towards the leeward side of the jet but also shows the significant levels of laser scatter with counts as high as 300. Figure 6.4(b) shows the non-resonant background image slightly off the $R_1(13)$ excitation. High levels of laser scatter with counts as high as 300 are also observed here, although the CH signal with counts near 330 and higher is clearly not seen in the non-resonant background image. Figure 6.4(c) shows the average CH-PLIF signal after subtraction with the average non-resonant

background. CH-PLIF signal can be observed both at the base of the flame near the injector and also along the trajectory of the jet. There is lack of signal near $x/d_J = 2$ and this is due to the decrease in laser fluence. To compensate for the very poor laser sheet profile, the laser sheet was remotely translated to a total of three different locations, that were separated by 5 mm ($x/d_J \sim$ 0.5).

Due to the high levels of laser scatter present, it is necessary to subtract the average non-resonant background image from the instantaneous PLIF images. This is illustrated in Fig. 6.5 for an instantaneous CH-PLIF image obtained using R(13) excitation. Subtraction of the non-resonant background was observed to significantly help with removing the laser scatter, while maintaining the spatial profile of the CH-PLIF signal. A sequence of data processing steps was also undertaken to lessen the effects of laser scatter and highlight the CH-PLIF signal. The data processing sequence is presented in Fig. 6.6. Following non-resonant background subtraction, a 2 x 2 pixel Wiener filter was applied to reduce the scattering noise. A 2 x 2 pixel binning operation was then performed, which resulted in the image transforming from 1024 x 1024 pixels to 512 x 512 pixels. Although this reduced the digital spatial resolution to about 0.070 mm/pixel, it was judged to improve the overall quality of the image. Finally, a 2 x 2 pixel median filter was applied in order to attenuate the CH-PLIF signal. This data processing sequence was also applied to the OH-PLIF images, as presented in Fig. 6.7. However, due to the relatively higher OH-PLIF signal, the laser scattering appears to be less significant for the OH-PLIF images. The signal-to-noise ratio for the CH-PLIF and OH-PLIF images were estimated by the method outlined in Mitsingas *et al.* (2019). The SNR was estimated to be 2 – 3 for the OH-PLIF and 1.5 – 2 for the CH-PLIF. Although there would be a slight tradeoff due to increased laser scatter, it is believed that increased laser power would provide better SNR.

This work demonstrates CH-PLIF for three different reacting jet in vitiated crossflow flames that correspond to three different jet equivalence ratios: $\phi_J = 1.5, 2.1,$ and 2.7. Average OH*-CL images for these three cases are presented in Fig. 6.8. The OH*-CL images show that the flame position and the flame shape shifts with increasing equivalence ratio. This has been described previously in Chapter 5.
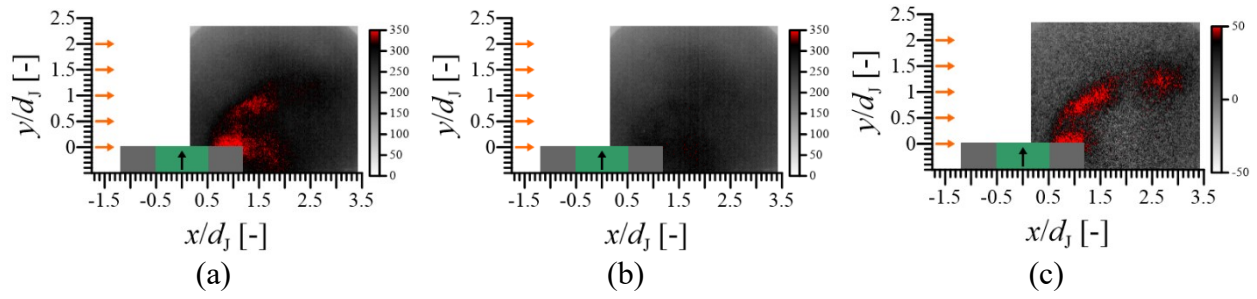
Figure 6.4: Influence of laser scatter on CH-PLIF images using an average of 100 laser shots: (a) raw CH-PLIF, (b) non-resonant background, (c) CH-PLIF after background subtraction.
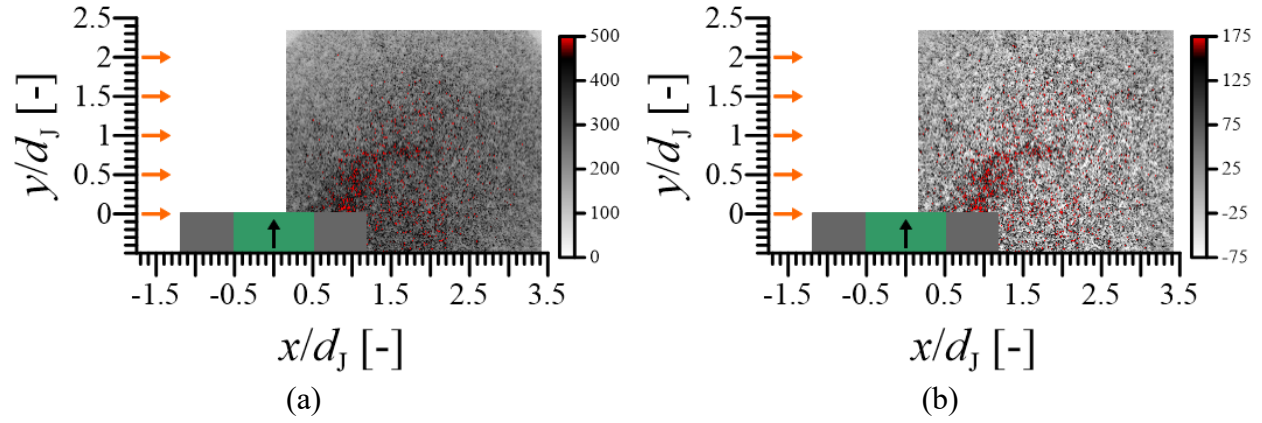
Figure 6.5: Comparison of instantaneous CH-PLIF images: (a) raw image, (b) after average non-resonant background subtraction.

(a)

(b)

(c)

(d)
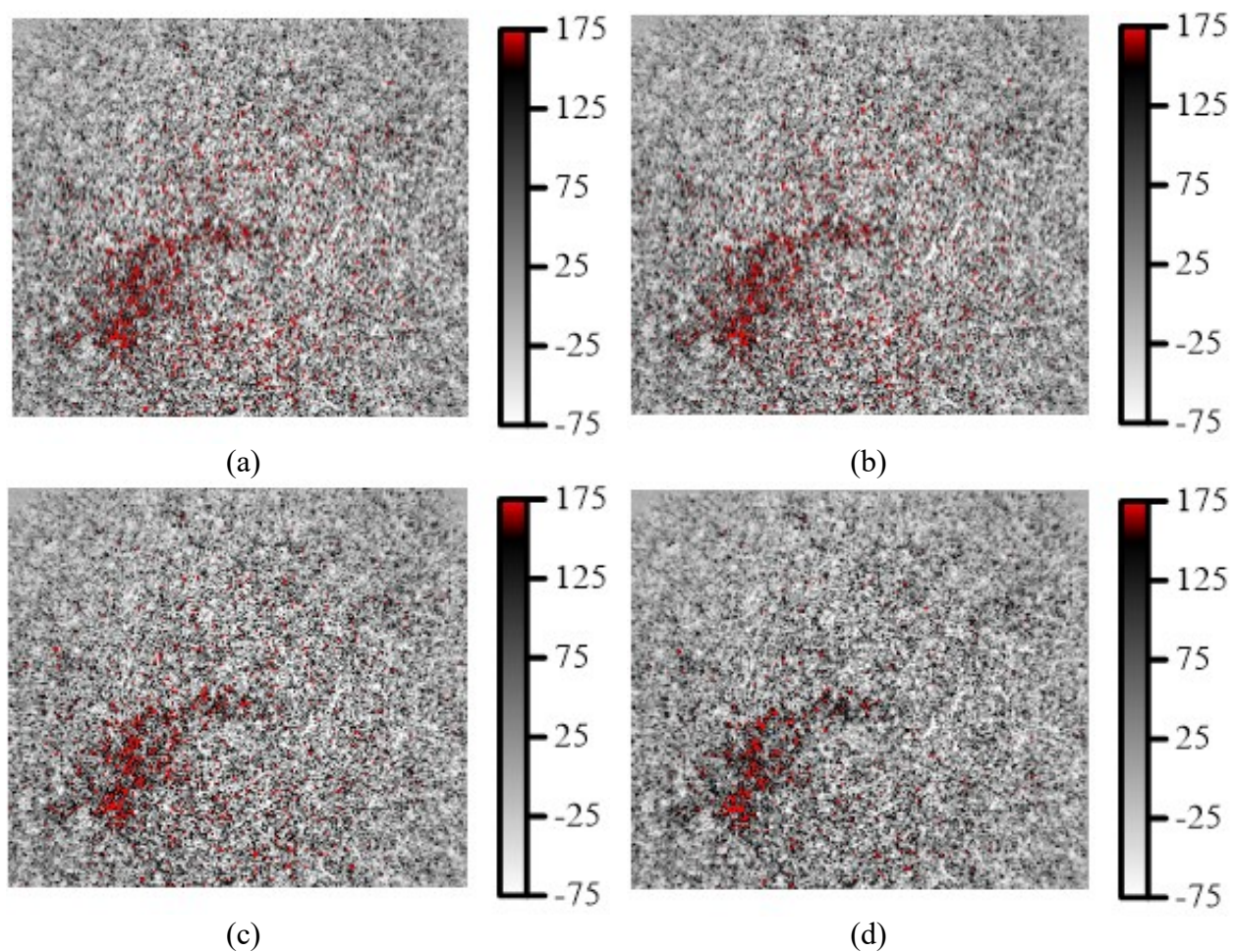
Figure 6.6: CH-PLIF data processing sequence: (a) non-resonant background subtracted, (b) 2 x 2 pixel Wiener filter applied, (c) 2 x 2 pixel binning, (d) 2 x 2 median filter applied.
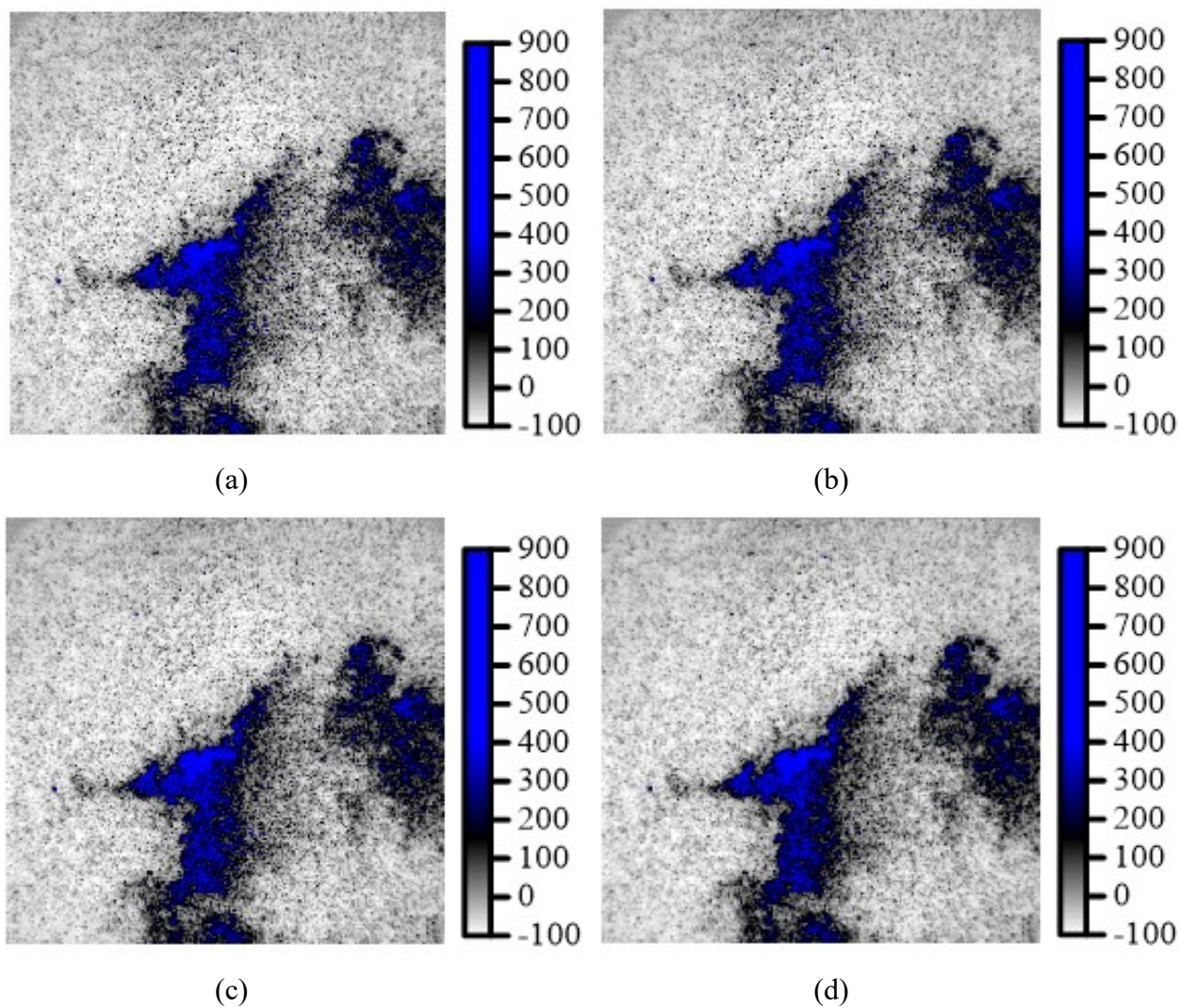
Figure 6.7: OH-PLIF data processing sequence: (a) non-resonant background subtracted, (b) 2 x 2 pixel Wiener filter applied, (c) 2 x 2 pixel binning, (d) 2 x 2 median filter applied.
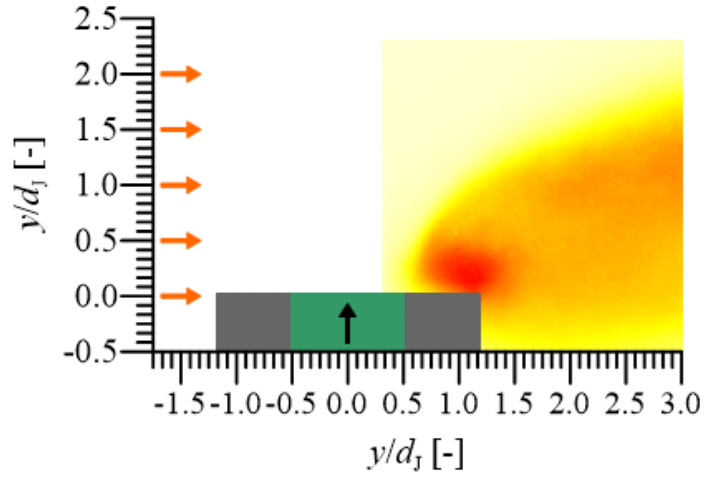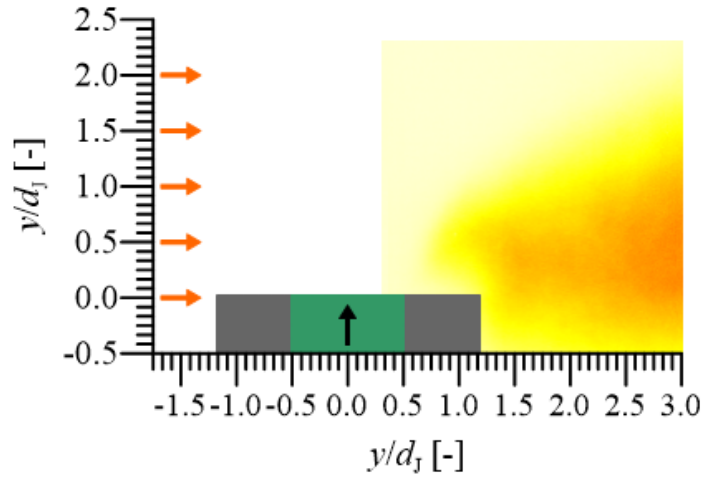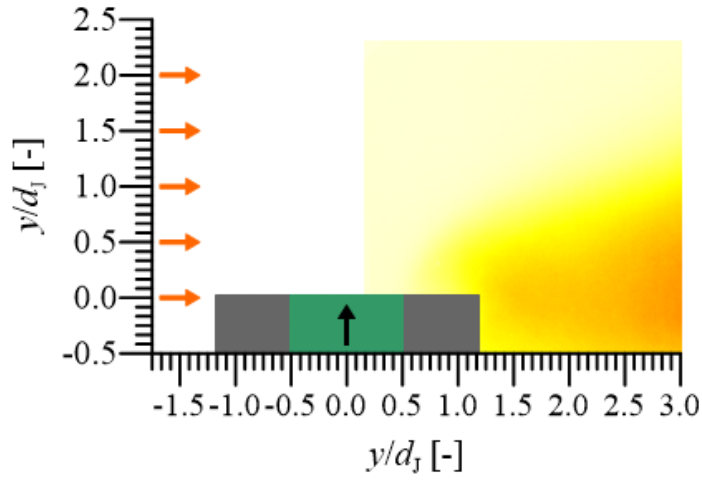
Figure 6.8: Averaged OH*-CL images for three jet-in-crossflow flames:
(a) ϕ_J = 1.5, (b) ϕ_J = 2.1, and (c) ϕ_J = 2.7.

137

6.3 Results and Discussion

6.3.1 Demonstration of CH/OH spectroscopy at rig condition

Figure 6.9 presents the simulated CH and OH spectra between 310.7 and 311.7 nm from LIFBASE for a pressure of 500 kPa, temperature of 2000 K, and velocity of 120 m/s. The rotational lines were corrected for collisional broadening and shift as well as Doppler broadening and shift. The collisional parameters for OH were obtained from a shock-tube study (Davidson *et al.*, 1996) and these are the same collisional parameters as used by Singla *et al.* (2006) for OH-PLIF measurements within a high-pressure rocket combustor. The CH collisional parameters are not available in literature to the best of the author's knowledge. Therefore, the same collisional parameters as those used for OH was also assumed for CH.

Figures 6.10 to 6.15 present instantaneous and average (100 laser shots) fluorescence imaging at six different dye laser wavelengths. Certainly, CH-PLIF is observed at the R(13) excitation in Fig. 6.10 and the R(11) excitation in Fig. 6.13. OH-PLIF is also clearly evident for the $P_2(5)$ excitation in Fig. 6.11 and the $P_1(7)$ excitation in Fig. 6.14. Tuning the dye laser near 311.03 nm to the regions with overlapping CH and OH transitions did not facilitate simultaneous OH and CH detection for this highly turbulent flame. OH fluorescence dominated over the CH fluorescence and it was unclear which signal corresponded to CH and which signal corresponded to OH. The dye laser wavelength was instead tuned to slightly longer wavelengths to maximize
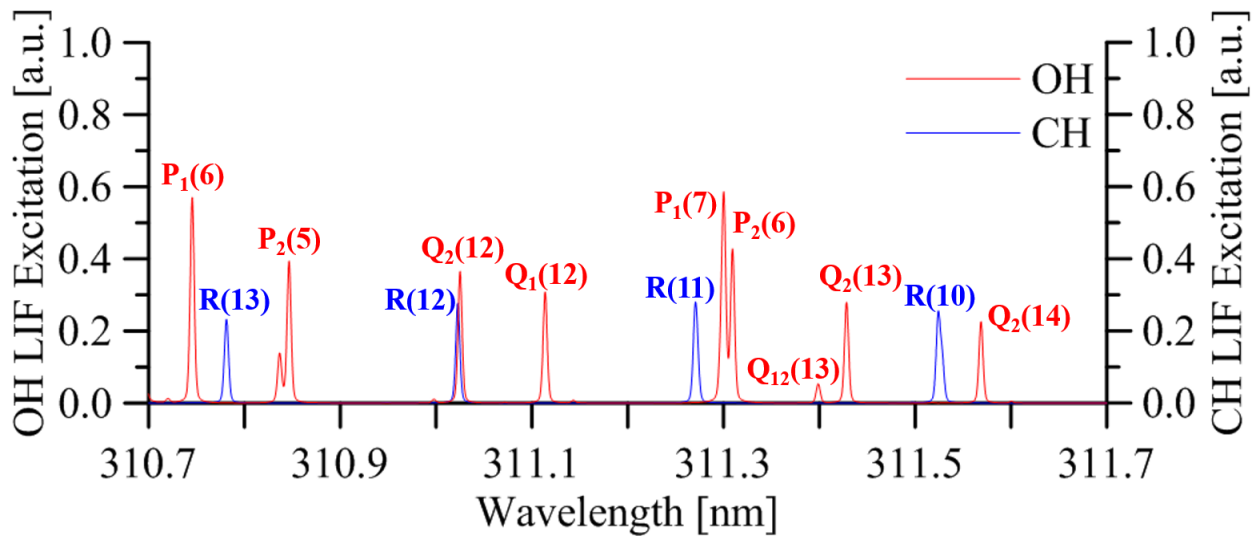
Figure 6.9: Simulated CH and OH spectra from LIFBASE at 500 kPa and 2000 K that was corrected for collisional and Doppler effects.

138
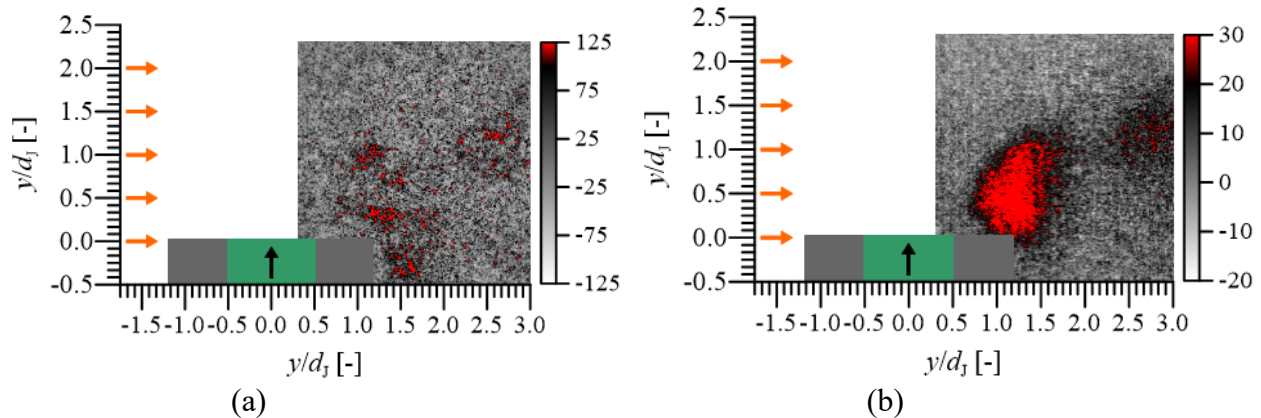
Figure 6.10: CH-PLIF using R(13) excitation near 310.78 nm:
(a) instantaneous image, (b) average image.
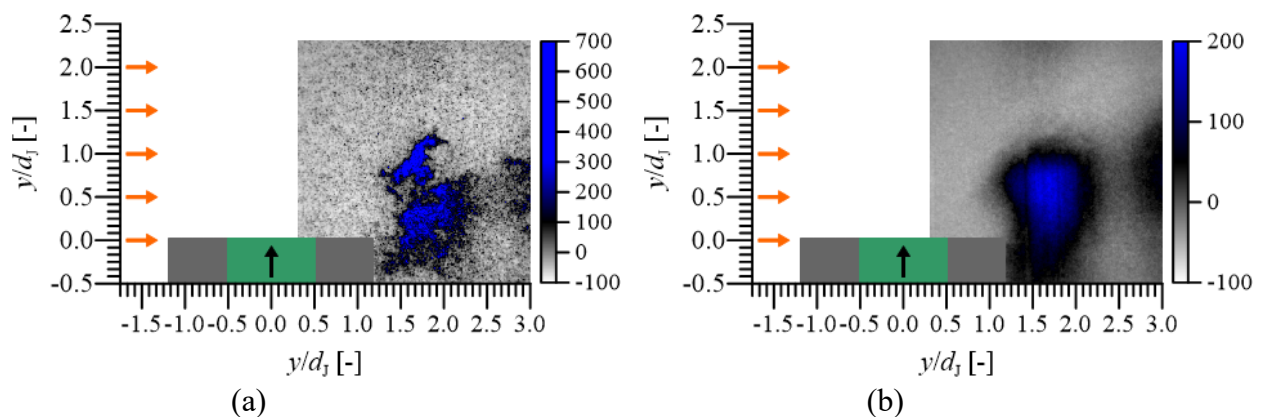
Figure 6.11: OH-PLIF using P$_2$(5) excitation near 310.85 nm:
(a) instantaneous image, (b) average image.
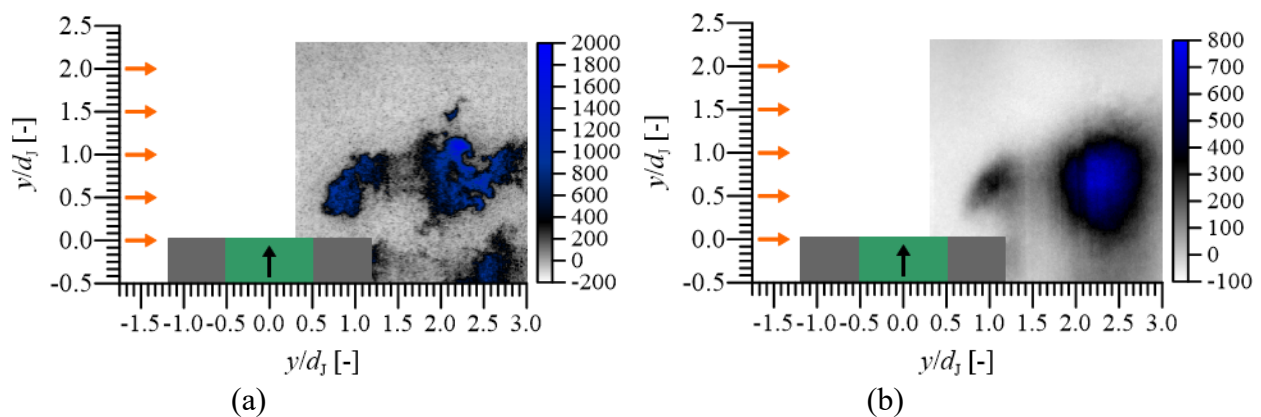
Figure 6.12: OH-PLIF using Q$_2$(12) excitation near 311.03 nm:
(a) instantaneous image, (b) average image.
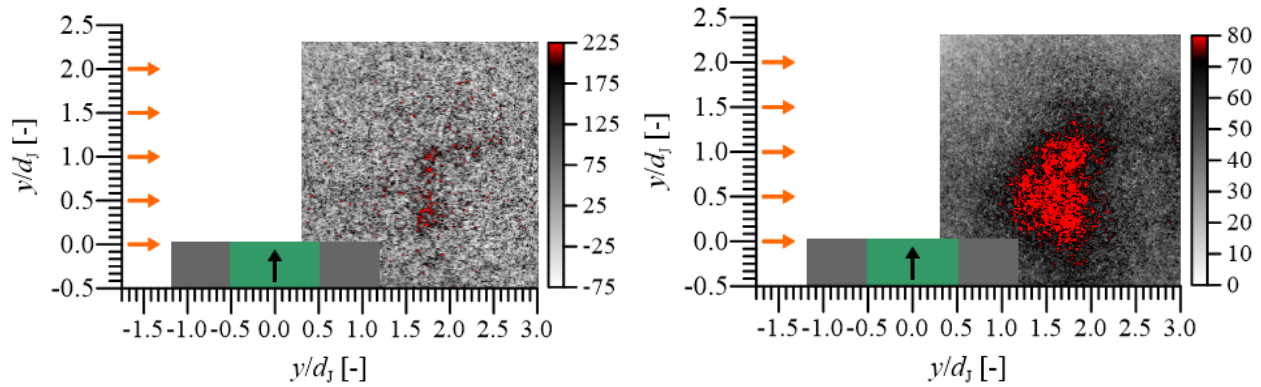
Figure 6.13: CH-PLIF using R(11) excitation near 311.27 nm:
(a) instantaneous image, (b) average image.
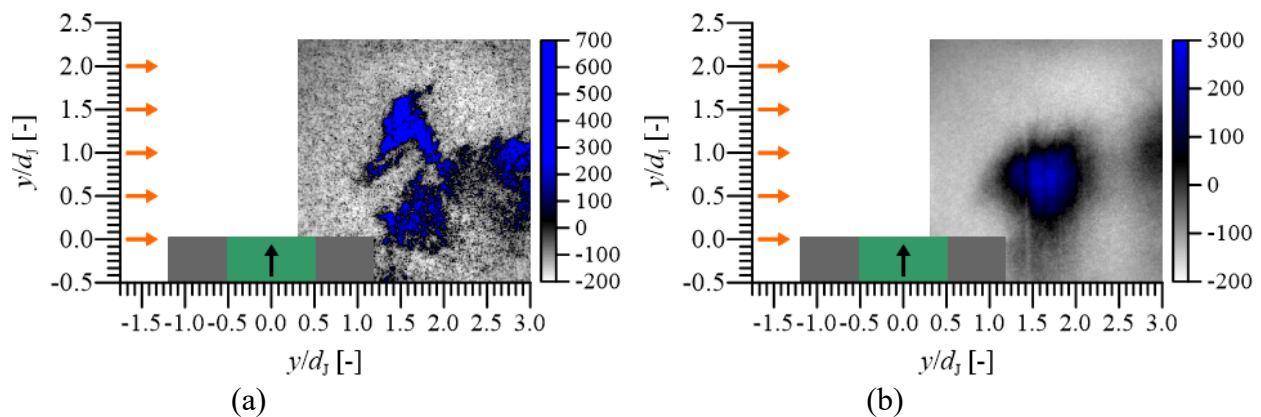
Figure 6.14: OH-PLIF using $P_1(7)$ excitation near 311.30 nm:
(a) instantaneous image, (b) average image.
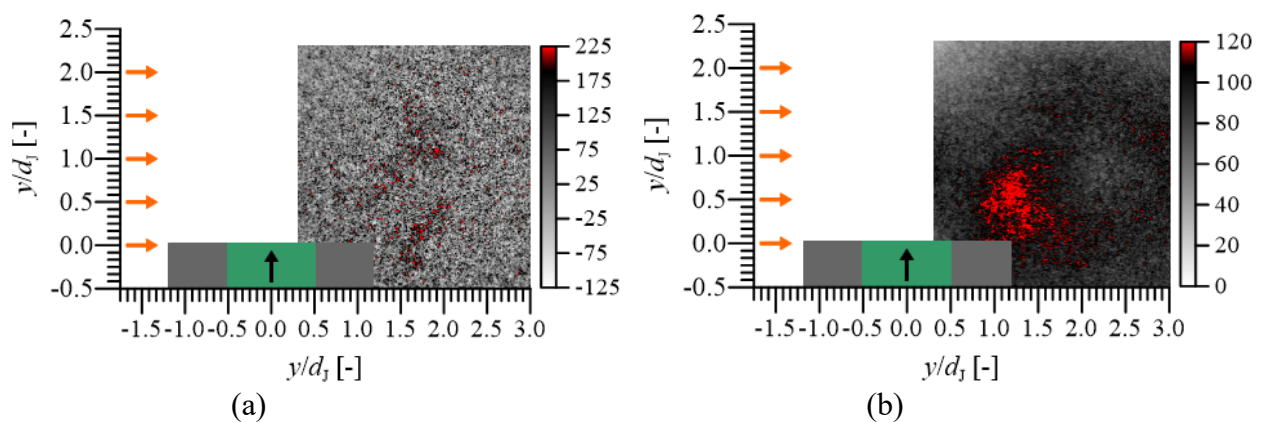
Figure 6.15: CH-PLIF using R(10) excitation near 311.53 nm:
(a) instantaneous image, (b) average image.

the OH signal from the $Q_2(12)$ transition, which is shown in Fig. 6.12. Tuning the dye laser to the R(10) excitation at a longer wavelength of 311.53 nm showed noticeably more scatter compared to the R(11) or R(13) transitions, which indicates approaching the edge of the long-wavelength-pass edge filter. It should be noted that although these wavelengths are within the 0% transmittance region of the filter, scatter from laser light at various angles may still pass through the filter. Finally, it should be noted that the laser sheet for the $Q_2(12)$ excitation appears to be at a different position than the $P_2(5)$ and the $P_1(7)$ laser sheet positions. While changing the laser wavelengths, the frequency-doubling unit in the dye laser was also tuned to ensure near-optical doubling efficiency. Although tuning the BBO crystal also tunes a compensator unit, it is apparent that slight variations between the BBO crystal and the compensator may cause significant changes in the laser sheet position. This is due to the laser beam traveling on the order of 10 meters between the exit of the dye laser and the test section.

6.3.2 Comparison of jet-in-crossflow flames

Instantaneous CH-PLIF images at the R(13) excitation and OH-PLIF images at the $P_2(5)$ excitation were obtained at three different equivalence ratios and at a 1 kHz repetition rate. The laser sheet for these images were traversed by 5 mm increments in the x/d_J direction ($x/d_J \sim$ 0.5) and the instantaneous images were cropped to show regions of sufficient laser fluence. Comparing the OH-PLIF images in Figs. 6.16(a), 6.17(a), and 6.18(a) shows features that agree in trend with the averages OH*-CL images in Fig. 6.8. The flame is positioned closer to the orifice exit for less rich conditions ($\phi_J = 1.5$) and moves away from the orifice exit and in the wake of the elevated nozzle with increasingly richer equivalence ratios ($\phi_J = 2.1$ and 2.7).

The CH-PLIF images show the reactions immediately downstream of jet injection for the $\phi_J = 1.5$ case. CH signal is also seen here in the shear layer that interacts with the crossflow. This seems to indicate that near-stoichiometric regions are present at these locations, likely due to significant mixing with the crossflow in these regions. The OH*-CL images also seems to indicate regions of peak heat-release at these regions. As the flame position moves towards the wake of the elevated injector at $\phi_J = 2.1$ and 2.7, significant mixing with the vitiated crossflow is believed to occur just downstream of the elevated injector in the wake region of the elevated nozzle. For these conditions, CH signal is visible both in the top shear layer where the jet interacts with the crossflow

and in the bottom shear layer where reactions are occurring. It should also be pointed out that the broken CH reactions seen in this experiment are similar to the heated air, high-velocity crossflow reactions observed by Micka *et al.* (2012) using B-X excitation of CH.

(a)   (b)
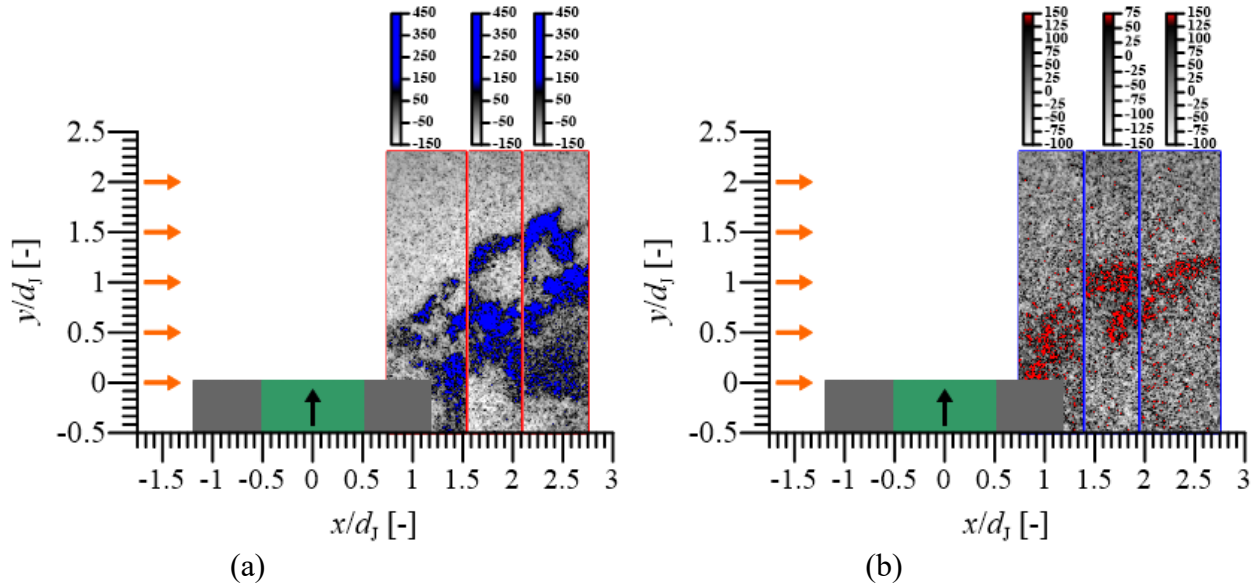
Figure 6.16: Jet-in-crossflow flame at $\phi_J = 1.4$:
(a) OH-PLIF with $P_2(5)$ excitation, (b) CH-PLIF with R(13) excitation.

(a)   (b)
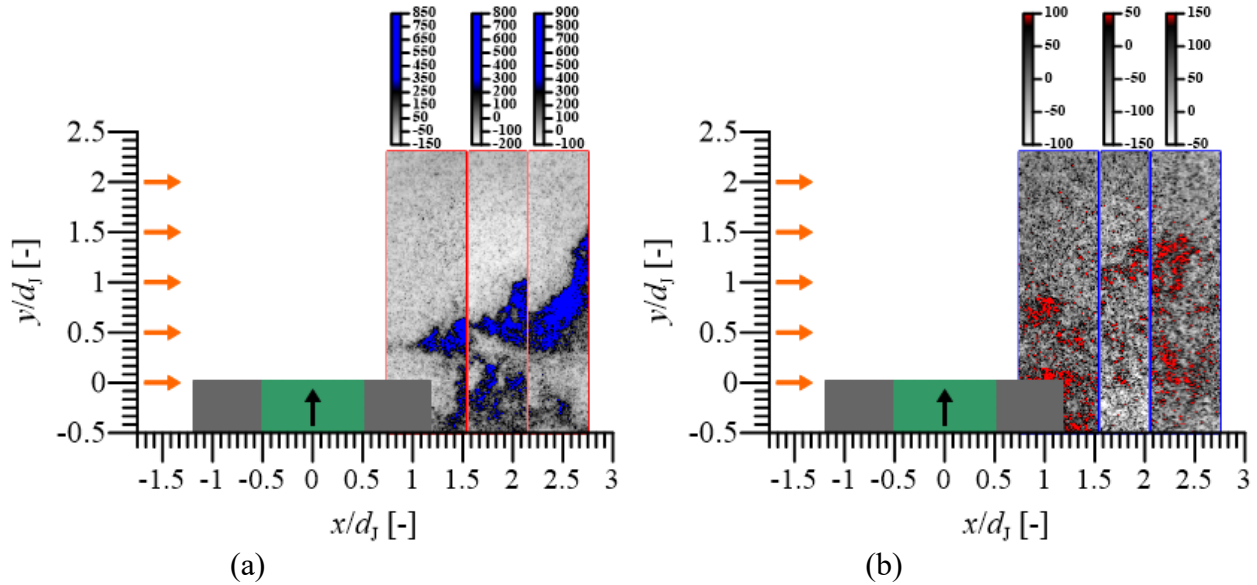
Figure 6.17: Jet-in-crossflow flame at $\phi_J = 2.1$:
(a) OH-PLIF with $P_2(5)$ excitation, (b) CH-PLIF with R(13) excitation.
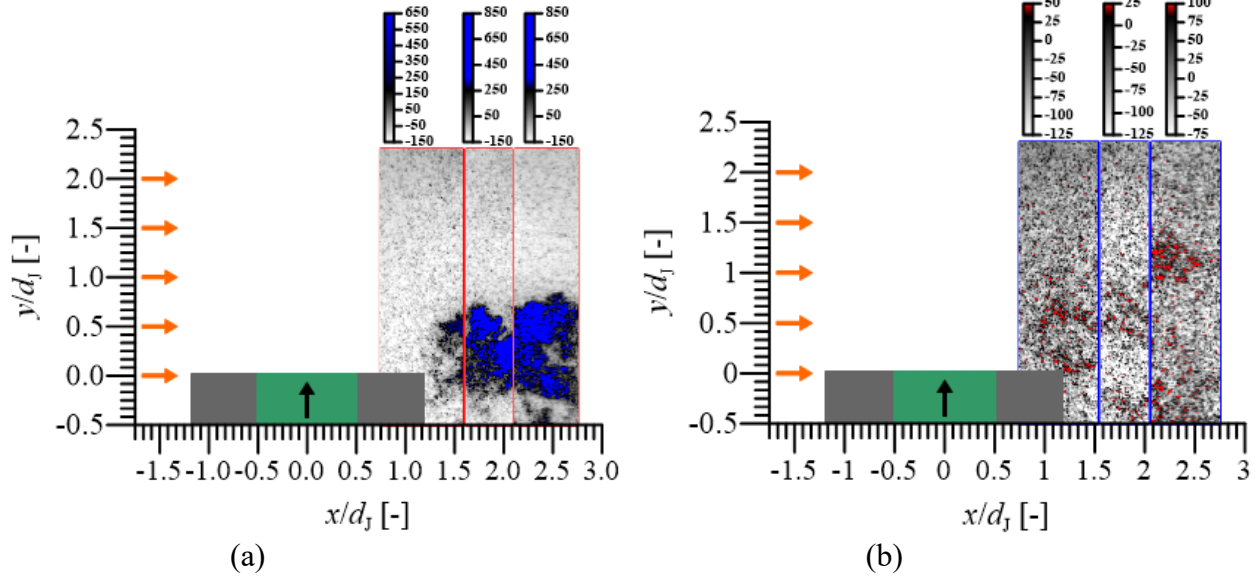
Figure 6.18: Jet-in-crossflow flame at $\phi_J = 2.7$:
(a) OH-PLIF with $P_2(5)$ excitation, (b) CH-PLIF with $R(13)$ excitation.

Turbulent premixed combustion regimes have been delineated in the existing literature and are summarized in a recent review paper by Driscoll *et al.* (2020). These regimes are determined using a ratio of velocity fluctuation (u') to the laminar flame speed (S_L) and the ratio of an integral length scale (L) to the calculated flame thickness based on the Peters correlation ($\delta_{L,P}$). Correlations were used for the velocity fluctuation and this was determined to be 14% of the crossflow velocity. The integral length scale was assumed to be 33% of the jet diameter. Using the composition at the jet exit, the ratio of u'/S_L was determined to be between $80 - 330$ and the ratio of $L/\delta_{L,P}$ was determined to be between $7 - 29$ for the conditions in this chapter. This is believed to lie within the *broken reactions* regime. Using a stoichiometric jet composition based on mixing with the crossflow, u'/S_L was determined to be between $16 - 26$ and the ratio of $L/\delta_{L,P}$ was determined to be between $90 - 140$. These would fall within the *broadened preheat* regime, which neighbors the *broken reactions* regime. This indicates that although a definite conclusion cannot be drawn without velocity measurements, there is at least reason to suspect that the levels of turbulence is so high that broken reactions are not out of the question.

6.4 Summary and Conclusions

CH-PLIF using R-branch excitation in the C-X electronic system is demonstrated in this work at high repetition rates and at realistic gas turbine conditions within a staged model combustor. Although two custom AFRL filters were used, there is a noticeable amount of laser scatter in the CH-PLIF images due to scatter of laser light at various angles passing through the filter. Certainly, increasing the laser energy while remaining in the CH C-X linear LIF regime would help with increasing the CH signal at the cost of slightly increased scattering levels. Scattering effects were not as apparent for the OH-PLIF due to the increased signal levels. An image processing procedure was developed to lessen the effects of scatter: non-resonant background subtraction, 2 x 2 pixel Wiener filter, 2 x 2 pixel binning, and a 2 x 2 median filter. These helped lessen the influence of the background scatter. Measurements were obtained at three different CH and three different OH transitions by tuning the dye laser at steady-state rig conditions. Indeed, higher levels of scatter were observed for R(10) compared to R(13). Using the R(13) excitation at three different reacting jet conditions showed regions of peak CH signal near regions of peak average OH*-CL intensity. However, the CH-PLIF images showed evidence of broken, thickened, non-premixed layers similar to the previous jet-in-crossflow work by Micka *et al.* (2012).

7. SUMMARY AND CONCLUSIONS

This Ph.D. dissertation is a compilation of five distinct but closely related research efforts, that have been separated into Chapter 2 – 6:

2. Development of a perforated plate burner to produce the vitiated crossflow with negligible swirl that is desirable for reacting jet in vitiated crossflow experiments.

3. NO_X reduction within an axially staged gas turbine model combustor through increasing the exit Mach number.

4. Development of an optically-accessible secondary combustion zone for the use of laser and optical techniques to characterize the reacting jet in crossflow.

5. The application of OH*-chemiluminescence and OH-PLIF for the reacting jet in a high-speed crossflow to characterize flame shape and flame structure.

6. The demonstration of CH-PLIF using R-branch excitation in the C-X electronic system within a 1 MW gas turbine model combustor.

Each of these chapters have their own detailed summary and conclusions and therefore only a few brief summary points and conclusions are highlighted here:

- The key challenge of designing the PPB was that the velocity of the premixed natural gas and air mixture through the holes needed to be low enough for the stabilization of a flame on the downstream surface of the plate, but high enough so that flashback did not occur.

- Features incorporated into the design for flashback mitigation included a flame arrestor plate, several red-line aborts in the operating software, and a burst-disc installed in the plenum upstream of the PPB. A laser ignition system utilizing a hydrogen pilot flame was also designed for the PPB ignition.

- Very good performance of the PPB was observed during testing at engine-relevant conditions. The ignition process using a combination of the laser ignition and a hydrogen diffusion flame pilot was successful.

- A PPB stability diagram was developed as a function of the NG-air equivalence ratio and the PPB hole velocity. The operational range of the PPB was found to be somewhat

restricted in terms of the premixed gas equivalence ratio, but the burner was operated very successfully within this range.

- The motivation behind development of the PPB for engine-relevant operation was to use it as the source of vitiated crossflow with negligible swirl for reacting jet in vitiated crossflow experiments. This was demonstrated through the transverse injection of premixed natural gas and air in an axially staged combustor configuration. The vitiated crossflow from the PPB was demonstrated to successfully auto-ignite the axial stage premixed jet.

- Since the PPB effectively produces vitiated crossflow without the swirling component and thereby allows for easier comparison with numerical simulations, tremendously valuable data sets can be acquired from this experiment.

- The impact of higher exit Mach numbers and lower axial residence times for reduction in NO_X produced by the axial stage was very clear. This reduction in NO_X is hypothesized to be due not only to the reduced axial residence time, which results in lower thermal NO_X production, but also to the reduced static temperature and potentially better mixing of the jet with the vitiated crossflow (referred to in this work as the *Mach number effect*).

- At a constant residence time $\tau_{AX} = 1.4$ ms, the NO_X produced from the axial stage showed a strong decrease with higher exit Mach numbers for conditions corresponding to a range of axial equivalence ratios. This effect was observed to be strongest (60 – 70% reduction) at the highest adiabatic exit total temperatures: $T_{0,EX} = 1900$ K for $S_{AX} = 6.4\%$ and $T_{0,EX} = 2020$ K for $S_{AX} = 20.7\%$. The reduction in NO_X emissions through an increase in the Mach number has not been previously reported in literature to the best of our knowledge.

- The effect of axial residence time (1 – 2.3 ms) on ΔNO_X produced by the two air splits at a constant $Ma_{EX} = 0.45$ was also investigated. The axial residence time was observed to have a stronger effect at conditions with staged combustor exit adiabatic total temperatures $T_{0,EX} > 1900$ K, likely due to the increased thermal NO_X production at higher temperatures. An increase in NO_X due to longer residence times as observed in this work agrees with established trends in the literature.

- An optically-accessible test section was developed to experimentally study reacting jets into a vitiated crossflow with negligible swirl at conditions corresponding to elevated inlet

146

- temperatures of 500 – 600 K, elevated combustor pressure of 500 kPa, and exit Mach numbers up to 0.7.

- Key design features for the new optically-accessible secondary combustion zone include a double-windowed design, a unique air-cooling scheme using forced convection of air in-between the inner and outer windows, and carefully designed water-cooling circuits to cool the metal hardware.

- The optically-accessible secondary combustion zone is ideally suited to investigate features of the reacting jet in vitiated crossflow. Successful operation has been demonstrated here with chemiluminescence imaging.

- Using the newly developed optically-accessible secondary combustion zone, the stabilization mechanisms for a reacting jet was investigated and the crossflow velocity was observed to have a strong impact on the stabilization of the premixed NG-air flame.

- At the crossflow speed corresponding to $Ma_\infty = 0.15$ (~120 m/s), a minimum ϕ_J near 1.4 was needed to stabilize the flame near the injector. This is likely due to rapid mixing of the jet with the crossflow; such that once auto ignition occurs, the local flame speed cannot maintain a flame in the highly turbulent wake region. However, reactants are still believed to be consumed downstream of the optical access.

- 50 kHz OH*-CL shows that as ϕ_J approaches 1.4, the flame kernel in the wake of the elevated injector begins to grow. A separate flame kernel develops on the leeward side of the jet. These two kernels merge to create a stabilized reacting jet-in-crossflow flame near the leeward side of the jet. Flame stabilization near the injector is marked with a significant increase in ΔNO_X emissions, compared to the downstream reaction.

- Based on averaged OH*-CL, the flame position shifts with increasing jet equivalence ratios from 1.5 to 2.8, both near the injector and several diameters downstream. Increased liftoff distance may be due to the flame stabilizing at locations corresponding to maximum flame speed (increased pre-flame mixing for richer jets). The downstream shift near the wall may be due to reactions occurring in the wake of the elevated injector rather than the leeward side of the jet.

- OH-PLIF images taken at $4 < x/d_J < 6$ shows that the flame at $\phi_J = 1.5$ has significantly more interactions with the crossflow at the bottom of the jet compared to the $\phi_J = 2.5$

flame. The greater post-flame mixing for the ϕ_J = 1.5 flame is believed to be a contributing factor towards lower ΔNO_X emissions at this condition, compared to the ϕ_J = 2.5 flame.

- Stabilization of the flame, as indicated by the 10 kHz OH*-chemiluminescence imaging, was not observed within our viewing region for higher crossflow Mach numbers. Hydrogen was blended into the natural gas to reduce the chemical time scale. Minimum levels of hydrogen concentration for stabilization near the injector are reported for two different higher crossflow Mach numbers based on the jet equivalence ratio.

- CH-PLIF using R-branch excitation in the C-X electronic system is demonstrated in this work at high repetition rates and at realistic gas turbine conditions within the staged model combustor. Although two custom AFRL filters were used, there is a noticeable amount of laser scatter in the CH-PLIF images due to scatter of laser light at various angles passing through the filter.

- An image processing procedure was developed to lessen the effects of scatter: non-resonant background subtraction, 2 x 2 pixel Wiener filter, 2 x 2 pixel binning, and a 2 x 2 median filter. These helped lessen the influence of the background scatter.

- Measurements were obtained at three different CH and three different OH transitions by tuning the dye laser at a steady-state rig condition. Indeed, higher levels of scatter were observed for R(10) compared to R(13). Using the R(13) excitation at three different reacting jet conditions showed regions of peak CH signal near regions of peak average OH*-CL intensity. However, the CH-PLIF images showed evidence of broken, thickened, non-premixed layers similar to the previous jet-in-crossflow work by Micka *et al.* (2012).

There is probably several careers worth of future work and certainly dozens of future Ph.D. dissertations that would help towards further understanding this reacting jet in a high-speed crossflow problem. Financial support for the research is the main limiting factor towards its completion as laser technology is already available and diagnostics theory has been developed in the literature. Funding was a strain throughout this research program as well, mainly due to the high cost of hardware that can survive engine-relevant conditions and limited research budgets.

Three of the biggest adverse outcomes to this dissertation from the financial strains were:

- Not having optical access from the beginning of the rig commissioning. Design work for this project began in earnest in October 2016 and rig commissioning work was in full-swing by October 2017 with the first-fire of the perforated plate burner. Design for optical access only began in October 2018 and design efforts were delayed due to continued emissions testing. Commissioning of optical access only began in September 2019 and all of the chemiluminescence and PLIF data for this dissertation was acquired in the months of October 2019 to January 2020. In my opinion, more insights were gained towards understanding the physics of this problem in these 4 months than the previous two years of testing.

- The financial constraints on the optical-access fabrication was significant and multiple rounds of design iterations were required to meet the budget. Most significantly, the design was altered from originally providing 250 cm of optical access in the axial direction to only providing 100 cm due to financial constraints. With the flame residing well downstream of the jet injector for many conditions, this has significantly affected the outcome of this dissertation.

- More time and budget for the PLIF measurements would have helped tremendously, especially for the CH-PLIF measurements. The CH-PLIF measurements were obtained with very low laser power. In addition, because OH-PLIF measurements only began in month 38 (!) of this Ph.D. research, due to lack of optical access, developing certain experimental strategies such as adequately correcting for the laser sheet profile was not possible in the limited timeframe. More test days with the OH-PLIF would also have resulted in near-injector measurements.

7.1   Proposed future work

Several research areas would build upon the work in this dissertation. Some of these have been detailed in contributions towards an NSF proposal that is pending submission. The future work on a variety of topics is very briefly outlined below:

- Perforated plate burner at engine-relevant conditions:
  - Fundamental studies of ignition, flashback, and blow-off for premixed flames.
  - Source of vitiated flow with negligible swirl for jet-in-coflow experiments.
- Complementary computational investigations:

- Development of a simplified chemical kinetics model to compare experimental results with numerical predictions. This model would also be used to compare different reaction mechanisms including GRI-Mech 3.0, San Diego, and Glarborg.
- Comparing the experimental and numerical results with different physically-inspired parameters involving the activation energy of the $O+N_2 \rightarrow NO+N$ reaction.
- Simulation of the reacting jet in high-speed vitiated crossflow using LES.

- Reacting jet-in-crossflow work involving laser-diagnostics:
  - Obtaining 5-10 kHz OH-PLIF measurements at near 283 nm and very close to the elevated injector; this is sorely missing from Chapter 5.
  - Comparison of measurements with a flush and elevated injector.
  - Analysis of the 50 kHz OH*-CL for jet dynamics using techniques such as POD or DMD.
  - CH_2O PLIF to image the pre-heat zone before OH formation.
  - Tracer PLIF diagnostics to study mixing effects in this partially-premixed configuration. The crossflow (vitiated or heated air) could be seeded with NO and the reacting or non-reacting jet could be seeded with acetone.
  - PIV to characterize the velocity fields.
  - Pure-rotational, two-beam CARS to obtain temperature measurements and relate these to the NO_X emissions reductions. Dual-pump CARS could also be used for temperature and species concentration measurements.
  - Burst-mode PLIF and PIV to obtain time-resolved measurements.

- CH-PLIF C-X diagnostics:
  - Development and application of CH-PLIF in the C-X electronic system using high-power CW lasers. CW-PLIF of OH was demonstrated in a recent paper from Stanford and due to the lower saturation LIF threshold for C-X CH compared to A-X OH, this may be a promising option for CH diagnostics.

APPENDIX

NATURAL GAS COMPOSITION

Facility natural gas delivered to the Zucrow Laboratories at Purdue University was used as the fuel for the work presented in this Dissertation. Since the composition of natural gas varies slightly on a day-to-day basis, an average mole fraction over a period of several months was used for the key constituents in order to determine properties such as molecular weight. Table A1 presents the mole fraction of the key constituents: methane (CH_4), ethane (C_2H_6), propane (C_3H_8), nitrogen (N_2), and carbon dioxide (CO_2). Air was used as the oxidizer for this experiment and the mole fraction for its key constituents were taken as: 20.95% oxygen (O_2), 78.08% nitrogen (N_2), 0.93% argon (Ar), and 0.04% carbon dioxide (CO_2). The molecular weight for natural gas and air mixtures were calculated to be 17.13 kg/kmol and 28.97 kg/kmol respectively. The stoichiometric air-to-fuel ratio for this composition of natural gas and air was calculated to be $\left(A / F \right)_S = 16.8$ using a specie balance.

Table A1: Key constituents of natural gas composition used for this experiment.

Molecule	Mole Fraction [%]
Methane	92.66
Ethane	6.12
Propane	0.27
Nitrogen	0.72
Carbon Dioxide	0.23

REFERENCES

Ahrens, D., Kolb, M., Hirsch, C., and Sattelmayer, "NOx formation in a reacting premixed jet in hot cross flow," *Proceedings of ASME Turbo Expo*, Dusseldorf, Germany, 2014.

Ahrens, D., Kolb, M., Hirch, C., Sattelmayer, T., "Influence of preflame and postflame mixing on NOx formation in a reacting premixed jet in hot cross flow", *Journal of Engineering for Gas Turbines and Power*, Vol. 138, 2016, pp. 1-10.

Chan, W.L., Kolla, H., Chen, J.H., Ihme, M., "Assessment of model assumptions and budget terms of the unsteady flamlet equations for a turbulent reacting jet-in-crossflow," *Combustion and Flame*, Vol. 161, 2014, pp. 2601-2613.

ARP1433, "Procedure for the Analysis and Evaluation of Gaseous Emissions from Aircraft Engines, *SAE International*, 2016.

Cabra, R., "Turbulent Jet Flames Into a Vitiated Coflow," Ph.D. Dissertation, Univ. California, Berkley, CA, 2004.

Canny, J., "A computational approach to edge detection, IEEE Transactions on Pattern Analysis and Machine Intelligence," Vol. 8(6), 1986, pp. 679-698.

Carter, C.D., Hammack, S., and Lee, T., "High-speed planar laser-induced fluorescence of the CH radical using the $C^2\Sigma^+–X^2\Pi(0,0)$ band," *Applied Physics B*, Vol. 116, 2014, pp. 515-519.

Carter, C.D., Hammack, S., and Lee, T., "High-speed flamefront imaging in premixed turbulent flames using planar laser-induced fluorescence of the CH C-X band," *Combustion and Flame*, Vol. 168, 2016, pp. 66-74.

Chemkin-Pro 18.1, ANSYS, Inc.: San Diego, 2017.

Cooper, C. and Alley, F., *Air Pollution Control: A Design Approach*, 3rd ed., Waveland Press, Long Grove, IL, 2002.

Davitian, J., Getsinger, D., Hendrickson, C., Karagozian, A.R., "Transition to global instability in transverse-jet shear layers," *Journal of Fluid Mechanics*, Vol. 661, 2010, pp. 294-315.

Driscoll, J.F., Chen, J.H., Skiba, A.W., Carter, C.D., Hawkes, E.R., Wang H., "Premixed flames subjected to extreme turbulence: some questions and recent answers," *Progress in Energy and Combustion Science*, Vol. 76, 2020, pp. 100802 1-36.

Dayton, J.W., Linevitch Jr., K., Cetegen, B.M., "Ignition and flame stabilization of a premixed reacting jet in vitiated crossflow", Proceedings of the Combustion Institute, Vol. 36, 2019, pp. 2417-2424.

El-Asrag, H.A., Pitsch, H., Kim, W., Do H., Mungal, G., "Damkohler number similarity for static flame stability in gaseous-fueled augmentor flows", *Combustion Science and Technology*, Vol. 183, 2011, pp. 718–737.

Elkady, A. M., Kalitan, D. M., Herbon, J., Leonard, G., Akula, R., Karim, H., and Hadley M., "Gas Turbine Emission Characteristics in Perfectly Premixed Combustion," *Proceedings of ASME Turbo Expo*, Vancouver, British Columbia, Canada, 2011.

Fleck, J.M., Griebel, P., Steinberg, A.M., Arndt, C.M., Aigner, M., "Auto-ignition and flame stabilization of hydrogen/natural gas/nitrogen jets in a vitiated cross-flow at elevated pressure", *International Journal of Hydrogen Energy*, Vol. 38, 2013, pp. 16441-16452.

Fleck, J.M., Griebel, P., Steinberg, A.M., Arndt, C.M., Naumann, C., Aigner, M., "Autoignition of hydrogen/nitrogen jets in vitiated air at different pressures", *Proceedings of the Combusion Institute*, Vol. 34, 2013, pp. 3185- 3192.

Glarborg , P., Miller, J.A., Ruscic, B., Klippenstein, S.J., "Modeling nitrogen chemistry in combustion," *Progress in Energy and Combustion Science*, Vol. 67, 2018, pp. 31-68.

Glassman, I., *Combustion*, 3rd ed., Academic Press, New York, 1996.

Goh, E., Sirignano, M., Li J., Nair, V., Emerson, B., Lieuwen, T., Seitzman, J., "Prediction of minimum achievable NOx levels for fuel-staged combustors", *Combustion and Flame*, Vol. 200, 2019, pp. 276-285.

Grout, R.W., Gruber, A., Yoo, C.S., Chen, J.H., "Direct numerical simulation of flame stabilization downstream of a transverse fuel jet in cross-flow," *Proceedings of the Combustion Institute*, Vol. 33, 2011, pp. 1629-1637.

Johnson, M. R., Littlejohn, D., Nazeer, W. A., Smith K. O., and Cheng, R. K., "A comparison of the flowfields and emissions of high-swirl injectors and low-swirl injectors for lean premixed gas turbines," *Proceedings of the Combustion Institute*, Vol. 30, 2015, pp. 2867-2874.

Hammack, S.D., Skiba, A.W., Lee, T., Carter, C.D., "CH PLIF and PIV implementation using C-X (0,0) and intra-vibrational band filtered detection," *Applied Physics B*, Vol. 124, pp. 34 – 38.

Han, D., "The effects of carbon dioxide addition on turbulent premixed flames", Ph.D. Dissertation, Purdue University, West Lafayette, IN, 2017.

Heister, S.D. and Karagozian, A.R., "Vortex modeling of gaseous jets in a compressible crossflow", *Journal of Propulsion and Power*, Vol. 6(1), 1990, pp. 85-92.

Humble, R.W., Henry, G.N., Larson, W.J., *Space Propulsion Analysis and Design*, McGraw-Hill, New York. 1995.

Karagozian, A.R., "Transverse jets and their control," *Progress in Energy and Combustion Science*, Vol. 36, 2010, pp. 531–553.

Karagozian, A.R., "The jet in crossflow," *Physics of Fluids*, Vol. 26, 2014, pp. 1-17.

Kolb, M., Ahrens, D., Hirch, C., Sattelmayer, T., "A model for predicting the lift-off height of premixed jets in vitiated cross flow", *Journal of Engineering for Gas Turbines and Power*, Vol. 138, 2016, pp. 1-9.

Kolla H., Grout R.W., Gruber, A., Chen, J.H., "Mechanisms of flame stabilization and blowout in a reacting turbulent hydrogen jet in cross-flow," *Combustion and Flame*, Vol. 159, 2012, pp. 2755-2766.

Lamont, W.G., Roa, M., Meyer, S.E., and Lucht, R.P., "Emission measurements and CH* chemiluminescence of a staged combustion rig for stationary gas turbine applications, *Journal of Engineering for Gas Turbines and Power*, Vol. 134, 2012.

Lamont, W.G., Satija, A., Roa, M., and Lucht, R.P., "Dual-pump CARS temperature and H2/N2 measurements and a new system for simultaneous vibrational and pure rotational CARS measurements," *51st AIAA Aerospace Sciences Meeting*, AIAA, Grapevine, TX, 2013

Lefebvre, A.H. and Ballal, D.R., *Gas Turbine Combustion: Alternative Fuels and Emissions*, 3rd ed., Taylor & Francis Group, Boca Raton, 2010.

Lemmon, E. W., Huber, M. L., McLinden, M. O., "NIST Standard Reference Database 23: Reference Fluid Thermodynamic and Transport Properties-REFPROP, Version 9.1", *National Institute of Standards and Technology, Standard Reference Data Program*, Gaithersburg, 2013.

Leonard, G., Stegmaier, J., "Development of an Aeroderivative Gas Turbine Dry Low Emissions Combustion System," *Proceedings of ASME International Gas Turbine and Aeroengine Congress and Exposition*, Cincinnati, OH, 1993.

Lieuwen, T., McDonell, V., Peterson, E., Santavicca, D., "Fuel flexibility influences on premixed combustor blowout, flashback, autoignition, and stability," *Journal of Engineering for Gas Turbines and Power*, Vol. 130, 2008, pp. 1-10.

Lieuwen, T.C., Yang, V., *Gas Turbine Combustion*, Cambridge University Press, New York, U.S.A., 2013.

Lyra, S., Wilde, S., Kolla, H., Seitzman, J.M., Lieuwen, T.C., Chen, J.H., "Structure of hydrogen-rich transverse jets in a vitiated turbulent flow," *Combustion and Flame,* Vol. 162, 2015, pp. 1234-1248.

Megerian, S., Davitian, J., de B. Alves, L.S., Karagozian, A.R., "Transverse-jet shear-layer instabilities. Part 1. Experimental studies," *Journal of Fluid Mechanics*, Vol. 593, 2007, pp. 93-129.

Micka, D.J. and Driscoll J.F., "Stratified jet flames in a heated (1390 K) air cross-flow with autoignition," *Combustion and Flame*, Vol. 159, 2012, pp. 1205-1214.

Miller, R. W., "Measurement of Gas flow via critical flow venturis", *ASME*, 1984.
Mitsingas, C.M., Hammack, S.D., Mayhew, E.K., Rajavasanth, R., McGann, B., Skiba, A.W., Carter, C.D., and Lee, T., "Simultaneous high speed PIV and CH PLIF using R-branch excitation in the $C^2\Sigma^+$-$X^2\Pi$ (0,0) band," *Proceedings of the Combustion Institute*, 2019.

Minamoto, Y., Kolla, H., Grout, R.W., Gruber, A., Chen, J.H., "Effect of fuel composition and differential diffusion on flame stabilization in reacting syngas jets in turbulent cross-flow," *Combustion and Flame*, 2015, Vol. 162, 2015, pp. 3569-3579.

Nair, V., Sirignano, M., Emerson, B., Halls, B., Jiang, N., Felver, J., Roy, S., Gord, J., Lieuwen, T.C., "Counter rotating vortex pair structure in a reacting jet in crossflow," Proceedings of the Combustion Institute, Vol. 37, 2019, pp. 1489-1496.

Nair, V., Wilde, B., Emerson, B., Lieuwen, T.C., "Shear layer dynamics in a reacting jet in crossflow", *Proceedings of the Combustion Institute*, Vol. 37, 2019, pp. 5173-5180.

North, A., Magar, M., Chen, J.-Y., Dibble, R., and Gruber, A., "Effect of Pressure, Environment Temperature, Jet Velocity, and Nitrogen Dilution on the Liftoff Characteristics of a N_2-in-H_2 Jet Flame in a Vitiated Co-flow," *Eurasian Chemico-Technological Journal*, Vol. 16, 2014, pp. 141-148.

Panda, P.P., Roa, M., Szedlacsek, P., Laster, W.R., Lucht, R.P., "Structure and dynamics of the wake of a reacting jet injected into a swirling, vitiated crossflow in a staged combustion system", *Experiments in Fluids*, Vol. 56, 2015, pp. 1–20.

Panda, P.P., Roa, M., Slabaugh, C.D., Peltier, S., Carter, C.D., Laster, W.R., Lucht, R.P., "High-repetition-rate planar measurements in the wake of a reacting jet injected into swirling vitiated crossflow," *Combustion and Flame*, Vol. 163, 2016, pp. 241-257.

Panda, P.P., Busari, O., Lucht, R.P., Laster, W.R., "Effect of the nature of vitiated crossflow on the flow-field of a transverse reacting jet," *Experiments in Fluids*, Vol. 58, 2017, pp. 1-20.

Panda, P.P., Busari, O., Roa, M., Lucht, R.P., "Flame stabilization mechanisms in reacting jets in swirling vitiated crossflow", *Combustion and Flame*, Vol. 207, 2019, pp. 302–313.

Pinchak, M.D., Shaw, V.G., Gutmark, E.J., "The Effects of nozzle geometry and equivalence ratio on a premixed reacting jet in vitiated cross-flow", *Combustion and Flame*, Vol. 191, 2018, pp. 353–367.

Pinchak, M.D., Shaw, V.G., Gutmark, E.J., "Flow-field dynamics of the non-reacting and reacting jet in a vitiated cross-flow," *Proceedings of the Combustion Institute*, Vol. 37, 2019, pp. 5163-5171.

Pinchak, M.D., Shaw, V.G., Gutmark, E.J., "The effect of cross-flow fuel injection on the reacting jet in vitiated cross-flow", *Combustion and Flame*, Vol. 199, 2019, pp. 352-364.

Prathap, C., Galeazzo, F.C.C., Kasabov, P., Habisreuther, P., Zarzalis, N., Beck, C., Krebs, W., Wegner, B., "Analysis of NOx formation in an axially staged combustion system at elevated pressure conditions, *Journal of Engineering for Gas Turbines and Power*, Vol. 134, 2012.

Rashwan, S. S., Ibrahim, A. H., Abou-Arab, T. W., Nemitallah, M. A., Habib, M. A., "Experimental investigation of partially premixed methane-air and methane-oxygen flames stabilized over a perforated-plate burner," *Applied Energy*, Vol. 169, 2016, pp. 126-137.

Roa, M., Lamont, W.G., Meyer, S., Szedlacsek, P., and Lucht, R.P., "Emission measurement and OH-PLIF of reacting hydrogen jets in vitiated crossflow for stationary gas turbines", *Proceedings of ASME Turbo Expo*, Copenhagen, Denmark, 2012.

Rodrigues, J. M. N., and Fernandes, E. C., "Stability Analysis and Flow Characterization of Multi-Perforated Plate Premixed Burners", *17th International Symposium on Application of Laser Techniques to Fluid Mechanics*, Lisbon, Portugal, 2014.

Shaaban, S., "On the performance of perforated plate with optimized hole geometry", *Flow Measurement and Instrumentation*, Vol. 46, 2015, pp. 44-50.

Segalman, I., McKinney, R.G., Sturgess, G.S., Huang, L.M., "Reduction of NOx by Fuel-Staging in Gas Turbine Engines – a commitment to the future," In *AGARD Conference Proceedings*, 1993.

Sieder, E.N. and Tate, G.E., "Heat transfer and pressure drop of liquids in tubes", *Industrial and Engineering Chemistry*, Vol. 28, 1936, pp. 1429-1435.

Sirigano, M.D., Nair, V.D., Sunkara, D., Emerson, B.L., Seitzman, J., Lieuwen, T.C., "Impact of flame lifting on nitrogen oxide emissions from premixed reacting jets in a vitiated crossflow," *Proceedings of ASME Turbo Expo*, Phoenix, Arizona, 2019.

Sirigano, M.D., Nair, V.D., Emerson, B., Seitzman, J., Lieuwen, T.C., "Nitrogen oxide emissions from rick premixed reacting jets in vitiated crossflow," *Proceedings of the Combustion Institute*, Vol. 37, 2019, 5393-5400.

Skiba, A.W., Wabel, T.M., Carter, C.D., Hamamck, S.D., Temme, J.E., Lee, T., and Driscoll, J.F., "Reaction layer visualization: A comparison of two PLIF techniques and advantages of kHz-imaging," *Proceedings of the Combustion Institute*, Vol. 36, 2017, pp. 4593-4601.

Skiba, A.W., Carter, C.D., Hamamck, S.D., and Lee, T., "A simplified approach to simultaneous multi-scalar imaging in turbulent flames," *Combustion and Flame*, Vol. 189, 2018, pp. 207-211.

Slabaugh, C. D., Pratt, A. C., Lucht, R. P., Meyer, S. E., Benjamin, M., Lyle, K., Kelsey, M., "The development of an optically accessible, high-power combustion test rig," *Review of Scientific Instruments*, Vol. 85, 2014.

Slabaugh, C.D., Pratt, A.P., and Lucht, R.P., "Simultaneous kHz OH-PLIF/PIV for the study of turbulent combustion at engine conditions," *Applied Physics B*, Vol. 118, pp. 109-130.

Sullivan, R., Wilde, B., Noble, D.R., Seitzman, J., and Lieuwen, T., "Time-averaged characteristics of a reacting fuel jet in vitiated cross-flow," *Combustion and Flame*, Vol. 161, 2014, pp. 1792-1803.

Steinberg, A.M., Sadanandan, R., Dem, C., Kutne, P., Meier, W., "Structure and stabilization of hydrogen jet flames in cross-flows", *Proceedings of the Combustion Institute*, Vol. 34, 2013, pp. 1499-1507.

Tertzakian, P., *The End of Energy Obesity*, John Wily & Sons, 2009.

Tester, J., Drake, E., Driscoll, M., Golay, M., and Peters, W., "Sustainable Energy: choosing among options," The MIT Press, Cambridge, MA, 2005.

Turns, S. R., *An Introduction to Combustion: concepts and applications*, 3rd ed., McGraw-Hill, New York, 2012.

Van Maaren, A., Thung, D. S., and De Goey, L. R. H., "Measurement of Flame Temperatures and Adiabatic Burning Velocity of Methane/Air Mixtures," *Combustion Science and Technology*, Vol. 96, 1994, pp. 327-344.

Vitoshinski, C., "Uber Strahlerweiterung und Strahlablenkung," In: Th. von Karman und T. LeviCivita (Heraugeber): Vortrage aus dem Gebeit der Hydro- und Aerodynamik, (Innsbruck 1922), pp. 248-251, Julius Springer, Berlin 1924.

Wagner, J.A., Grib, S.W., Dayton, J.W., Renfro, M.W., Cetegen, B.M., "Flame stabilization analysis of a premixed reacting jet in vitiated crossflow," *Proceedings of the Combustion Institute*, Vol. 36, 2017, pp. 3763-3771.

Wagner, J.A., Renfro, M.W., Cetegen, B.M., "Premixed jet flame behavior in a hot vitiated crossflow of lean combustion products," *Combustion and Flame*, Vol. 176, 2017, pp. 521-533.

Workbench 19.0, ANSYS, Inc., San Diego, 2017.

Yi, T., Halls, B.R., Jiang, J., Sirignano, M.D., Emerson, B.L., Lieuwen, T.C., Gord, J.R., and Roy, S., "Autoignition-controlled flame initiation and flame stabilization in a reacting jet in crossflow," *Proceedings of the Combustion Institute*, Vol. 37, 2019, pp. 2109-2116.

VITA

Neil S. Rodrigues graduated Magma Cum Laude from Fairfield University in 2012 with a BS in Mechanical Engineering and minors in Mathematics, Physics, and Philosophy. He completed his MS in Mechanical Engineering at Purdue University in 2014, working under the guidance of Professor Paul E. Sojka in spray characterization of Newtonian and non-Newtonian liquids. He worked as a Pilot Plant Engineer and Product Delivery Engineer at Xerox Corporation from 2014 – 2016 in the area of dip coating using complex solutions and dispersions. He then returned to Purdue University in 2016 and worked primarily in the areas of advanced combustor concepts and laser-based diagnostics for his Ph.D. Dissertation under the guidance of Professor Robert P. Lucht. He hopes to embark on a career in research within the areas of propulsion and energy while potentially also teaching core engineering disciplines such as thermodynamics and fluid dynamics in the somewhat distant future. He is a reviewer of the Elsevier journal *Chemical Engineering Science*.

PUBLICATIONS

Publications directly related to doctoral research presented in this Dissertation.

Peer-Reviewed Journal Articles

I. **Rodrigues NS**, Busari O, Senior WCB, McDonald CT, North AJ, Chen Y, Laster WR, Meyer SE, Lucht RP. The Development and Performance of a Perforated Plate Burner to Produce Vitiated Flow with Negligible Swirl under Engine-Relevant Gas Turbine Conditions. *Review of Scientific Instruments 90*. July 2019, pp. 075107-1 – 075107-14, (2019) doi.org/10.1063/1.5100180.

II. **Rodrigues NS**, Busari O, Senior WCB, McDonald CT, Chen Y, North AJ, Laster WR, Meyer SE, Lucht RP. NO_X Reduction in an Axially Staged Gas Turbine Model Combustor through increase in the Combustor Exit Mach Number. *Combustion and Flame 212*. January 2020, pp. 282 – 294, doi.org/10.1016/j.combustflame.2019.10.039.

III. **Rodrigues NS**, McDonald CT, Satija A, Busari T, North AJ, Laster WR, Meyer S, Lucht RP. Reacting Jets in Vitiated Crossflow at High Speeds: The development of an optically-accessible secondary combustion zone for reacting jets in high speed vitiated crossflows at engine-relevant conditions. [Manuscript in-progress for submission to *Combustion Science and Technology or Measurement Science and Technology*]

IV. **Rodrigues NS**, Busari T, McDonald CT, Satija A, North AJ, Laster WR, Lucht RP. Transverse injection of rich, premixed, NG-Air and NG-H2-Air reacting jets into a high-speed vitiated crossflow with negligible swirl. [Manuscript in-progress for submission to *Combustion and Flame or International Journal of Hydrogen Energy*].

V. **Rodrigues NS**, Satija A, Busari T, McDonald CT, North AJ, Laster WR, Lucht RP. Demonstration of high-repetition-rate CH-PLIF in the C-X electronic system within a 1 MW staged gas turbine model combustor using R-branch excitation. [Manuscript in-progress for submission to *Applied Physics B*].

Conference Proceedings and Presentations.

1. **Rodrigues NS**, Busari T, Senior WCB, Chen Y, North A, Portillo JE, Meyer S, Lucht RP. Development and Performance of a Perforated Plate Burner under Gas Turbine Engine-Relevant Conditions. *54th AIAA/SAE/ASEE Joint Propulsion Conference*, Cincinnati, OH. July 2018.

2. **Rodrigues NS**, Busari T, Senior WCB, Chen Y, North A, Laster WR, Meyer S, Lucht RP. Effect of Mach Number and Low Residence Time on the NO_X Emissions Produced by a Staged Gas Turbine Model Combustor. *11th U.S. National Combustion Meeting*, Pasadena, CA. March 2019.

3. **Rodrigues NS**, McDonald CT, Busari T, Senior WCB, North AJ, Chen Y, Laster WR, Meyer S, Satija A, Lucht RP. Reacting Jets in Vitiated Crossflow at High Speeds: The Development of an Optically-Accessible Secondary Combustion Zone. *55th AIAA/SAE/ASEE Joint Propulsion Conference*, Indianapolis, IN. August 2019.

Publications based on research contributions not included in this Dissertation.

Peer-Reviewed Journal Articles

VI.   Shin D, Bokhart AJ, **Rodrigues NS**, Sojka PE, Gore JP, Lucht RP. An experimental investigation of spray characteristics for alternative aviation fuels using a hybrid pressure-swirl airblast atomizer at Lean Blowout conditions. *Journal of Propulsion and Power* [in-press].

VII. Shin D, **Rodrigues NS**, Bokhart AJ, Sojka PE, Gore JP, Lucht RP. Spray characteristics of standard and alternative aviation fuels at cold start condition. *AIAA Journal* [manuscript submitted].

VIII. Busari O, Senior WCB, **Rodrigues NS**, Satija A, Gejji R, Meyer SE, Lucht RP. Experimental investigation of a DLN injector using acetone-PLIF. [Manuscript in-progress for submission to *ASME Journal of Gas Turbines and Power*]

IX.   Busari O, Rodrigues NS, McDonald CT, Satija A, North AJ, Laster WR, Lucht RP. Transverse injection of NG-H2-Air reacting jets. [Manuscript in-progress for submission to *Combustion and Flame*].

Conference Proceedings and Presentations.

4. Bokhart AJ, Shin D, **Rodrigues NS**, Sojka PE, Gore JP, Lucht RP. Spray Characteristics of a Hybrid Airblast Pressure-Swirl Atomizer at Near Lean Blowout Conditions using Phase Doppler Anemometry. *56th AIAA Aerospace Sciences Meeting,* Kissimmee, FL. January 2018.

5. Shin D, Bokhart AJ, **Rodrigues NS**, Sojka PE, Gore JP, Lucht RP. Spray Characteristics of a Hybrid Airblast Pressure-Swirl Atomizer at Cold Start conditions using Phase Doppler Anemometry. *14th International Conference on Liquid Atomization & Spray Systems*, Chicago, IL. July 2018.

6. Shin D, Bokhart AJ, **Rodrigues NS**, Sojka PE, Gore JP, Lucht RP. Spray Formation at Cold Start and Elevated Ambient Pressure conditions using a Hybrid Airblast Pressure-Swirl Atomizer. *57th AIAA Aerospace Sciences Meeting,* San Diego, CA. January 2019.

7. **Rodrigues NS**, Satija A, Lucht RP. Gas density measurements of an underexpanded jet using digital holographic interferometry and dual-pump coherent anti-Stokes Raman scattering. *56th AIAA/SAE/ASEE Joint Propulsion Conference* [Abstract submitted].

8. McDonald CT, **Rodrigues NS**, Busari O, Satija A, North AJ, Laster WR, Lucht RP. Comparison of Elevated and Flush Injectors for a Transverse, Premixed, Reacting Jet in Vitiated Crossflow. *56th AIAA/SAE/ASEE Joint Propulsion Conference* [Abstract submitted].

9. Busari O, **Rodrigues NS**, McDonald CT, Satija A, North AJ, Laster WR, Lucht RP. Confined transverse injection of a premixed H_2 enriched Natural Gas/Air reacting jet from a flush injector into a vitiated crossflow. *56th AIAA/SAE/ASEE Joint Propulsion Conference* [Abstract submitted].

Book Chapters

A. *Spray Characteristics of Conventional and Alternative Aviation Fuels.* Shin D, Hasti V, Rizk N, Bokhart AJ, **Rodrigues NS**, Corber A, Sojka PE, Gore JP, Lucht RP. [In-press].

Publications based on research performed during MS Degree at Purdue.

Peer-Reviewed Journal Articles

X. **Rodrigues, N.S.**, Kulkarni, V., Gao, J., Chen, J., Sojka, P.E. Spray formation and atomization characteristics of non-Newtonian impinging jets at high Carreau numbers. *International Journal of Multiphase Flow 106*, September 2018.

XI. **Rodrigues, N.S.**, Kulkarni, V., Gao, J., Chen, J., Sojka, P.E. An Experimental and Theoretical Investigation of Spray Characteristics of Impinging Jets in Impact Wave Regime. *Experiments in Fluids 56:50*, February 2015.

XII. Kulkarni, V., **Rodrigues, N.S.**, Sojka, P.E. Regimes of Secondary Atomization in Shear Thinning Drops. [Manuscript in-progress for submission to *Journal of Fluid Mechanics*]

Conference Proceedings and Presentations.

10. **Rodrigues, N.S.**, Sojka, P.E. Drop Characteristics of two gelled fluids at High Generalized Herschel–Bulkley Extended Jet Reynolds Numbers using Impinging Jets. *14th International Conference on Liquid Atomization & Spray Systems*, Chicago, IL. July 2018.

11. **Rodrigues, N.S.**, Gao, J., Chen, J., Sojka, P.E. Spray Characteristics of Non-Newtonian Impinging Jets using Digital In-Line Holography. *28th Annual Conference on Liquid Atomization and Sprays Systems*, Dearborn, MI. May 2016.

12. Kulkarni, V., **Rodrigues, N.S.**, Sojka, P.E. Breakup Morphology of Inelastic Drops at Higher Weber Numbers. *28th Annual Conference on Liquid Atomization and Sprays Systems*, Dearborn, MI. May 2016.

13. **Rodrigues, N.S.**, Gao, J., Chen, J., Sojka, P.E. Spray Formation of Herschel–Bulkley Fluids using Impinging Jets. *68th Annual Meeting of the APS Division of Fluid Dynamics*, Boston, MA. November 2015.

14. Sojka, P.E., **Rodrigues, N.S.** Drop Characteristics of non-Newtonian Impinging Jets at High Generalized Bird-Carreau Jet Reynolds Numbers. *68th Annual Meeting of the APS Division of Fluid Dynamics*, Boston, MA. November 2015.

15. **Rodrigues, N.S.**, Sojka, P.E. Spatially Resolved Gelled Propellant Spray Characteristics of Impinging Jets. *ASME 2015 International Mechanical Engineering Congress & Exposition*, Houston, TX. November 2015.

16. **Rodrigues, N.S.**, Gao, J., Chen, J., Sojka, P.E. An Experimental Investigation of the Primary Atomization of Viscoelastic Impinging Jets. *ASME 2015 International Mechanical Engineering Congress & Exposition*, Houston, TX. November 2015.

17. **Rodrigues, N.S.**, Mallory, J.A., Sojka, P.E. Impinging Jet Spray Formation using Viscoelastic Liquids. *AIAA 2015 Propulsion and Energy*, Orlando, FL. July 2015.

18. Collins, P., **Rodrigues, N.S.**, Mallory, J.A. An Experimental Investigation of Sheet Velocity and Jet Diameter Assumptions of Non-Newtonian Impinging Jets. *AIAA 2015 Propulsion and Energy*, Orlando, FL. July 2015.

19. **Rodrigues, N.S.**, Sojka, P.E. Spatially Resolved Drop Characteristics of a Non-Newtonian Impinging Jet Spray. *27th Annual Conference on Liquid Atomization and Sprays Systems*, Raleigh, NC. May 2015.

20. **Rodrigues, N.S.**, Kulkarni, V., Gao, J., Chen, J., Sojka, P.E. Non-Newtonian Impinging Jet Spray Formation at Low Generalized Bird-Carreau Jet Reynolds Numbers. *27th Annual Conference on Liquid Atomization and Sprays Systems*, Raleigh, NC. May 2015.

21. **Rodrigues, N.S.**, Kulkarni, V., Sojka, P.E. Jet Velocity Profile Effects on Spray Characteristics of Impinging Jets at High Reynolds and Weber Numbers. *67th Annual Meeting of the APS Division of Fluid Dynamics*, San Francisco, CA. November 2014.

22. Gao, J., **Rodrigues, N.S.**, Sojka, P.E., Chen, J. Spatially-Resolved, Three-Dimensional Spray Characterization of Impinging Jets by Digital In-Line Holography. *67th Annual Meeting of the APS Division of Fluid Dynamics*, San Francisco, CA. November 2014.

23. **Rodrigues, N.S.**, Gao, J., Chen, J., Sojka, P.E. Spray Formation of a Gel using Impinging Jets. *Gallery of Fluid Motion, 67th Annual Meeting of the APS Division of Fluid Dynamics*, San Francisco, CA. November 2014.

24. Gao, J., **Rodrigues, N.S.**, Sojka, P.E., Chen, J. Measurement of Aerodynamic Breakup of Non-Newtonian Drops by Digital In-Line Holography. *ASME 4th Joint US-European Fluids Engineering Division Summer Meeting*, Chicago, IL. August 2014.

25. **Rodrigues, N.S.**, Sojka, P.E. A Parametric Investigation of Gelled Propellant Spray Characteristics Utilizing Impinging Jet Geometry. *52nd AIAA Aerospace Sciences Meeting,* January 2014.